Thèse n° 9477

Contact Design for Silicon Heterojunction Solar Cells

Présentée le 6 juillet 2022

Faculté des sciences et techniques de l'ingénieur
Laboratoire de photovoltaïque et couches minces électroniques
Programme doctoral en photonique

pour l'obtention du grade de Docteur ès Sciences

par

Luca Massimiliano ANTOGNINI

Acceptée sur proposition du jury

Prof. E. Charbon, président du jury
Prof. C. Ballif, Dr M. G. Boccard, directeurs de thèse
Dr P. Delli Veneri, rapporteuse
Dr A. Cruz, rapporteur
Dr R. Butté, rapporteur

École
polytechnique
fédérale
de Lausanne

2022

Everybody can do it.
But do you have the patience?
— Jackie Chan

A Timéo,
et à ceux qui rendent l'avenir possible

Abstract

Today more than ever the world needs clean energy sources and thus a fast deployment and scaling up of the photovoltaic industry. In this context improving solar cell efficiency plays a major role. Today, crystalline silicon (c-Si) solar cells cover more than 95% of the photovoltaic market. In order to achieve the maximum single junction efficiency for this material, technologies featuring carrier selective passivating contacts are foreseen to be the next successors of actual industrial cells. Among them, the silicon heterojunction (SHJ) solar cell is a promising technology which demonstrated efficiencies up to 26.7%. Its main specificity consists in the use of intrinsic amorphous silicon (a-Si:H) to provide surface passivation to the c-Si, which allows to reach very high operating voltages in comparison to other c-Si based technology. The contact stack is then completed by doped a-Si:H layers to provide charge selectivity as well as a transparent conductive oxide (TCO) layer to support lateral transport. The major drawbacks of the use of a-Si:H and TCO layers is the large parasitic absorption occurring in those layers, as well as the high resistivity to carrier extraction. To address this challenge, a strong focus on alternative non-silicon based thin films with wider band gap has built up in the literature. This still poses fundamental understanding questions as the a priori identification of an efficient contact based on its work function was shown to be challenged in the recent years, due to various unpredicted effects reducing the effect of the work function of the material.

A first part of this thesis focuses on reviewing the fundamental process behind carrier selectivity and discuss the ability of different models from the literature to draw information directly from the peculiar shapes of J-V curves commonly observed in the solar cells featuring newly developed materials. We first discuss the simple four ideal diodes model of Roe to explain the occurrence of S-shapes and kinks depending on the contact quality. We discuss from a theoretical point of view how to improve the model by modifying the ideal diodes by other circuit elements as well as adding bulk recombinations. We test the theory experimentally and identify modifications that should be incorporated in the model. Our findings should be useful to model and identify bottlenecks occurring when developing new materials for any heterojunction contact technology such as perovskite solar cells. It brings also further the fundamental discussion about passivation, selectivity and conductivity of solar cells.

In a second part of the thesis, we explore the development of doped nano-crystalline silicon layers deposited via PECVD, a promising material to replace classical amorphous silicon layers which provides highly conductive and transparent passivating contacts to SHJ solar cells. First, we investigate the influence of TMB and BF_3 as dopant sources on the transparency and

contact properties of nc-Si:H(p) layers as well as their integration in solar cells. We expose the roles of both gases to modify the crystallinity of the layer and find different optimum conditions for both of them to lead high efficiencies, illustrated by a certified 23.9%-efficient solar cell. We report also on further optimization steps of this front junction architecture resulting in certified efficiency of 24.44%.

We deepen our analysis by performing accurate series-resistance breakdown of our best front-junction solar cells. We compare different methods of characterization for the contact resistivity, namely transfer length method (TLM) and symmetrical samples, and perform injection dependent analysis using a state of the art model for the lateral transport [Haschke 2020]. We evaluate precisely a contact resistivity of 100 mΩ cm^2 for those layers. We also attempted to resolve a possible injection dependence of the contact resistivity, which could have an important impact in the realization of localized contacts. We conclude that if such injection behaviour exists, its impact on ρ_c between maximal power and open circuit conditions remains much below 100 mΩ cm^2.

We explore next the *n*-type nc-Si:H layers for application as window layer. In particular, we investigate thickness and doping series to unravel the layer properties along its growth direction. We observe that an increase of the PH_3 flow leads to an amorphization of the first 10-15 nm of the layers and determine a range of doping to optimize the contact properties. This results in an interplay between finding a strong doping in the nucleation zone or having a higher crystallinity at the n/TCO interface. In order to improve the low doping of the nucleation zone of nc-Si:H(n) at the i/n interface, a thin a-Si:H(n) buffer layer is introduced and shown to improve the passivation, selectivity and contact resistivity. Finally, we also report on the beneficial effect of an additional SiO_x capping layer which not only forms a double anti-reflective coating (DARC) but also improves impressively all contact properties, broadening the optimal parameter window. We then explore an optimization pathway of our *n*-type layer. Thinning down the a-Si:H(n) layer to 2.5 nm, adding on top the optimally doped 12.5 nm nc-Si:H(n) layer, and using a IZrO / SiO_x bilayer as DARC allows to improve the current of the solar cell as well as reaching impressive contact resistivity (ρ_c) values of 15 mΩcm^2 for this thin contact, resulting in an efficiency up to 23.7 %, V_{oc} of 733 mV, *FF* of 81.6 % and J_{sc} of 39.6 mA cm^{-2}.

The absorption loss in the front silicon layers remains however the highest share of losses, and therefore we explore theoretically the opportunity of using thinner front side layers or using thin TCO / silicon nitride bilayers to reduce the absorption losses. We finish the discussion by presenting an optimization roadmap, showing a possibility for double-side contacted SHJ cells to reach efficiencies above 26 % without requiring any patterning or localization step.

Keywords : silicon solar cells, high-efficiency, heterojunction, carrier selective passivating contact, nanocrystalline silicon, charge carrier transport, transparent conductive oxide.

Résumé

Aujourd'hui plus que jamais, le monde a besoin de sources d'énergies neutres en carbone et donc de déployer et étendre rapidement l'industrie photovoltaïque. Dans ce contexte, améliorer l'efficacité des cellules solaires joue un rôle majeur. Actuellement, les cellules en silicium cristallin couvrent plus de 95% du marché et les nouvelles technologies de contacts passivants et sélectifs continueront à en améliorer l'efficacité. Parmi celles-ci, les cellules à hétérojonctions représentent une promesse d'amélioration de l'efficacité avec des démonstrations expérimentales atteignant déjà 26.7%. Sa principale spécificité consiste en l'utilisation d'une couche mince de silicium amorphe intrinsèque (a-Si:H) qui fournit une passivation de surface et permet d'atteindre de très hauts voltages en comparaison des autres technologies. Le contact est complété par l'empilement de couches minces dopées de a-Si:H ainsi que d'un oxyde transparent conducteur (TCO) permettant le transport latéral des charges.
Le principal inconvénient de l'utilisation de ces couches est l'importante absorption parasite à l'avant de la cellule, ainsi que la parfois grande résistivité à l'extraction des porteurs de charges. Pour adresser ces défis, une attention importante a été portée dans la littérature sur le développement de matériaux alternatifs avec une plus grande bande interdite que celle des couches de silicium. Cela pose cependant des questions fondamentales sur l'identification a priori d'un contact performant basé sur son travail d'extraction (WF). En effet, un grand nombre de résultats expérimentaux ont défié cette interprétation, en raison de la présence imprévue d'effets réduisant l'impact du WF de ces matériaux. Une première partie de cette thèse est consacrée aux mécanismes fondamentaux derrière la sélectivité des charges et discute l'aptitude de différents modèles de la littérature à tirer des information directement des formes particulières observées dans les courbes *J-V* des cellules solaires possédant des matériaux nouvellement développés. Nous discutons le modèle simple de Roe consistants en quatre diodes pour décrire l'apparition de courbes en "S" et de saturations dépendant de la qualité du contact. Nous analysons d'un point de vue théorique comment améliorer le modèle et comment modifier les diodes idéales par d'autres éléments de circuit ainsi que la façon d'ajouter les recombinaisons de l'absorbeur. Nous testons notre théorie expérimentalement et identifions des modifications nécessaires au modèle. Nos découvertes devraient être utiles pour identifier les limitations apparaissant durant le développement de certains nouveaux matériaux. Nos travaux continuent aussi la discussion fondamentale sur le rôle de la passivation, de la sélectivité et de la conductivité dans la réalisation de contacts idéaux.
Dans une deuxième partie de cette thèse, nous développons des couches dopées p de silicium nano-cristallin (nc-Si:H(p)), un matériau prometteur pour remplacer les couches amorphes

classiques. Premièrement, nous étudions l'influence du gaz précurseur du dopant sur la transparence et les propriétés de contact. Nous exposons le rôle de chaque gaz sur la modification de la cristallinité de la couche et trouvons des optimums pour chacun d'eux, menant à de hautes efficacités, illustré par une certification à 23.9%. Un optimization plus poussé de cette structure de cellule avec la jonction à l'avant, menant à une efficacité certifiée de 24.44%. Nous approfondissons notre analyse en réalisant une décomposition de la résistance série de nos meilleures cellules. Nous comparons différentes méthodes pour la caractérisation de la résistance de contact, à savoir les échantillons TLM et symétriques, et réalisons un analyse tenant compte de la dépendance en injection de chaque élément et identifions une résistance de contact de 100 mΩ cm^2 pour ces couches.
Nous explorons ensuite des couches nc-Si:H de type n. En particulier, nous réalisons des séries en épaisseurs et dopages pour éclaircir les propriétés du matériau le long de la direction de croissance. Il est montré qu'un grand flux de dopant mène à une amorphisation des premiers 10-15 nm de la couche. Nous observons un jeu complexe entre la réalisation d'une couche de nucléation fortement dopée ou d'une haute cristallinité à l'interface n/TCO. Afin d'améliorer le bas dopage dans la zone de nucléation, une fine couche de a-Si:H(n) est introduite et mène à une amélioration de la passivation, de la sélectivité et de la résistance de contact. Finalement, nous montrons également l'effet bénéfique d'une couche supplémentaire de SiO_x qui non seulement réalise un double anti-reflect (DARC), mais aussi améliore significativement toutes les propriétés du contact. Nous explorons ensuite une route d'optimisation. Réduire l'épaisseur de la couche a-Si:H(n) et utiliser une bicouche d'IZrO / SiO_x permet d'améliorer le courant ainsi que d'atteindre des résistances de contact de 15 mΩcm^2 et résulte en une efficacité de 23.7 %.
Néanmoins, l'absorption parasite de la couche avant reste la plus grande source de pertes. Par conséquent, nous explorons théoriquement l'opportunité d'utiliser des couches de silicium plus fines ou des bi-couches de TCO / nitrure de silicium. Nous terminons par présenter une route d'optimisation montrant la possibilité d'obtenir des cellules contactées des deux côtés pouvant atteindre des efficacités de plus de 26 %, sans avoir recours à des contacts localisés ou à des techniques de gravures de couches.

Mots clés : cellules solaires de silicium, hétérojonctions, contacts sélectifs au porteur de charges et passivants, silicium nano-cristallin, transport de porteur de charges, oxyde transparent et conducteur.

Contents

Abstract **i**

List of acronyms and symbols **ix**

1 Introduction **1**
1.1 Photovoltaics - General context 2
1.2 Photovoltaics - Basic operation and limitations 5
1.2.1 Photogeneration and recombination losses 6
1.2.2 Measuring and diagnosing solar cells 15
1.3 Junction formation 17
1.4 Solar Cells technologies 21
1.5 Problematic and structure of this work 27

2 Experimental details and methods **33**
2.1 Solar Cell Fabrication 33
2.1.1 Wafer preparation and wet chemistry 33
2.1.2 Plasma enhanced chemical vapour deposition 33
2.1.3 Magnetron sputtering 35
2.1.4 Screen-printing 36
2.1.5 Process flow for silicon heterojunction solar cells 36
2.2 Material Characterisation 37
2.2.1 Ellipsometry 37
2.2.2 Dark lateral conductivity 38
2.2.3 Raman spectroscopy 39
2.2.4 UV-Vis-NIR Spectroscopy 40
2.2.5 SIMS 40
2.2.6 TEM 40
2.2.7 Transfer Length Method 42
2.2.8 Line resistance 43
2.2.9 Hall effect 44
2.2.10 Four Point Probes 44
2.3 Device Characterization 45
2.3.1 Photoconductance decay measurement 45
2.3.2 Photoluminescence 45

2.3.3 Solar Cell Current-voltage characteristics 46
2.3.4 J_{sc}-V_{oc} method and series resistance extraction 46
2.3.5 External and internal quantum efficiency 48

3 Circuit model for contact limited solar cell 49
3.1 Introduction 49
3.2 Roe's model and limitations 53
3.2.1 Roe's equation 53
3.2.2 Beyond ideal diodes kinetics and external series resistance 57
3.2.3 Effect of bulk recombination 58
3.3 Experimental Comparison 62
3.3.1 Experimental Methods 62
3.3.2 Device nearly compatible with Roe's model 63
3.3.3 Samples of different contact qualities 67
3.4 Conclusion 72

4 Influence of the Dopant Gas Precursor in nc-Si:H(*p*) Silicon Layers 73
4.1 Abstract 73
4.2 Introduction 74
4.3 Experimental Details 76
4.3.1 Solar cell preparation 76
4.3.2 Solar Cell characterisation 78
4.3.3 Characterization on reference layers 79
4.4 Results and Discussion 80
4.4.1 TMB and BF_3 doping series 80
4.4.2 BF_3-doped layer thickness series 86
4.5 Record cell and outlook 87
4.6 Conclusion 89

5 Injection dependent Series Resistance Breakdown 91
5.1 Chapter Structure 91
5.2 Transport in p/N/p samples under illumination 92
5.2.1 Motivation 92
5.2.2 Experimental details 92
5.2.3 Results and Discussion: Transport in Large TLM Sample 93
5.2.4 Results and Discussion: Transport below the diffusion length 96
5.2.5 Conclusion 98
5.3 Comparison of TLM and Symmetric Samples for Accurate Series Resistance Breakdown 100
5.3.1 Abstract 100
5.3.2 Introduction 100
5.3.3 Experimental details and method 103
5.3.4 Results and discussion 105

5.3.5 Solar Cell Series Resistance Breakdown 109
5.3.6 Conclusion 111

6 Thin n-type Nanocrystalline Silicon for Rear-Junction application 113
6.1 Abstract 113
6.2 Introduction 114
6.3 Experimental details and Method 116
6.4 Results and discussion 118
6.4.1 nc-Si:H(n) single layer thickness and doping series 118
6.4.2 Integration of nc-Si:H(n) in the whole front stack of solar cells 124
6.5 Optical gain of replacing front TCO by SiN_x 130
6.6 Roadmap to increase efficiency 135
6.7 Conclusion and perspectives 138

7 Conclusion and perspectives 141

A Appendix 145
A.1 Pysch's law and impact of R_s on FF and η 145
A.2 S-shapes modelling - additional information 150
A.2.1 Effect of bulk recombination: derivation of S-shape positions 150
A.2.2 Activation energy plot 152
A.2.3 S-shape dependence on wafer types 153
A.3 Appendix to nc-Si:H(p) development 156
A.3.1 Passivation quality of samples with high BF_3 flows. 156
A.3.2 Effect of the SiOx DARC deposition 156
A.3.3 SIMS chemical composition and AFM surface topography of nc-Si:H(p) layers 160
A.3.4 Activation energy influence on samples treatments 160
A.3.5 Variability of ellipsometry data fit 164
A.3.6 BF_3 thickness series - transport properties 165
A.3.7 Additional certified J-V results 166
A.3.8 Additional J-V results - nc-Si:H vs. nc-SiO_x:H DARC and forward bias. . 167
A.4 Appendix to nc-Si:H(n) development 168
A.4.1 Raman spectra as a function of dopant flow 168
A.4.2 Contact resistance extraction from thin TCO solar cells 168
A.5 Perimeter Losses 174
A.5.1 Mathematical model 174
A.5.2 Perimeter losses and wafer thickness impact on solar cell 176

Bibliography 179

Remerciements 197

List of acronyms and symbols

Semiconductor Basics

E_g	Band gap energy
E_c	Conduction band energy
E_v	Valence band energy
E_F	Fermi level
E_{Fn}	Electron quasi-Fermi level
E_{Fp}	Hole quasi-Fermi level
FCA	Free carrier absorption
J_n	Electron current density
J_p	Hole current density
n_i	Intrinsic carrier density
n	Total electron density
n_0	Equilibrium electron density
Δn	Excess electron density
p	Total hole density
p_0	Equilibrium hole density
Δp	Excess hole density
SCR	Space charge region
S_{eff}	Effective surface recombination velocity
τ	Carrier lifetime
U	Recombination rate
WF	Work function

Materials

a-Si:H	Hydrogenated amorphous silicon
a-Si:H(i)	Intrinsic hydrogenated amorphous silicon
a-Si:H(n)	n-doped hydrogenated amorphous silicon
a-Si:H(p)	p-doped hydrogenated amorphous silicon
c-Si	Crystalline silicon

c-Si(n)	n-doped crystalline silicon
c-Si(p)	p-doped crystalline silicon
Cz	Czochralski
FZ	Float-Zone
nc-Si:H	Hydrogenated nanocrystalline silicon
nc-Si:H(n)	p-type hydrogenated nanocrystalline silicon
nc-Si:H(p)	n-type hydrogenated nanocrystalline silicon
Ag	Silver
Al	Aluminum
AZO	Aluminum-doped zinc oxide
ITO	Indium tin oxide
SiNx	Silicon nitride
SiOx	Silicon oxide
TCO	Transparent conductive oxide
ARC	Anti-reflective coating
DARC	Double anti-reflective coating
Deposition Processes	
PECVD	Plasma enhanced chemical vapor deposition
PVD	Physical vapor deposition
DC	Direct current
RF	Radio frequency
CO_2	Carbon dioxide
CH_4	Methane
H_2	Hydrogen
NH_3	Ammonia
PH_3	Phosphine
SiH_4	Silane
TMB	Trimethylborane
Characterizations	
η	Energy conversion efficiency
FF	Fill factor
J_{sc}	Short-circuit current density
V_{oc}	Open-circuit voltage

I	Current
J	Current density
V	Voltage
I-V	Current-voltage
J-V	Current density-voltage
iJ	Implied-current density
iV	Implied-voltage
iV_{oc}	Implied-open-circuit voltage
pJ	Pseudo-current density
pV	Pseudo-voltage
pFF	Pseudo-fill factor
FF_0	Fill factor zero
MPP	Maximum power point
R_{s}	Series resistance
E_a	Activation energy
Φ_c	Crystallinity factor
ρ_c	Contact resistivity
σ_d	Dark coplanar conductivity
μ	Mobility
R_{sh}	Sheet resistance
EQE	External quantum efficiency
IQE	Internal quantum efficiency
PL	Photoluminence imaging
RS	Raman spectroscopy
SE	Spectroscopic ellipsometry
TLM	Transfer length method

Solar Cell Technologies

IBC	Interdigitated back-contact
PERC	Passivated emitter and rear cell
PERL	Passivated emitter and rear locally diffused cell
Poly-Si	Polycrystalline silicon
POLO	Polycrystalline silicon on oxide
SHJ	Silicon heterojunction
TOPCon	Tunnel oxide passivated contact

1 Introduction

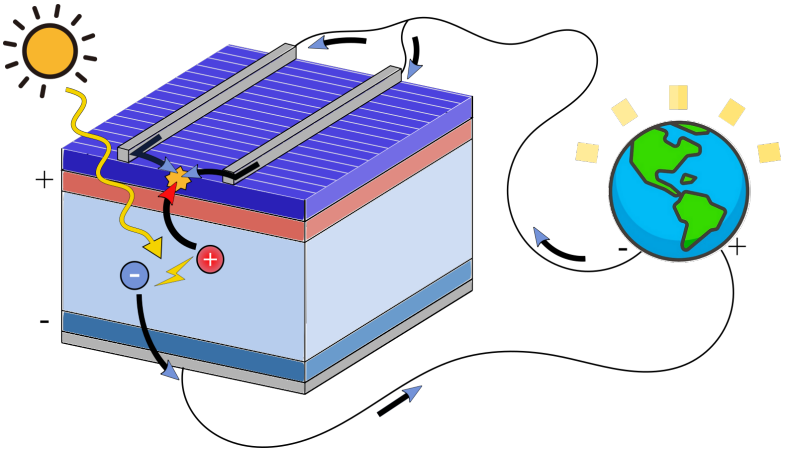

Figure 1.1: Scheme of a typical crystalline silicon solar cell.

Solar cells, the unit element of solar panels, are devices able to convert light power into electrical power, as shown in Figure 1.1: first the light is absorbed in the solar cell and generates electron-hole pairs, which creates an electro-chemical potential. Then those charges need to be separated and extracted through positive and negative terminals with minimal losses. They can then flow through an external circuit where they provide useful electrical power. Solar cells have evolved tremendously since the discovery of the photovoltaic effect in 1839 by Edmond Becquerel and their efficiency has continuously increased. As each day the sun provides earth with the equivalent of 14'000 times the world daily energy consumption, harvesting just a fraction of it could solve mankind's energy problems.

In section 1.1, we will review the general context of photovoltaics and motivate the quest for high efficiency solar cells. In section 1.2, we will review the physical principle of solar cells and the main source of power losses to be taken into account. In section 1.4, we will review the different solar cell technologies that are foreseen to minimize those losses and further improve the efficiency of c-Si solar cell in the next decade. Finally, in section 1.5, we will introduce the goal of this thesis and the main contributions achieved.

1.1 Photovoltaics - General context

Global warming due to anthropogenic CO_2 emissions poses one of the biggest challenges our society has to face. Today, about 50 $GtCO_{2eq}$ are emitted annually, with the largest 75% share coming from energy production using fossil fuels. The remaining share comes from agriculture, forestry and land usage (18.4%), waste (3.2%), and industry emissions where carbon dioxide is a by-product of a chemical conversion process (5.2%), such as for cement. Those first 75% originate from fossil fuel combustion and can be further divided into 30% coming from coal (more than half of it being used for electricity production), 25% from oil (more than half being used for transportation), 15% from gas and about 5% from diffuse emissions of CH_4 linked to the oil, coal and gas value chains [ClimateWatch 2021, OurWorldInData 2020a]. Continuing at this rate of emission, our CO_2 budget to keep global warming below 1.5 °C compared to pre-industrial levels will be expired already by 2030. This means that we entered in the last decade to take impactful actions on the situation in order to avoid unprecedented catastrophic consequences on the climate, biodiversity and human health on a global scale [IPCC 2018].

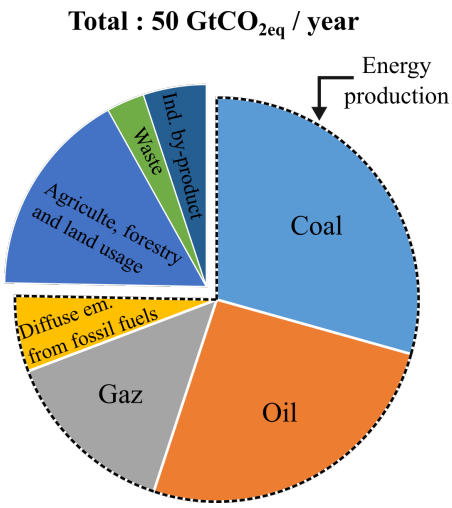

Figure 1.2: Source of CO_2 emissions in 2019.

Therefore, we need to replace our energy dependency on fossil fuels towards CO_2-free and sustainable energy sources, such as provided by solar photovoltaics (PV), wind or hydro electricity. Indeed, these sources of energy offer the possibility to reduce drastically our emissions thanks to their very low CO_2 intensity (CI) as presented in Table 1.1. Compared to traditional fossil fuels, they can reduce the emissions by a factor of 10 to 50.

Note that the carbon intensity of solar energy depends strongly on the electricity mix used to

	CO_2 intensity [gCO_{2eq}/kWh]	
Technology	min.	max.
Hard Coal	753	1095
Gas	403	513
Nuclear	5.1	6.4
Large Hydro	85	147
Onshore Wind	7.8	16
Solar PV, poly-Si	23	83

Table 1.1: CO_2 intensity (CI) of the main technologies for energy production, calculated over the whole life cycle of the power plant. Data from [UNECE 2021]. Carbon capture and storage technologies were not considered for fossil fuels emissions.

produce the poly-silicon (*e.g.* with a Chinese mix of about 750 gCO_{2eq}/kWh or with a Norway mix of 9 gCO_{2eq}/kWh [Moro 2018]), and even lower values could be obtained for example in the case of relocating part of the production in Europe, in areas where clean energy is already available.

In 2019, the total primary energy consumption related to fossil fuels amounted to 136'000 TWh/yr [BP 2021]. Replacing it by clean energy sources as well as covering the new need in energy from emerging countries and the increase in population will happen most likely through an extensive electrification of society, which luckily will be accompanied by an improved energy efficiency [Kurtz 2020]. In turns, demand for new renewable electricity, and in particular for PV, is expected to grow drastically. Focusing on PV, the different scenarios for the energetic transition developed by institutes such as IEA, IRENA or IPCC schedule an expansion of the global PV module installed capacity of 8.5 to 15 TW by 2050, with a yearly production up to 0.6 TW/yr close to that date [IEA 2021, IRENA 2019, IPCC 2014]. This is already an increase of 5 times the actual production of 0.13 TW/yr and of 15 to 30 folds the actual installed capacity, which reaches about 0.6 TW. However, these predictions are pushed further away by the International Technology Roadmap for PV [VDMA 2021], who postulates a need for 60 TW of PV by 2050, with a production of 2 TW/yr already expected by 2030. A reason among others for the discrepancy between those numbers comes from the fact that the first institutions produce their assessment reports on a 7-year cycle which does not allow to track the rapid progress made in the field of PV technology [Victoria 2021][1].

Fortunately, PV, as well as other new renewable energy technologies and batteries, has followed up to today a *learning curve*, *i.e.* an impressive exponential decay of its price correlated with its increased production [Verlinden 2020] at a pace which traditional fossil fuels cannot compete with. This means that since 1970, each time the cumulative production was doubled, the PV industry has experienced a decrease in the manufacturing cost of 22% - or even 40% in the last decade [Verlinden 2020]. More widely speaking, these learning curves are the sign of a healthy economic growth of those industries, where the technology was successfully adapted to an ever growing market. In turn, despite the fact that fossil fuels prices do not reflect their negative impact on climate and human health, PV electricity is nowadays one of the least expensive on the market (see Figure 1.3), having decreased its price by a factor of 10 in the last decade. It can now reach below 1 ct$/kWh in sunny regions and is seeing its global installed capacity grow exponentially.

The thrive of PV industry has been possible and is set to continue thanks to a constant R&D effort and improvements in reducing the manufacturing cost, through [Verlinden 2020]:

- standardization of the entire supply chain.
- improvements on the whole material value chain (*e.g.* reduce silicon losses and silver consumption).

[1] A new version of the IPCC scenario to mitigate climate change will be available in March 2022: https://www.ipcc.ch/report/sixth-assessment-report-working-group-3/

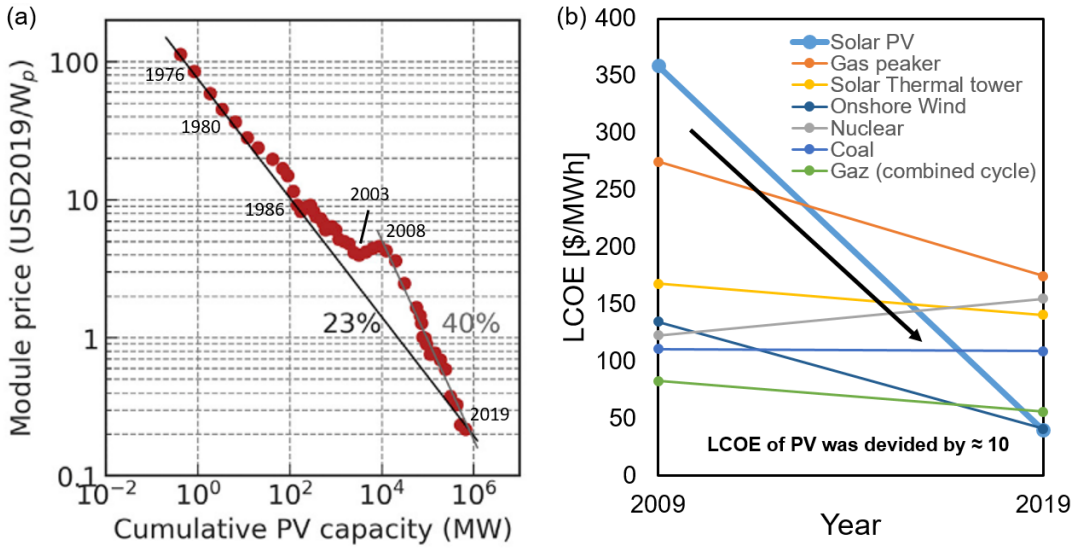

Figure 1.3: (a) PV module price versus cumulative capacity (learning curve). Reproduced from [Victoria 2021]. (b) Levelized cost of electricity from new power plants. Reproduced from [OurWorldInData 2020b].

- increase in lifetime and reliability of PV modules, with warranties of typically of 25 years and which are likely set to become longer.
- massive development of the Chinese industry (economy of scale).
- the increase of automated steps and a major reduction in manufacturing tool cost.
- and last but not least, an exceptional increase of solar cell efficiency, *i.e.* the portion of energy in the form of sunlight that can be converted into electricity by the solar cell.

The last point, improving solar cells efficiency, has been a major lever to reduce costs, decreasing the impact of all other components in terms of $/W. In fact, it triggered an important industrial shift towards higher efficiency technologies while precluding new products with lower efficiency to take important market shares. Three important historical lessons are to be drawn from Figure 1.4(a) where efficiency governed the market trend. First, it shows the very fast replacement of multi-crystalline wafers by higher quality mono-crystalline ones, despite the initial higher processing cost of the latter, thanks to an average $+4\%_{abs}$ solar cell efficiency boost. It also shows the low penetration of the various *thin-film* technologies compared to c-Si, despite their lower processing cost. Finally, the industry is massively updating their production lines to modify the contacting technology by shifting from the so-called *Al-BSF* to the *PERC* solar cells (concepts that we will review in the next sections) allowing a boost of the efficiency from about 20 % to up to 24 % in production. Regarding the future, it is commonly admitted that over the next years the industry will update their production lines towards passivating contact technologies, such as TOPCon or SHJ solar cell, that we will describe below,

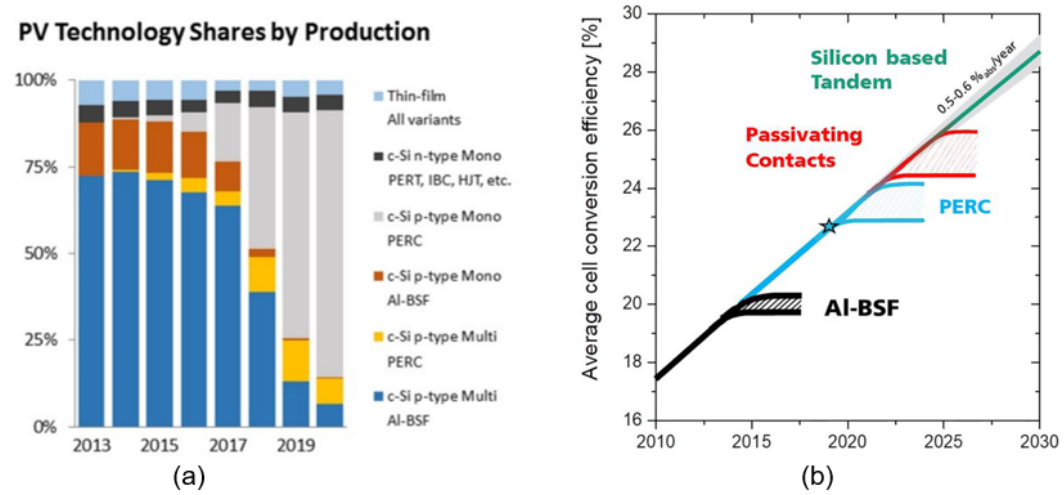

Figure 1.4: (a) Market share of the main PV-technologies in the recent years [PV-TECH 2019]. (b) Foreseen evolution of solar cell efficiency for industrially relevant technologies [Hermle 2020].

while on the longer term, tandem solar cell technology is awaited to bring efficiency beyond the 30% limit [Hermle 2020].

Moreover, higher solar cell efficiency does not only reduce the cost of electricity, but also decrease even more the CO_2 footprint of PV and improve the energy payback time. To cite an actual example, to thrive through competitiveness against the Chinese industry (~ 60% of the market share in 2018 [Wilson 2020]), European actors such as Meyer-Burger are aiming for the high-end market of high efficiency solar cells to rebuild a European industry, scheduling a 5 GW production line for 2026 [PV-magazine 2021b]. In conclusion, to enable a massive integration of PV in society and keep its healthy growth rate, the solar cell efficiency has been a major asset and nowadays the market is ready to accept an increased production price of 0.1\$/W for a 3.5 $\%_{rel.}$ power increase [Verlinden 2020].

1.2 Photovoltaics - Basic operation and limitations

Solar cell technologies are mainly based on semiconductor materials that can convert the solar spectrum into electric power by transforming photons into electron/hole (e^-/h^+) pairs inside the so-called *absorber* and by subsequently avoiding the recombination of those charges to finally extract them with minimal resistance through dedicated positive and negative contacts. Therefore, any solar cell efficiency is dictated by the way it manages its different *optical*, *recombination*, and *resistive* properties. We will describe them shortly and provide the corresponding limiting efficiency calculated considering the AM1.5G solar spectrum and a temperature of 300 K for crystalline silicon (c-Si). All the processes described in this section are illustrated on Figure 1.5.

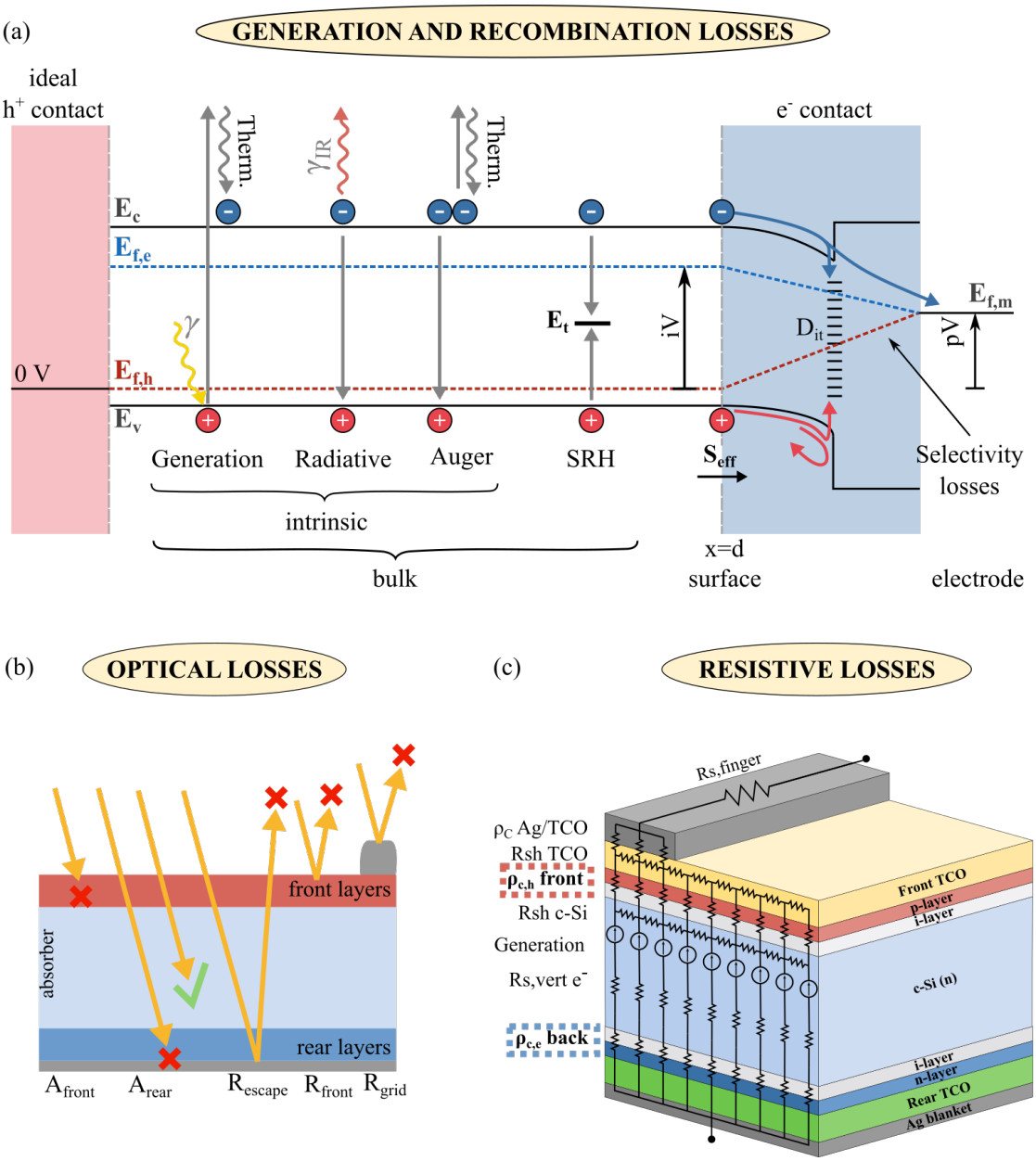

Figure 1.5: Main sources of losses in c-Si solar cell. (a) Generation and recombination losses (including selectivity and finite conductivity of the contact). (b) Optical losses from bad light management. (c) Resistance modelling example of a top/rear SHJ unit cell.

1.2.1 Photogeneration and recombination losses

Photogeneration losses : As a first approximation, in intrinsic semiconductor materials in thermal equilibrium, the electrons are confined to an ensemble of low energy states forming the so-called *valence band*. Since they fill all the available states, they cannot change positions and no significant current can flow. The next available states are situated in the so-called

conduction band. However, they are separated by a bandgap of forbidden energy, characterized by an energy range E_g which needs to be overcome to transfer an electron from the valence band to the conduction band. For a photon to be absorbed, it needs to have an energy higher than E_g to excite an electron to an available state. Therefore, the absorber is transparent to all photons with lower energy than the bandgap and those will be lost, which shapes the wavelength-dependent absorption coefficient $\alpha(\lambda)$. This accounts already for a loss of 23% of the incident light power for a c-Si absorber.

When a photon is absorbed in the semiconductor, it gives its energy $E_\gamma > E_g$ to an electron of the valence band, allowing it to reach the conduction band. This electron will be able to move freely in neighboring states in the conduction band and conduct current (hence the name). Similarly, the state left empty in the valence band allows now electrons to move one after the other, making the available state move in the opposite direction, and for this reason it is useful to think about it as the movement of a positive charge: a hole. Unfortunately, when the electron is excited to higher energy level in the conduction band (or if the hole is generated for below the valence band edge), it will thermalize and dissipate its excess energy until it reaches the band edge. Thermalization accounts for another 33% loss of the sun power in the case of c-Si absorber.

Current Balance : As the photon flux creates continuously e^- / h^+ pairs in the absorber, this process will be inevitably compensated by the recombination of the charge carriers, otherwise an infinite amount of charges would be created. These mechanisms are balanced with the current we drain from the solar cell which can be written as (in units of $\mathrm{mA\,cm^{-2}}$)

$$J_{Gen} = J_{out} + J_{Rec} \tag{1.1}$$

This balance defines the e^- and h^+ densities in the bulk of the absorber, n and p, respectively. As discussed previously, those quickly thermalize separately with their respective conduction and valence band, and the populations can be described out of equilibrium by the mean of their electro-chemical potential - the *quasi-Fermi level* (qFL). In the case of a non-degenerate semiconductor for which Boltzmann approximation holds, these relationships are

$$n = n_0 + \Delta n = N_c \exp\left(\frac{E_{F,e} - E_c}{k_B T}\right) \quad \text{and} \quad p = p_0 + \Delta p = N_v \exp\left(\frac{E_v - E_{F,h}}{k_B T}\right), \tag{1.2}$$

where N_c and N_v are the effective densities of states in the conduction and valence bands, E_c and E_v are the energy level of the conduction- and valence-band edges, k_B the Boltzmann constant, T the temperature, $E_{F,e}$ and $E_{F,h}$ the electron and hole qFL, n_0 and p_0 are their equilibrium concentrations, and finally $\Delta n = \Delta p$ is the excess carrier concentration due to illumination and applied voltage.

The energy difference between the two chemical potentials defines the maximum work that

the absorber can provide, leading to the definition of the *implied voltage*

$$iV = \frac{E_{F,e} - E_{F,h}}{q} = \frac{k_B T}{q} \ln\left(\frac{np}{n_i^2}\right) \approx \frac{k_B T}{q} \ln\left(\frac{(N_D + \Delta n)\Delta_n}{n_i^2}\right), \tag{1.3}$$

where n_i is the intrinsic carrier density related to the equilibrium concentration by $n_i^2 = n_0 p_0 = N_c N_v \exp\left(\frac{E_v - E_c}{2k_B T}\right)$, and in the second equality we approximated the formula for the case of an n-type material, with N_D the donor density. Therefore, the balance equation 1.1 between generation and recombination defines iV, or equivalently the maximum injection level Δn the device can reach for a given illumination, as well as the maximum current that can be extracted from the device at this injection level $iJ(\Delta n) \equiv J^{Gen} - J^{rec}(\Delta n)$. The relation $iJ(\Delta n) = f(iV(\Delta n))$ is the so-called *implied J-V* curve and define the maximum power that can be drawn from the solar cell as $iP = iJ \times iV$. To compute the latter, it is necessary to assess the different recombination mechanisms, which are reviewed next.

Bulk Recombination losses : The first mechanism is the *radiative recombination*, a *two-body* process where an electron recombines with a hole by emitting a photon with energy equal to E_g. The expression for the radiative rate (in [$cm^{-3}\,s^{-1}$]) is given by

$$U_{Rad} = r_{ec}(np - n_i^2) \approx \begin{cases} r_{ec} N_D \Delta n & \text{if } \Delta n \ll N_D \text{ (low injection)} \\ r_{ec} \Delta n^2 & \text{if } \Delta n \gg N_D \text{ (high injection)} \end{cases} \tag{1.4}$$

where r_{ec} is the radiative recombination coefficient and in the second equality we approximated the formula for the case of an n-type material.

The second mechanism is the *Auger recombination*, a *three-body* process, where an e^- / h^+ pair recombines and gives their energy to an additional e^- or h^+ which then thermalizes. The recombination rate for the Auger process is given by

$$U_{Auger} = C_n n^2 p + C_p p^2 n \approx \begin{cases} C_n N_D^2 \Delta n & \text{if } \Delta n \ll N_D \text{ (low injection)} \\ (C_n + C_p)\Delta n^3 & \text{if } \Delta n \gg N_D \text{ (high injection)} \end{cases} \tag{1.5}$$

where $C_{n/p}$ are the Auger coefficients and the approximation for n-type material was applied again in the second equality.

The third mechanism is the *Shockley-Read-Hall* recombination. In this case, the presence of a bulk defect allows for an energy level inside the bandgap, which can capture both electrons and holes from their respective band and make them recombine. With $\sigma_{n/p}$ the electron and hole capture cross sections respectively, N_t the trap density, E_t the energy level of the defect,

v_{th} the thermal velocity of the charge carriers, we have

$$U_{SRH} = \frac{v_{th} N_t (np - n_i^2)}{\frac{1}{\sigma_p}(n + n_1) + \frac{1}{\sigma_n}(p + p_1)} \approx \begin{cases} \Delta n \left(\frac{1 + \frac{2n_i}{N_D} \cosh\left(\frac{(E_t - E_i)}{k_B T}\right)}{\sigma_n v_{th} N_t} \right)^{-1} & \text{if } \Delta n \ll N_D \text{ (low inj.)} \\ \Delta n \left(\frac{2}{\sigma_n v_{th} N_t} \right)^{-1} & \text{if } \Delta n \gg N_D \text{ (high inj.)} \end{cases} \tag{1.6}$$

where n_1 and p_1 simplify the notation and are given by $n_1 = n_i \exp\left((E_t - E_F^i)/k_B T\right)$ and $p_1 = n_i \exp\left((E_F^i - E_t)/k_B T\right)$, and E_F^i is the intrinsic fermi level in the absence of doping. In the approximation, we assumed $\sigma_n = \sigma_p$ for simplicity. The SRH recombination rate therefore varies between two constants at low and high injection, that are independent from the doping level and Δn. In contrast to radiative and Auger recombination mechanisms that are of *intrinsic* nature to the semiconductor material, SRH recombination can be greatly reduced by using high quality materials, such as mono-crystalline Czochralski (CZ) silicon wafer, or even better, float-zone (FZ) wafers. The latter ones are however more expensive and are usually used for research purposes only [2].

Surface recombination losses : In the majority of c-Si solar cells, the primary recombination source is surface recombination. It exists due to the presence of dangling silicon bonds that create defect states within the bandgap. Without loss of generality, it is possible to define the surface recombination rate (in units [$\mathrm{cm}^{-3}\,\mathrm{s}^{-1}$]) as

$$U_{surf} = \frac{S_{eff}\left(n(x = d), p(x = d)\right) \Delta n(x = d)}{W} \tag{1.7}$$

where S_{eff} is the surface recombination velocity (in [$\mathrm{cm\,s}^{-1}$]) and is a measure of how efficiently carriers recombine at the surface, Δn is the carrier density bordering on that surface and W is the wafer thickness. Note that the "surface" is arbitrarily located at a position $x = d$ where the carrier concentration $\Delta n(x = d)$ is known, often at the edge of the c-Si space-charge region, *i.e.* at the limit where the qFL of the absorbers can still be considered flat and separated.

It is not easy to model surface recombination velocity and several formalisms exist depending on the passivation strategy, such as an extended SRH formalism [Mcintosh 2017], models of the amphoteric nature of defects at the c-Si surface [Olibet 2007] or different analytical computations in the case of a highly-doped diffused surface in direct contact with a metal [Cuevas 1989, Cuevas 1996]. However, the fact that this recombination rate is inversely proportional to W allows for a simple experimental procedure to extract S_{eff} from a series of measurements on wafers with different thicknesses (see *e.g.* [Manzoor 2021] for a recent example).

Intuitively, surface recombination can be minimized, either by reducing the defect density or by decreasing one or both carriers conductivities close to this surface [Onno 2019]. The first

[2] However, it is worth mentioning that CZ wafer quality greatly improved in the last decade, which together with their lower price also contributed to the recent improvements in PV performance.

strategy can be embodied by the reduction of the surface defect density N_s and is referred to as *chemical passivation*. In the case of the reduction of conductivity of only one carrier type, we talk about *field-effect passivation* which can be realized by different means, such as a highly doped diffused region close to the surface [Cuevas 1989], a band-bending induced by the junction with a material of different work function (WF) than the c-Si absorber [Sze 2006] or by a material that possesses a strong fixed charge Q_f [Cuevas 2018].

Therefore, S_{eff} takes room temperature values

- up to $1 \times 10^7\,\mathrm{cm\,s^{-1}}$ for unpassivated direct metal/silicon contact[3].
- in the range of 100–1000 $\mathrm{cm\,s^{-1}}$ for highly doped diffused surfaces, reducing the conductivity to a given carrier-type but unfortunately increasing the amount of Auger recombination in this area [Cuevas 1989].
- and below 10 $\mathrm{cm\,s^{-1}}$ for surfaces passivated with different thin films, such as hydrogenated amorphous silicon a-Si:H or silicon oxide SiO_x which strongly reduce the defect density or aluminum oxide (AlO_x) and silicon nitride (SiN_x) that possess strong negative and positive charges [Cuevas 2018].

Now that we have defined the different recombination rates in [$\mathrm{cm^{-3}\,s^{-1}}$], we can relate each of them to a current density in [$\mathrm{mA\,cm^{-2}}$] by $J = q \times W \times U$, and the balance equation 1.1 now reads

$$qWG - J_{out} = qW\left(U_{Rad} + U_{Auger} + U_{SRH}\right) + qS_{eff}\Delta n \tag{1.8}$$

where we defined the average carrier generation rate G. It is also common to define a specific lifetime (in [s]) associated with each process as $U = \Delta n/\tau(\Delta n)$, without any loss of generality, and the balance equation (divided by qW) now reads as

$$G - \frac{J_{out}}{qW} = \frac{\Delta n}{\tau_{Rad}} + \frac{\Delta n}{\tau_{Auger}} + \frac{\Delta n}{\tau_{SRH}} + \frac{\Delta n}{\tau_{Surf}} \equiv \frac{\Delta n}{\tau_{eff}} \tag{1.9}$$

where the identification of each term can be done with equation 1.8. The sum of the inverse lifetimes is defined as the inverse of the effective lifetime τ_{eff}, and can be measured via photo-conductance decay measurement (PCD) with different methods of analysis (transient, quasi-steady-state (QSS) and generalized mode) [Sinton 1996]. Figure 1.6 shows a typical injection dependence of τ_{eff} here with a moderate effect of SRH and surface recombination. The latter effect is shown by a tailing at low injection while radiative and Auger recombination lead to a decrease of the lifetime at high injection.

[3] Note that the effective surface recombination velocity at 300 K cannot be infinite because it will be limited by the thermal velocity of the carriers $v_{th} = 1 \times 10^7\,\mathrm{cm\,s^{-1}}$, which is related to the bulk conductivity, *i.e.* to how fast the bulk can provide carriers to recombine. As carriers recombine at the surface, the latter is depleted of charges and the conductivity is reduced in its vicinity, thus "passivating" the surface in a self-limiting way [Onno 2019].

The typical injection level (Δn) reached by solar cells under operating conditions varies in the region indicated on the graph. It reaches in particular about 1×10^{15} cm^{-3} at the *maximal power point* (MPP), *i.e.* when an optimal trade-off is found between increasing Δn, and thus iV, without increasing too much the recombination that would compromise the maximal current we can extract from the solar cell $iJ = J^{Gen} - J^{rec}$. Likewise, Δn reaches values about 1×10^{16} cm^{-3} at *open-circuit* (OC) conditions, *i.e.* when $J^{Gen} = J^{rec}$ forcing the recombination to balance the photogenerated current.

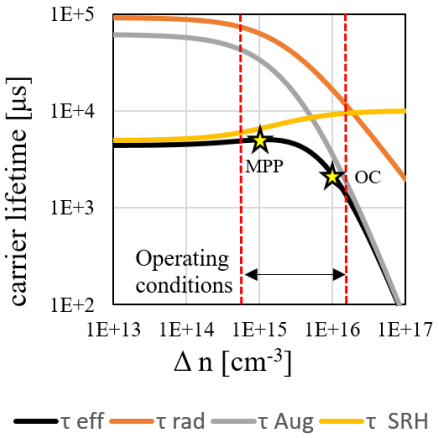

Figure 1.6: (a) Typical bulk lifetime components.

The radiative, Auger and SRH processes together form the *bulk* recombination of the absorber. The first two are both of *intrinsic* nature and dictate the maximum efficiency that can be achieved with a given semiconductor material. In fact, the limiting efficiency for c-Si was originally computed by taking into account only radiative recombination [Shockley 1961], reaching $\eta^{SQ} = 32\%$. This model was then updated to take into account Auger recombination, free-carrier absorption (FCA) and assuming a perfect Lambertian light trapping scheme and an undoped wafer [Tiedje 1984, Kerr 2003, Richter 2013]. An optimal efficiency of $\eta^{Richter} = 29.4\%$ was computed with an optimal wafer thickness $W = 110\,\mu$m (sometimes called the *Richter-limit*). However, nowadays the bulk quality of typical industrial grade CZ wafer is not perfect and still some SRH recombination subsists. It has been shown by Augusto *et al.* that if excellent surface passivation is achieved, this remaining effect decreases slightly the maximum effiency to $\eta^{Augusto} \approx 29\%$, and that the optimum thickness is found for wafers of 40–60 µm [Augusto 2020].

This is to be compared with the maximum efficiency ever measured for a c-Si single junction device of $\eta^{record} = 26.7\%$ established by Yoshikawa *et al.* [Yoshikawa 2017]. Those authors also discussed a maximal practical efficiency of $\eta^{pract} = 27.1\%$ that they estimate could be reached using their solar cell design and fabrication process. To reach such a high efficiency, it is necessary to tackle all the other following sources of power mitigation such as selectivity, resistive and optical losses.

Selectivity and conductivity losses : Said in an intuitive way, once the absorber is inflated with carriers, e^- and h^+ need to be extracted towards two different contacts to generate an electrical current. This means that to extract meaningful power out of the solar cell, not only the qFL splitting in the absorber (iV) should be maximized by providing excellent bulk and surface passivation, but current should be extracted through distinct positive and negative contacts. The latter can be realized in various ways, but they always feature at the end a metal electrode. The later allows only for a single Fermi level $E_{f,m}$, and therefore electron and hole qFLs will

collapse towards a single energy level in its vicinity, equivalent to an infinite recombination. As a consequence, it results in a difference between the implied voltage and the voltage measured between the two contacts, the so-called *pseudo-voltage pV*. To avoid this, it is important that only a single qFL decays at a contact, *i.e.* that $E_{f,e}$ remains constant while $E_{f,h}$ drops to the same level at the negative (electrons) contact and vice-versa at the positive (holes) contact. This very important property that the contact needs to fulfil is called *selectivity*.

Moreover, to avoid power losses when the current flows from the absorber to the external electrodes passing through the contacts, the latters should provide a high *conductivity* to the "majority-carrier" (the carrier type intended to be collected).

***Passivation*, *selectivity* and *conductivity* are therefore the three ideal properties that the contacts of a solar cell need to fulfil - and contacting technologies that attempt to achieve these three goals are named *Carrier Selective Passivating Contact* (CSPC).**

In fact, those three properties are not independent and can be related to measurable quantities. For this we will follow the arguments of Onno *et al.* who themselves bring forward the base physical principles exposed by Würfel *et al.* stating that the electrons and holes can only move in a direction to minimize their electrochemical potential [Wurfel 2015, Onno 2019]. First, we write the voltage drop of each charge carrier through the contact as well as the continuity equation for the current, assuming no generation or recombination inside the contact:

$$\left(E_{f,e} - E_{f,m}\right) \equiv q\Delta V_e \equiv -q\rho_{c,e}J_e \tag{1.10}$$

$$\left(E_{f,m} - E_{f,h}\right) \equiv q\Delta V_h \equiv q\rho_{c,h}J_h \tag{1.11}$$

$$J_{out} = J_e + J_h \tag{1.12}$$

Here, we defined without any loss of generality the carrier specific contact resistivities $\rho_{c,e}$ and $\rho_{c,h}$ (in units of $[\Omega\,\mathrm{cm}^{-2}]$) which are injection and voltage dependent, *i.e.* $\rho_{c,e} = f_e(iV, \Delta V_e)$ and $\rho_{c,h} = f_h(iV, \Delta V_h)$, where the functions f_e and f_h depend on the actual implementation of the contact. Combining those equations, we can express the voltage drop for the electrons as

$$\Delta V_e = \frac{\rho_{c,e}}{\rho_{c,h}}\Delta V_h - \rho_{c,e}J_{out} \tag{1.13}$$

Therefore, to realize a good electron contact with minimal drop of their quasi-Fermi level, the first term of equation 1.13 tells us that a high asymmetry of the contact resistivity should be realized ($\rho_{c,e}/\rho_{c,h} \ll 1$), which is the condition for ideal selectivity. The second term indicates that a low absolute value for the contact resistivity of electron $\rho_{c,e}$ ($\rho_{c,e} \ll 1$) should be achieved as well, which is the condition for ideal conductivity.

To establish a metric for passivation, the discussion is made easier by considering open-circuit conditions, however the metric eventually found also describes the passivation quality away

from OC conditions [Onno 2019]. The implied voltage reads

$$iV = \Delta V_e + \Delta V_h \tag{1.14}$$

$$= -\rho_{c,e} J_e + \rho_{c,h} J_h \tag{1.15}$$

$$\overset{\text{OC}}{=} \left(\rho_{c,e} + \rho_{c,h}\right) J_h \tag{1.16}$$

where in the last line we used the fact that at OC $J_e + J_h = 0$. This last equation implies that a high passivation is accomplished by achieving a high sum of the partial contact resistivity ($\rho_{c,e} + \rho_{c,h} \gg 1$). Note that the same analysis can be done for the hole-contact, and therefore the requirements to reach perfect passivation, selectivity and conductivity are

for e$^-$-contact			for h$^+$-contact	
$\rho_{c,e}/\rho_{c,h}$	$\ll 1$	(selectivity)	$\rho_{c,h}/\rho_{c,e}$	$\ll 1$
$\rho_{c,e}$	$\ll 1$	(conductivity)	$\rho_{c,h}$	$\ll 1$
$\rho_{c,e} + \rho_{c,h}$	$\gg 1$	(passivation)	$\rho_{c,e} + \rho_{c,h}$	$\gg 1$

Looking at the conditions to realize those three properties, it is trivial to see that achieving conductivity and passivation implies a high selectivity. However, the opposite is not true, and a high selectivity with either of the two other properties does not imply the third one. Examples that we will introduce later are the Al-BSF contact, that has great selectivity and conductivity, but poor passivation, and the SHJ contacts that can have great passivation and selectivity but poor conductivity[4] [Onno 2019].

Resistive losses : We already introduced in the text above two resistive effects that are given by the absorber finite conductivity and the contact resistivity. Those effects were discussed assuming one dimensional physics and a perfect conductivity once the current is extracted from the contact. In practice however, the currents can never be collected on the whole area of the solar cell as it needs space for the light to come in. Therefore, lateral transport towards the electrodes needs to be discussed in a two-dimensional model, as well as the current transport inside the metallic grid. Rigorously, as the current through the solar cell is inhomogeneous because of generation, the exact computation of the resistive power losses should be made by discretizing the absorber, the contact and the additional conductive layers in small resistive elements and compute the following integrals

$$P_e = \frac{1}{A} \iiint_V \frac{\left|\vec{J}_e\right|^2}{\sigma_e} dV, \quad \text{and} \quad P_h = \frac{1}{A} \iiint_V \frac{\left|\vec{J}_h\right|^2}{\sigma_h} dV$$

for the electron and holes, respectively, where the partial conductivities depend on the local carrier densities and A is the area of the solar cell. The total resistive power loss is then $P_{tot} = P_e + P_h$.

[4] From our understanding, this makes the appellation "Carrier Selective Passivating Contact" a misnomer, and it would be preferred to rename it as "Contact Selectively Conductive and Passivating" (CSCP).

Fortunately, in practice the analysis can be simplified in many relevant cases. For example, if we can assume a perfect selectivity of the contact and admit that most of the photogeneration will occur in the vicinity of the front surface (technically, 2/3 of J^{Gen} occurs in the first 10 µm). In this case, the electrons and holes take independent distinct paths and it is easier to model the resistive losses. We introduce here a recent model developed by Haschke *et al.* [Haschke 2020] that we will discuss in depth in chapter 5. It introduces relevant parameters to discuss SHJ solar cells and an illustration of the equivalent resistance circuit is shown on Figure 1.5(c) overlaid over a unit cell. It includes the contact resistivity for the electron at the back contact $\rho_{c,e}^{back}$, the contact resistivity for the holes at the front contact $\rho_{c,h}^{front}$, the wafer finite conductivity through the vertical resistance for the electron $R_{s,e}^{vert}$ and the lateral sheet resistance of the holes $R_{sh,h}^{c-Si}$, as well as the sheet resistance of an additional TCO conductive layer R_{sh}^{TCO} and the contact resistance between the later and the silver $\rho_c^{TCO/Ag}$, and finally the fingers resistance R_s^{finger}.

At the rear, the discussion is simplified thanks to the high conductivity provided by the full area silver layer which decouples the lateral transport and contact resistivity for electrons.

At the front side, the power losses description remains complex and is the result of the interplay of two conductive sheets connected by $\rho_{c,h}^{front}$. In particular, the lateral transport can be provided by the absorber, whose conductivity can be modulated by the excess charges as $\sigma_h \approx q\mu_h \Delta n$ and $\sigma_e \approx q\mu_e(N_D + \Delta n)$. In this paradigm, it is therefore important to maximize the passivation to increase Δn as well as to find materials allowing very low front contact resistivity. In this way, one can benefit from the lateral transport provided by the absorber without further need for the extra conductivity provided by the TCO layer. Typically, reaching $\rho_c^{front} < 10\,\mathrm{m\Omega\,cm^2}$ would allow for a lateral transport uniquely through the c-Si with minimal additional resistance (given finger width of 50 µm) and open the possibility of TCO free SHJ solar cell (see Appendix A.1 for more detailed analytical expressions of the series resistance in relevant configurations).

Finally, note that in this example, the hole contact was placed at the front, but the opposite can also be described by the same model, provided the relevant carrier conductivity is used to model the vertical and lateral transport in the absorber.

Optical Losses : The optical properties depend on how much of the light is effectively absorbed in the absorber, compared to the light that is reflected out of the cell or parasitically absorbed in any other parts. It depends on i) the absorber finite thickness W and its wavelength-dependent absorption coefficient $\alpha(\lambda)$, ii) the transparency of the front and rear layers, iii) the metal-grid shadowing, and iv) the reflection at the front, that should be minimized, and v) the reflection at the rear, that needs to be maximized to allow multiple paths of the light through the absorber. An illustration of the different optical losses can be found on Figure 1.5(b).

Most common light management strategies for c-Si technologies include texturing of the absorber surface and anti-reflection coatings (ARC) to reduce the reflection losses and increase

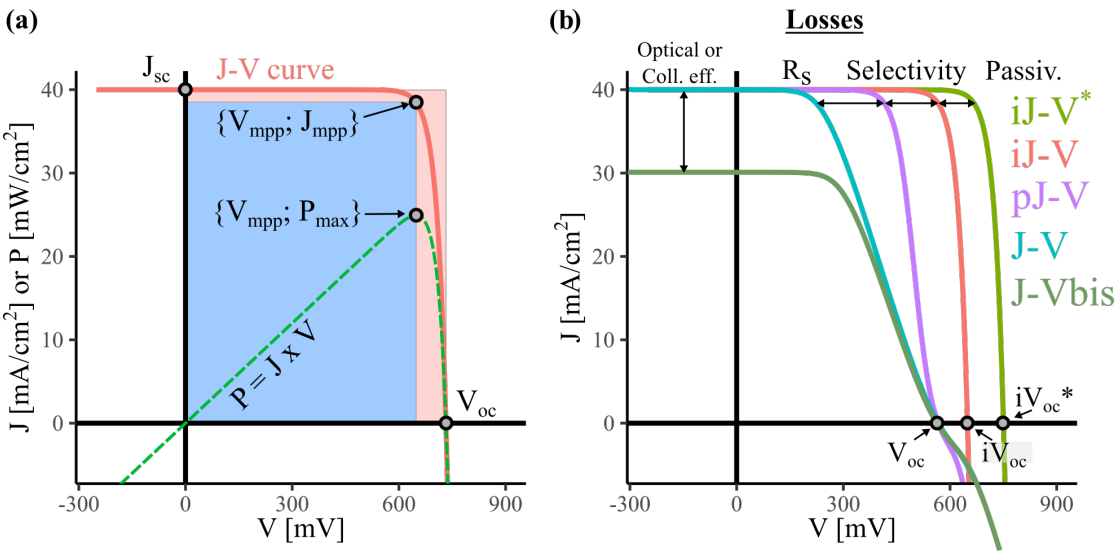

Figure 1.7: (a) Typical J-V *curve of a finished solar cell. (b) The different type of* J-V *curves as described in the text allowing to decompose the different losses in the solar cell.*

the light trapping, reducing the metal area fraction - or even placing the contact at the backside, and finally developing contacting layers as transparent as possible. At the rear side, using a thick film of low refractive index to separate the metal and the absorber is a strategy used to provide better infrared rear-reflection.

1.2.2 Measuring and diagnosing solar cells

In the previous sections, we have defined and described the different loss mechanisms that can affect a solar cell. Now, we introduce the mean to assess its performance.

The *J-V* curve is the current-voltage characteristic of a finished solar cell (such as presented on Figure 1.1) taken under specific illumination and temperature conditions. For terrestrial PV application, the standard test conditions (STC) for the measurement correspond to the AM1.5G spectrum with 1000 $\mathrm{W\,m^{-2}}$ (= 1 sun) and 25 °C. A typical example of a *J-V* curve is shown in Figure 1.7(a) together with the corresponding power density curve ($P = J \times V$). The maximum value of the power density curve defines the maximal power point (MPP) with the corresponding voltage (V_{mpp}) and current density (J_{mpp}), representing the ideal operating conditions of the solar cell.

Four important parameters are extracted from the *J-V* curve :

- **The open-circuit voltage (V_{oc})** is the potential of the device when no current is extracted. It depends on the passivation quality and the selectivity of the solar cell.
- **The short-circuit current (J_{sc})** is the current of the solar cell at zero voltage. It depends on the optical properties of the cell (see difference between *J-V* and *J-V*bis in Figure

1.7(b)), but can also be affected by very strong collection efficiency issue such as passivation, selectivity, shunts or series resistance. In the ideal case (no collection issue), J_{sc} varies linearly with illumination and we have $J_{sc} \approx J_{Gen}$.

- **The fill factor (*FF*)** is defined as the ratio of the blue to red area in Figure 1.7(a), which reads

$$FF = \frac{V_{mpp} J_{mpp}}{V_{oc} J_{sc}} \tag{1.17}$$

  It is affected by the combined effect of passivation, selectivity, shunts and series resistance.

- **The power conversion efficiency (η)** is defined as the ratio of the maximal power extractable from the solar cell compared to the incoming power of light P_{light} ($1000\,\mathrm{W\,m^{-2}}$ at STC), *i.e.*:

$$\eta = \frac{P_{max}}{P_{light}} = \frac{V_{oc} J_{sc} FF}{P_{light}} \tag{1.18}$$

As the metrics derived from the *J-V* curve are dependent on several sources of losses, various methods are applied to characterize and decouple them. In Figure 1.7(b), we present the different types of *J-V* curves that allow to decompose the transport losses in the solar cell, which we describe below.

The theoretical maximum implied *J-V* curve (*iJ-V)**, can be computed using a theoretical model accounting only for intrinsic recombination losses, such as Richter's parametrization [Richter 2013]. For a given photogenerated current, the implied open-circuit voltage is maximal and reaches $iV_{oc}{}^{*}$.

The measured implied *J-V* curve (*iJ-V*), is the measure of the maximal current that can be extracted from a solar cell (iJ) given its implied voltage (iV), once real passivation losses are taken into account, such as SRH bulk recombination and surface recombination. This curve is measured on solar cell precursors, prior to metallization, using PCD measurement [Sinton 1996] (see also section 2.3). This technique relies on the inductive measurement of the conductivity decay of the absorber after its exposition to a flash, allowing to reconstruct the function $iV(\Delta n)$ and $J_{rec}(\Delta n)$ for a given injection level Δn. Then, to evaluate iJ, which cannot be directly probed at operating conditions, one can use the balance equation 1.1 in the form $J_{Gen} - J_{out} = J_{rec}(\Delta n)$ to relate measurements taken under different conditions. Indeed, one should notice that the r.h.s of this equation is uniquely a function of Δn, and therefore the equality holds no matter if on the l.h.s less current is photogenerated or more current is drained (superposition principle). Therefore, the maximal current that can be extracted for a given Δn can be calculated from the measured $J_{rec}(\Delta n)$ as $iJ = J_{Gen}(1\,\mathrm{sun}) - J_{rec}(\Delta n)$, provided a reference illumination level, *e.g.* measuring $J_{Gen}(1\,\mathrm{sun}) \approx J_{sc}(1sun)$ on a finished device with the same optical properties [Kerr 2003].

The measured pseudo *J-V* curve (*pJ-V*), is a similar concept, except the voltage is measured at the electrodes of the contacts, *i.e.* after the qFLs recombined but without taking into account

additional external series resistance effects, such as imposed by the transport in the TCO or the metallic grid. Therefore, the *pJ-V* curve bears additionally the voltage losses due to selectivity issues. As in practice it is again not possible to measure directly the pseudo-voltage in a solar cell under operating conditions, one relies on similar arguments to those used for the *iJ-V* curve construction using the so-called J_{sc}-V_{oc} method [Wolf 1963, Sinton 2000, Bowden 2001]: The solar cells is measured at different illumination levels (ill), recording each time $V_{oc}(ill)$ and $J_{sc}(ill)$. Then, the illumination level can be expressed as a fraction of 1 sun as $ill = J_{sc}(ill)/J_{sc}(1Sun)$ or measured from an external calibrated sensor. The maximum current that can be extracted from the device at this illumination is $pJ(ill) = J_{sc}(1Sun)\,(1 - ill)$ and the pseudo-voltage is simply $pV(ill) = V_{oc}(ill)$. The latter does not suffer from external resistance effect as no current is flawing out of the device during the measurement.

On Figure 1.8, we represent the band-diagram corresponding to the different *J-V* curves as well as equivalent electrical circuits to situate the different voltages and currents at play in a solar cell under operating conditions. This electrical circuit proposed by Onno *et al.* represents the same losses described in Figure 1.5(a), represented by different voltage-dependent elements whose lengths are illustrated proportional to their resistance value [Onno 2019]. Intrinsic Auger and radiative recombination are represented by diodes with ideality factor of $n = 2/3$ and $n = 1$ respectively [Cuevas 2014], while surface and selectivity recombination are represented by injection-dependent resistors that shunt the absorber. To model surface recombination, the resistances of the absorber to e^- and h^+ are added to represent the fact that surface recombination velocity is ultimately limited by the rate at which carriers are provided through the absorber [Onno 2019]. In this more general view, the total selectivity losses take into account both absorber and contact resistivity, *i.e.* $\rho_{tot,e} = \rho_{abs,e} + \rho_{c,e}$ and $\rho_{tot,h} = \rho_{abs,h} + \rho_{c,h}$, and the condition for ideal selectivity provided by equation 1.13 can be generalized to $\rho_{tot,h}/\rho_{tot,e} \gg 1$ (considering ideal hole contact on the left side for simplicity) [Onno 2019].

1.3 Junction formation

In this section, we give an introduction to the general understanding of junction formation based on their energy-band diagram properties and how they can be used to create selective charge carrier extraction. For this, we will follow the discussion in [Allen 2019], which gives useful insights on the mechanisms at stake. However, many other phenomenological descriptions exist in the literature, *e.g.* involving parameters not present on an energy band diagram such as the carrier mobilities [Wurfel 2015], and it is not possible to cover them all.

As we introduced above, selectivity is provided by an asymmetry of the partial contact resistivities, which can be computed from the averaged conductivities over the contact [Onno 2019]. Conceptually, an efficient way to modulate theses conductivities (visually, the distance between Fermi level and the respective band edge) is to create band bending at the surface of the absorber. This can be achieved by contacting the latter with either a low or high work-function

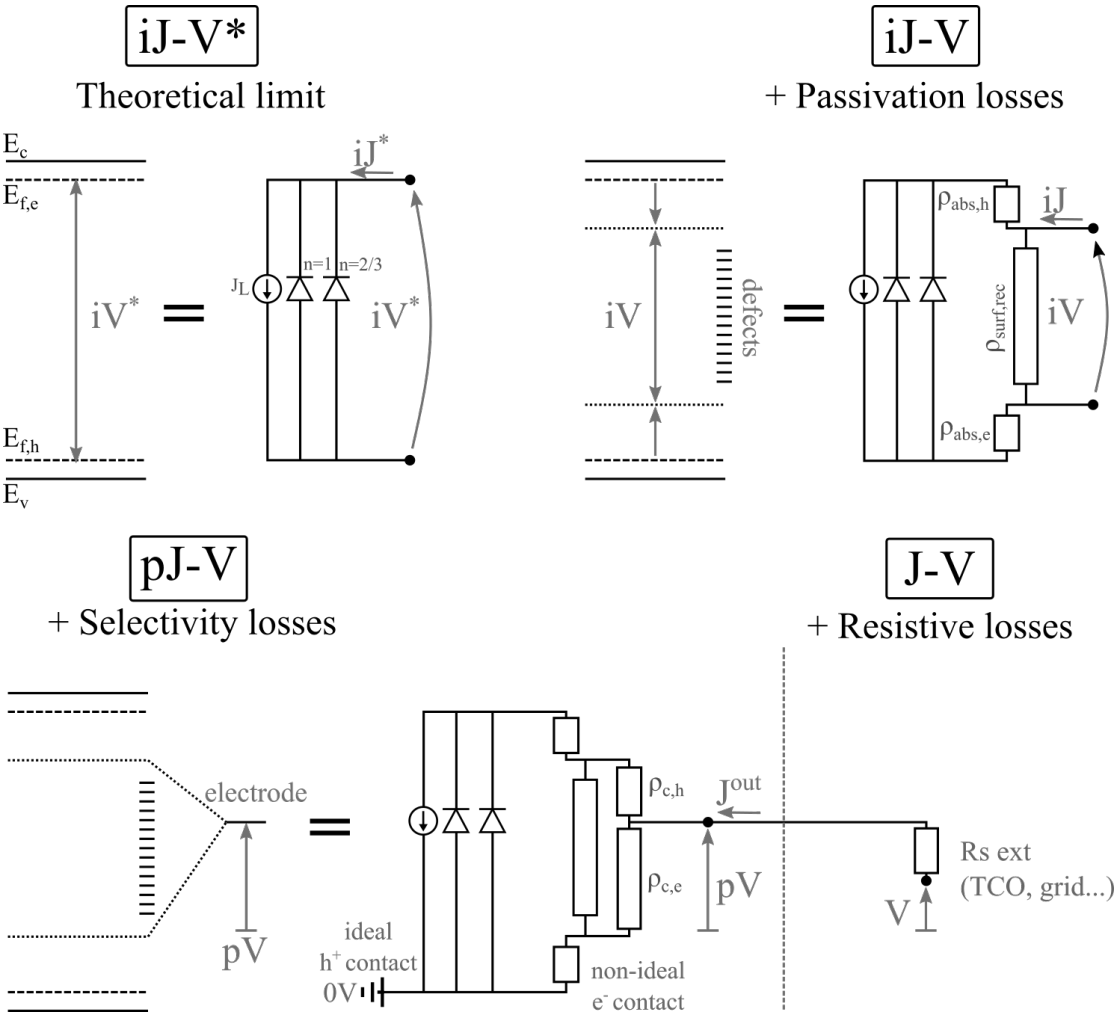

Figure 1.8: Illustration of the band and circuit diagrams corresponding to the (a) iJ-V**, (b)* iJ-V*, (c)* pJ-V *and (d)* J-V *curves.*

material (WF, difference of energy between the Fermi and vacuum level), bending the bands downwards (for e^- contact) or upwards (for h^+ contact) as the Fermi levels align on both sides. As can be seen in Figure 1.9(a)-(b) (for an electron contact), this results in a barrier for holes that decreases their conductivity while increasing the one of electrons, and which therefore provides carrier selectivity. This description of the band bending is called "Schottky-Mott alignment" [Sze 2006]. It is well suited to describe semiconductor-metal contact, but note that the same visualization and interpretation can be applied to a semiconductor-semiconductor contact (Figure 1.9(b^{bis}), where the same quadratic band bending is applied in the left semiconductor and the barrier height (the built-in potential) is given again by the WF difference of the two semiconductors.

Unfortunately, in practice the WF effect can be reduced by the presence of surface defects, interface dipoles or metal induced gap states. These will deplete the absorber of carriers near

the surface resulting in a pinning of the Fermi level of the latter down to the defect levels, often at mid-gap. In consequence the bending will be reduced or even go in the opposite direction (as shown in Figure 1.9(c)), mitigating the desired carrier selectivity for this interface. This effect is called "Fermi-level pinning" and was demonstrated by plotting the measured barrier height as function of various metal work functions, showing a slope much lower than one [Sze 2006].

To overcome Fermi-level pinning, several strategies can be employed. The first one is to use materials with extreme work function to lower the barrier height, providing those materials exist and are stable. The second one is to use heavy doping by diffusing dopant at the absorber surface (1.9(d)). With this strategy, the system consists now of three parts, the metal electrode and two semiconductors of different WFs (as shown in Figure 1.9(b^{bis})). This diffused homojunction provides conductivity asymmetry to the intended carrier type as well as reduces the barrier depletion width, allowing here efficient tunnelling of the electrons. However, heavy doping increases Auger type recombination which creates strong recombination current. Therefore, it is not possible to obtain at the same time a high passivation and selectivity with this strategy.

The third approach, employs a thin layer to passivate surface defects and avoid direct contact of the absorber with the metal electrode. Once the source of Fermi level pinning is treated, the electrode work function can provide band bending as in Figure 1.9(a). The passivating layer can also create selectivity, *e.g.* by providing asymmetric barrier heights to electrons and holes. In practice, the passivated layer should either be kept thin enough to allow for direct tunnelling or have sufficiently low barrier height for one carrier type to allow for thermionic emission [Sze 2006]. The transport across those barriers remains complicated to describe, and defect assisted mechanisms seem to play a central role [Messmer 2018, Procel 2020].

This passivating layer strategy can be seen as a metal-insulator-semiconductor (MIS) contact. In practice however, the band bending in Figure 1.9(e) is provided by an additional doped semiconductor inserted between the passivation layer and the electrode, forming a metal-semiconductor-insulator-semiconductor contact. This is for example the case of the silicon heterojunction that we will introduce in the next section. The situation can become even more complex, with an additional shallow diffusion of dopant in the absorber, which can happen in the case of the TOPCon contact (see next section).

Finally, let us make the important remark that the theoretical framework developed in this section is valid in the dark under equilibrium conditions. However, a solar cell is operated under illumination and under external bias, which creates two relevant Fermi levels in the absorber. As a consequence, the general Schottky-Mott rule can not be applied to calculate the barrier heights and very large differences can be seen on the band diagram in the dark or under illumination. This can be further assessed by simulation of the semiconductor energy band diagram (Figure 1.10). Hopefully, this shows that under operating condition the majority carriers on both side of the p-n junction have a similar conductivity under illumination

compared to the dark, and the Schottky-Mott interpretation remains relevant to discuss this part. Conversely, the minority carrier conductivity on both side of the p-n junction is much higher than in the dark. The different barriers predicted in the dark keep their qualitative beneficial impact, however their ability to reduce the minority carrier conductivity can be reduce by orders of magnitude, which can result in large selectivity losses.

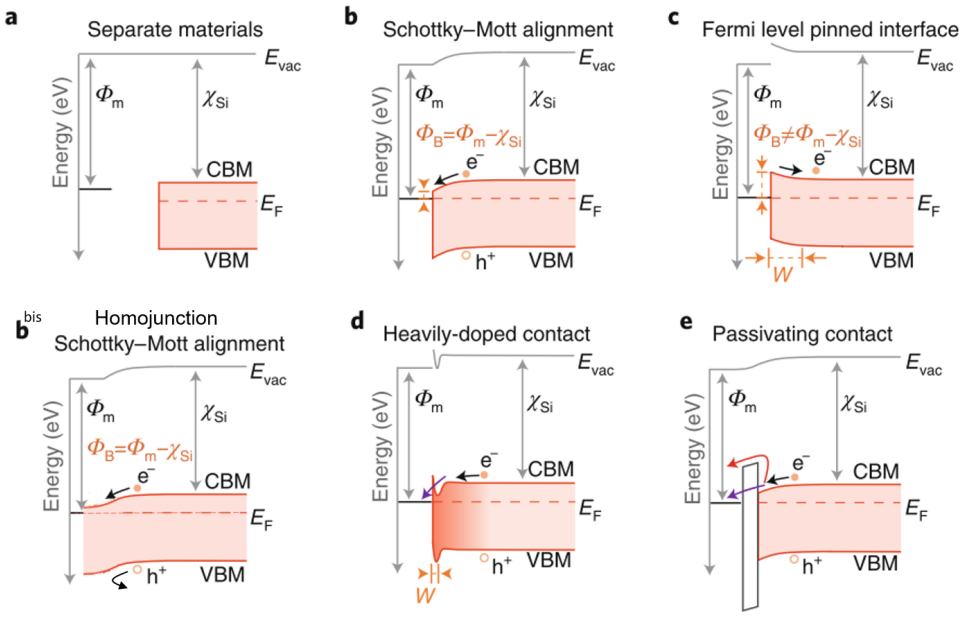

Figure 1.9: Energy band diagram of the junction formation mechanisms of an electron contact. Φ_M is the work function of the electrode, while χ_{Si} is electron affinity of the absorber. Reproduced from [Allen 2019].

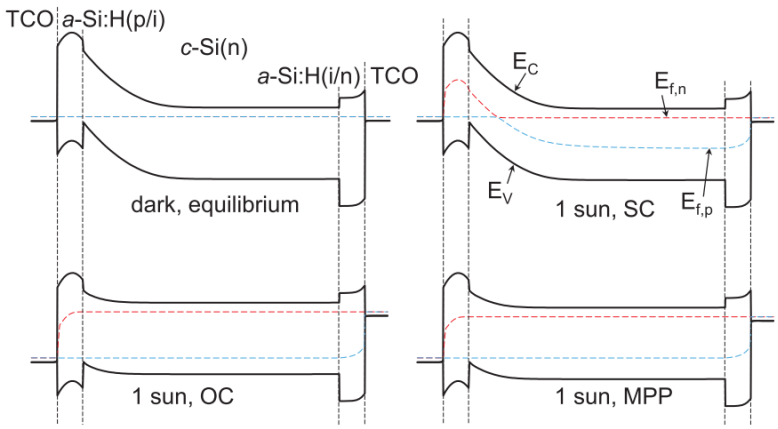

Figure 1.10: Energy band diagrams of a heterojunction solar cell in equilibrium, short-circuit (SC), open-circuit (OC), and maximum power point (MPP) conditions. Reproduced from [Haschke 2018].

1.4 Solar Cells technologies

The main technologies to contact c-Si are presented in this section. They are the building blocks of the main silicon-based solar cell presented on Figure 1.11, among which the silicon heterojunction that is the focus of this thesis. Moreover, some of these contact schemes allow for different architectures that we will mention along those lines. These architecture properties are classified by pairs and the solar cell is therefore either:

- a front or rear junction (FJ or RJ), meaning that the p-n junction is either placed at the front or the back side of the cell,
- front-back contacted, when the contacts are placed on both sides, or interdigitated back contacted (IBC), when the contacts are both placed on the rear side to minimize front-light absorption,
- monofacial, when it features a full area back contact and the light is collected only from the front side, or bifacial, when a grid can be employed for both the rear and front metallization allowing for light collection at both sides.

Finally, Figure 1.12 presents the most recent record efficiencies reached with those contact technologies and architectures.

Al-BSF, for aluminum back-surface field, takes its name from the full area screen-printed aluminum layer at the rear side. This direct silicon-metal contact induces a high surface defect density, that creates strong recombination. Fortunately, this interface is screened partially by the creation of a highly p^+ doped region in the wafer upon the diffusion of Al at high temperature, which acts as a p-type dopant in silicon and creates a better selectivity towards holes[5]. On the front side, the electron contact is formed by a highly n^+ doped region (the front surface "field", FSF). The latter is created by the diffusion of phosphorous atoms *e.g.* thanks to a $POCl_3$ tube furnace, creating a buried p-n junction inside the wafer which also provides lateral conductivity for the electrons. The front side is textured and covered by a non-stoichiometric silicon nitride (SiN_x) film to form an anti-reflective coating. After-this, the front side is contacted by screen-printing a silver metallic grid, with nowadays typical finger width and height of 15–50 µm and 10–20 µm respectively. The silver is deposited on the nitride, and then penetrates down to the wafer during a short firing step, *i.e.* a fast annealing at high temperature, generally higher than 800 °C. This step allows at the same time to diffuse hydrogen from the SiNx, which will passivate defects in the wafer and at interfaces and increase passivation, as well as to form the BSF at the back-side by diffusion of the aluminum. Unfortunately, as the doping in this region is increased, Auger recombination gets stronger and ultimately limit the efficiency of solar cells featuring such contacting schemes to $\eta^{BSF} \approx 20\%$ [Yan 2021].

[5]The so-called back-surface field, even though the physical mechanisms for charges separation is not supported by a field, but by an asymmetry in the conductivities to holes and electrons.

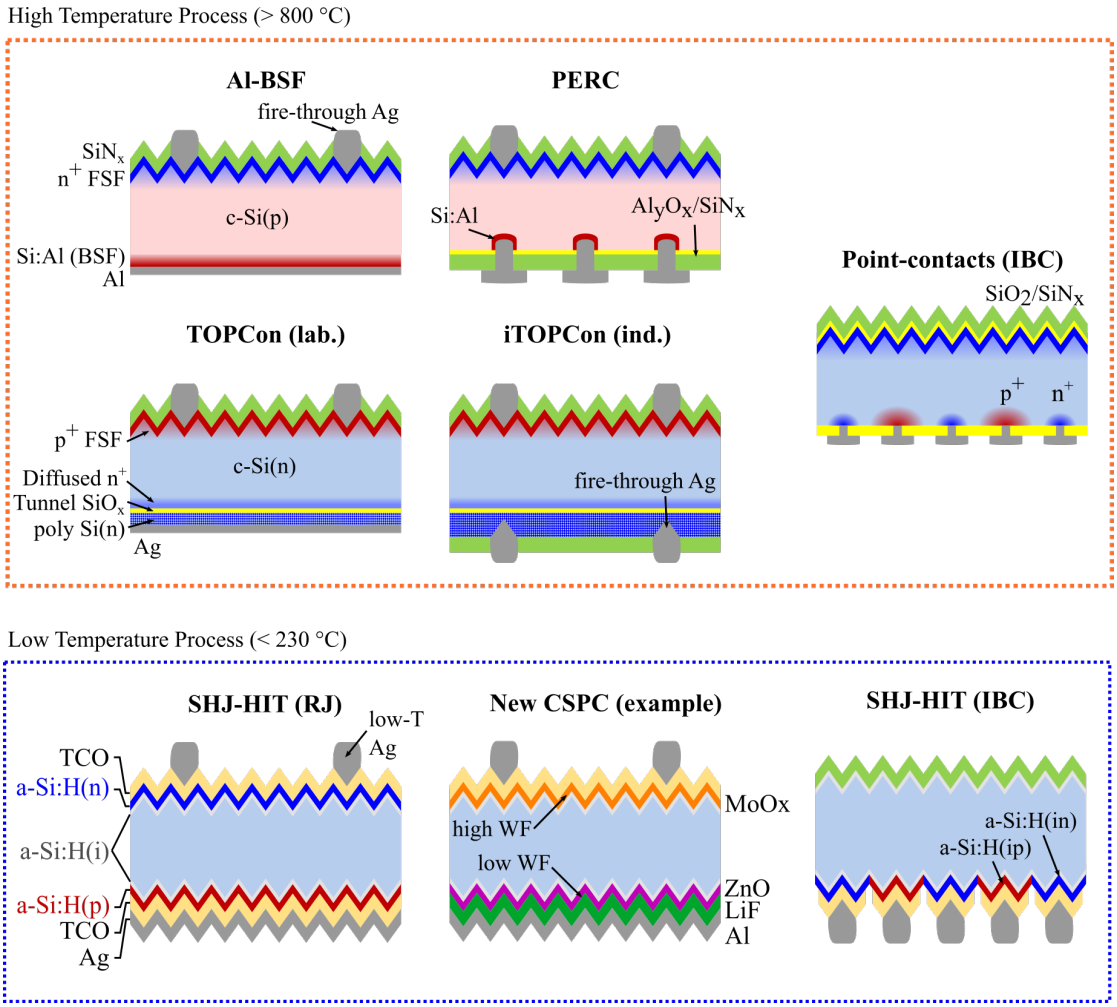

Figure 1.11: Main types of c-Si solar cells.

PERC, for passivated emitter and rear contact, circumvents the limitation imposed by the Al-BSF by localising the rear contact[6]. Indeed, as the Al-BSF provides a very low contact resistivity ($\rho_{c,p}^{bsf} = 5\,\mathrm{m\Omega\,cm^2}$ [Brendel 2016]), it can be restricted to a smaller area while a better passivation scheme is applied everywhere else. This is realized by depositing first a full area passivation layer on the backside, such as a SiO_2/SiN_xor Al_2O_3/SiN_x stack, prior to the Al deposition. Then local contacting is realized, *e.g.* using a laser that breaks locally the passivation layer and allows diffusion of the dopant. Provided an optimal fraction of the area is used, a better passivation / conductivity trade-off can be found than with the Al-BSF technology, which depends on the selectivity of the back surface field [Brendel 2016]. As another advantage, the presence of the passivation stack enhances the rear reflection and yields current gain in the infrared. In turns, this type of solar cell demonstrated high efficiency up to $\eta^{PERx} = 25.0\%$ [Zhao 1998], which was the world record efficiency for c-Si

[6]Similar strategies to the one described here exist, such as the PERL (passivated emitter, rear localized), and the whole family of theses solar cells is sometimes called PERx.

single junction solar cell from 1999 to 2014 [Green 2014]. Such high efficiencies were however only established on a small scale laboratory design involving costly photolithography steps for the realization of the local contact. With more industrially compatible PERC processes (iPERx), this technology is seen to saturate around $\eta^{iPERx} \approx 24.0\%$ on the average production line, an efficiency reached by Longi in 2019 [LONGi 2019]. In conclusion, the PERC design offers a significant boost of efficiency compared to the Al-BSF design, with a minor modification of the production lines, which explains the market trend to shift to this second technology (see Figure 1.4). It remains however limited intrinsically by the use of diffused junctions, that leads to strong Auger recombination current, limiting the maximal theoretical efficiency close to 24% [Kruse 2020, Yan 2021]. The initial point-contacts solar cell from SunPower adapted the PERx concept to the IBC architecture to increase the optical gain at the front side. However, this technology suffers from the same transport limitation, which seemingly pushed SunPower to adopt passivating contact strategies (described below) [Glunz 2021]

Recognizing the limitations of buried diffused junctions led the scientific community to develop various new contacting schemes. The successful strategies all have in common to employ an intermediate passivating layer that passivates the c-Si surface and a charge carrier separation layer inserted between the passivation layer and the metal electrode. This second layer generates an induced band bending inside the absorber, thanks to its difference of work function (WF, Fermi level position with respect to vacuum level) with c-Si. Indeed, this induces a junction that provides carrier selectivity without creating additional Auger recombination, unlike heavy doping [Sze 2006, Glunz 2021, Allen 2019]. To form an electron contact, a low WF material should be selected and conversely for hole contact.

TOPCon, for tunnel oxide passivating contact, consists of a very thin silicon oxide (SiO_2) deposited on the wafer surface for passivation completed by a highly doped poly-silicon layer (poly-Si) that creates the band-bending in the c-Si. The oxide must be kept thin enough ($< 1.5\,nm$) to allow tunnelling of the charge carriers through it, hence its name. A similar strategy called passivating oxide locally opened (POLO) employs a thicker oxide ($> 1.5\,nm$) that later needs to be broken-up to form local pinholes allowing the current to flow. However, it shares close processing steps with those of the TOPCon technology that are described next. First, the oxide needs to be formed either by chemical or thermal oxidation, or UV-ozone treatment. Then the poly-Si is deposited, either via plasma-enhanced or low pressure chemical vapour deposition (PECVD and LPCVD) or sputtering. Then, the latter needs to undergo a high temperature annealing step ($> 800\,°C$) to allow for its crystallization and its dopant activation. During this step, dopant can also diffuse to the c-Si forming a buried junction. Therefore, a first step of optimization is to control the temperature profile to form only a shallow non-limiting diffusion and avoid heavy-doping Auger recombination features. Then it is necessary to accumulate hydrogen in the SiO_2 layer to allow the later to effectively passivate dangling bonds at the wafer surface [Lehmann 2019]. This step can be achieved by forming gas anneal (FGA) or by the deposition of a SiN_x layer that is then fired to release its hydrogen (as in the classical cells above). Finally, the screenprinted metallization (Ag or

Ag/Al paste) needs to be fired through the nitride to contact the cell. It is common at the laboratory scale to avoid this last challenge for demonstration and strip-off the SiN_x layer and evaporate or sputter a full area metal layer (see Figure 1.11). However, for industrial application, it is relevant to try to achieve at the same time all the different high temperature processes (dopant activation, hydrogenation and metal fire-through) to reduce production line complexity [Ingenito 2018]. However, this requires to work with usually thicker poly-Si layer to prevent the metal paste to reach the absorber and thus restrict the use of this layer to the rear side of the cell due to its non-ideal transparency in the UV and visible range. The efficiency of this technology nowadays surpasses PERC solar cells, reaching up to $\eta^{TOPCon} = 26.0\%$ for lab-scale demonstration on p-type wafer with localized p^+ diffusion for the front and n-type poly-Si at the rear [Richter 2021]. For large area application, the industrial LONGi recently managed to reach an efficiency of $\eta^{iTOPCon} = 25.2\%$ on n-type wafer [Green 2021]. Finally, the POLO solar cell from ISFH adopted similar concept to the IBC architecture, allowing to reach an efficiency of $\eta^{POLO-IBC} = 26.1\%$ [Haase 2018].

SHJ, standing for silicon heterojunction, provides the highest ever measured efficiency for c-Si single junction device of $\eta^{SHJ-IBC} = 26.7\%$. Beyond efficiency, this technology benefits from an architecture well suited for bifacial applications as well as better temperature behaviour than the other technologies, which enhance its energy yield [Haschke 2018].

The SHJ solar cell was originally introduced by Sanyo (now Panasonic) in the 1990s under the name "heterojunction with intrinsic thin film" (HIT). It features as its name indicates a junction with a thin intrinsic hydrogenated amorphous silicon (a-Si:H(*i*)) layer. This material is well suited to reduce the dangling-bond density at the c-Si surface thanks to its amorphous nature and to its high hydrogen content. On top of that, n-type and p-type doped hydrogenated amorphous silicon (a-Si:H(*n*) and a-Si:H(*p*)) layers are subsequently deposited to create a band bending in the absorber and provide selectivity towards electrons and holes, respectively. Those layers are typically deposited via PECVD[7], necessary to incorporate hydrogen in the material, using gas mixtures of SiH_4 and H_2 and different boron or phosphorous precursors for the dopant. Note that to avoid hydrogen effusion of those layers and conserve the passivation, it is important that the temperature of the process never exceeds about 230 °C, especially for the stability of the a-Si:H(*i*)/a-Si:H(*p*)stack [De Wolf 2009]. Therefore, low temperature metallization should be used such as adapted silver paste for screen-printed.

These layers have the advantage to provide the highest surface passivation among all contacting schemes to c-Si as well as a high selectivity. However, the contact resistivity remains high, in particular for $\rho_{c,h}^{a-Si(p)}$ which can reach several hundreds $m\Omega\,cm^2$, preventing the use of the c-Si natural lateral conductivity [Haschke 2020], and itself being much more resistive than the diffused junction or the poly-Si layers. In consequence, additional transparent conductive oxide (TCO), mainly indium tin oxide (ITO) are used on the front side to circumvent this limitation. Those materials are degenerate n-type semiconductors, with doping concentration

[7] Note that hot wire chemical vapour deposition (CVD) is also used, *e.g.* by Sanyo.

in the range $n_{TCO} \approx 10^{19} - 10^{21}\,\mathrm{cm}^{-3}$. They require a careful optimization of their conductivity $\sigma_{TCO} = q\mu_{TCO}n_{TCO}$ as a high doping concentration will enhance the free-carrier absorption (FCA), resulting in optical losses in the infrared. Usually, TCO with high mobility are looked after to circumvent this trade-off [Cruz 2022].

An advantage provided by the use of TCO, is that they can act as efficient diffusion barrier against various metals. Therefore, they are compatible with wider type of metallization, for example with copper plating [Lachowicz 2021], an interesting alternative to reduce the costly use of silver. Moreover, indium, a critical raw material[8], present in the TCO, can be drastically reduced together by implanting optimal front and rear optical reflection design [Boccard 2021, Cruz 2019b] or even be completely eliminated by using aluminum doped zinc-oxide (AZO) [Morales-Vilches 2019, Senaud 2021a].

However, a major drawback of SHJ is the strong parasitic absorption in the layer stacks of a-Si:H(i)/a-Si:H(n or p)/TCO, with a J_{sc} loss of more than 2 mA cm^{-2} [Holman 2014, Boccard 2019]. Therefore, the best efficiency reported were obtained with the IBC configuration. However, a strong focus of the community was paid to increase the layer stack transparency, *e.g.* by alloying them with carbon or oxygen or replacing them by more transparent material. This led very recently, in November 2021, LONGi to achieve an efficiency of 26.3% in rear-junction bifacial configuration, the world record for front/back contacted solar cells [Pv-magazine 2021a], showing the possibility to reach very high efficiency without the IBC design.

Novel CSPC : to address the challenges imposed by the low transparency of a-Si:H and poly-Si contact, a strong focus on alternative thin films with wider band gap has built up. This interest actually stemmed from the understanding of the organic thin film as well as dye-sensitized or perovskite solar cells communities where it was already known that carrier selectivity can be achieved without using doping but instead by using material of extreme WF compared to c-Si (WF 4.3eV for lightly doped n-Si) [Battaglia 2016]. Among many relevant material categories to be cited, transition metal oxide (TMO) such as MoO_x, WO_x, V_2O_x or NiO_x offer suitable properties to form transparent hole selective contacts thanks to their wide bandgap (> 3 eV) and large WF (> 5 eV) [Bullock 2016]. They can exhibit a sufficiently low contact resistance to be used in full area contact scheme and the best efficiency so far reached by using one of those new material as selective contact as been established so far by MoO_x in the stack c-Si(n)/a-Si:H(i)/MoO_x/ITO with a screen-printed metallization, replacing a-Si:H(*p*) [Dréon 2020]. On the electron contact, TiO_x is a promising material for front application [Matsui 2020], while for the rear side a ZnO/LiF_x/Al stack was shown able to reduce plasmonic absorption compared to the use of ITO in standard SHJ design. Used in conjunction with MoO_x for the hole contact, a dopant-free solar cell was able to reach an efficiency of 21.4% [Zhong 2020]. This list is far from being exhaustive and there is an even wider unexplored area of materials to be investigated, which could offer optimal alignment to c-Si such as the

[8]Critical raw materials are resources which are economically and strategically important for the European economy, but have a high-risk associated with their supply [CRM-alliance 2020].

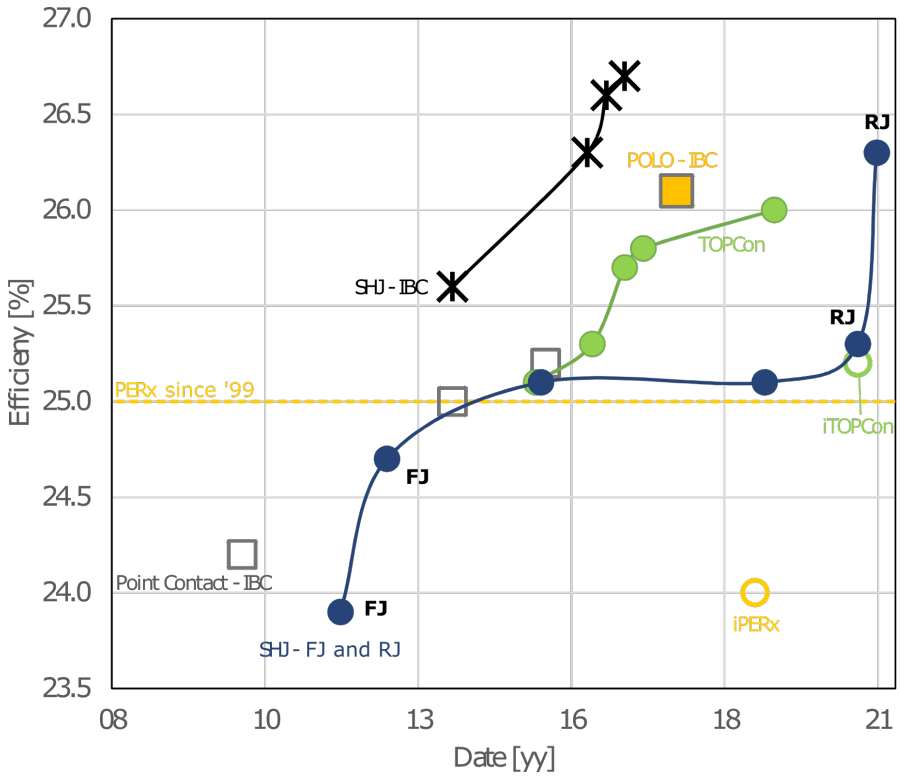

Figure 1.12: High-end efficiencies of single junction c-Si solar cell. Data from Green's efficiency Tables 41-59 [Green 2021].

III-nitride family [Fioretti 2018, Fébba 2021]. Finally studying these contacts is of interest for the whole solar cell community, since some of them were developed in the organic thin-film community and others find applications both in low-temperature full-area solar cell or high-temperature contact. The ultimate hope of this research is to a find a single material that will provide at the same time surface passivation, selectivity and conductivity while being highly transparent. Novel materials are also interesting to offer a wider range of processing possibilities, *e.g.* by being resistant to high temperature or acting as diffusion barrier against metal such as Al or Cu, broadening the possibility for front side metallization.

1.5 Problematic and structure of this work

Nowadays, very high efficiency c-Si solar cells are already obtained by different industrial actors [Chen 2019] and it seems that production lines will routinely output solar cells with efficiencies of ≈ 26% in a near future, helping in the urgent need for PV expansion. However, the list of industrial actors realizing such achievement remains thin. It is therefore scientists role to study those astounding results, democratize the knowledge behind those discoveries and foresee the limitations and future paths for the evolution of the technology. Throughout this thesis different goals were followed, and contributions were achieved both for the field of novel CSPC development as well as for very high efficiency SHJ solar cells. We expose next the structure of the thesis and the motivation for each parts.

Chapter 2 - Experimental details and methods : We describe there the main processing techniques and sample preparation steps as well as the different characterization methods used in this thesis.

Chapter 3 - Model Investigation for S-shapes curve description : As explained in section 1.3, the mechanisms behind junction formation are not yet fully understood. In practice, the development of new promising materials and their inclusion into solar cells often lead to unpredicted results, leading to "S-shapes" and saturations in their J-V characteristics [Fioretti 2019, Fébba 2021, Dréon 2020]. Figure 1.13 presents results of such typical studies, where an indium gallium nitride material was attempted to be synthesized motivated by its previously reported ideal band alignment with c-Si [III 2009]. Unfortunately, the results of such strategies often fall far away from theoretical predictions. This is because properties such as the conduction or valence band positions with respect to vacuum or bandgap have a wide range of possible values for a given material and are highly dependent on the deposition conditions and substrate. Moreover, interface states can pin the Fermi level and reduce the effect of the work function of the material.

Therefore, to understand the causes of the bottlenecks, it is important to be able to extract *in situ* information from the created final solar cell. Thanks to the recent re-examination of the working principle of solar cells (presented in the first part) [Wurfel 2015, Bivour 2017,

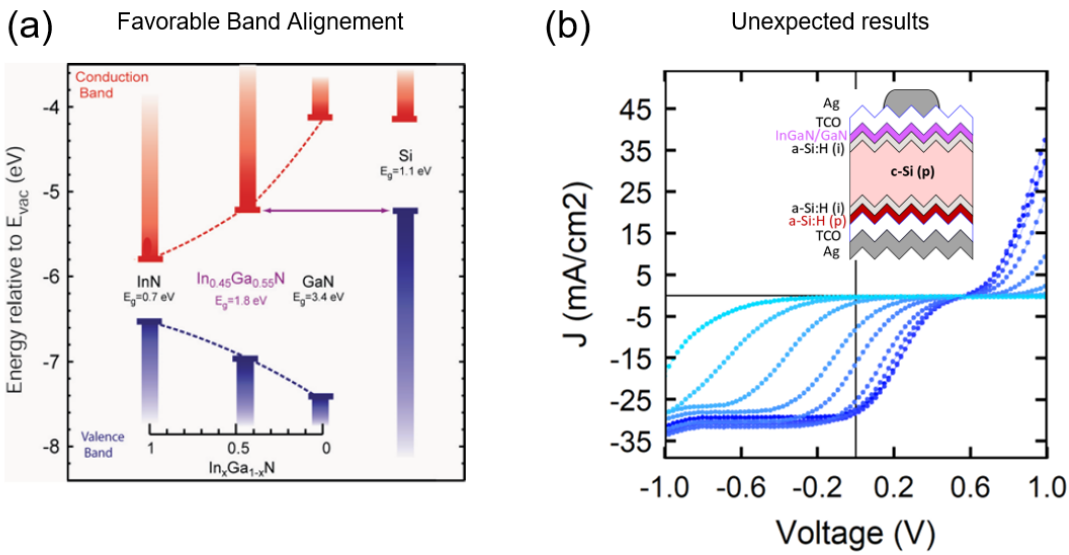

Figure 1.13: (a) Energy bands alignment of InN, InGaN and GaN compared to c-Si. Reproduced from [III 2009]. (b) Resulting J-V *curve of devices incorporating InGaN layer in the electron contact stack. Reproduced with permission from Dréon J. and Thomet J. (internal report).*

Onno 2019], available interpretations in terms of carrier selectivity issue can explain the losses of voltage at open-circuit, which can be attributed to an asymmetry of the carrier partial conductivities. However, this does not allow for direct extraction of band diagram parameters, without further modelling. Moreover, valuable information is present on the whole *J-V* curve which is often not reported or analysed, such as saturation in forward bias beyond OC conditions. Figure 1.14 shows a possible modelling of SHJ solar cells that relates the transport processes and barriers of the energy-band diagram to an equivalent circuit that can generate a resulting *J-V* curve. The circuit follows a topology in agreement with the proposed vision of Onno *et al.*, with the injection dependent resistors represented here by diodes, and therefore is adapted to describe selectivity issues. However, its high complexity makes it unpractical and prone to over-fitting. In contrast, a much simpler model consisting of only four diodes was introduced by Roe *et al.* to describe solar cells limited by their contacts [Roe 2019]. A first goal of this thesis was set to assess its experimental validity and confront it to solar cells and symmetrical samples whose contacts have been deliberately engineered to issue selectivity losses. As a second step, we propose a modification of this model to take into account the difference observed between experiments and theory.

(a) Energy Band Diagramm and Transport Mechanisms

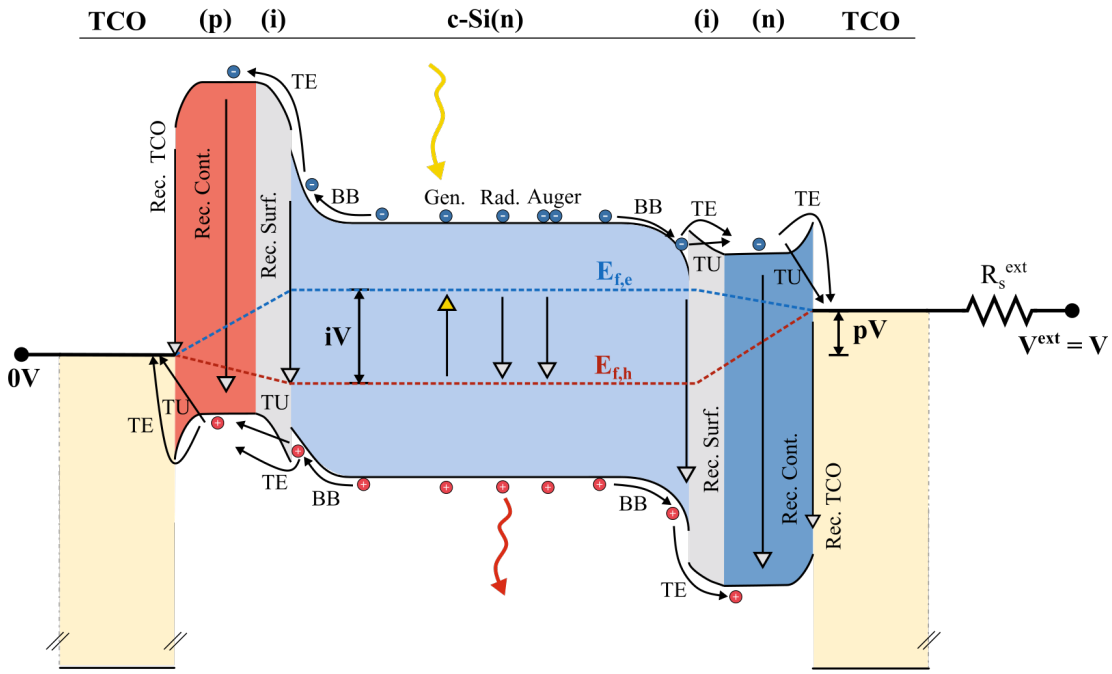

(b) Equivalent Circuit (full complexity)

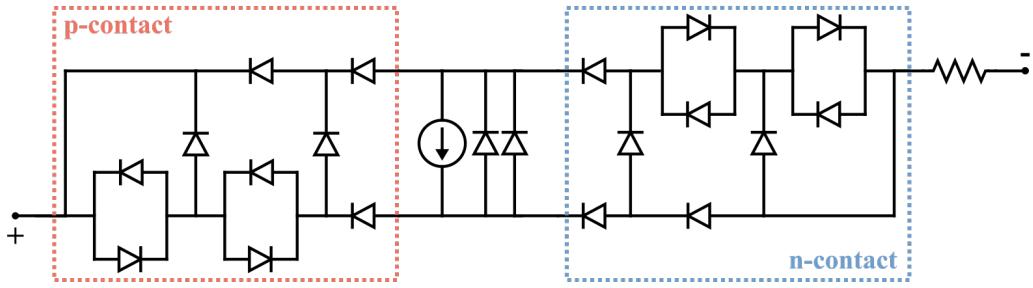

Figure 1.14: (a) Energy band diagram of a SHJ solar cell under illumination and external bias. Generation, recombination and transport processes are represented by arrows. BB indicates band bending effects, TE thermionic emission, TU tunnelling (direct or trap assisted). (b) Equivalent circuit model where each of the different indicated process on the band-diagram are represented by a diode (one arrow = one diode), except the photogeneration that is modelled by a current source and the recombination at the TCO interface, that is assumed to be infinite due to the impossibility to achieve quasi-Fermi level splitting here and which is modelled by a simple wire.

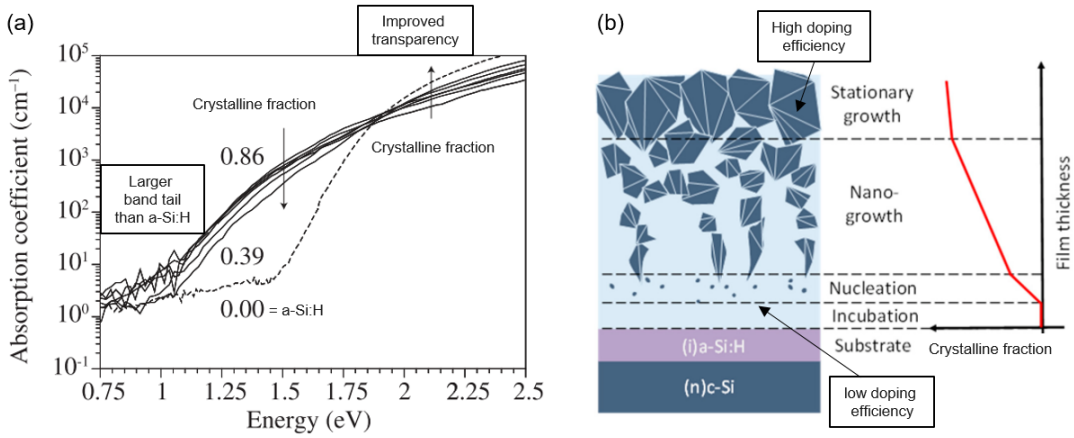

*Figure 1.15: (a) Absorbtion coefficient spectrum of nc-Si:H depending on its crystalline volume fraction. Adapted from [Shah 2010]. (b) Cross-sectional sketch of a nc-Si:H layer grown on top of a-Si:H(*i*). Adapted from [Mazzarella 2020].*

Chapters 4, 5 and 6 - Development of nc-Si:H layer as efficient CSPC : To achieve high efficiencies with SHJ solar cell (such as presented on Figure 1.12), a lot of attention has been paid towards optimizing each layer of the contact stack, often composed of several sub-layers each, as well as their influence on subsequent layer growth. E.g. the a-Si:H(*i*) passivation layer is often composed of a first very porous part that avoid epitaxial growth on the wafer [Luderer 2022]. In a similar way, the surface roughness prior to TCO deposition can influence its crystallinity during the growth and care should be taken not to degrade its mobility [Cruz 2019a]. To achieve more efficient transparency, a-Si:H layers can unfortunately only be thinned down up to a critical thickness, before degrading transport and passivation properties [Boccard 2019, Umishio 2020]. To circumvent this poor opto-electrical trade-off, nano-crystalline silicon layers (nc-Si:H) were intensively investigated as they offer better properties than a-Si:H in terms of transparency and conductivity (See Figure 1.15(a)).

In *Chapter 4*, we develop *p*-type nc-Si:H layers and investigate the influence of $B(CH_3)_3$ (trimethyl boron or TMB) and BF_3 as dopant source on the material properties and its performance in solar cells. We observe that both gases enable high efficiencies but yield a different crystallinity and effective doping. A high BF_3 flow lowers the series resistance thanks to a low activation energy, while maintaining a high crystallinity. This allows fill factors up to 83%, however with the apparition of a parasitic absorption in the UV. A low TMB flow enables simultaneously a high crystallinity and a low activation energy. As an illustration of this layer potential, a 23.9%-certified efficiency is achieved with a $2 \times 2\,cm^2$ screen-printed device. We finally suggest that similar transport vs. transparency trade-offs can be reached for both dopant types for front junction application, while high BF_3 flow leading to lower series resistance might be of interest when placed on the rear side.

In *Chapter 5*, we explore several approaches to perform accurate series resistance (R_s) breakdown of our state of the art $2 \times 2\,cm^2$ screen-printed solar cell. Notably, two very important

variables are the contact resistivities of the front and rear contact, ρ_c^{front} and ρ_c^{rear} respectively. We investigate different ways to measure them independently of the solar cells using TLM or symmetrical vertical structures under illumination and attempt to discuss the existence of an injection dependant behaviour of the contact resistivities. Then, we present injection dependent breakdown of the series resistance of the solar cells developed in chapters 4.

In chapter 6, we expose our development of *n*-type nc-Si:H layer for window layer application. We perform thickness series alongside PH_3 doping series to study the inhomogeneous properties of the nc-Si:H(*n*) layer along its growth direction. We give a particular care in analysing the impact of the PH_3 flow upon the creation of an amorphous lowly doped nucleation zone, as well as studying the TCO impact on the contact quality. We explore further the integration of nc-Si:H(*n*) layer in the whole contact stack when a thin a-Si:H(n) layer is introduced underneath. We also report on the beneficial effect of an additional SiO_x capping layer to form both a double anti-reflective coating (DARC) and reduce strongly $\rho_{c,n}$. We complete the discussion by analysing the optical losses of the solar cell and explore the opportunity to use thin TCO completed by SiN_x to form a complete ARC with less parasitic absorption. Finally, to give perspective to our results, we expose an optimization roadmap to increase our solar cell efficiency, in comparison with the most recent record efficiency of 26.3% reached by LONGi for double-side contacted RJ solar cell.

In the *Conclusion*, we summarize our results obtained and our contribution to the field.

2 Experimental details and methods

This chapter details the main experimental methods used through this thesis. We describe first in section 2.1 the different steps of the solar cells fabrication as well as the different deposition techniques. Then, in section 2.2 we present the characterization methods used to assess various properties of the deposited individual materials. Finally, in section 2.3 we expose the methods used to evaluate the solar cell properties at the device level, resulting from the coupling of all the materials and processes constituting the contact stacks.

2.1 Solar Cell Fabrication

2.1.1 Wafer preparation and wet chemistry

The SHJ solar cells fabrication is based on crystalline silicon wafer. In this work, we use monocrystalline <100> float-zone (FZ) *n*-type and *p*-type wafers of resistivity of 2 Ω cm for their low defect density and high purity bulk properties. Those wafers are sawn from a single crystal ingots using wire sawing, reaching typically thickness of the order 200–300 µm. Due to the sawing damage, the wafers edges and surfaces typically suffer from high defect density, which are removed using isotropic alkaline wet etching. After this, texturization of the wafer is realized using an anisotropic potassium hydroxide (KOH) etching along the <111> planes, creating random pyramids of 2–10 µm heights. As a result of those steps, the wafer thickness is reduced down to 180–240 µm. Then, the latter undergoes a cleaning process to remove possible contaminants. Finally, before the cell processing, the wafer is dipped in a solution of 5% diluted hydrofluoric acid (HF) for 60 s in order to remove the native oxide (1–2 nm) present at its surface.

2.1.2 Plasma enhanced chemical vapour deposition

Plasma enhanced chemical vapour deposition (PECVD) is a crucial technique for SHJ solar cell, as it allows for the deposition of intrinsic and doped hydrogenated silicon layers, which provide surface passivation and carrier selectivity for this technology.

Typically, PECVD is realized in a parallel plate reactor as shown in Figure 2.1, in which precursor gases are decomposed in their various radicals at low temperature (150–250 °C) and pressure (typically a few mbar) thanks to a radio-frequency (RF) plasma, allowing to grow various thin films.

The precursor gases used for a-Si:H and nc-Si:H layer deposition throughout this thesis were

- Silane (SiH_4) - as the main precursor for silicon-based layers.
- Hydrogen (H_2) - used to increase the hydrogen content of the layers, in addition to the one present in SiH_4, as well as an etching agent in the realization of nc-Si:H layers.
- Phosphine (PH_3), diluted at 98 % in H_2 - used as phosphorous source for the *n*-type doping of silicon layers.
- Trimethylboron ($B(CH_3)_3$ or TMB) or boron trifluoride (BF_3), both diluted at 98 % in H_2- used as boron source for *p*-type silicon layers.
- Carbon dioxide CO_2 - used for alloying silicon to form silicon oxide SiO_x layers.

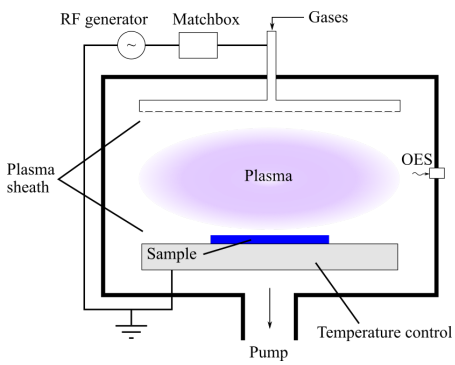

Figure 2.1: Schematic of PECVD reactor. Reproduced from [Cattin 2020].

Prior to deposition, the chamber is maintained at a very low pressure of the order of 1×10^{-6} mbar to avoid contamination. For the deposition, the substrate sample is first entered in the chamber, passing by a load-lock, and is held on the bottom electrode. Then, the selected precursor gases are mixed, before entering the chamber uniformly through a metal plate with a regular hole array (the shower head). Their flow is controlled individually using mass flow controller (MFC) for each gas, allowing to control the overall composition in the chamber. The pressure of the chamber is controlled via a butterfly valve on the pumping outlet. The temperature of the sustrate is regulated as well using a PID controller. Once the gas flow, pressure and substrate temperature are stabilized, an alternating electric field is generated between the two plates at a specific frequency and power thanks to a RF generator and matchbox system. Electrons are accelerated within this field, gaining sufficient energy to ionize the molecules of the precursor gases and lighting the plasma. Those radical ions are able to move within the plasma and diffuse towards the walls and plate of the reactors where they are adsorbed and react with each other to form a film.

The main advantage of this technique is that it allows to realize such reactions which would typically require much higher temperatures to dissociate the precursor gas molecules. The control of the film growth is however complex and depends on various parameters such as gas flow ratios, pressure, incoupled power, substrate temperature, excitation frequency,

deposition time, substrate properties and reactor conditioning (such as coating of the walls prior to deposition).

In this thesis, two main reactor designs were used, whose main parameters are given in the following table. The KAi-M system is composed of two chambers dedicated to intrinsic and doped layers, respectively.

Reactor	Frequency [MHz]	Plate distance [mm]	Electrode size [mm × mm]
Kai-M	13.56 / 40.68	12-15	612 × 502
Octopus	13.56 / 40.68	12-15	163.35 × 153.35

Table 2.1: PECVD reactors specification

2.1.3 Magnetron sputtering

In this thesis, magnetron sputtering (referred to simply as sputtering later) was used for the deposition of indium tin oxide (ITO) and indium zirconium oxide (IZrO) as TCO, as well as for rear silver layer and front grid deposition (for 1×1 cm^2 solar cells design, see Figure 2.3(c)).

Sputtering deposition relies on ejecting material from a source target onto an opposite substrate. The process is illustrated on Figure 2.2. First, a typically inert gas such as argon is introduced in the chamber and ionized thanks to a plasma. Unlike PECVD, the plasma is confined close to the target thanks to a magnetic field, which also accelerates the ionized particles towards the target. As they enter in collision with the latter, they eject neutral atoms of the target towards the substrate, forming a layer. The deposition rate of this technique typically depends on the distance between the target and the substrate as well as deposition power and pressure (as a high pressure decreases the Ar ion kinetic energy).

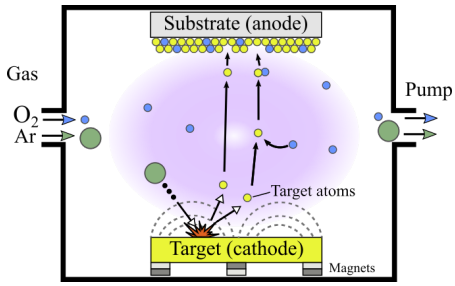

Figure 2.2: Schematic of a sputtering deposition chamber.

The layer properties can be further tuned by introducing an additional gas, such as O_2 in the chamber, that will react with the target atoms and alloys the material. This is typically used to control the conductivity of TCO, where an increased oxygen content (that can be regulated with the flow of O_2) typically reduces the conductivity.

The sputtering tool used in this thesis is a MRC-II system, in which the substrate samples are clamped or taped with a front shadow mask to a holding plate. This one travels laterally at constant speed in front of the target to allow for homogeneous deposition. Prior to deposition on the sample, a pre-sputtering time is set to allow for stabilized plasma conditions and constant target state during deposition. Ag and ITO layers were deposited using DC-sputtering,

and an In_2O_3(90):SnO_2(10) target for the latter, while RF-sputtering was used for IZrO layers, with a 2% weight target of ZrO_2 in In_2O_3.

2.1.4 Screen-printing

Silver grids were deposited on the front of solar cells using screen-printing, a standard industrial technique. A paste composed of silver nano-particles and organic-based ligands is squeegeed on the solar cell through a fine mesh, defining the front grid design (Figure 2.3(a) and (b)). After that, the cell is annealed for 30 min at 210 °C in order to evaporate the remaining solvents present in the paste. As the front grid will be responsible of shadowing loss, fingers as narrow as possible need to be realized, without compromising their conductivity. State-of-the-art screen printing line used in this thesis ranged in 25–35 µm widths, while their contribution to the solar cell series resistance was of the order of 0.1–0.15 $\Omega\,cm^2$ (see section 2.2.8 and Figure 2.8).

In this thesis, $2 \times 2\,cm^2$ solar cells were realized using screen-printing for the front side, while $1 \times 1\,cm^2$ solar cells use front silver grids which were realized by sputtering through a shadow mask. Device using this second method were systematically annealed at 210 °C for 30 min to mimic the conditions of screen-printing.

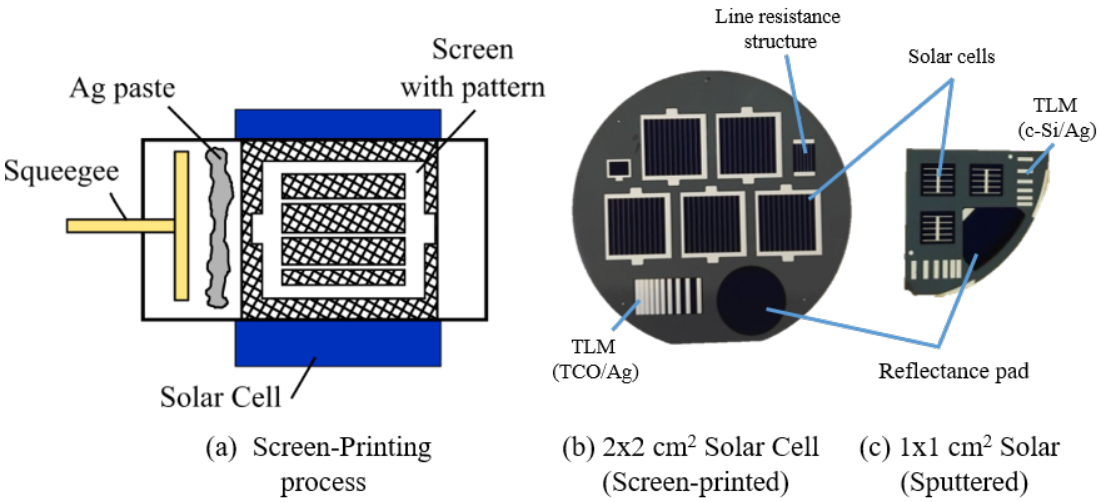

Figure 2.3: (a) Schematic of the screen-printing process. (b) $2 \times 2\,cm^2$ *solar cells design with screen-printed front grid. (c)* $1 \times 1\,cm^2$ *solar cell design based on quarter wafer with sputtered front grid.*

2.1.5 Process flow for silicon heterojunction solar cells

Figure 2.4 presents the process flow used to realize SHJ solar cells throughout this thesis. All the structures were based on 2 Ωcm, n-type or p-type FZ c-Si textured wafers of thickness $t = (195 \pm 10)\,\mu m$ (after texturization). After texturing, cleaning and native oxide removal,

a-Si:H or nc-Si:H intrinsic and doped layers were deposited via PECVD in the KAI-M system to create surface passivation and carrier selectivity. Usually, the layers forming either the "in" or "ip" stacks were deposited in a single run without vacuum break between the intrinsic and doped layer to avoid contamination and increase reproducibility. The intrinsic layers were deposited in a dedicated chamber, while a second chamber was reserved for doped layer. The latter was systematically pre-coated when changing the dopant type used in the deposition.

Then, TCOs, either ITO or IZrO, were sputtered on both sides through a shadow mask, defining the area visible on Figure 2.3(b) and (c). On the rear side a 100 nm thick Ag layer was sputtered. If the solar cells were fabricated in front junction (FJ) configuration, the deposition on the rear side was done on the whole area of the wafer, which also serves as protective layer for the device manipulation. If the rear-junction (RJ) configuration was adopted, the deposition of TCO and Ag on the back-side were done through shadow masks, requiring precise alignment of the front and rear square areas. This patterning step is required to avoid increased recombination in the non-illuminated area when measuring the solar cells.

After this, the front silver grid was either realized by screen printing, for the $2 \times 2\,\text{cm}^2$ solar cells design (Figure 2.3(b)), or sputtered through a shadow mask for the $1 \times 1\,\text{cm}^2$ solar cells (Figure 2.3(c)). Finally, the samples were annealed in both cases at 210 °C for 30 minutes to cure sputtering-damage, evaporate the ligands of the screen-printed paste or simply mimic the effect of screen-printing annealing for the sputtered cells. At this stage, the solar cells are considered finished and ready to be characterized. We use the 1x1.1 cm^2 cells to analyse large trends of V_{oc} and FF with typical values lower than 720 mV and 80% respectively, while the 2x2 cm^2 cells allow us to discuss higher efficiency trends in more details.

Additional steps allowing to reach higher efficiencies were also performed for some devices. First, a double anti-reflective coating (DARC) was realized to minimize the solar cell reflection even further. In this case, the front TCO layers were thinned down from their 115 nm for front application as single anti-reflective coating (ARC) to 75 nm (two-third of the thickness). Then, after the metallization of the solar cell, an additional 120 nm SiO_x layer was deposited on the whole front surface via PECVD, forming the DARC. Finally, some of the best cells presented were placed in forward-bias in the dark for two weeks as is done in [Cattin 2021], allowing an increase of V_{oc} and FF of the order of +2mV and +0.7%$_{abs}$, respectively.

2.2 Material Characterisation

2.2.1 Ellipsometry

The thicknesses of thin layers (< 30 nm) reported were measured using variable-angle spectroscopic ellipsometry (SE) from layers deposited on glass substrates or polished wafers. Spectra were acquired in the range 1.5-6 eV at angles of 50°, 60° and 80° using a Horiba Jobin Yvon ellipsometer and modelling was performed using the DeltaPsi2 software. For a-Si:H(i), a-Si:H(p), a-Si:H(n), and SiO_x layers, a single Tauc-Lorentz (TL) model with surface roughness was used.

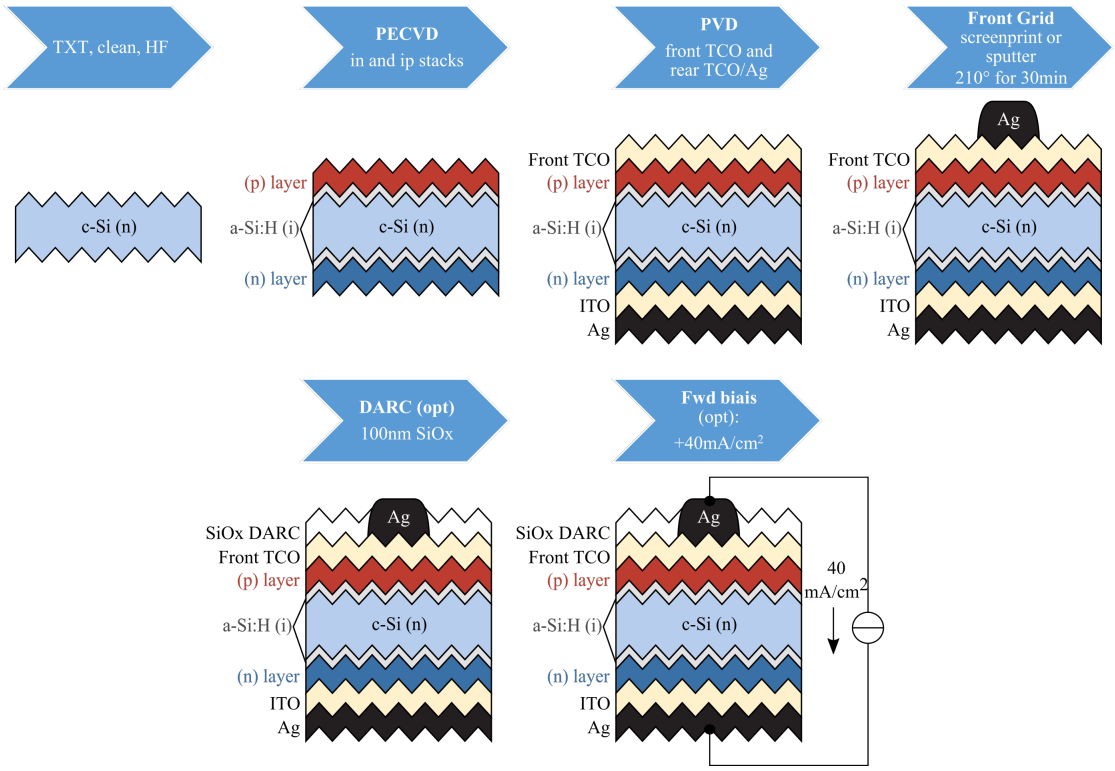

Figure 2.4: Process flow of SHJ solar cells (here in front junction configuration).

For nc-Si:H and thin TCO materials, since the growths of these are substrate dependent, the whole stack of materials including the underneath layers were measured and modelled altogether. For example, the stack Glass / a-Si:H(i)/ nc-Si:H are modelled by first fixing the Glass / a-Si:H(i) characteristics from a previous measurement. Then the nc-Si:H layer is modelled as a double TL with peaks at 3.36 eV and 4.25 eV, as suggested in [Yuguchi 2012] and a surface roughness is added. Note that modelling the nc-Si:H with a single TL or otherwise with a double TL and an additional harmonic oscillator and testing various starting conditions was systematically investigated, leading to similar thicknesses (see Figure A.13).

2.2.2 Dark lateral conductivity

Dark lateral conductivity and related activation energy were measured as a metric of the layer active doping. Samples were prepared by depositing layer stacks on glass substrates and then evaporating 100 nm-thick Al pads at room temperature. The samples were then placed in an N_2 atmosphere of approximately 1 mbar on a thermally conductive chuck. The temperature was ramped from 25 °C to 180 °C in 15 min, held for 90 min, and then ramped down to 25 °C during 4 hours. The resistance between the two pads was measured using two-probe pogo-pins on each pad and electrometers. The activation energy of the dark lateral conductivity (E_a) and room temperature conductivity (σ_{RT}) were calculated on the descending temperature

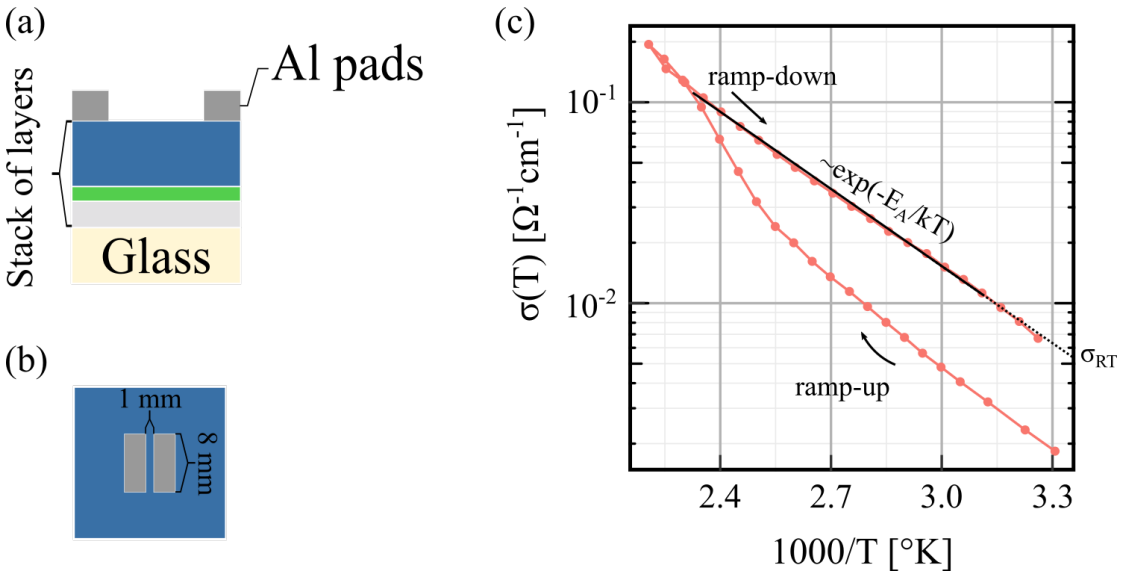

Figure 2.5: (a) Cross-section of dark lateral conductivity sample. (b) Top view of the same sample. (c) Data extraction.

ramp, by fitting the data between 30 °C to 145 °C with the formula

$$\sigma(T) = \sigma_0 exp(-E_A/k_B T) \tag{2.1}$$

with k_B being the Boltzmann factor and σ_0 a pre-factor equal to the extrapolated conductivity at infinite temperature. Figure 2.5 presents the sample details as well as the usual data extraction.

2.2.3 Raman spectroscopy

Raman spectroscopy was used to characterize the microstructure of a-Si:H and nc-Si:H layers throughout this thesis, using a Monovista Confocal Raman System. To obtain an accurate background shape and extract the crystalline and amorphous phase features, Raman spectra were fitted with Gaussians centered around 315, 420, 480, 510, 520 and 625 cm^{-1} [Bermejo 1979] (see Figure 2.6(a)). The Raman crystallinity (X_c) is then computed as

$$X_c = \frac{A_{510} + A_{520}}{A_{480} + A_{510} + A_{520}} \tag{2.2}$$

were the A_{480} is the amplitude of the gaussians used to fit the amorphous peak, whereas A_{510} and A_{520} are the amplitudes of the two gaussians used to fit the asymmetric crystalline peak [Smit 2003]. Figure 2.6(b) presents example of spectrum of a-Si:H and nc-Si:H layers of various crystallinity, normalized to collapse together the common amorphous part of the spectrum. Two wavelengths of laser were used for different purposes explained below, due to their different penetration depths (Figure 2.6(c)). For the characterization of the crystallinity

of nc-Si:H layers, spectra can be acquired directly on textured wafer. This has the advantage to allow probing directly the same sample where solar cells were processed as well as obtaining a higher signal than on glass or polished substrates, thanks to the lower reflection. Moreover, the wafer having a high thermal conductivity, it evacuates efficiently the heat generated by the laser in the sample, avoiding thus unwanted recrystallisation of the layer. Note that in contrasts, for layers deposited on glass or on a thick amorphous layer (> 40 nm) which have poor thermal conductivities, the laser intensity should be adapted to avoid recrystallisation.

To take into account the substrate dependence of nc-Si:H growth, they were always studied in the whole stack a-Si:H(*i*)/ nc-Si:H. To avoid the contribution of the c-Si and the a-Si:H(i) layer underneath, a 325 nm UV laser was used to probe only the top 10-15 nm of the layers [Carpenter III 2017]. To study nc-Si:H layers thinner than 10–15 nm, thicker amorphous layers were used underneath to prevent an overestimation of the crystallinity of the layer (Figure 2.6(d)). Finally, Raman spectroscopy was also used to evaluate the transparency of the developed layers. Using a 442 nm laser with a probing depth down to the wafer, we used the c-Si signal counts attenuation to measure the absorption of the layer stack at this wavelength, as was used in [Ledinský 2016], giving a good indication of the transparency in the visible wavelength.

2.2.4 UV-Vis-NIR Spectroscopy

A UV-Vis-NIR spectrometer equipped with an integrating sphere was used to determine the optical properties of materials within the 200–3300 nm spectral range. The total transmittance T, total reflectance R and absorption $A = 1 - T - R$ were measured on layers or stack of layers deposited on glass, while the solar cells reflectance was measured on the final device on a circular TCO pad, free of front metallization (see Figure 2.3(b)).

2.2.5 SIMS

Secondary ion mass spectrometry (SIMS) was used to characterize the chemical composition of layer stacks (see chapter 4) deposited on mechanically polished (111) n-type wafers. The measurements were performed at the Luxembourg Institute of Science and Technology, using A CAMECA SC-Ultra instrument operating with a Cs^+ or $O_2{}^+$ bombardment at a low impact energy (1 keV).

2.2.6 TEM

Transmission electron microscopy (TEM) was performed to characterize the overall microstructure of layer stacks (see chapter 4) deposited on a mechanically polished (111) c-Si wafer. The measurements were performed at the Interdisciplinary Centre for Electron Microscopy at EPFL, using the conventional focused ion beam lift-out method in a Zeiss NVision 40 dual beam FIB/scanning electron microscopy system. The lamella were then analyzed by

TEM in a double Cs-corrected TFS Titan Themis.

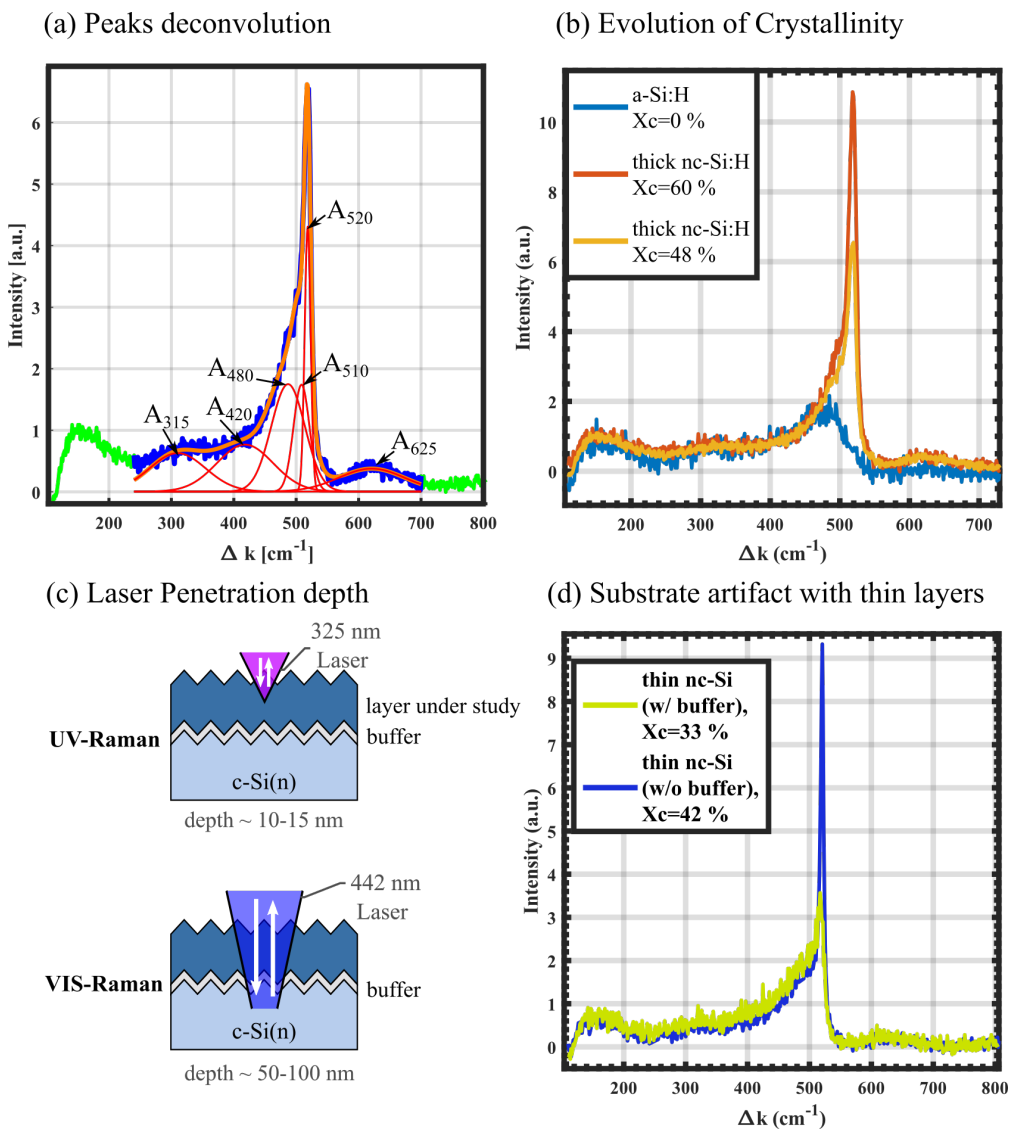

Figure 2.6: (a) Gaussian peaks deconvolution of a nc-Si:H Raman spectrum. (b) Raman spectra of a-Si:H and nc-Si:H layers with different crystallinity. (c) Schematic of the laser penetration using different laser wavelengths. (d) Effect on the measurement of the substrate when measuring thin layers.

2.2.7 Transfer Length Method

Transfer length method (TLM) was used to extract the contact resistivity ρ_c of various contact stacks as well as the sheet resistance of either TCO or c-Si. The TLM structure is illustrated on Figure 2.7 and visible on the sample of Figure 2.3. It is formed of a conductive base on top of which contact pads of widths d are patterned with varying inter-pad distance L. Measuring the resistance between two pads $R_{s,tot}^{TLM}$ and applying a linear fit allows to extract ρ_c and R_{sh} as [Meier 1984].

$$R_{s,tot}^{TLM}(L) = R_{sh}\frac{L}{W} + 2R_c \tag{2.3}$$

$$R_c = L_T\frac{R_{sh}}{W} \tag{2.4}$$

$$\rho_c = R_c L_T W \tag{2.5}$$

where R_c is the contact resistance (in [Ω]), L_T is called the transfer length, W is the sample widths and $L_T \times W$ is the contact area through which the current flows. Note that this approximation is valid only if $d \gg L_T$, otherwise one should replace eq. 2.5 by the more general formula valid for short pads $R_c = R_{sh}\frac{L_T}{W}\coth\left(\frac{d}{L_T}\right)$ [Berger 1972, Basset 2021]. Throughout this thesis we used the first approximation to compute the presented results. However, we verified that no significantly different results were obtained using the more general formula.

In this thesis, we used TLM samples for various purposes:

First, the sheet resistance of TCOs R_{sh}^{TCO} and the contact resistivity of TCO with silver $\rho_c^{TCO,Ag}$ were measured with TLM, in particular in the case of very thin TCO, with which four point probe measurements (see next section) were not possible to perform (punch-through). In this case, the TCO were deposited on the full area of the sample, followed by the sputtering (through a shadow mask) or screenprinting of silver pads. The pad inter distances were measured using an optical microscope. The samples edges were then cut to leave no place for current to flow outside the channel of width W delimited by the pad design, forming the so-called mesa-isolation [Meier 1984]. Importantly, to be able to characterize TCOs grown on various layers influencing their properties, *e.g.* during the growth [Cruz 2019a], the wafer type was adjusted to form a blocking junction in the dark, constraining the current to flow in the TCO only (see Figure 2.7(c), where a p-type wafer is used to prevent current to form a junction with the n-type contact on which the TCO was grown). Note that throughout this thesis, it was constantly observed that $\rho_c^{TCO,Ag} < 1\,\mathrm{m\Omega\,cm^2}$, and therefore we do not report it further in the text.

Second, the contact resistivity from the wafer to the electrode provided by the layer stack $\rho_{c,e/h}$ was measured using TLM, together with the sheet resistance of the wafer R_{sh}^{c-Si}. In this case, the PECVD layers were deposited on the full area of the wafer, and then TCO and silver were both sputtered through shadow mask to form the pads, followed by mesa-isolation. Some TLM samples were measured under illumination, illuminated from the rear side to allow for an homogeneous illumination under the pads using a flipping table [Basset 2021, Senaud 2021a].

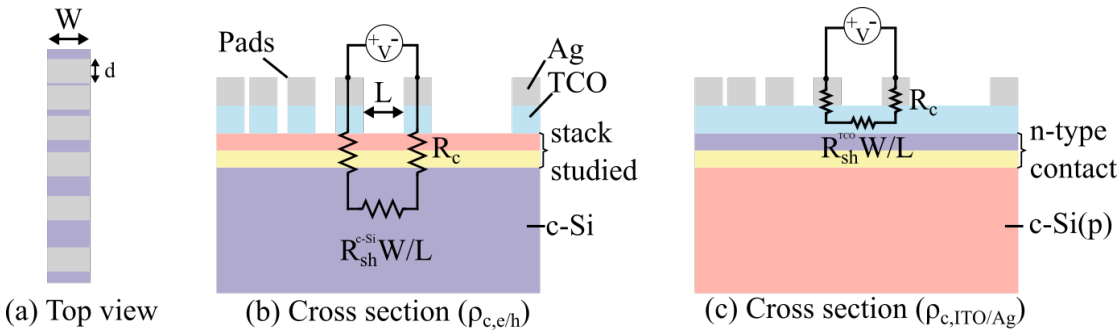

Figure 2.7: Schematic of TLM samples. The texture is not represented for simplicity. (a) Top view. (b) Cross section, structure for the characterisation of the contact resistance from the wafer to the electrode $\rho_{c,e/h}$. (c) Structure for the characterization of $\rho_c^{TCO,Ag}$ and R_{sh}^{TCO}.

2.2.8 Line resistance

The screen-printed fingers of the front grid of solar cells were characterized by measuring the structure presented on Figure 2.3(b). The resistance between the two busbars R_{bb2bb} was evaluated using a set of two Kelvin probes and the finger line resistance R_{line} (in [$\Omega\,\mathrm{cm}^{-1}$]) was calculated as $R_{line} = R_{bb2bb}\frac{n}{l_f}$, where n is the number of fingers and $l_f = 1\,\mathrm{cm}$ is the finger length in this structure. The line resistance of a finger is related to its conductivity ρ, thickness t_f and width w_f by $R_{line} = \frac{\rho}{t_f w_f}$.

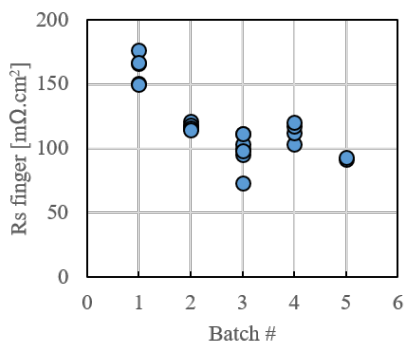

Figure 2.8: Finger series resistance among various batches in this thesis

The contribution of the fingers to the normalized series resistance (in [$\Omega\,\mathrm{cm}^{-2}$]) of the corresponding solar cell can then be computed as follows: First, the power losses along the finger in a unit cell are computed considering the current extracted from the solar cell increases linearly along the finger [Meier 1984]

$$P_{finger} = \int_0^{l_f} dy R_{line} I^2(y) = \int_0^{l_f} dy R_{line}\left[\int_0^y dy' pJ\right]^2 = \frac{1}{3} l_f^3 p^2 R_{line} J^2 \tag{2.6}$$

where $l_f = 2\,\mathrm{cm}$ is the finger length (in the solar cell this time), p is the pitch of the grid and J is the current density extracted from the solar cell. Normalizing by the power produced by this same unit area, $P_{unit} = JVl_f p$, we have

$$P_{finger,norm} = \frac{P_{finger}}{P_{unit}} = \frac{1}{3} l_f^2 p R_{line}\frac{J}{V} = \underbrace{\frac{1}{3} l_f^2 p \frac{\rho}{t_f w_f}}_{\equiv R_s^{finger}}\frac{J}{V} \tag{2.7}$$

where R_s^{finger} is given in $\Omega\,\mathrm{cm}^2$ and was generally in the range 0.1–0.15 $\Omega\,\mathrm{cm}^2$ for all the batches measured in this thesis, while the variations within one batch was lower than 0.02 $\Omega\,\mathrm{cm}^{-2}$ (Figure 2.8).

2.2.9 Hall effect

Hall measurements were used to characterize the properties of TCOs, namely their mobility μ_{TCO} and their carrier concentration N_{TCO}, using an ECOPIA HMS-500 setup. The description of the method can be found elsewhere [Sze 2006, Senaud 2021a]. For sample preparation, TCOs were deposited on glass which were cut as 1×1 cm^2 or 2×2 cm^2 squares. In the particular case of studying TCO properties after the deposition of a subsequent dielectric layer such as SiO_x to form a double anti-reflective coating, the corners of the glass were masked during the deposition to keep the TCO accessible for contacting afterwards.

2.2.10 Four Point Probes

Sheet resistance of TCOs R_{sh}^{TCO} were acquired using four point probes measurements (4PP). The sheet resistance is related to the film conductivity ρ and thickness t by $R_{sh} = \frac{\rho}{t}$. The measurement is carried out by using four probes equally distant from one another in which the two outside probes inject a current and the two inside ones measure the voltage drop, allowing to remove any contribution to the resistance from the measurement system. As the current not only flows along a line, but also in the plane perpendicular to the probes, the sample must be large enough and a geometric correction factor should be used to take this into account, *i.e.* [Valdes 1952]

$$R_{sh} = \frac{\pi}{\ln(2)}\frac{V}{I} = 4.532\frac{V}{I} \tag{2.8}$$

The contribution of the TCO to the normalized series resistance (in [$\Omega\,\mathrm{cm}^{-2}$]) can be calculated easily in the case where lateral current transport in the solar cell happens solely through the TCO and not the wafer (otherwise see chapter 5). We proceed similarly as for the computation of the resistive losses in the fingers. First, the power losses in a unit cell for the current to reach the finger through the TCO is computed considering a homogeneous current density extraction in the TCO [Meier 1984]

$$P_{TCO} = 2\int_0^{p/2} I^2(x)\frac{R_{sh}^{TCO}}{l_f}dx = 2\int_0^{p/2}\left[\int_0^x J l_f dx'\right]^2\frac{R_{sh}^{TCO}}{l_f}dx = \frac{1}{12}R_{sh}^{TCO} l_f p^3 J^2 \tag{2.9}$$

Normalizing by the power produced by this same unit area, $P_{unit} = JVl_f p$, we have

$$P_{TCO,norm} = \frac{P_{TCO}}{P_{unit}} = \underbrace{\frac{1}{12}R_{sh}^{TCO}p^2}_{\equiv R_s^{TCO}}\frac{J}{V} \tag{2.10}$$

where R_s^{TCO} is given in $\Omega\,\mathrm{cm}^2$ and gives $R_s^{TCO} = 0.285\,\Omega\,\mathrm{cm}^2$ for a $100\,\Omega/\mathrm{sq}$ TCO and a standard grid pitch $p = 0.185\,\mathrm{cm}$.

2.3 Device Characterization

2.3.1 Photoconductance decay measurement

Photoconductance decay (PCD) measurements were used to characterize the effective minority carrier lifetime, implied open-circuit voltage iV_{oc} and implied J-V curves of solar cell precursors. For this we used a WCT-120 photoconductance lifetime tester from Sinton. The measurement goes as follows [Sinton 1996]: After its exposition to a flash, the time dependent photoconductivity $\sigma(t)$ of the c-Si absorber is measured, as well as its rate of decay at each time $\frac{d\sigma}{dt}(t)$. The photoconductivity being a function of the excess carrier density, it can be inverted to find the latter as $\Delta n = \frac{\sigma - q\mu_n N_D}{q(\mu_n - \mu_p)}$ (assuming here a n-type absorber) [Senaud 2021a]. Then, the recombination rate and effective lifetime can be computed thanks to the continuity equation that reads at open-circuit conditions

$$\frac{d\Delta n}{dt} = G(t) - U(t) = G(t) - \frac{\Delta n}{\tau_{eff}(\Delta n)}(t) \tag{2.11}$$

As throughout this thesis, most samples reached $\tau_{eff} > 1\,\mathrm{ms}$, a value much longer than the flash decay, the analysis was carried out in the transient mode, *i.e.* assuming $G(t) = 0$ which simplified the lifetime extraction to $\tau_{eff}(\Delta n) = \frac{\Delta n}{\frac{d\Delta n}{dt}}(t)$ [Nagel 1999, Kerr 2002]. The construction of the implied J-V curve and extraction of iV_{oc} and iFF follows from our explanations given in section 1.2.2.

2.3.2 Photoluminescence

Photoluminescence (PL) imaging is another technique that allows to probe the excess minority carrier density. It consists of illuminating the sample by a laser (in our case with a central wavelength of 808 nm) and measuring the infrared photons re-emitted by band-to-band recombination using a CCD Camera coupled with filters that eliminate the signal from the light source [Trupke 2007]. The illumination occurs continuously during the measurement (quasi-steady state), therefore generation balances recombination leading to $G = \frac{\Delta n}{\tau_{eff}(\Delta n)}$. As only the radiative recombination is measured, the current measured by the CCD camera is given by $I_{PL} = A_i r_{rec} \Delta n (N_D + \Delta n)$ (for a n-type wafer), where A_i is a calibration constant and r_{rec} is the radiative recombination rate [Hallam 2014]. Therefore, a well passivated area emits more IR light than a poorly passivated one due to the higher carrier concentration there. This technique is thus used to record mapping of passivation homogeneity. An advantage compared to PCD measurements is that PL imaging allows for the characterization of passivation losses on a metallized sample.

The incident photon flux can be varied by adjusting the current of the laser, which can be

calibrated using a reference cell. Measuring the sample under 1 sun conditions allows the computation of iV_{oc} map of the device provided accurate calibration constant [Hallam 2014]. Considering that for SHJ solar cells it is common to have $J_{mpp} = 0.95 \times J_{sc}$ (see Figure A.3(b)), measuring the sample under 5% sun allows to extract the mapping of the implied voltage at maximal power point iV_{mpp}. Finally, it is possible to construct the map of the implied fill factor *iFF* from those two previous maps, as $iFF = \frac{J_{mpp} iV_{mpp}}{J_{sc} iV_{oc}} \approx 0.95 \times \frac{iV_{mpp}}{iV_{oc}}$.

2.3.3 Solar Cell Current-voltage characteristics

The current-voltage characteristics of solar cells (*J-V* curve) is the most important characterization of a finished solar cell, as introduced in section 1.2.2. In our laboratory, the solar cells *J-V* curves were collected using a class AAA WXS-90S-L2 solar simulator from Wacom. The light source consists of a 400 W halogen lamp and a 500 W Xenon Lamp coupled with dedicated filters and optics, allowing to illuminate homogeneously a 90×90 mm^2 area. The spectrum was regularly calibrated using a set of encapsulated reference solar cells to yield the correct current in the different parts of the spectrum to respect as close as possible the AM1.5G standard with an illumination density of 1000 W m^{-2}. Measurements at lower illumination were performed using neutral density filters consisting of a metallic grid mesh. The solar cells were held on a gold chuck with a vacuum pump and the temperature of the chuck was regulated by Peltier elements to 25 °C.

2.3.4 J_{sc}-V_{oc} method and series resistance extraction

The J_{sc}-V_{oc} method allows for the characterization of the pseudo *J-V* curve of a solar cell, as described in section 1.2.2. For the J_{sc}-V_{oc} method, the open circuit voltage (V_{oc}) and short-circuit current (J_{sc}) are measured at one sun and at lower illuminations using a neutral density filter. This method is very similar to the *Suns-Voc* method [Sinton 2000], but it has the advantage that the operations are performed on the very same setup as for the *J-V* curve characterization and benefits from the same light calibration and temperature control. The obtained V_{oc} are then shifted up to a current $J = J_{sc}^{1sun} - J_{sc}^{shaded}$ to construct the pseudo *J-V* curve (*pJ-V*), as shown in Figure 2.9. By construction, the *pJ-V* curve corresponds to the *J-V* curve for a same level of internal injection Δn without series-resistance losses. Therefore, R_s can be computed as the difference between the voltage and the pseudo-voltage for a fixed current (corresponding to a given injection level) [Bowden 2001][1] :

$$R_s = \frac{pV(J) - V(J)}{J} \tag{2.12}$$

One assumption for the validity of this method is that J_{sc}^{shaded} varies linearly with the illumination level [Bowden 2001].

[1] In the rest of the thesis, we occasionally referred to the J_{sc}-V_{oc} method as *Bowden's method*, with reference to Bowden *et al.*'s review paper on series-resistance characterization method [Bowden 2001], even though such type of measurements can be traced back to early work from Wolf *et al.* [Wolf 1963].

Moreover, assuming no selectivity losses, the pseudo-voltage is equal to the implied voltage and the injection can be computed using [Adachi 2015]

$$\Delta n = \sqrt{\frac{(n_0 - p_0)^2}{4} + n_0 p_0 \exp\frac{iV}{k_B T} - n_0 p_0} - \frac{n_0 + p_0}{2}, \tag{2.13}$$

where $n_0 \approx N_D$, and $p_0 \approx n_i^2/n_0$ for a n-type wafer. Using those relations, it is therefore possible to relate every series resistance to an injection value and construct the curves $R_s(\Delta n)$ or $R_s(pV)$.

Typically, the R_s at MPP and fill factors without the effects of series resistance (*pFF*) were obtained by comparing the *J-V* curve of a device at 1 sun with the one at a lower illumination level giving the smallest difference between J_{mpp}^{1Sun} and $J_{sc}^{1sun} - J_{sc}^{shaded}$. This illumination level was in most of the case close to 5 % sun. However, we systematically investigated 3 % sun and 10 % sun illuminations during the data acquisition, as for some rare solar cells these corresponded to their respective MPP.

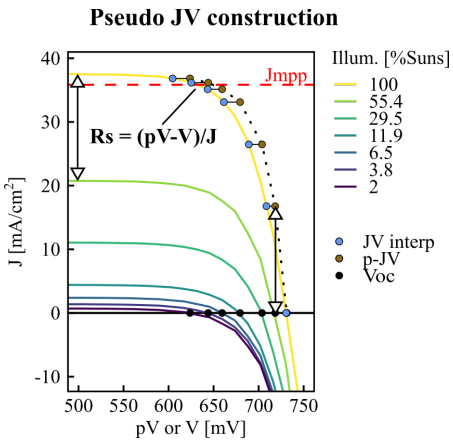

Figure 2.9: Pseudo J-V *curve construction using the* J_{sc}-V_{oc} *method. Note that the two arrows have the same size.*

Once the series resistance has been evaluated, there exist different approaches to compute the pseudo fill factor (*pFF*) of the *pJ-V* curve. First, assuming the solar cell follows a two-diode model with series resistance and shunt, Green proposed an empirical model to approximate the fill factor of the circuit free from the R_s, R_{sh} and the second recombination diode. This pseudo fill factor, denoted FF_0, is given by

$$FF_0 = \frac{v_{oc} - \ln(v_{oc} + 0.72)}{v_{oc} + 1} \quad \text{with} \quad v_{oc} \equiv \frac{qV_{oc}}{nk_B T} \tag{2.14}$$

where n is the ideality factor of the single remaining diode [Green 1981, Khanna 2013] and can be obtained as $n = \frac{1}{k_B T}\frac{V_{oc} - pV_{mpp}}{\ln(J_{sc}/J_{mpp})}$. Second, without assuming a two-diode model necessarily, but however requiring a shunt-free solar cell, the pseudo fill factor can also be calculated from

$$pFF = FF + \frac{J_{mpp}^2}{V_{oc} J_{sc}} R_s \approx FF + 0.05 \times R_s \tag{2.15}$$

where the second approximation with a factor of 5 holds well for typical SHJ values, as demonstrated experimentally in [Pysch 2007] and can be used as a rule of thumb to evaluate the impact of series resistance. In appendix A.1, we give a derivation and arguments for these formula and approximation. Note that both formula for FF_0 and *pFF* yields very similar results within $\pm 0.3\,\%_{\text{abs.}}$ for many device measured throughout this thesis (see Figure A.3(c)).

2.3.5 External and internal quantum efficiency

External quantum efficiency (EQE) measures the spectral ratio of the number of collected electric charges compared to the incoming photon flux on a solar cell held at short-circuit, *i.e.* what amount of e^- / h^+ pairs is created and collected per incoming photon at a given wavelength. Therefore, EQE measurements give insights into loss mechanisms affecting the J_{sc} of a solar cell. Typically, in the 300–600 nm range photons are quickly absorbed in the first 10–100 nm of the device and are therefore representative of losses at the front of the device, whereas infrared photon in the 900–1200 range can be impacted both by FCA at the front and rear of the solar cell (*e.g.* in the TCO) as well as by their multiple reflection on the front and back of the solar cell. On top of that, the whole EQE can be impacted by non-optimal reflection (usually optimized to be minimum around 600 nm) and collection efficiency problem, such as in the case of strong passivation issues or shunts.

From EQE measurements, it is possible to evaluate the expected short circuit current that could be obtained under an illumination defined by the AM1.5G spectrum as

$$J_{sc}^{EQE} = \int_{300nm}^{1200nm} AM1.5G(\lambda) EQE(\lambda) \frac{\lambda}{hc} d\lambda \tag{2.16}$$

where $AM1.5G(\lambda)$ is given in [$\mathrm{W\,m^{-2}\,nm^{-1}}$], h is Planck's constant, and c is the speed of light.

The EQE can be renormalized to remove the reflected photons from the incoming beam, defining the internal quantum efficiency (IQE)

$$IQE(\lambda) = \frac{EQE(\lambda)}{1 - R(\lambda)} \tag{2.17}$$

allowing to study the impact of absorption and collection efficiency problem alone.

Throughout this thesis, the EQE curves were acquired using a system developed in-house with a lock-in amplifier and a xenon arc lamp shining a $1 \times 1.5\,\mathrm{mm}^2$ monochromatic light spot between the grid fingers of the solar cell. This small beam as the advantage to allow probing $1 \times 1\,\mathrm{cm}^2$ or $2 \times 2\,\mathrm{cm}^2$ solar design in the same way. However, in the case of collection efficiency issue, the low illumination condition of this small spot yields stronger losses than during a measurement at 1 sun such as for the *J-V* characteristics acquisition, and therefore an additional bias light was used in those cases.

3 Circuit model for contact limited solar cell

3.1 Introduction

As mentioned in chapter 1, the silicon heterojunction (SHJ) technology avoids large recombination (*i.e.* avoid quasi-Fermi levels collapsing immediately at the wafer surface) of classical cells (Al-BSF or PERC) thanks to the introduction of thin layers of intrinsic hydrogenated amorphous silicon (a-Si:H(i)) that passivate the defects at the wafer surface and separate it from direct contact with the metallic electrodes. On top of that, doped hydrogenated amorphous silicon (a-Si:H(n) and a-Si:H(p)) layers are used to create charge selectivity towards holes and electrons at each contact. Finally a transparent conductive oxide (TCO) is used to provide low lateral resistance towards the metallic finger grid as well as a low contact resistance with the metal.

One of the most important losses affecting the efficiency of SHJ solar cells is the important parasitic light absorption in those a-Si:H and TCO films [Holman 2014]. In the past years, research on new contacts using various more transparent materials have been performed in order to overcome this front light absorption issue, such as the development of hydrogenated nanocrystalline silicon thin films (nc-Si:H) [Seif 2016] or more exotic silicon-free materials such as AZO:SiO_2, zinc tin nitride or molybdenum oxide [Zhong 2019, Lin 2020, Fébba 2021, Dréon 2021]. These materials open a wider optical, electrical and processing parameter space, which are hoped to allow decoupling of different losses in the solar cell.

A contact with ideal transport properties should provide passivation (avoid large recombination at the wafer surface), selectivity (towards holes vs electrons extraction) and large conductivity (for the majority carrier) [Onno 2019]. Contacts developed towards achieving this goal are therefore named carrier selective passivating contact (CSPC). In the recent years, an important axis of research to form CSPC was to select materials with work function of extreme difference compared to the one of crystalline silicon (c-Si) [Allen 2019]. This interface of materials of high/low WF induces a band bending in the c-Si, ideally following the Mott-Schottky rule, as well as an asymmetric band offset towards holes and electrons that should, in principle, provide carrier selectivity.

However, in practice the development of a new promising material and its inclusion into solar cells often lead to unpredictable results. This is because properties such as the conduction or valence band position with respect to vacuum or bandgap have a wide range of possible values for a given material and are highly dependent on the deposition technique and conditions, or substrate. Moreover, the possible creation of surface dipoles, Fermi level pinning due to interface defects or parasitic Schottky barriers all reduce the effect of the material to a lower effective WF difference [Sze 2006], mitigating the selectivity of the contact. Finally, the charge transport can occur through mechanisms that are not only dependent on the WF difference, contrary to the classical thermionic emission (TE), and other parameters can play an important role on the transport such as barrier thickness, defect density and band tail states in the case of direct or trap-assisted tunnelling (TU).

All these effects strongly impact the properties of the contact, and the resulting solar cell *J-V* curve often exhibits non-ideal behaviours such as kinks, saturations and S-shapes [Fioretti 2019, Fébba 2021, Dréon 2020]. To allow for a direct in situ investigation of the solar cell bottlenecks, it is therefore useful to be able to extract information directly from those features of the measured *J-V* curves. Therefore, a suitable model is needed for this purpose.

Figure 3.1 presents some of the most popular circuit models used to describe solar cells in the literature. Following the partial conductivity framework of Würfel *et al.* that describes with physical based arguments the charge separation mechanisms (see section 1.2.1) [Wurfel 2015], Onno *et al.* developed a circuit model that allows to take into account selectivity, passivation and conductivity losses [Onno 2019]. The latter is represented on Figure 3.1(b), where the effect of surface recombination and selectivity losses are embodied by five different contact resistivities. In all generality, those can be voltage dependent and therefore implement any type of current transport process. This model also has the advantage to provide quantitative definitions for passivation, selectivity and conductivity metrics [Onno 2019]. However, it requires extra-steps of modelling of those specific resistivities to relate the model to parameters of a band diagram. Trying to model all the transport and recombination mechanisms occurring in a SHJ solar cell, such as presented on Figure 1.14, would be too complex and introduce too many fitting parameters. Therefore, a simpler approach needs to be developed.

On the one hand, a first simpler model of solar cells is provided by the popular "*lumped-skin model*" of Brendel *et al.* [Brendel 2016]. In the latter, selectivity losses (as defined by Onno *et al.*)[1] are completely neglected, and all the recombination mechanisms are lumped into a single diode of parameters j_{0c}, while the contact resistivity ρ_c is simply connected in series. While this approach proved useful to describe diffused junctions, which possess good selectivity but poor passivation, and find optimal contact fraction [Brendel 2016], it is not able to describe S-shapes characteristics nor differences between V_{oc} and iV_{oc} [Glunz 2017, Onno 2019].

[1] Brendel *et al.* also define a "selectivity" metric $S = (k_B T)/(q j_{0c} \rho_c)$, which relates the resistance of the majority carriers through ρ_c to the resistance of the minority carriers through the diode (slope at zero bias). Note the different use of vocabulary compared to Onno *et al.*. Within the latter authors paradigm, this metric relates more to a ratio of passivation vs. conductivity.

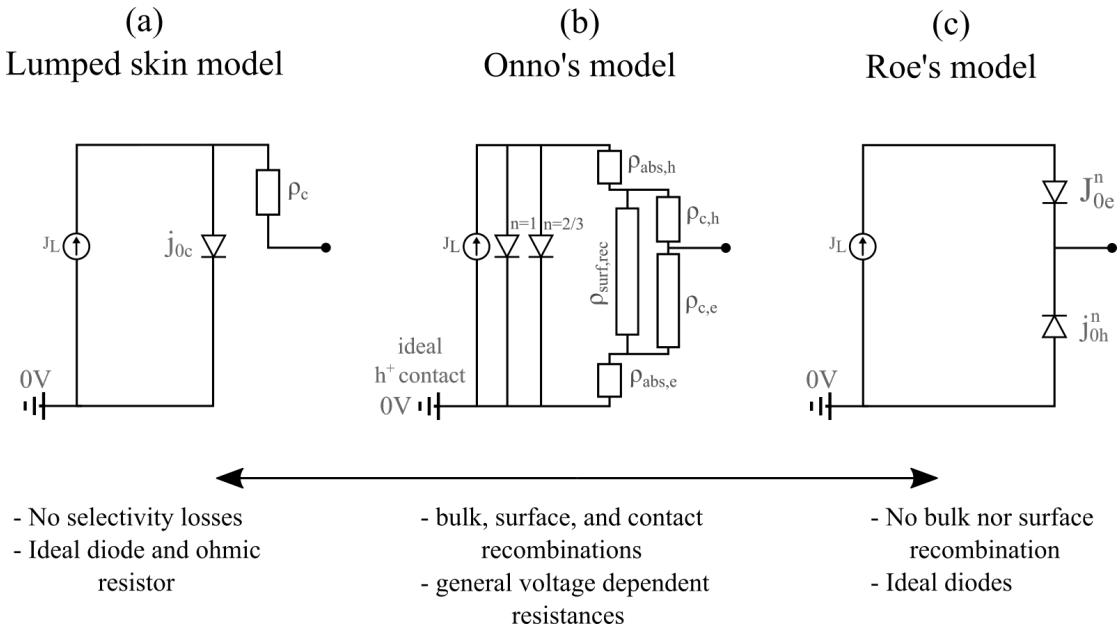

Figure 3.1: Solar cell equivalent circuit models from (a) Brendel et al. *[Brendel 2016], (b) Onno* et al. *[Onno 2019], and (c) Roe* et al. *[Roe 2019]. In every model, we used an ideal hole contact for simplicity, however they can all be generalized to two non-ideal contacts.*

On the other hand, recently Roe *et al.* proposed another simple model to describe solar cells limited by their contacts [Roe 2019]. It consists of a single current source and four diodes to describe the partial electron and hole currents at each contact, predicting that every *J-V* curves feature two S-shapes and saturation plateaus commonly observed in the development of novel contact [Fébba 2021]. This model has the advantage to provide a simple explanation of the different features appearing in the *J-V* curves of solar cells limited by their contacts and allow to fit this behaviour according to only four diode parameters.

Then, studying the relation of those diode parameters among themselves or with temperature can allow to identify the relevant transport mechanisms at each interface [Sze 2006]. E.g. in [Dréon 2021, Fébba 2021] thermionic emission behaviours were identified using activation energy plots, allowing to relate the solar cell limitations to a parasitic Schottky barrier height, meaning that the intended WF effect of the material under study was reduced by additional effects.

However, *Roe's model* derivation is based on many limiting assumptions (e.g. no bulk recombination, no other voltage dependence of the partial current than the simple diode equation). Moreover, no experimental validation of the theory has been carried out so far. The goal of this chapter is therefore to assess the validity of this model by confronting it to solar cells and symmetrical sample results and provide a new model and its understanding to fit better the data (see Figure 3.2). First, in section 3.2, we will introduce the framework of *Roe's model*, the main parameters entering the latter and propose an alternative graphical resolution of the

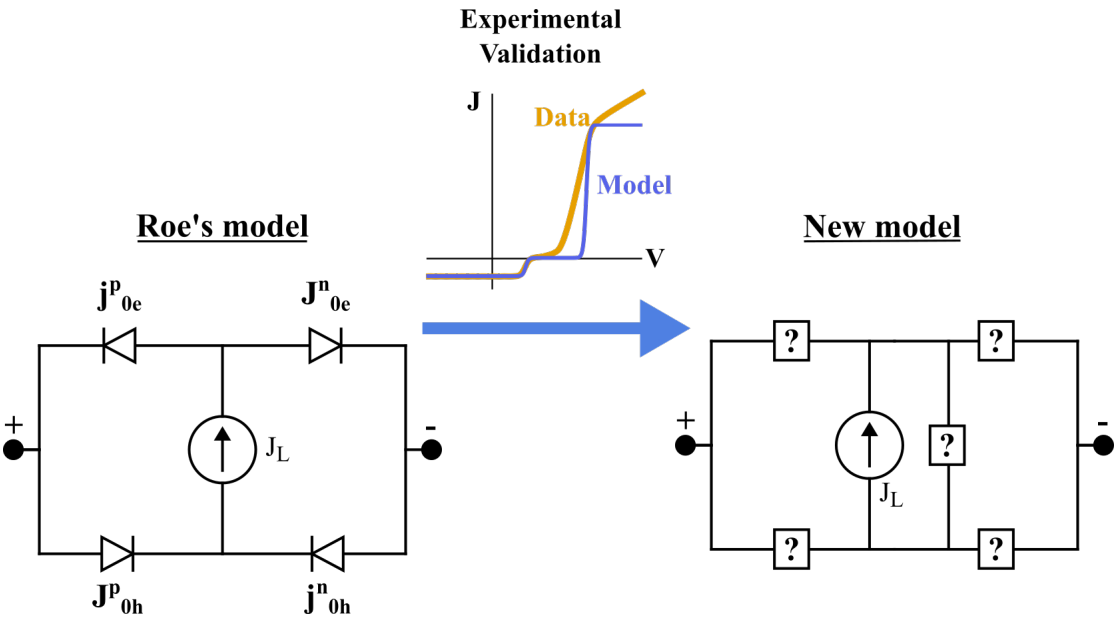

Figure 3.2: Chapter graphical abstract. By confronting the initial model to real experimental data, we construct a more advanced model to describe better contact-limited solar cells.

system to the original paper to obtain the full device *J*-*V* curve. Then in section 3.2, we will review other kinetics than ideal diodes that might be relevant for accurate modelling as well as discuss the inclusion of bulk recombination in the model. In particular, we will discuss how it modifies the interpretation of the different saturations and step heights observed. Finally, in section 3.3, we will study a series of solar cells and symmetrical samples where the contacts have been deliberately engineered to achieve different levels of selectivity, and discuss how the resulting data can be explained in a self-consistent way with the new modelling elements introduced. We will conclude by providing a new circuit model that describes various stages of contact quality and should be helpful to interpret the results for the development of novel materials as CSPC for SHJ solar cells.

3.2 Roe's model and limitations

3.2.1 Roe's equation

In this section, we want to introduce *Roe's model* as an initial step of modelling for contact-limited solar cells. As an alternative to the original publication [Roe 2019], we show an equivalent circuit-diagram corresponding to this model and explain its different features using a graphical resolution.

Figure 3.3(a) shows the example of an energy band-diagram of a solar cell limited by its contacts. At each interface, an energy barrier is present for both electrons and holes, resulting in a drop of both their respective quasi-Fermi level (qFL). Outside the contacts, both qFLs collapse to the same energy due to infinite recombination, modelling the fact that the electrodes (TCO or metal) do not allow for qFL splitting. To model this type of solar cell, *Roe's model* assumes an absorber with flat qFL (constant splitting), where at each interface electrons and holes partial currents flow according to the following diode equations, continuity equations and Kirchhoff's laws:

$$J_1 = j_{0e}^p \left(\exp \frac{qV_1}{k_B T} - 1 \right), \tag{3.1}$$

$$J_2 = -J_{0e}^n \left(\exp \frac{-qV_2}{k_B T} - 1 \right), \tag{3.2}$$

$$J_3 = -J_{0h}^p \left(\exp \frac{-qV_3}{k_B T} - 1 \right), \tag{3.3}$$

$$J_4 = j_{0h}^n \left(\exp \frac{qV_4}{k_B T} - 1 \right), \tag{3.4}$$

$$J = J_1 + J_3 \tag{3.5}$$

$$= J_2 + J_4 \tag{3.6}$$

$$= J_1 + J_2 + J_L, \tag{3.7}$$

$$V = V_1 + V_2 \tag{3.8}$$

$$= V_3 + V_4 \tag{3.9}$$

where V_1 and V_2 represent the electron qFL drop across the left and right contacts, respectively, and similarly for V_3 and V_4 for the hole qFL at the left and right contacts, respectively. J_1 and J_2 are the electron current across the left and right contacts (modulo a change of sign to respect electric circuits conventions), and J_3 and J_4 are the hole current across the left and right contacts. For the saturation current densities ($J_{0e}^n, J_{0h}^p, j_{0e}^p, j_{0h}^n$), we adopted the notation to use a capital letter for the majority carrier at each respective contact (*e.g.* J_{0e}^n for the electron saturation current at the electron contact) and write in lower-case for the minority carrier at each respective contact (*e.g.* j_{0e}^p for the electron saturation current at the hole contact). Finally, J_L is the photogenerated current density.

To our understanding, this system of equations can be represented by the equivalent circuit shown in Figure 3.3(b), where the bottom line represents the mechanisms occurring on the hole current path and is formed of two diodes face-to-face, while the top line represents the electron transport and is formed of two diodes back-to-back (due to the change of sign between electron and electrical current). The infinite recombination at the electrodes is represented by the outer connections of the electron and hole current line in a single line. Therefore, any parasitic electron current flowing through the hole contact results in voltage

losses that are dictated by the diode equations 3.1-3.4, and reciprocally for the hole current flowing through the electron contact.

This system of equations can be solved analytically to yield the solar cell J-V curve as a function of a given set of saturation current densities $\{J^n_{0e}, J^p_{0h}, j^p_{0e}, j^n_{0h}\}$, the photogenerated current J_L, and the temperature T [Roe 2019]:

$$J(V) = -\left(J_L + j^p_{0e} + j^n_{0h}\right) + \frac{J_L + J^n_{0e} + j^p_{0e}}{1 + \frac{J^n_{0e}}{j^p_{0e}} \exp\left(\frac{-qV}{k_B T}\right)} + \frac{J_L + J^p_{0h} + j^n_{0h}}{1 + \frac{J^p_{0h}}{j^n_{0h}} \exp\left(\frac{-qV}{k_B T}\right)}. \tag{3.10}$$

Figure 3.3(e) depicts an example of the model curve (yellow solid line). The equation predicts that every J-V curve will possess two S-shapes with plateaus in between. First, in reverse bias, the current reaches a saturation value of $-\left(J_L + j^p_{0e} + j^n_{0h}\right) \approx -J_L$, since in practice the parasitic current j^p_{0e} and j^n_{0h} are orders of magnitude lower than J_L, J^n_{0e} or J^p_{0h}. Then, it exhibits a first inflexion occurring at the lowest voltage between

$$V_e \equiv \frac{k_B T}{q} \ln\left(J^n_{0e} / j^p_{0e}\right) \tag{3.11}$$

and

$$V_h \equiv \frac{k_B T}{q} \ln\left(J^p_{0h} / j^n_{0h}\right), \tag{3.12}$$

resulting in a saturation, the "first step". Then a second step occurs, with inflexion point at the largest voltage between V_e and V_h this time. In other words, the first saturation occurring on the J-V curve is determined by which charge carrier experiences the lowest asymmetry of saturation current between the two contacts. Since those steps are defined each by the kinetic properties of a single charge carrier, we also refer to them as the *"electrons' step"* and the *"holes' step"*. The saturation height of the first step depends then on which charge carrier saturates first and is approximatively equal to the saturation current of the latter, while the second step is the sum of both majority carrier saturation current densities and J_L, *i.e.*

$$J^{1st}_{step} = \begin{cases} J^n_{0e} - j^n_{0h} \approx J^n_{0e} & \text{if } V_e < V_h \\ J^p_{0h} - j^p_{0e} \approx J^p_{0h} & \text{if } V_e > V_h \end{cases} \tag{3.13}$$

and

$$J^{2nd}_{step} = J_L + J^p_{0h} + J^n_{0e}. \tag{3.14}$$

To give a more intuitive vision to the formations of those S-shapes, we pictured on Figure 3.3(c)-(e) a graphical way to solve the system of equations 3.1-3.9.

First, in (c), we plot the currents of the two characteristic diodes on the electrons path as a function of the voltage at their respective ends, except that the first diode is shifted by $-J_L$. The equivalent circuit of the top line can be obtained by summing the voltages $V_1 + V_2$ for a fixed current J_2, and gives the thick blue line. Then, we can proceed similarly for the hole path

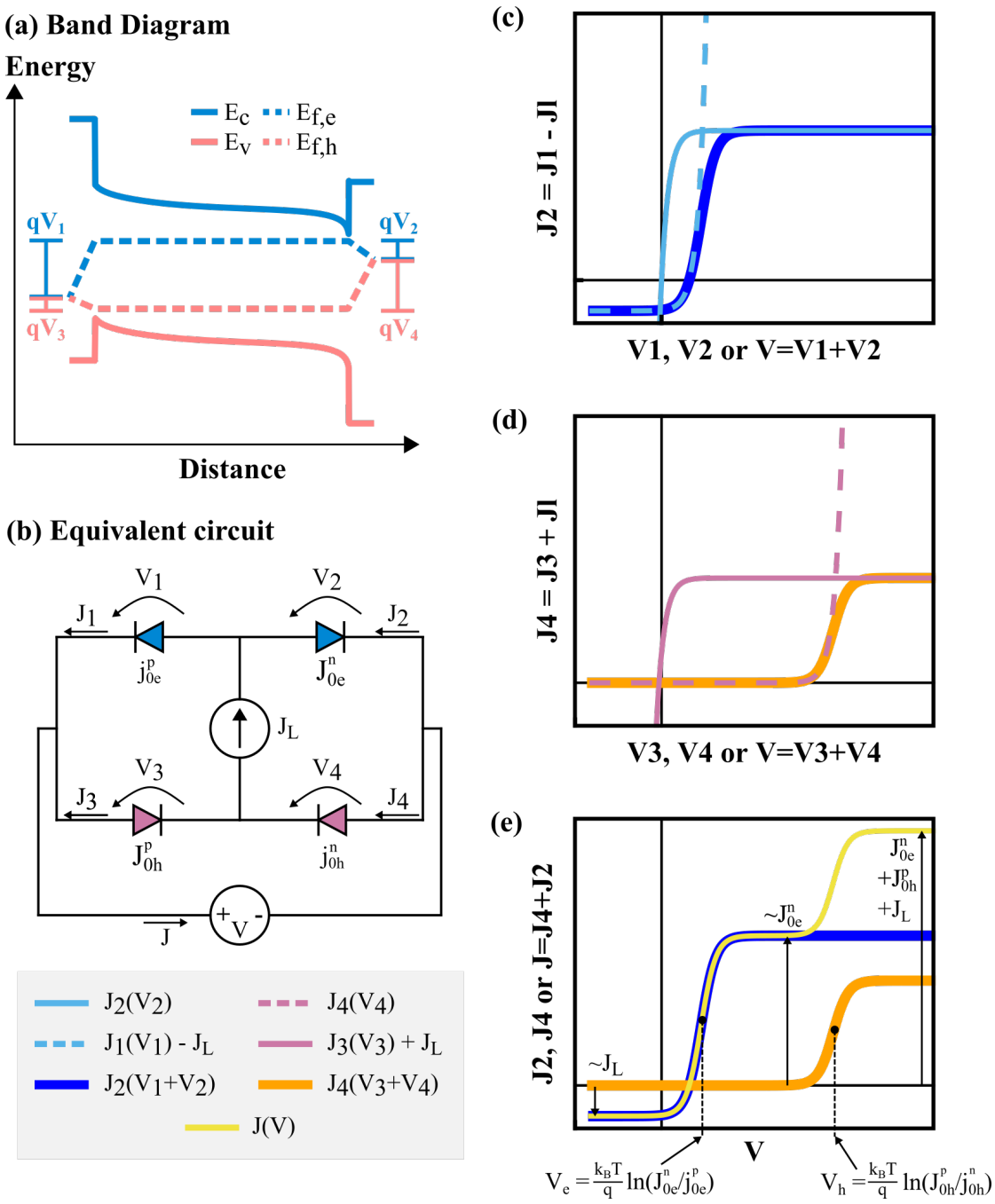

Figure 3.3: (a) Example of band diagram of a solar cell limited by its contacts. (b) Equivalent circuit for a solar cell limited by its contacts. It consists of two diodes back-to-back on the electron path, two diodes face-to-face on the hole path and a current source in between for the photogeneration. The two diodes on the left/right side represent the hole/electron contact, respectively. (c) J-V *characteristics of the diodes on the electron path (light blue solid and dashed curves) as well as* $J_2(V = V_1 + V_2)$ *(thick blue curve). (d)* J-V *characteristics of the diodes on the hole path (light red solid and dashed curves) as well as* $J_4(V = V_3 + V_4)$ *(thick orange curve). (e) Repetition of* $J_2(V)$ *and* $J_4(V)$*, as well as* $J(V) = J_2(V) + J_4(V)$ *(yellow curve) being the* J-V *curve of the whole solar cell described by equation 3.10.*

and obtain the thick orange line in (d). Finally, in (e) the complete J-V curve of the device is obtained by summing the current of the electron and hole path for a fixed voltage, resulting in the yellow curve. We can thus interpret the S-shape positions as the voltage thresholds that open paths for the current flowing from right to left on either the electron or hole line. This is the opposite current direction than when the cell delivers power to the external load and therefore the opening of this current path dissipates power.

As a remark, we note that to apply this graphical procedure, we only used the fact that the different currents and voltages are related by the continuity equations and Kirchoff's law, while the ideal diodes parametrization was just an arbitrary input. In other words, it would be possible to replace those diodes by any other circuit elements, and still be able to construct easily a graphical solution for the resulting J-V curve. We will discuss in the next section other possible choices than the ideal diode parametrization. The graphical resolution would not hold however if extra recombination paths are added, adding extra nodes and loops in the circuit, and we will discuss those in section 3.2.3.

3.2.2 Beyond ideal diodes kinetics and external series resistance

In this section we will discuss how to go beyond the limitation of Roe's model.

The first limitations is rather trivial: the model does not take into account pure series resistance effect of real cells, such as the losses in the metallic grid and the TCO. However, this can be easily solved numerically by computing first $J(V)$ with 3.10 and then expressing the external voltage by adding the resistive losses as $V^{ext}(J) = V + R_s^{ext} J(V)$.

We will discuss now in depth the kinetics of the model. While Roe's model can describe the position and the height of the S-shapes of solar cells J-V curves, the assumption that the transport at each interface follows an ideal diode behaviour is limiting, and in practice several different processes could occur for holes and electrons at each interface. Below we review different relevant transport equations taken from [Sze 2006]. A first transport model compatible with the functional form of equations 3.1-3.4 is the thermionic emission (TE, also named ideal Schottky diode), if the contact is treated as a metal-semiconductor (MS) interface with the respective current equation being

$$J^{TE,MS}(V) = A^* T^2 e^{-\frac{q\phi_B}{k_B T}} \left(e^{\frac{qV}{k_B T}} - 1 \right) \equiv J_0^{TE} \left(e^{\frac{qV}{k_B T}} - 1 \right), \tag{3.15}$$

where ϕ_B is equal to the WF difference of the metal and semiconductor and A^* is the Richardson's constant. Another model respecting the hypothesis is the one of diffusion in anisotype semiconductor-semiconductor heterojunctions where the band offsets are treated as graded junction, giving the electron current

$$J_e^{D,aniso}(V) = \frac{q D_e n_i^2}{L_e N_A} \left(e^{\frac{qV}{k_B T}} - 1 \right) \equiv J_0^{D,aniso} \left(e^{\frac{qV}{k_B T}} - 1 \right) \tag{3.16}$$

where D_e (diffusion coefficient of electron), n_i, L_e (diffusion length of electron) and N_A are all properties of the receiving side. Similar relation holds for holes.

Those two models both respect the functional form of equations 3.1-3.4, and we could expect in several situations that TE modelling could be applied to describe any of the four processes of the model, while the second equation could be used only to model the minority current at a given contact (holes at the electron contact or electrons at the hole contact). The two types of mechanisms can be differentiated by their different temperature behaviours and can be analysed in an activation-energy plot. However, other types of modelling are worth investigating, such as the case of diffusion in a metal-semiconductor contact leading *e.g.* in the case of n-type semiconductor

$$J_e^{D,MS}(V) \approx \frac{q^2 D_e N_C}{k_B T} \sqrt{\frac{2qN_D(\psi_{bi} - V)}{\epsilon_s}} e^{\frac{-q\phi_B}{k_B T}} \left(e^{\frac{qV}{k_B T}} - 1 \right) \equiv J_0^{D,MS}(V) \left(e^{\frac{qV}{k_B T}} - 1 \right), \tag{3.17}$$

where ψ_{bi} is the built-in potential and ϵ_s is the permittivity of the semiconductor, or the case of diffusion in an isotype heterojunction (semiconductors with the same doping type) leading

to

$$J^{D,iso}(V) = \frac{q\psi_{bi}A^*T}{k_B}\left(1-\frac{V}{\psi_{bi}}\right)e^{\frac{-q\psi_{b1}}{k_BT}}e^{\frac{-q\phi_b}{k_BT}}\left(e^{\frac{qV}{k_BT}}-1\right) \equiv J_0^{D,iso}(V)\left(e^{\frac{qV}{k_BT}}-1\right). \tag{3.18}$$

In these cases the prefactor is voltage dependant and the "diode" never saturates in reverse bias. Moreover, n-n isotype junctions have been reported to never saturates in reverse bias, and rather present an exponential dependence on voltage such as the case of Si-Ge junctions [Opdorp 1969, Peibst 2014]. This could be explained intuitively by the fact that in reverse bias, the barrier at the junction becomes thinner allowing for tunnelling (TU). Different TU processes can be described by complex equations [Sze 2006] but the exponential behaviour of the reverse current can be approximated by

$$J^{TU,Rev}(V) = J_0^{TU}\left(e^{\frac{-qV}{nk_BT}}-1\right), \text{ for } V<0 \tag{3.19}$$

with n the ideality factor of the diode. If tunnelling occurs as one of the processes, the corresponding diode of the equivalent circuit of Figure 3.3(b) must be flipped and the corresponding saturations of the J-V curve should instead be replaced by an exponential increase.

Finally, several of those processes are illustrated on Figure 1.14.

3.2.3 Effect of bulk recombination

One important assumption to derive Roe's equation is that bulk recombinations are negligible with respect to contact recombination. Here, we explore how the presence of bulk recombination can affect the qualitative shape of the J-V curve in comparison to the simpler case described by Roe's equation. We include as a particular case the description of symmetrical samples.

To this aim, we modified the simple four-diode circuit of Figure 3.3 to add an extra diode in parallel with the current source to model bulk recombinations. Here, we model this additional diode simply by $J_{rec}(V_{rec}) = J_{0,rec}\left(\exp\frac{qV_{rec}}{nk_BT}-1\right)$, with an ideality factor of $n=1$, but other values could be used without affecting the following qualitative discussion. Figure 3.4(a) shows the modified circuit diagram. The circuit's equations become then

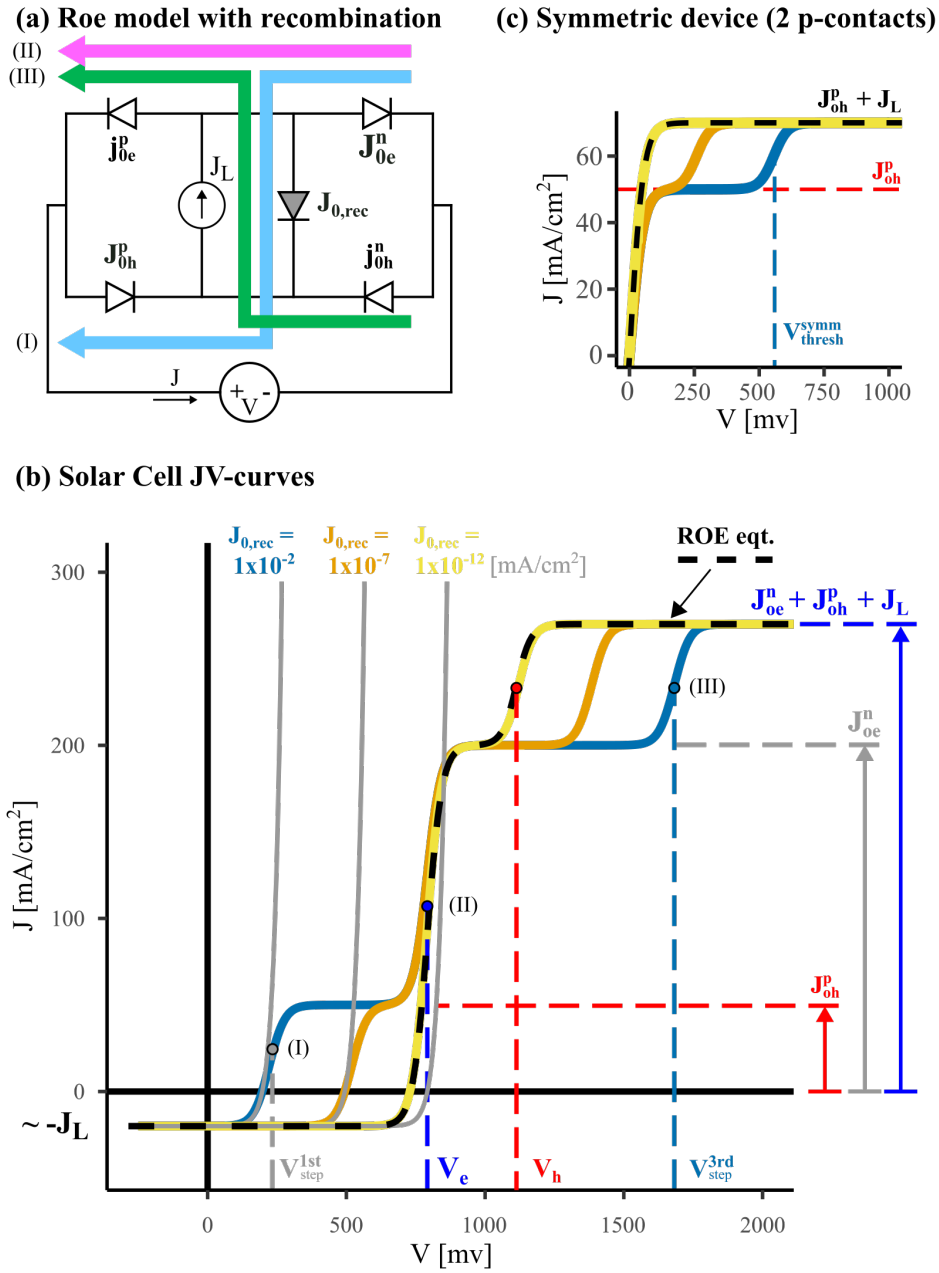

Figure 3.4: Modification of Roe's model to include bulk recombination. (a) Equivalent electrical circuit and current paths (I, II, III) opening at different voltage thresholds. (b) JV-curves of the simulated circuits, with contact diode parameters $J^p_{0h} = 50$, $j^p_{0e} = 10^{-11}$, $J^n_{0e} = 200$, $j^n_{0h} = 10^{-17}$ mA/cm^2 *as well as* $J_L = 20$ mA/cm^2 *for every case and with three different* $J_{0,rec}$ *values for the recombination diode. The dashed black line is Roe's equation,* i.e. *the model with no recombination and* V_n *and* V_p *are the corresponding positions for the electron- and hole- steps. (c) Corresponding* J-V *curves of a symmetrical device featuring twice the same p-contact (positive voltage only).* V^{1st}_{step}, V^{2nd}_{step} *and* V^{thresh}_{symm} *are defined in the main text.*

$$J_1 = j_{0e}^p\left(\exp\frac{qV_1}{k_BT}-1\right), \quad (3.20)$$

$$J_2 = -J_{0e}^n\left(\exp\frac{-qV_2}{k_BT}-1\right), \quad (3.21)$$

$$J_3 = -J_{0h}^p\left(\exp\frac{-qV_3}{k_BT}-1\right), \quad (3.22)$$

$$J_4 = j_{0h}^n\left(\exp\frac{qV_4}{k_BT}-1\right), \quad (3.23)$$

$$J_{rec} = J_{0,rec}\left(\exp\frac{qV_{rec}}{k_BT}-1\right) \quad (3.24)$$

$$J = J_1 + J_3 \quad (3.25)$$

$$= J_2 + J_4 \quad (3.26)$$

$$= J_2 + J_3 + J_L - J_{rec}, \quad (3.27)$$

$$V = V_1 + V_2 \quad (3.28)$$

$$= V_3 + V_4 \quad (3.29)$$

$$= V_1 + V_4 - V_{rec}, \quad (3.30)$$

This system cannot be solved analytically due to the coupling through exponential functions of the different variables and needs to be numerically solved.

Figure 3.4(b) presents the resulting J-V curves for a solar cell where the impact of bulk recombination is gradually increased by increasing $J_{0,rec}$ and becomes non-negligible with respect to contact recombination. When $J_{0,rec}$ is very small, the simulation matches with Roe's equations as expected and the S-shape positions and heights can be analyzed accordingly to our description of section 3.2.1.

Conversely, when bulk recombination is not negligible anymore compared to selective losses, the positions and the heights of the steps behave differently. Hopefully, it is still possible to easily describe them in terms of the parameters of the model. To understand the different voltage thresholds, one can observe that the extra recombination diode allows for new current paths in the equivalent circuit on Figure 3.4(a). As with the previous model, current can flow either through the top line (the electron line) as long as $V > V_e$ and along the bottom line (the hole line) as long as $V > V_h$. The recombination diode allows extra paths along the blue and green lines when those two previous paths are blocked. Which lines open first and allow current to flow depends on the parameters of the diodes. Hopefully, even if the system of equations 3.20-3.30 is not solvable, it is possible to characterize analytically the different voltage thresholds shown in Figure 3.4(b). *The detailed derivations can be found in Appendix A.2.* In the following, we describe those results and their implications on the interpretation of the different S-shape positions and heights.

The first step occurs when the current can flow through the blue line. The corresponding height and position of the S-shape depend on which of the reverse diodes will saturates first and is given by

$$J_{step}^{1st} \approx \min\left(J_{0h}^p, J_{0e}^n\right) \quad \text{and} \quad V_{step}^{1st} \approx \frac{k_BT}{q}\ln\left(\frac{J_{0h}^pJ_{0e}^n}{J_{0,rec}\left(J_M+\frac{1}{2}J_L-\frac{1}{2}J_m\right)}\right) \approx \frac{k_BT}{q}\ln\left(\frac{\min\left(J_{0h}^p, J_{0e}^n\right)}{J_{0,rec}}\right) \quad (3.31)$$

where at the denominator we use the notation $J_M = \max\left(J_{0h}^p, J_{0e}^n\right)$ and $J_m = \min\left(J_{0h}^p, J_{0e}^n\right)$, and the second approximation is valid if $J_M \gg J_m$ and J_L. Intuitively, within this second approximation, the bulk recombination diode plays a similar role as the parasitic diodes j_{0e}^p

on the electron line or j_{0h}^n on the hole line, and it is either back-to-back with the diode J_{0e}^n or face-to-face with the diode J_{0e}^n.

The second step occurs when additional current can flow through the pink path in our example of Figure 3.4 where we picked $J_{0h}^p < J_{0e}^n$, and therefore allow the current to saturate at a higher value than previously, namely at J_{0e}^n. Of course the reasoning can be adapted to the case $J_{0h}^p > J_{0e}^n$ where the additional current would flow through the bottom line. Therefore, the position of the second step is dependent on which majority carrier saturation current is the largest and the corresponding height and position are given by (Appendix A.2)

$$J_{step}^{2nd} \approx \max\left(J_{0h}^p, J_{0e}^n\right) \quad \text{and} \quad V_{step}^{2nd} \approx \begin{cases} \frac{k_B T}{q} \ln\left(\frac{J_{0h}^p}{j_{0h}^n}\right) & \text{if } J_{0h}^p > J_{0e}^n \\ \frac{k_B T}{q} \ln\left(\frac{J_{0e}^n}{j_{0e}^p}\right) & \text{if } J_{0h}^p < J_{0e}^n \end{cases} \tag{3.32}$$

Intuitively, as the voltage becomes large enough to allow the current to flow in parallel through the electron or hole line as well as the previous path, it replaces the limitation of the smallest saturation current between J_{0h}^p and J_{0e}^n by the largest. Importantly, this influences how the different steps would be identified on an experimental J-V curve compared to Roe's simpler model, where it was depending on whether the ratio J_{0h}^p / j_{0h}^n is $<$ or $>$ J_{0e}^n / j_{0e}^p (equations 3.11 and 3.12).

Finally, this new model predicts a third saturation once current can flow through the green line, allowing the current to flow through all the branches of the system and adding in parallel J_{0h}^p, J_{0e}^nandJ_L. For this one, we find (Appendix A.2)

$$J_{step}^{3rd} = J_{0h}^p + J_{0e}^n + J_L \quad \text{and} \quad V_{step}^{3rd} \approx \frac{k_B T}{q} \ln\left(\frac{J_{0,rec}}{j_{0h}^n j_{0e}^p} \frac{1}{2}(J_L - J_{0h}^p + 2J_{0e}^n)\right) \tag{3.33}$$

For symmetrical samples (Figure 3.2.3 (c)), the impact of recombination also modifies the expected J-V curves. Indeed, the latter are a special case of solar cell with zero selectivity and according to Roe's equation (eqt. 3.10), their J-V curves should feature a single S-shape centered at 0 V. However, if the contacts are very resistive for both carrier types and limit the rates of charge extraction, which is a situation we expect to encounter when describing contact-limited solar cells, it is intuitive that bulk recombination should be included in the model to describe the suppression of photogenerated charges. Indeed, in this situation it would require excessively large voltage to dissipate J_L in the diodes of the contact, and therefore it flows first through the bulk recombination. In the case of two symmetric p-contacts, the step positions and heights are given by (Appendix A.2)

$$J_{symm}^{1st} = J_{0h}^p \quad \text{and} \quad V_{symm}^{1st} = 0\,\text{V} \tag{3.34}$$

and

$$J_{symm}^{2nd} = J_{0h}^p + J_L \quad \text{and} \quad V_{thresh}^{symm} = \frac{k_B T}{q} \ln\left(\frac{J_{0,rec}}{j_{0e}^p} \frac{2J_{0h}^p + \frac{1}{2}J_L}{J_{0h}^p}\right) \tag{3.35}$$

Analogous relations can be written for symmetric n-contacts.

Finally let us comment on the implementations of additional features to the model, such as surface recombination. Unfortunately, the latter would require extra assumptions to be described accurately. Indeed, as discussed in [Onno 2019], if the effect of surface recombination becomes strong enough to make both electrons and holes qFL collapse at the c-Si surface, one should consider the modulation of resistivity of the absorber for both charge carriers close to the surface as well as the recombination mechanisms.

Moreover, the contact of solar cells is formed of a stack materials of the form c-Si(n) / dielectric / doped-layer / TCO and therefore more complex current equations might be required. E.g. the c-Si(n) / dielectric / doped-layer part could be modelled as a semiconductor-insulator-metal interface, while the doped-layer / TCO interface could be modelled as a semiconductor-metal junction. The kinetics of transport of each element of the equivalent circuit could be thus implemented by several elements in series and in parallel.

Finally, adding the fact that the carriers can recombine not only at the TCO interface, but also inside the contact or at the c-Si surface, we obtain a complex band diagram and equivalent circuit introduced on Figure 1.14(a)-(b).

3.3 Experimental Comparison

In the last theoretical sections, we discussed the simple model of Roe and how it could be modified to take into account different transport mechanisms or types of recombination. We ended up mentioning the circuit model of Figure 1.14(c), which on the one hand has the advantage to show all the possible physical mechanisms in a single view, but on the other hand has the disadvantage of being overly complex and imply a risk of over fitting the measured *J*-*V* curves.

In this section, we will explore real solar cells engineered with contacts of diverse quality to mimic situations that can occur when developing contacts based on new materials. We will discuss which new features should be implemented in Roe's model to represent this series of samples, while trying to keep the complexity to minimum.

3.3.1 Experimental Methods

For this, we engineered well known a-Si:H(*n*) and a-Si:H(*p*) layers with different dopant flows during the PECVD deposition. We complete this series by adding a layer with no dopant at all, and n-type and p-type nc-Si:H layers as reference for quasi-perfect contacts. The development of the latter will be deeply explained in the next chapters. Table 3.1 describes the different layer deposition conditions, as well as their thickness characterized by ellipsometry and their dark lateral conductivity.

	for n-contact					for p-contact		
Label	**i(0)**	**n(3)**	**n(10)**	**n(29)**	**n(nc)**	**p(3.2)**	**p(87)**	**p(nc)**
PH_3 or TMB [sccm]	0	3	10	29	50	3.2	87	4
SiH_4 [sccm]	95	95	95	95	15	48	48	15
H_2 [sccm]	400	397	390	371	2024.5	82.1	0	2005
t_{dep} [s]	80	80	80	80	300	35	23	210
Thickness [nm]	30	30	30	30	30	12	12	25
σ_{RT}^{dark} [S/cm]	$1.5e^{-12}$	$3.0e^{-7}$	$4.9e^{-5}$	$1.6e^{-4}$	$2.8e1$	$8.2e^{-8}$	$2.0e^{-6}$	$1.1e^{0}$

Table 3.1: Label, deposition parameters and characterization of the layers of the present study.

We then processed solar cells and symmetrical samples based on n-type c-Si. This absorber was first coated on both sides by thin a-Si:H(i) layers to reduce the surface defect density and provide chemical passivation. The layers of Table 3.1 were then applied on each side to form n-iNi-p, n-iNi-n and p-iNi-p precursors. Then, TCOs were sputtered on both sides (highly doped to reduce lateral resistive losses) through a shadow mask, defining a $1 \times 1\,\text{cm}^2$ area. On the front side, a Ag grid was sputtered while it was deposited on the full area layer on the rear-side. Finally, the samples were annealed at 210 °C for 30 minutes to cure sputtering-damage and mimic the effect of screen-printing annealing. Finally, implied open circuit voltages were measured after PECVD deposition, and PL images were acquired on the final devices. They both showed good passivation properties, with iV_{oc} above 735 mV for every samples and comparable PL signal in the area covered or uncovered with TCO, showing that high passivation was maintained up to the final stage of fabrication. In the following parts, we will label the final device by their precursor structure, *e.g.* i(0)-iNi-p(87), omitting the presence of the TCO and Ag layers that are unchanged among the samples.

3.3.2 Device nearly compatible with Roe's model

In this first section, we start by considering the samples matching the closest Roe's modelling: the solar cell **i(0)-iNi-p(87)** and the corresponding symmetrical samples **i(0)-iNi-i(0)** and **p(87)-iNi-p(87)**. Their J-V curves taken at different illuminations are presented on Figure 3.5(a)-(e). In (c), due to the use of an undoped n-layer the solar cell shows indeed a very low V_{oc} of about 220 mV, much lower than the previously measured iV_{oc} which testifies that bulk recombination is negligible as compared to selectivity losses. In the following, we try first to fit the data using Roe's model with an additional series resistance as shown by the equivalent circuit in (d). The resulting fitting parameters are found in Tables 3.2 and 3.3.

First, in (a), we observe that the saturation current of the i(0)-iNi-i(0) symmetrical sample depends on illumination. This is expected as the step height is given by $J_L + J_{0e}^{i(0)}$. J_L can be evaluated independently from a similar solar cell by taking the short-circuit current of the latter. It results that the step heights in (a) are comparable to J_L and that J_{0e} is much smaller in comparison, and unfortunately hard to evaluate precisely from the saturation observed.

Turning to (b), we observe that this time the saturation of p(87)-iNi-p(87) is much larger than

J_L and depends on the illumination level. In other words, $J_{0h}^{p}(87)$ is a function of J_L. This is expected since, in the dark, two p-contacts deposited on a n-type c-Si wafer should block efficiently any current to flow, while under illumination, the creation of free holes in the wafer makes it hole-conductive (with a respective hole qFL), making possible a large current of holes to flow at the junction [Senaud 2021a]. We will explore more in depth how current can flow in those p-iNi-p structures in chapter 5. For the moment, the presence of both electrons and holes qFL in the absorber makes the transport process of holes at this interface more similar to a majority carrier process such as TE in MS or isotype heterojunction, as if the p-layers were deposited on a p-type wafer instead. In [Roe 2019], the authors assumed an intrinsic absorber to compute relevant Schottky barrier heights using a single Fermi-level. On the contrary, we propose that any doping of the absorber can be used and the relevant J_0's values must be calculated using the qFL of holes and electrons resulting of illuminations, which seems much more reasonable regarding our understanding of solar cell physics. Note that this treatment is still valid with the hypothesis to use equation 3.10 as long as the J_0's do not depend on the applied voltage. Treating the observed saturations as an ideal Schottky barrier, we could extract an energy barrier $\phi_b \sim 0.2\,\text{eV}$ from the $\ln\left(J_{0h}^{p(87)}/T^2\right)$ vs $1/T$ plot (see Appendix A.2.2), which could match the valence band offset between a-Si:H(p) and c-Si(n) [Jarolimek 2015]. However, we note that the step does not saturate perfectly and keeps a slight linear increase at large bias, which could be the signature of an isotype heterojunction transport (eq. 3.18).

Turning now to the series resistance values, high series resistances are obtained for both samples. These are larger than the residual resistance of the lateral transport through the TCO and metallic grid that we evaluate to be in the range 0.8–1.2 $\Omega\,\text{cm}^2$ for the $1 \times 1\,\text{cm}^2$ solar cell design used here. Moreover, these series resistance increase at lower illumination which is unexpected for the TCO or the metallic grid. In the next paragraphs, we try to find an explanation to this behaviour and propose a modification of the model to account for it.

Looking at the solar cell in (c), we observe that it features two saturation plateaus that resemble the type of curves that Roe's model could predict: in particular, the heights of the plateaus are consistent with the observation in (a) and (b) for $J_{0h}^{p(87)}$ and $J_{0e}^{i(0)}$. By fitting the position of the second step, it is possible to extract the ratio $J_{0h}^{p(87)}/j_{0h}^{i(0)}$ and deduce $j_{0h}^{i(0)}$, while by fitting the first step we could extract only the ratio $J_{0e}^{i(0)}/j_{0e}^{p(87)}$, since we only know that $J_{0e}^{i(0)} \ll 1$. However, we observe it is not possible to fit accurately the whole J-V curve by using a single value of R_s^{ext}. Indeed, $R_s^{ext} = 3.5\,\Omega\,\text{cm}^2$ fits accurately the electrons (first) step, while $R_s^{ext} = 1.6\,\Omega\,\text{cm}^2$ is more adapted for the holes step. Removing the contribution of the TCO and finger grid, and dividing by 2 for the symmetrical samples, we find a resistance value of roughly the same order of magnitude at 1 Sun from the solar cell and the symmetrical samples that can be attributed to the hole- and electron-contact, respectively (*i.e.* $\rho_{c,n}^{SolarCell} = 2.7$–$2.3\,\Omega\,\text{cm}^2$ compared to $\rho_{c,n}^{Symm} = 3.4$–$2.6\,\Omega\,\text{cm}^2$ and $\rho_{c,p}^{SolarCell} = 0.7$–$1.1\,\Omega\,\text{cm}^2$ compared to $\rho_{c,p}^{Symm} = 0.2$–$0.4\,\Omega\,\text{cm}^2$). This motivates a modification of Roe's model where separate resistance elements are added in series with the respective hole and electron diodes for the majority carriers at each contact. In this way, the effect of those additional voltage drops will be present on the J-V curve only

when current is flowing in these branches, corresponding to the range around the respective electrons and holes steps on the *J-V* curves. This slight modification yields a much better fit of the *J-V* curve in (c). Physically, this could be representing the effect of both c-Si/doped-layer and doped-layer/TCO junctions, which could also be modelled as two diodes in series, where the second one looks ohmic as long as it has a much higher saturation current than the other one. If this second element had a more complicated current-voltage relation, one elegant way to deconvolute it from the solar cell *J-V* curve is to compare it with the so-called "spectator architecture" where the test layer is deposited on top of a reference layer that provides good contact properties [Fébba 2021].

i(0)-iNi-i(0)	$Illum$ [%]	$J_L\left[\frac{mA}{cm^{-2}}\right]$	$J_{0e}^{i(0)}\left[\frac{mA}{cm^{-2}}\right]$	$j_{0h}^{i(0)}\left[\frac{mA}{cm^{-2}}\right]$	$R_s\left[\Omega\,\mathrm{cm}^2\right]$
	100	32	1×10^{-1}	1×10^{-4}	8
	50	16	1×10^{-1}	1×10^{-4}	10
	10	3	1×10^{-1}	1×10^{-4}	12
	5	1.5	1×10^{-1}	1×10^{-4}	12

p(87)-iNi-p(87)	$Illum$ [%]	$J_L\left[\frac{mA}{cm^{-2}}\right]$	$J_{0h}^{p(87)}\left[\frac{mA}{cm^{-2}}\right]$	$j_{0e}^{p(87)}\left[\frac{mA}{cm^{-2}}\right]$	$R_s\left[\Omega\,\mathrm{cm}^2\right]$
	100	30	220	1×10^{-4}	1.6
	50	15	175	1×10^{-4}	1.7
	10	3	50	1×10^{-4}	2.5
	5	1.5	18	1×10^{-4}	2.5

Table 3.2: Parameters used to fit the J-V *curves on Figure 3.5(a) and (b).*

$Illum$ [%]	$J_L\left[\frac{mA}{cm^{-2}}\right]$	$J_{0e}^{i(0)}\left[\frac{mA}{cm^{-2}}\right]$	$j_{0h}^{i(0)}\left[\frac{mA}{cm^{-2}}\right]$	$J_{0h}^{p(87)}\left[\frac{mA}{cm^{-2}}\right]$	$j_{0e}^{p(87)}\left[\frac{mA}{cm^{-2}}\right]$
100	30	1×10^{-1}	1×10^{-4}	230	2×10^{-4}

$R_s\left[\Omega\,\mathrm{cm}^2\right]$	$\rho_{c,h}\left[\Omega\,\mathrm{cm}^2\right]$	$\rho_{c,e}\left[\Omega\,\mathrm{cm}^2\right]$
1.2	0.6	2.3

Table 3.3: Parameters used to fit the J-V *curve of the i(0)-iNi-p(87) solar cell on Figure 3.5(c).*

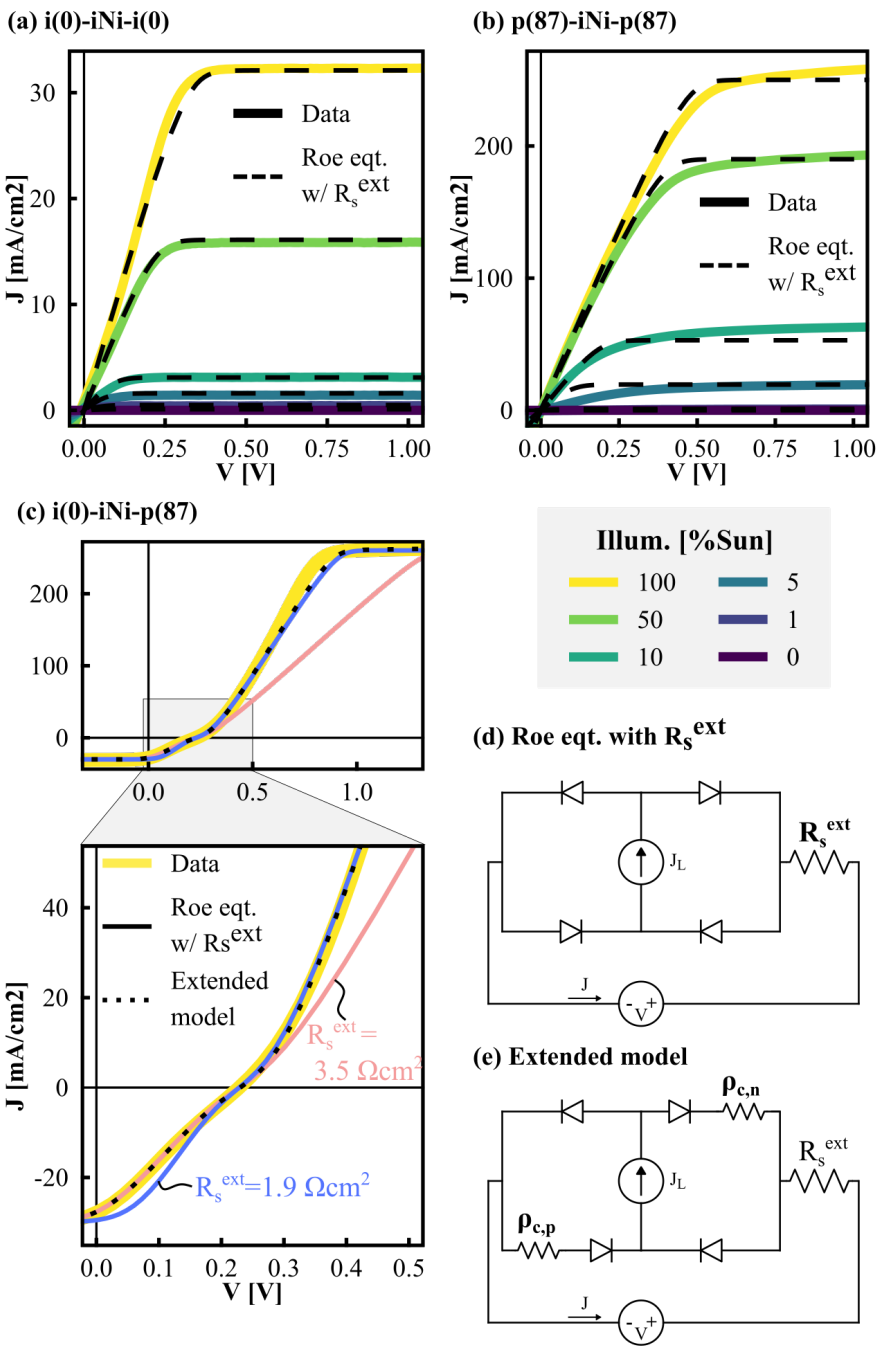

Figure 3.5: J-V *curves at different illuminations of the samples matching the closest Roe's model. (a) and (b): symmetrical samples featuring the i(0) and p(87) layer. (c) Corresponding i(0)-iNi-p(87) solar cell at 1 Sun. (d) Equivalent circuit model used for the two types of fitting presented. The parameters used for the different fitting lines are presented in Tables 3.2-3.3*

3.3.3 Samples of different contact qualities

We will now discuss the series of solar cells and symmetrical samples featuring all layers from Table 3.1. The resulting solar cell and symmetrical sample *J-V* curves are presented on Figure 3.6 and 3.7, respectively. To vary systematically the solar cell selectivity quality, four types of n-layers (i(0), n(3), n(10), n(29)) are combined with two types of p-layers (p(3.2) and p(87)), alternating between solid and dashed lines as we change the p-layer doping.

On top of that, we added as a reference the *J-V* curve of a solar cell with two quasi-ideal contacts **n(nc)-iNi-p(nc)** (dotted line), featuring two nanocrystalline silicon layers that are the best contacts to silicon developed throughout this thesis (see chapters 4 and 6). According to the symmetrical samples, those contacts present ohmic properties on the whole range of measured current. Therefore, this is quite intuitive that this device, since it is not limited by its contacts, cannot be described by Roe's modelling (the diodes of the model have a saturation current so high that they lead to ohmic contact) and it is limited by bulk recombination as well as external resistive losses present in all the other devices. This solar cell could be better described as a first approximation by a single diode model with series resistance, or even better by considering the effect of lateral transport coupling in the TCO and the wafer as we will discuss in chapter 5. For the moment, we can use this curve to situate the bulk recombination diode and compare it to the other solar cells presented to understand when recombination needs to be included to identify correctly the saturation steps as presented in Figure 3.4.

We will now discuss for each curve whether it can be described already by Roe's model or if new elements need to be introduced :

First, the solar cell **i(0)-iNi-p(87)** (solid yellow curve) is the same as the one presented on Figure 3.5, and we already discussed that it can be described by Roe's equation with two minimal modifications, *i.e.* adding an external resistance (to model the lateral losses in the TCO and in the Ag grid) and two different contact resistances at the n-contact and p-contact. Therefore, the first step height can be interpreted as $J_{0e}^{i(0)}$ and the second step height as $J_{0h}^{p(87)}$. While the first step is much smaller than J_L, we have a higher and measurable saturation current density for the p-contact of $J_{0h}^{p(87)} \approx 220\,\mathrm{mA\,cm^{-2}}$, which varies with illumination due to different hole densities in the wafer.

When reducing the doping of the p-layer with the structure **i(0)-iNi-p(3.2)** (dashed yellow curve), we can see that the second step height ($J_{0h}^{p(3.2)}$) falls down, accordingly to its identification as the hole saturation steps in Roe's modelling view. The first step, corresponding to the electrons saturation respectively, is also moved slightly to lower voltages. There is still no contradiction with the model so far, since by reducing the doping of the p-layer from *p(87)* to *p(3.2)*, we also have $j_{0e}^{p(3.2)} > j_{0e}^{p(87)}$ (*e.g.* due to a decrease of the induce band bending [Bivour 2014]) while $J_{0e}^{i(0)}$ is unchanged and therefore the electron step V_e occurs earlier.

Starting to increase the PH_3 flow in the *n*-type layer, the electron selectivity of the device increases impressively and much higher V_{oc} are obtained with the **n(3)-iNi-p(3.2)** and **n(3)-**

iNi-p(87) solar cell (orange curves). Accordingly, in Roe's modelling vision, the electron step shifts to higher voltage as $J_{0e}^{n(3)} > J_{0e}^{i(0)}$. However, $J_{0e}^{n(3)}$ remains small compared to J_L as the first step saturation height is close to zero. When the p-contact is changed, the second step height is reduced by about 200 mA cm^{-2} and the electron step moves to lower voltages, similarly to what was described for the two yellow curves. However, the second step height is higher by about 50 mA cm^{-2} in comparison to the yellow curves, despite the fact they feature the same p-contact stack. The same difference can be observed on the symmetrical samples. Fortunately, if we take into account the moderate slope of the orange curve, both yield similar saturation current densities for $J_{0h}^{p(87)}$ and $J_{0h}^{p(3.2)}$ extrapolated at 0 V. The difference of slope induced therefore by the change of n-layer can be interpreted as an isotype behaviour of this contact, such as described by equation 3.18.

Turning to the **n(29)-iNi-p(87)** device (solid blue curve), we observe that in the power quadrant, it is almost superposed with the reference, showing that it is limited by bulk recombination. Beyond V_{oc} it gradually moves away from the reference. In this second portion of the curve, a small kink is visible after V_{oc} (which can become clearer by plotting the derivative but not shown for simplicity). When bulk recombinations are limiting, the first saturation height is attributed to the smallest majority saturation current, which is there the hole current $J_{0h}^{p(87)}$. Then to explain that the exponential growth starts again only a few mV later, we can argue that the electron step position V_e should be positioned close and since no second saturation is observed, we should have $J_{0e}^{n(29)} \gg 1000$ mA cm^{-2}. Next, using the less good p-layer in **n(29)-iNi-p(3.2)** (dashed blue curve), the kink after V_{oc} goes close to zero accordingly, as expected due to the smaller value of $J_{0h}^{p(3.2)}$ compared to $J_{0h}^{p(87)}$. Therefore, completing Roe's modelling approach by adding the bulk recombination allows to describe saturation occurring after V_{oc} which can be useful to discuss for example results observed in the literature for new contact development such as with MoO_x cell [Dréon 2020, Dréon 2021]. However, we can give another interpretation to this last portion of the curve with exponential growth, which could come from tunnelling through the n-contact. This second interpretation makes sense with what is described in the next paragraph.

The last set of samples to investigate is that featuring the n(10) layers (mauve curves). Those samples are more problematic to describe in terms of the elements we used so far (*i.e.* without tunnelling). Indeed when going from n(29)-iNi-p(87) to **n(10)-iNi-p(87)**, the fact that the height of the first kink after V_{oc} decreases could be identified to a large decrease of the electron saturation current density to a value $J_{0e}^{n(10)}$ becoming close to 1, much smaller than $J_{0h}^{p(87)}$. Therefore, it should occur first after V_{oc} according to our reasoning of section 3.2.3. However, this is in contradiction with the fact that the current then increases exponentially again without saturating a second time due to the hole contact ($J_{0h}^{p(87)} \approx 220$ mA cm^{-2}). If we look now at the corresponding symmetrical **n(8)-iNi-n(8)** sample, it is also problematic to describe, even when adding bulk recombination. Indeed, it quickly saturates at a value of about 10 mA cm^{-2}, which could be identified to $J_{0e}^{n(3)}$ in Roe's model with recombination. However, the current starts to grow exponentially right after and rise at values much higher than J_L, without saturating.

Since those samples do not match our modelling, we need to modify the theory further. Fortunately, we can find consistency of this exponential behaviour when using the n(8) layer both in the symmetrical sample and the solar cells. The single ideal diode yielding the saturation of electron current should be replaced by another element creating an exponential growth in reverse bias. We propose to include the possibility of tunnelling (TU) at large enough bias. Such approaches have already been proposed in the literature to describe isotype junctions with different level of complexity, for example in the case of Si-Ge junction [Opdorp 1969, Peibst 2014]. To modify our circuit model, we need to add in parallel of the J_{0e}^{n} diode a second diode in the opposite direction that will describe the exponential growth due to tunnelling in far reverse bias of the contact, while the first diode describes the first saturation due *e.g.* to TE in the n-n contact at moderate reverse bias. In this way, after V_{oc} the solar cell saturates because of the moderate value of $J_{0e}^{n} \approx 10\,\mathrm{mA\,cm^{-2}}$ and then the current starts to grow exponentially again as the tunnelling diodes threshold voltage is passed.

Finally, let us mention that we also observed a strong current increase instead of a saturation regime using the same p-layers as here, but deposited on *p*-type wafer (see Appendix A.2.3). While not fully understood, this change of behaviour is also correlated with the higher doping of the p-type wafers used here ($N_A \approx 8 \times 10^{15}\,\mathrm{cm^{-3}}$), compared to one used in the n-type wafers ($N_D \approx 2 \times 10^{15}\,\mathrm{cm^{-3}}$). This higher wafer doping might help to enhance the transport via tunnelling in those isotype junctions, which explains the behaviour of the *J*-*V* curve at large bias.

While those considerations are important to model accurately the *J*-*V* curve behaviour on the whole range of voltages, in the power quadrant before V_{oc} tunnelling current is still low and does not significantly influence the solar cells efficiency. However, discussing its impact allows to identify the correct mechanisms corresponding to the various kinks and S-shapes in the whole *J*-*V* curve. The latter can then be fitted to the correct model and used to extract parameters of the underlying band-diagram and identify sources of bottlenecks in the development of new contacts. It is therefore, important to take tunnelling into account to have the correct interpretation of the shape of a whole *J*-*V* curve.

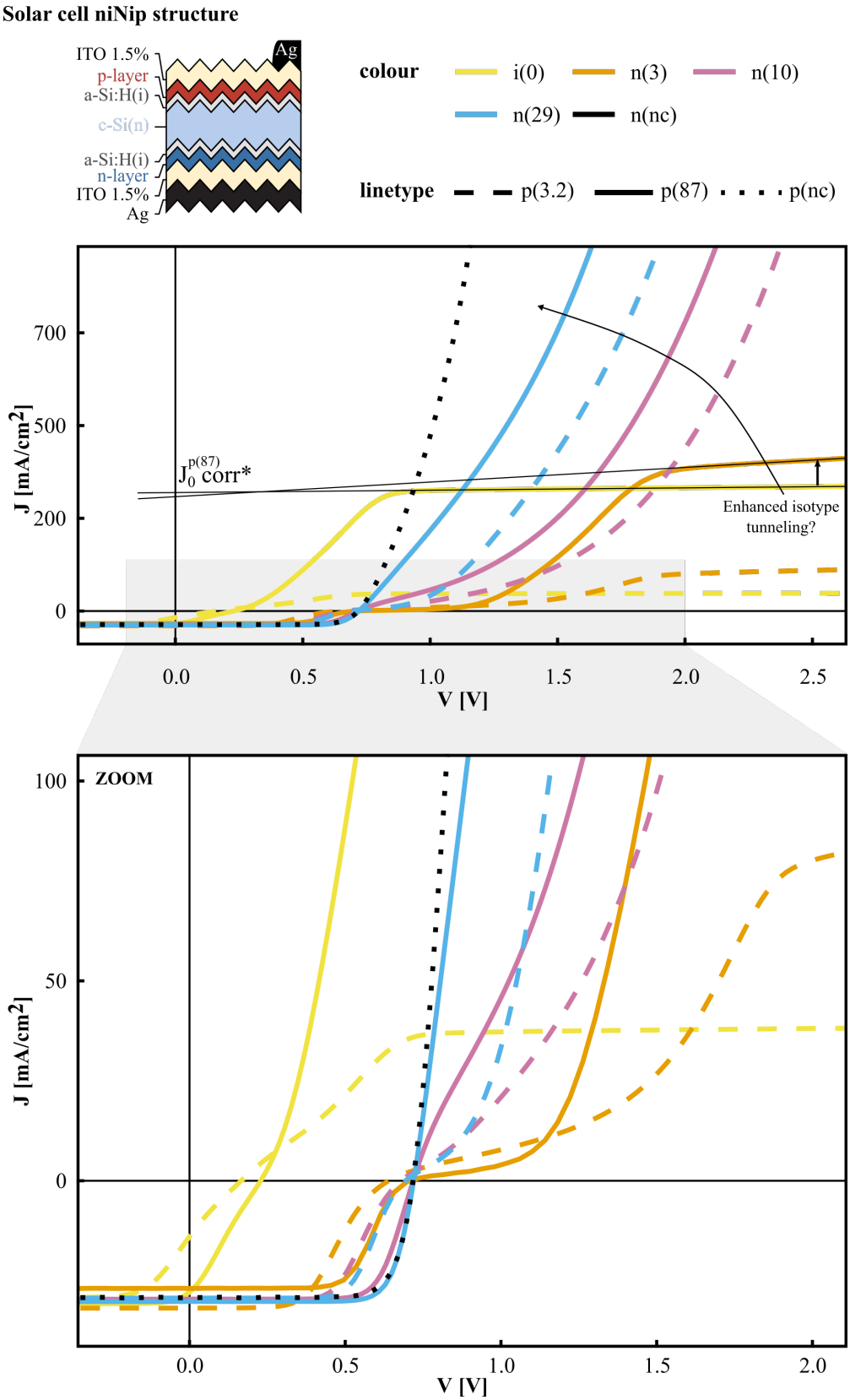

Figure 3.6: J-V *curves under 1 Sun of solar cells featuring n- and p-contact with various qualities.*

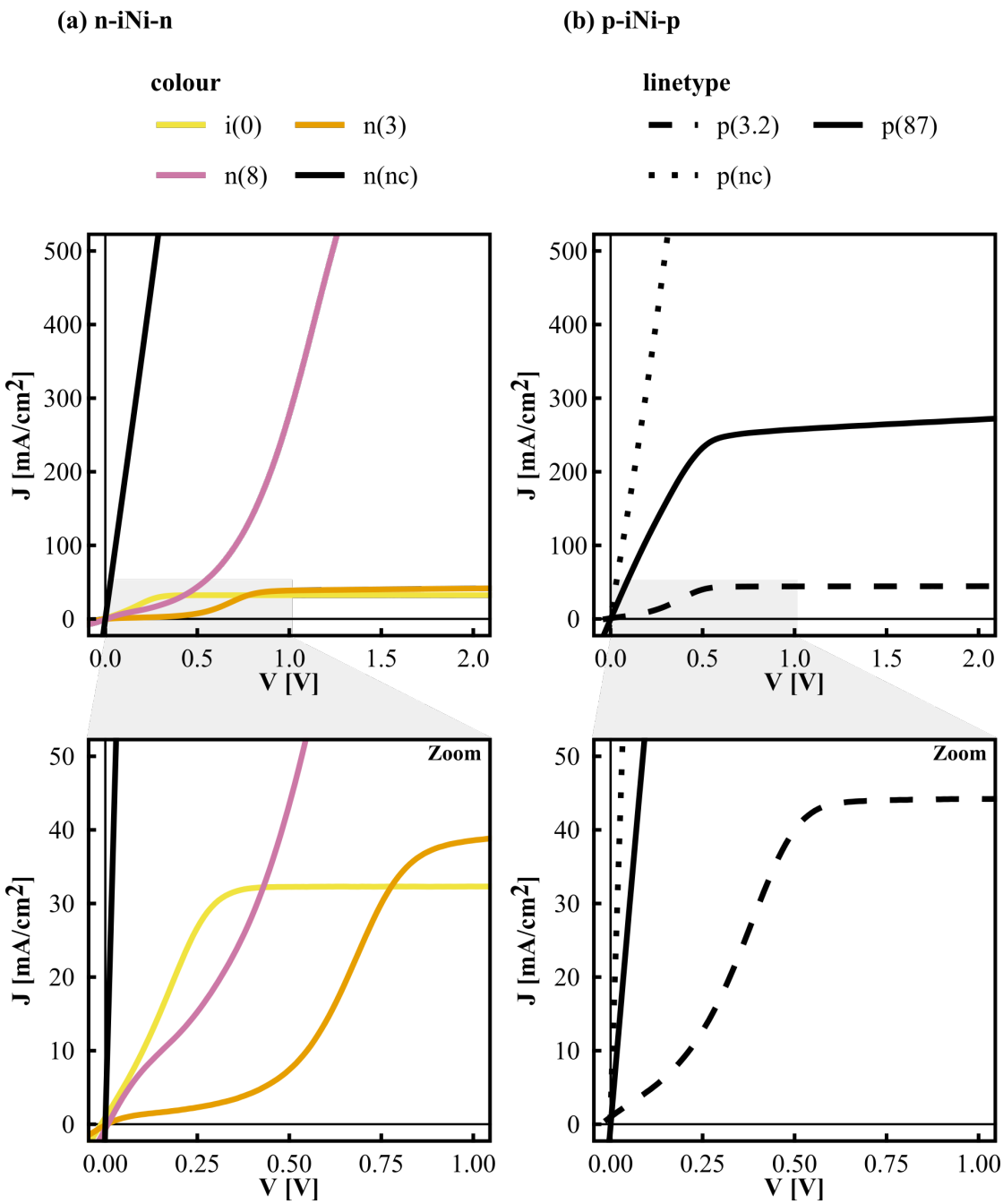

Figure 3.7: J-V *curves under 1 Sun of symmetrical samples formed with the same layer as the solar cell of Figure 3.6.*

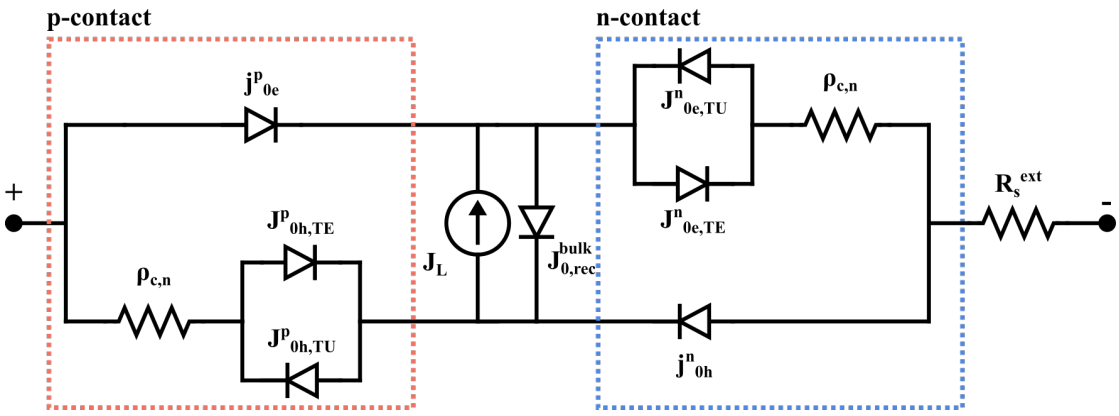

Figure 3.8: Final equivalent circuit model proposed to fit the samples with the various contact selectivities presented in this study.

3.4 Conclusion

In this chapter, we discussed the ability of the simple four ideal diode model of Roe to explain the S-shapes and kinks appearing on heterojunction solar cell *J-V* curves depending on their contact quality. We first discussed from a theoretical point of view how to improve the model by modifying the ideal diodes by other circuit elements. We then considered the impact of additional bulk recombinations on the model, simulated it, and gave simple relationships for the new positions and heights of the S-shapes in this new case for both solar cells and symmetrical samples. Then, we tested our theory experimentally on solar cells where the contacts were deliberately engineered to reach various selectivities. By studying case by case the gradual deviation from Roe's description, we figured out that the single diode kinetics should be modified as follows. First, another resistance should be added in series with the majority current diodes. These could *e.g.* represent the barrier at the c-Si/doped-layer and doped-layer/TCO interfaces respectively, or a bulk conductivity issue of the doped-layer itself. Second, we found necessary to consider several processes in parallel to explain the absence of saturation when increasing the doping level of the n-contact, namely a tunnelling diode letting current flow under large reverse bias. The occurrence of such effect when developing new contacts should be considered encouraging as it shows that the barrier height and thickness are moderate to allow such process. The final equivalent circuit summarizing those findings is presented in Figure 3.8, where all the additions were added on both contacts for more generality.

Our findings should be useful to model and identify bottlenecks occurring when developing new materials for any heterojunction contact technology such as SHJ or perovskite solar cells. It brings also further the fundamental discussion about passivation, selectivity and conductivity of solar cells, as discussed by *Onno et al.* [Onno 2019], by providing a defined parametrization of the circuit elements based on experimental data. To push further our understanding, we should address theoretically and experimentally the effect of surface recombination.

4 Influence of the Dopant Gas Precursor in nc-Si:H(*p*) Silicon Layers

This chapter is based on the following publication and oral presentation:

- L. Antognini, V. Paratte, J. Haschke, J. Cattin, J. Dréon, M. Lehmann, L.-L. Senaud, Q. Jeangros, C. Ballif and M. Boccard, *Influence of the Dopant Gas Precursor in P-Type Nanocrystalline Silicon Layers on the Performance of Front Junction Heterojunction Solar Cells.*, IEEE Journal of Photovoltaics, vol. 11, no. 4, pages 944-956, 2021

- L. Antognini, V. Paratte, M. Truong, J. Cattin, J. Haschke, J. Dréon, L.-L. Senaud, S.Nicolay, B. Paviet-Salomon, M. Despeisse, C. Ballif and M. Boccard, "Multilevel improvement in the window layers stack of Silicon Heterojunction Solar Cell", Oral presentation at the European PV Solar Energy Conference and Exhibition (EUPVSEC), Online, 2020

4.1 Abstract

Silicon heterojunction solar cells can employ p-type hydrogenated nanocrystalline silicon nc-Si:H(p) on their front side, since these can provide better transparency and contact resistance compared to hydrogenated p-type amorphous silicon layers a-Si:H(*p*). We investigate here the influence of $B(CH_3)_3$ (trimethylboron or TMB) and BF_3 as dopant source on the layer properties and its performance in solar cells. Both gases enable high efficiencies but yield a different crystallinity and effective doping. A high BF_3 flow lowers the series resistance through a low activation energy of dark lateral conductivity and maintains a high crystallinity. This allows reaching fill factors up to 83%, however with the apparition of a parasitic absorption in the UV. A low TMB flow enables simultaneously a high crystallinity and a low activation energy. As an illustration of this layer potential, a 23.9%-certified efficiency is achieved with a $2 \times 2\,cm^2$ screen-printed device. We finally suggest that similar transport vs. transparency trade-offs can be reached for both dopant types for front junction application, while high BF_3 flow allowing lower series resistance might be of interest when placed on the rear side.

4.2 Introduction

The silicon heterojunction (SHJ) technology enables reaching conversion efficiency of up to 26.3% for double-side contacted solar cells [Pv-magazine 2021a], 26.7% for interdigitated back contact cells [Yoshikawa 2017], and average efficiency above 23% in several laboratories and production industries [Zhao 2018, Chen 2019, CEA 2021]. Standard SHJ designs use hydrogenated amorphous silicon (a-Si:H) for both surface passivation (a-Si:H(i)) and selective layers (a-Si:H(n) and a-Si:H(p)), completed by indium tin oxide (ITO) for lateral charge transport and anti-reflection. Although these layer stacks enable excellent surface passivation and carrier selectivity, SHJ solar cells suffer from important parasitic light absorption and possible charge transport losses due to the relatively low transparency [Holman 2014] and doping efficiency of a-Si:H [Shah 2010, Bivour 2013], respectively.

Replacing the doped a-Si:H layers by nanocrystalline silicon (nc-Si:H(n) and nc-Si:H(p)) is a promising route to improve the efficiency of SHJ [Seif 2016] or to simplify the manufacturing process of IBC solar cells [Tomasi 2017]. Requirements to develop a good crystalline contact include [Seif 2016]:

1. Obtaining a fast nucleation of the crystalline phase of the doped nc-Si:H layers on top of the a-Si:H(i) passivation layer.
2. Reaching a high crystallinity to benefit from the higher transparency and doping efficiency of the crystalline phase.
3. Using plasma conditions that do not hinder passivation.

For the development of the n-doped contact, PH_3 is commonly used as the dopant precursor gas. In Ref. [Watahiki 2015], excellent solar cell results were obtained in a rear junction (RJ) configuration, i.e. with the n-layer at the front, with solar cells reaching an efficiency of up to 23.4%. The high transparency and the good contact properties of the nc-Si:H(n) were made possible by introducing a undoped nc-Si:H seed layer of about 5 nm, which enhances the crystallinity of the subsequent 20 nm-thick n-doped layer. By thinning down the layer to below 10 nm and alloying it with oxygen (to form a nc-SiOx:H(n) layer), it was possible to boost even more the transparency of the contact in RJ solar cells while keeping good transport properties [Mazzarella 2018a, Mazzarella 2018b]. Finally, a remarkable 25.1% efficiency device was obtained on a full size n-type M2 monocrystalline-silicon, featuring a 20 nm nc-SiOx:H(n) layer at the front together with optimized passivation layers (J_{sc} = 39.55 mA cm^{-2}, FF = 85.0%, V_{oc} = 747 mV) [Ru 2020].

On the hole-selective-contact side, nc-SiOx:H(p) layers are more difficult to obtain with as high conductivity than their (n)-type counterparts, making the front junction (FJ) configuration less attractive [Mazzarella 2015]. Indeed, it was reported to be challenging to obtain both a high crystallinity for layers thinner than 20 nm and a dark conductivity activation energy (E_a) as low as the values reached with nc-Si:H(n) (E_a of about 80 meV for p-layers compared to 30

meV for n layers [Zhao 2020]). These facts often motivate the p-doped layer's placement at the rear side where there is no constraint for the UV-Vis transparency, enabling the use of thicker or less crystalline materials [Haschke 2018]. However, by introducing an oxide pre-treatment [Boccard 2018] and investigating substrate temperature lower than 200 °C [Fioretti 2019] to promote crystallinity (see also Fig. 4.4) without impacting passivation, a solar cell efficiency of 23.5% was demonstrated as well with nc-Si:H(p) in front junction configuration, mainly enabled by the lower contact resistance [Haschke 2020]. In the present contribution, we will build upon those previous developments.

Overall, the incorporation of nc-Si:H layers in solar cells was studied in several ways, such as:

1. Varying the PECVD parameters (frequency, pressure, substrate temperature, the dilution ratio R = $[H_2]/[SiH_4]$) [Seif 2016],
2. Varying the silicon precursor gas [Seif 2016],
3. Developing different incubation layers and surface pre-treatments [Seif 2016], and
4. Investigating the influence on the subsequent TCO growth [Cruz 2019a].

Out of the directions that remain to be investigated, the impact of the boron doping and boron gas precursor (B_2H_6, BF_3 and $B(CH_3)_3$, also named TMB for trimethylborane) are still to clarify. An ellipsometric study reported that films prepared with B_2H_6 exhibit a delayed nucleation compared to their PH_3 and intrinsic counterparts [Hadjadj 2010]. Similarly, a higher ratio D = $[B_2H_6]/[SiH_4]$ leads to a lower Raman crystallinity and smaller crystallite sizes measured via XRD [Guo 2011]. However, the influence of boron on crystallinity is not trivial and other studies report contradictory effects: In Ref. [Koh 1999], using real-time spectroscopic ellipsometry, it was found that B_2H_6, TMB, and BF_3, combined with adequate surface treatment (e.g., hydrogen plasma treatment for TMB and BF_3), a high dilution ratio of R = $[H_2]/[SiH_4]$ = 200, doping level (D = 0.01 for B_2H_6 and TMB, D = 0.02-0.05 for BF_3, with D = $[X]/[SiH_4]$ where [X] is the dopant flow) and plasma power ($P = 200\,\mathrm{mW\,cm^{-2}}$ for B_2H_6 and TMB, $P = 700\,\mathrm{mW\,cm^{-2}}$ for BF_3) yield similarly dense, single-phase nc-Si:H layers. This last study also evidenced several advantages of BF_3 such as: i) avoiding carbon incorporation; ii) allowing a wider precursor gas flow range yielding a crystalline regime and iii) possessing a tolerance to higher plasma power and lower hydrogen-to-silane dilution leading to higher deposition rates without impinging crystallinity [Koh 1999]. Finally, in Ref. [Matsui 2004], by comparing SIMS measurement and Raman crystallinity, a dopant-to-silane dilution range was identified where the boron concentration can be increased by several orders of magnitude without affecting crystallinity.

In the present chapter, we aim to clarify the influence of the dopant source on the nc-Si:H(p) transparency and contact properties and its integration in solar cells. Hereafter, we present two batches of solar cells. First, with a "TMB and BF_3 doping series", we study the impact of the TMB and BF_3 flow on layers of similar thicknesses and report on their crystallinity

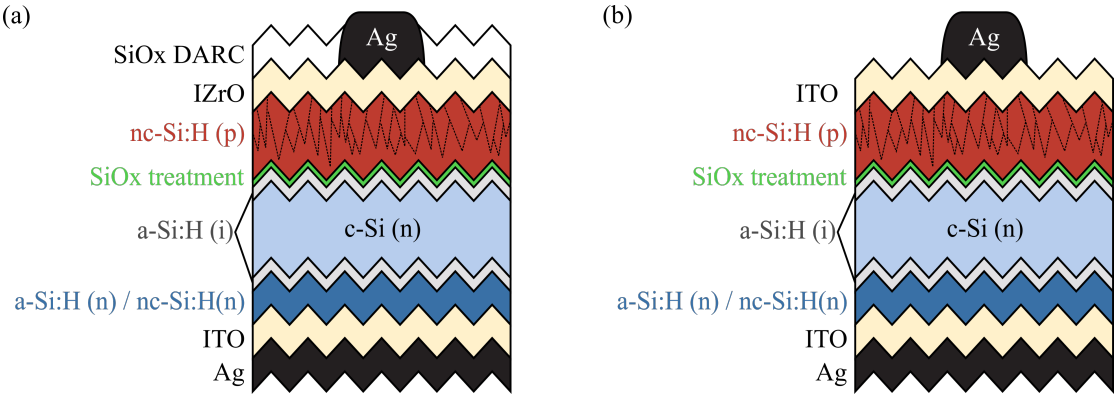

Figure 4.1: Scheme of the solar cells processed in this study. (a) Samples of the " TMB and BF_3 doping series" (b) Samples of the "BF_3-doped layers thickness series".

using UV-Raman spectroscopy, the dopant incorporation inclusion using dark conductivity measurement, and the layers chemical composition via SIMS measurements. Second, with a "BF_3-doped layer thickness series", we study the optical impact of using a high BF_3 flow. Optimization possibilities using both types of dopant sources are finally discussed, and we demonstrate the possibility to realize front-junction devices featuring a nc-Si:H(p) thinner than 30 nm, allowing properties close to their rear-junction counterparts. Finally, employing a double-antireflective coating, a $2 \times 2\,cm^2$ solar cell with a certified efficiency of $23.92 \pm 0.29\%$ is presented, featuring a nc-Si:H (p) layer on the front side and a single screen-print step.

4.3 Experimental Details

4.3.1 Solar cell preparation

The structure of the solar cells described in this section can be seen in Figure 4.1. The solar cell preparation was based on 10 cm diameter, 2 Ω cm, n-type FZ c-Si wafers. They were first placed in an alkaline etching solution to create random pyramids with a (111) orientation on both sides, resulting in a wafer thickness of about 195 µm. The wafers were then chemically cleaned. The native oxide was removed using a one minute bath in 5% diluted HF.

The silicon layers were deposited via PECVD in a parallel-plate plasma box KAI-M system. The latter is composed of two chambers dedicated to intrinsic and doped layers, respectively. All intrinsic layers were deposited at a substrate temperature of 200 °C while all the other PECVD layers are deposited in a dedicated chamber at 175 °C. First, a 7 to 10 nm-thick a-Si:H(i) layer was deposited for passivation on the backside, followed by an a-Si:H(n) / nc-Si:H(n) stack (or "in" stack).

For the deposition of the front "ip" stack, we used two different strategies for the two batches presented in this study in order to avoid process artifacts that could be present in a non-industrial environment. They differ notably by the coating of the chamber and holding plate

as well as the waiting time between the process of the different layers:

1. For the "TMB and BF_3 doping series", first the a-Si:H(i) front layer was co-deposited on all samples in the same condition as the rear a-Si:H(i) layer. Then, all samples were removed and stored in nitrogen. After a p-type coating of the doped chamber and holder plate, each sample was processed individually: a 1-2 nm SiOx layer was deposited on top of the a-Si:H(i) layer using a gas mixture of SiH_4, CO_2, and H_2. The role of this seed layer was to enhance the crystallinity of the subsequent nc-Si:H(p) layer without damaging the surface passivation [Boccard 2018]. Then, the nc-Si:H(p) layer was finally deposited with a hydrogen dilution of R = $[H_2]/[SiH_4]$ = 133, a varying dopant gas flow of 3 and 9.5 sccm for TMB and 9.5 and 50 sccm for BF_3 (both being diluted at 98% in H_2 corresponding to dilutions of D = $[X]/[SiH_4]$ of 0.004, 0.013, 0.066 respectively, with [X] being the actual TMB or BF_3 concentration). This sequence resulted in the "ip" stack.

2. For the "BF_3-doped layer thickness series", to avoid possible artifacts coming from air exposure and waiting time of the samples after the front a-Si:H(i) layer deposition, the ip stacks of each sample were processed in a single process without interruption. However, in this approach, the i-layer could be impacted by the previous nc-Si:H(p) deposition on the holder plate, the latter containing more or less dopant depending on the previous layer deposited. This, in turn, could affect the collection efficiency of the i-layer [Holman 2014], affecting the current of the solar cell and hindering our conclusions on the BF_3 absorption properties. We thus included in this fabrication batch similar solar cells to characterize this effect, where only the doped chamber and holder plate coating before the ip stack deposition is changed.

Next, for the "TMB and BF_3 doping series", a 125 nm (flat equivalent) indium zirconium oxide layer (IZrO) was used as TCO allowing a higher mobility than ITO for the same optical properties (See [Morales-Masis 2018, Rucavado 2019]). It was deposited on the front side via RF-sputtering in a MRC-II system using a target of 2% weight of ZrO_2 in In_2O_3 with gas flow ratio of [Ar], $[H_2]$ and $[O_2]$ of 99.2%, 0.4% and 0.4% respectively, a pressure of 10 mTorr and a power density of 1.65 $W\,cm^{-2}$. The deposition was made through a shadow mask defining five $2 \times 2\,cm^2$ solar cells per wafer. Subsequently, using DC-sputtering, a 220 nm-thick (flat equivalent) ITO was deposited on the full area of the backside followed by a 150 nm-thick (flat equivalent) Ag blanket. Contacting of the solar cells was performed by screen-printing a silver grid on the front side using a curing temperature of 210 °C for 30 minutes in a belt furnace.

Finally, a 100 nm-thick PECVD SiOx layer was deposited at 180 °C on the front side to form a double anti-reflective coating (DARC) [Herasimenka 2016, Cruz 2019b]. This minimizes the reflectance of the solar cell and reduces the TCO sheet resistance [Cruz 2019a, Boccard 2021], as we show in appendix A.3.2 for our samples, thus allowing to observe more clearly the impact of the contact resistance of the hole-selective stack on the total series resistance. For the present series, this extra step allowed to reduce the R_{sh}^{TCO} variation among the samples to lower than 15 Ω/sq.

For the "BF_3-doped layers thickness series", a simpler single ARC was realized on the front side with a 120 nm-thick (flat equivalent) ITO layer. It was deposited via DC-sputtering on a In_2O_3(90):SnO_2(10) target with a gas flow ratio of [Ar] to [O_2] of 98/2, at a pressure of 8 mTorr and a power of 2.2 W cm^{-2}.

Finally, the certified solar cell presented at the end of the study was produced using the same process order as the "TMB and BF_3 doping series". It was then placed in forward-bias in the dark for two weeks, with a current flow of 40 mA cm^{-2} corresponding to a carrier injection in the wafer similar to open-circuit condition under one sun. This step improves the surface passivation similarly to the beneficial effect of light-soaking [Cattin 2020].

4.3.2 Solar Cell characterisation

Along the process flow, the lifetime and implied open-circuit voltage (iV_{oc}) were measured after the deposition of the in-i and in-ip stacks using a WCT-120 photoconductance lifetime tester in the transient analysis mode. *I-V* curves of each solar cell were collected using a Wacom Electric Co. Super solar simulator with AM 1.5G illumination. Series resistance (R_s) at maximum power point (MPP) and fill factors without the effects of series resistance (FF_0) were obtained by comparing the *J-V* curve of a device at 1 Sun with the one at 0.05 Sun using the method described in section 2.3.4.

External quantum efficiency (EQE) curves were collected using a system developed in-house with a lock-in amplifier and a xenon arc lamp shining a 1 × 1.5 mm^2 monochromatic light spot between the grid fingers of the solar cell. For each wafer, the solar cell with the closest J_{sc} value to the median of the five cells, was chosen for the EQE measurement. TCO sheet resistance (R_{sh}^{TCO}) was measured using a transfer length method (TLM) structure screen-printed simultaneously with the front silver grid.

Raman spectra of nc-Si:H layers were acquired directly on the wafer on areas uncovered by TCO. To avoid the contribution of the c-Si and the a-Si:H(i) layer underneath, a 325 nm UV laser was used to probe only the top 10-15 nm of the layers [Carpenter III 2017]. To obtain an accurate background shape and extract the crystalline and amorphous phase features, Raman spectra were fitted with Gaussians centered around 315, 420, 480, 510, 520 and 625 cm^{-1} [Bermejo 1979]. The Raman crystallinity (X_c) is then computed as $X_c = \frac{A_{510}+A_{520}}{A_{480}+A_{510}+A_{520}}$ were the A's are the amplitudes of the respective amorphous and crystalline Gaussians [Smit 2003].

Finally, using a 442 nm laser with a probing depth down to the wafer, we used the c-Si signal counts attenuation to measure the absorption of the ip stack at this wavelength, as was used in [Ledinský 2016].

4.3.3 Characterization on reference layers

Dark conductivity samples were prepared by co-depositing ip stacks on glass substrates and then evaporating 100 nm-thick Al pads at room temperature. The samples were then placed in an N_2 atmosphere of approximately 1 mbar on a thermally conductive chuck. The temperature was ramped from 25 °C to 180 °C in 15 min, held for 90 min, and then ramped down to 25 °C during 4 hours. The resistance between the two pads was measured using two-probe pogo-pins on each pad and electrometers. The activation energy of the dark lateral conductivity (E_a) and room temperature conductivity (σ_{RT}) were calculated on the descending temperature range, by fitting the data between 30 °C to 145 °C with the formula $\sigma(T) = \sigma_0 exp(-E_A/k_B T)$, with k_B being the Boltzmann factor and σ_0 a pre-factor equal to the extrapolated conductivity at infinite temperature.

Transmission electron microscopy (TEM) was performed to assess the overall microstructure. The stack c-Si(n)/a-Si:H(i)/SiOx/nc-Si:H(p) (with a flow of 9.5 sccm of TMB in the nc-Si:H(p)) was deposited on a mechanically polished (111) c-Si wafer and the TEM sample was prepared using the conventional focused ion beam lift-out method in a Zeiss NVision 40 dual beam FIB/scanning electron microscopy system. The lamella was then analyzed by TEM in a double Cs-corrected TFS Titan Themis operated at 200 kV. Scanning TEM (STEM) high-angle annular dark-field images and corresponding energy-dispersive X-ray spectroscopy maps were acquired with a beam current of 400 pA.

The thicknesses of the layers were measured using variable-angle spectroscopic ellipsometry from co-deposited ip stacks on glass substrates. Spectra were acquired in the range 1.5-6 eV at angles of 50°, 60° and 80° using a Horiba Jobin Yvon ellipsometer. Modeling was performed in the DeltaPsi2 software as follows. First, a standard a-Si:H(i) layer was characterized and fitted to a single Tauc-Lorentz (TL) model, yielding a layer thickness of around 8 nm. The nc-Si:H(p) layers in the ip stacks were modeled as a double TL with peak at 3.36 eV and 4.25 eV, as suggested in Ref. [Yuguchi 2012]. Finally, surface roughness was added. Note that modeling the nc-Si with a single TL or otherwise with a double TL and an additional harmonic oscillator and testing various starting conditions gave similar thicknesses as those reported here.

Finally, the chemical composition along the ip stack depth was characterized via SIMS measurements performed on a double-side polished (111) n-type wafer. A CAMECA SC-Ultra instrument operating with a Cs^+ or $O_2{}^+$ bombardment at a low impact energy (1 keV) was used. Secondary ions were collected from an area of 60 µm in diameter and analyzed in different conditions to optimize the ionization yield of the elements of interest. Boron was analyzed as B^+ , whereas fluorine and oxygen were analyzed as negative ions (F^- and O^- respectively) at high mass resolution (2000). Silicon and hydrogen were collected as $SiCs^+$ and $HCs_2{}^+$ ions, respectively.

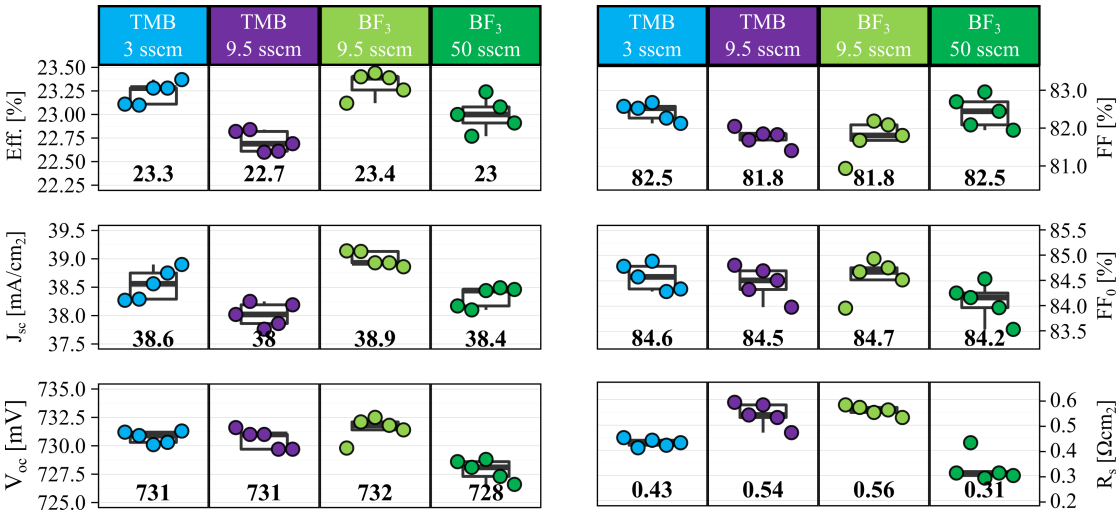

Figure 4.2: I-V *characteristics for the samples of the "TMB and BF_3 doping series" (after deposition of the SiOx DARC).*

4.4 Results and Discussion

4.4.1 TMB and BF_3 doping series

J-V results

The *J-V* results for the "TMB and BF_3 doping series" are presented in Figure 4.2. We will first describe here only the impact of the used dopant flow upon them, and discuss the relation to the material properties more in depth in the next sections. We observe that efficiency values close to 23.5% can be obtained both with TMB and BF_3. All devices feature high V_{oc} above 730 mV, except for the 50 sccm BF_3 flow, for which it is slightly lower of 2 mV and a 0.5% drop of the median FF_0 is also noticeable. This sample might suffer from a slightly lower passivation quality, as can be seen from the lifetime measurement of the solar cell precursor (given on Fig. A.6, possibly due to a longer waiting time before processing the a-Si:H(i) front layer, which was observed in previous experiments (not shown here) to negatively impact passivation. Despite this small passivation issue, increasing the BF_3 flow from 9.5 to 50 sccm allows reducing the series resistance of about 0.2 $\Omega\,cm^2$, pushing the *FF* up to 83% for the best cell. Yet, it also leads to a drop in the median J_{sc} of 0.5 $mA\,cm^{-2}$, which we will discuss in more details in the section below.

Then, comparing TMB and BF_3 with the same flow of 9.5 sccm, we observe a large difference in J_{sc} of about 1 $mA\,cm^2$, while the transport and passivation are very similar (same V_{oc}, *FF*, FF_0, and R_s). Finally, reducing the TMB flow from 9.5 to 3 sccm, we observe an increase of the median J_{sc} of 0.6 $mA\,cm^{-2}$ and an improvement of the median *FF* of 0.7% mainly through a reduction of the median R_s of 0.11 $m\Omega\,cm^2$. These improvements might come from the enhanced crystallinity of the layer,that we will discuss in the next sections.

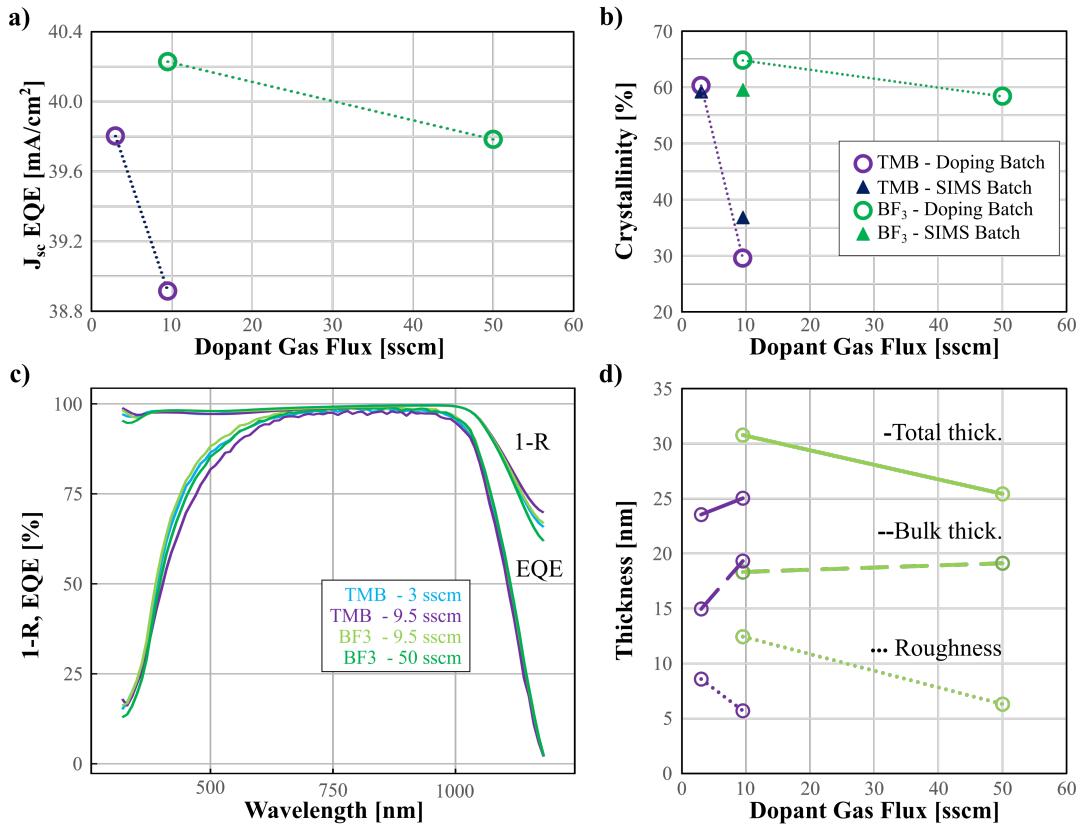

Figure 4.3: Analysis of the optical properties of the "TMB and BF_3 doping series". (a) Short-circuit current integrated from the convolution of EQE with AM1.5G. (b) Raman crystallinity for two different batches. (c) EQE and reflectance (displayed as 1-R) of the solar cell. (d) Thicknesses obtained from ellipsometry, with Total thick. = Bulk thick. + Roughness.

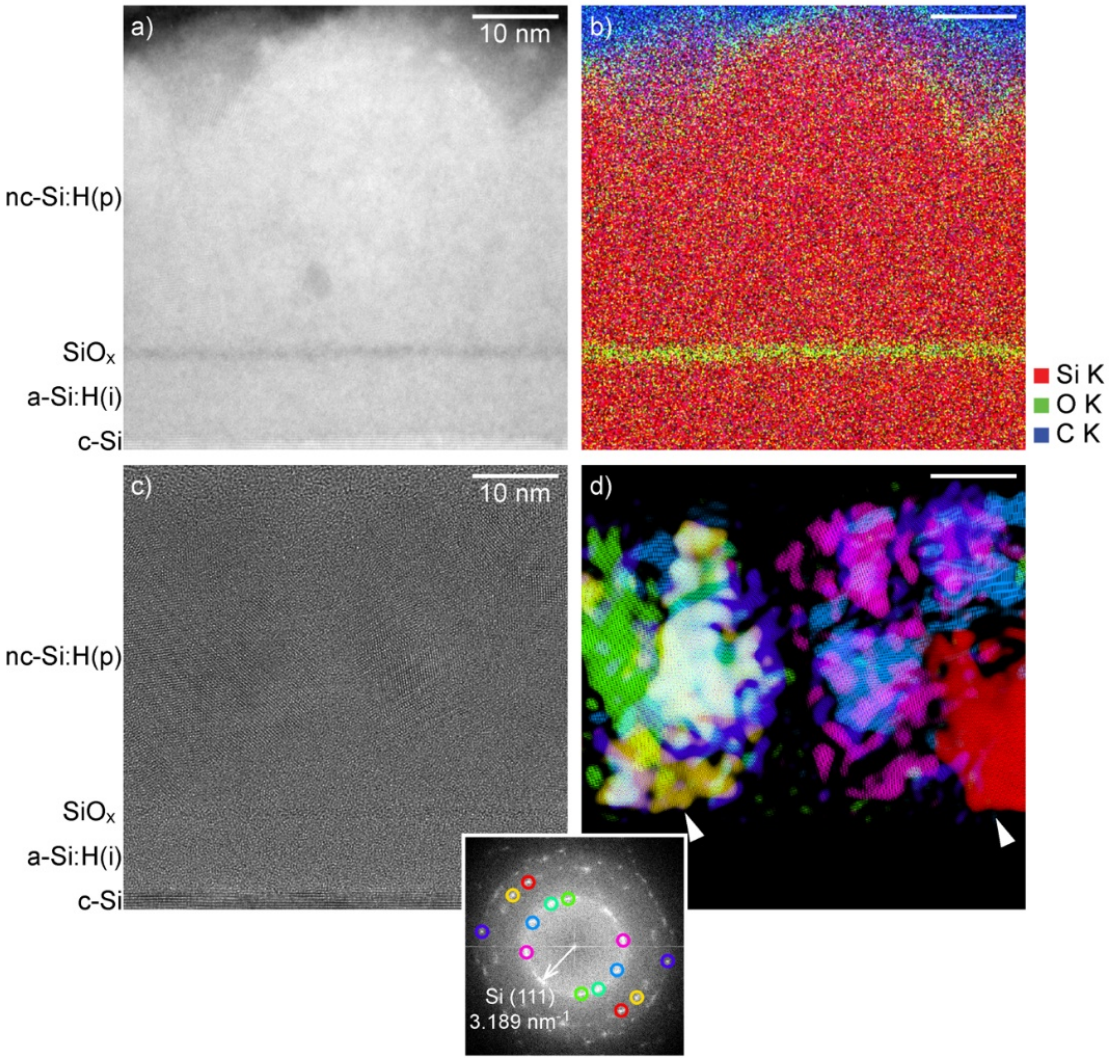

Figure 4.4: a) STEM HAADF image of the c-Si(n) / a-Si:H(i) / SiOx / nc-Si:H(p) stack, b) corresponding net EDX intensity map of the Si, O and C K edges, c) high-resolution TEM images, and d) corresponding inverse Fourier transform of a selection of Si reflections (Fourier transform provided as inset).

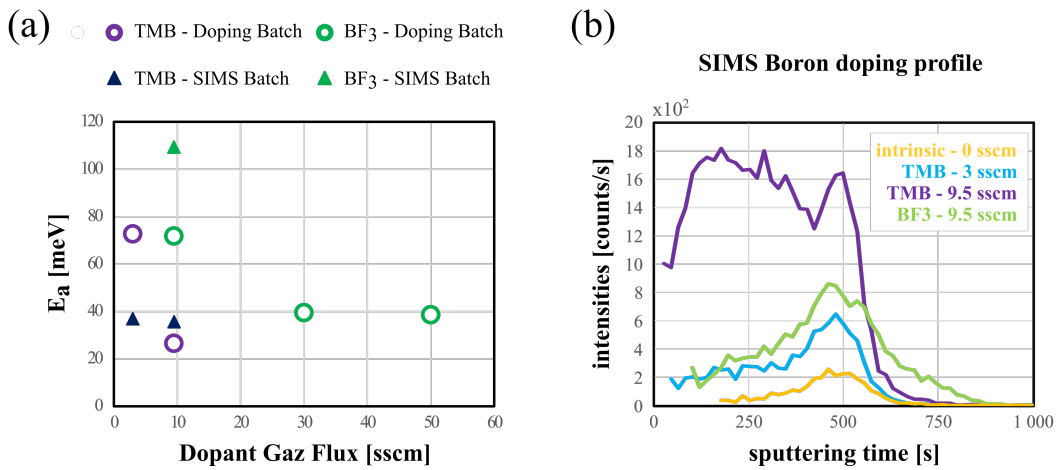

Figure 4.5: (a) Activation energy of the BF_3- and TMB- prepared nc-Si:H(p) layers for different dopant flows and two different batches of samples. (b) SIMS boron profile of c-Si(n) / a-Si:H(i) / SiOx / nc-Si:H(p) stacks deposited on DSP wafer. The influence of the other chemical elements (Si, F, O, H, C) is discussed on Fig. A.10.

Optical and material properties

Figure 4.3 presents the data relative to the optical properties of the "TMB and BF_3 doping series". We find again the same trend for the J_{sc} integrated from EQE than the one from *I-V* measurements. We also observe a clear correlation of the latter with the evolution of the crystallinity. Moreover, this observation is well reproduced among the different batches of this study. The EQE spectra show that the current difference is happening in the UV-blue part of the spectrum. Since the difference of reflectance among the samples is too low to explain the EQE trends in the 320-600 nm range, we can conclude to a parasitic absorption phenomenon. Finally, we also note a lower EQE also in the 600-1180 nm range for the layer prepared with 9.5 sccm of TMB. However, this difference can be ascribed to a more absorbing TCO, as a lower sheet resistance of the TCO was measured (not shown) and lower IR-reflectance (due to more absorption) of this sample.

Ellipsometry measurements show that all p-layers have similar total thicknesses (bulk + roughness) around 25-30 nm, with the small trend visible uncorrelated with the J_{sc} trends. These observations indicate that for the TMB samples, the transparency is mainly controlled by the Raman crystallinity of the sample, a change of crystallinity from 60% to 30% leading to a drop of J_{sc} of 0.6 mA cm^{-2} in the range 320-600nm of the spectrum. This is expected due to the higher absorption of the amorphous phase compared to the crystalline one.

However, the phenomenon is different for BF_3. Contrary to TMB, BF_3 does not strongly hinder the crystallization, either due to the absence of carbon [Cho 2018] or lower boron incorporation [Guo 2011], and only a small drop of crystallinity of 5% is observed when going from 9.5 to 50 sccm. However, despite this small change, we observe a significant J_{sc} drop of 0.4 mA cm^{-2} Further discussion on this absorption is provided in the "BF_3-doped layer

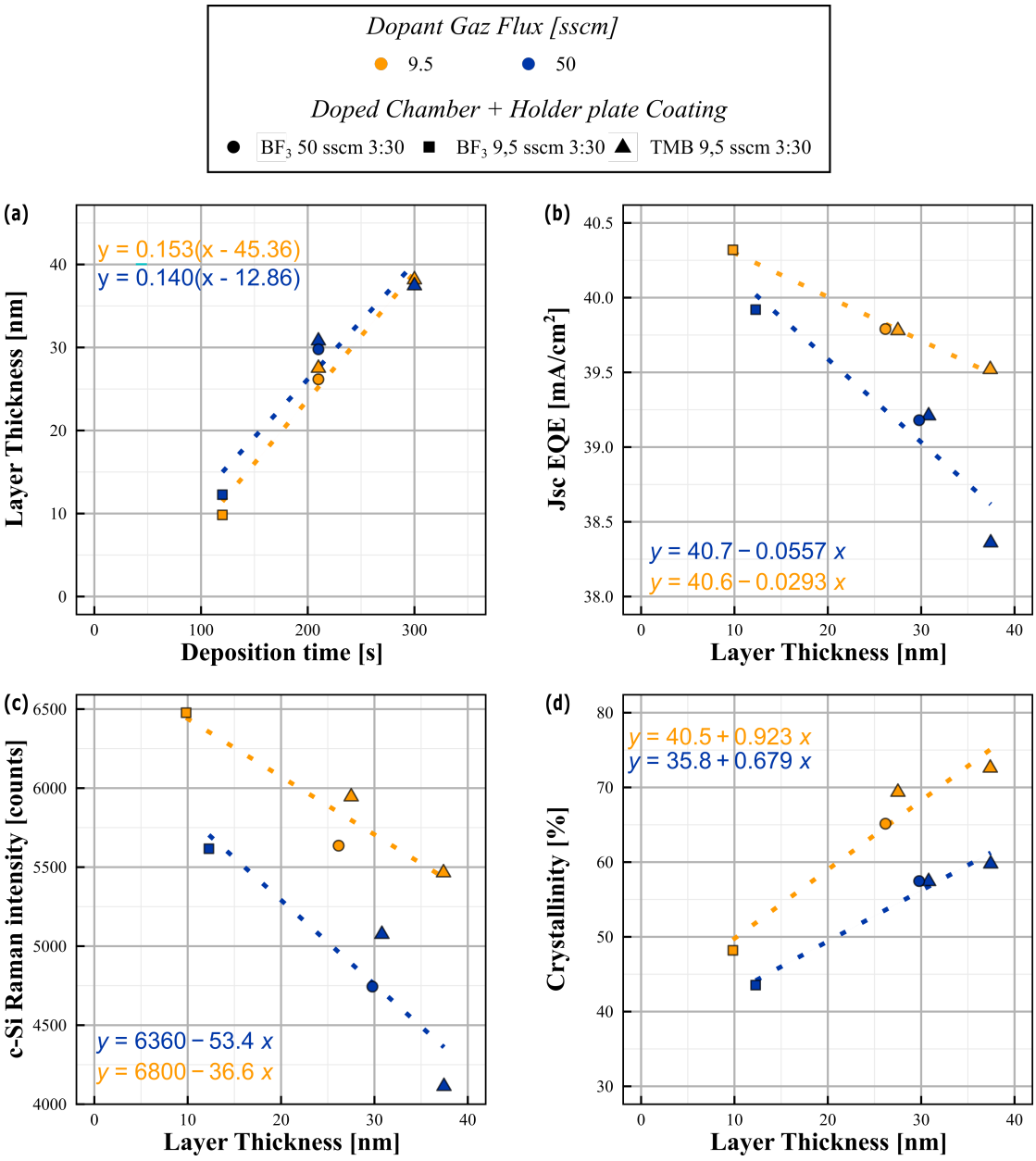

Figure 4.6: Analysis of the optical properties of BF_3-doped p-layer. (a) Total layer thickness (bulk + roughness) measured by ellipsometry v.s. deposition time of the p-layer. (b) Current integrated from EQE, (c) Raman signal from the underneath c-Si wafer measured with a 442 nm laser wavelength vs. p-layer thickness and (d) Crystallinity of the p-layer.

thickness series" section.

Completing the observation of the structural properties, TEM analysis was performed on the full c-Si(n) / a-Si:H(i) / SiO_x / nc-Si:H(p) stack with the 9.5 sccm TMB recipe which leads to the lower crystallinity among the layer presented in this study, however with a deposition time longer of 33% (see Figure 4.4). The total thickness of the full c-Si(n) / a-Si:H(i) / SiO_x / nc-Si:H(p) stack thickness approaches 40 nm, including a roughness on the order of 10 nm. Note that this thickness corresponds to the results given by ellipsometry, taking into account the longer deposition time of this layer, and thus confirms the validity of our ellipsometry model. The STEM EDX map and the inverse Fourier transforms of a selection of Si reflections computed from a high-resolution TEM image highlight the short nucleation zone of the nanocrystalline phase after the O-rich layer. Thanks to the SiOx pre-treatment [Boccard 2018] and the substrate temperature lower than 200 °C [Fioretti 2019], the Si crystalline domains do not exhibit the typically conical shape [Stradins 2009] but instead nucleate with a large cross-section already during the early stages of the growth (see arrowheads), and this already for the less crystalline layer recipe.

Transport, activation energy, and boron content

Figure 4.5(a) presents the dark conductivity activation energy (E_a) of the a-Si:H(i) / nc-Si:H(p) stacks co-deposited on glass substrate. With a 9.5 sccm of dopant gas flow, the sample prepared with TMB systematically exhibits the lowest E_a ($\approx$ 30 meV) compared to the one prepared using BF_3 ($\approx$ 70 meV or higher depending on the batch considered). However, the high E_a of BF_3 layers can be reduced to 30 meV as well by increasing the dopant flow. Finally, we can see that by reducing the TMB flow to 3 sccm, we can still reach a low E_a of 30 meV. However, this latter observation was not reproduced systematically, as can be seen by the differences between the "TMB and BF_3 doping series" and the "SIMS batch" and is discussed at the end of this section.

Correlating the E_a of Figure 4.5(a) with the crystallinity of Figure 4.3(b), we observe that a low activation energy is not always correlated with a high crystallinity. In the case of BF_3, both flows lead to similar crystallinities and increasing the dopant flow only decreases E_a, suggesting an increase of doping due to the higher flow of dopant precursor. On the other hand, layers doped with 3 sccm of TMB show a high crystallinity, but the B concentration in the film might be too low to reach a high doping, leading to a higher E_a than for larger TMB flows even though the latter have a lower crystallinity. In Figure 4.5(b), we see that the higher TMB flow of 9.5 sccm yields a higher B content in the layer as expected. The intrinsic reference also shows a small B amount, probably due to the chamber's contamination by the preceding p-layer deposition. Finally, the lower TMB flow of 3 sccm and the 9.5 sccm BF_3 layer show similar B contents, possibly due to the lower dissociation of BF_3 in the plasma [Koh 1999].

Considering the "SIMS Batch" characterization, we can therefore conclude that for TMB, even a low B incorporation can lead to a layer with a low E_a, possibly explained by a better dopant

activation in this more crystalline layer. Even though the 3 sccm TMB sample's activation energy is higher than for 9.5 sccm for the "TMB and BF_3 doping series", this translates into a better series resistance for the solar cell. The E_a observed for the layer doped with 9.5 sccm of BF_3 in the SIMS batch is intriguingly much higher than the one of the 3 sccm TMB sample despite similar B concentration on the SIMS profiles. This could suggest that some B is inactive when BF_3 is used.

The lack of correlation between the series resistance of the solar cell and the layers' dark conductivity activation energy could be explained by the following facts. First, we are looking at very small variations in the activation energy and series resistance. Second, the trends might be lower than batch-to-batch variations. Indeed, simulations of IBC-SHJ of the transport through the i-p-TCO hetero-interface and subgap energy states showed that all activation energies lower than 100 meV and a TCO doping higher than 1×10^{20} cm^{-3} enable reaching similar values of *FF* [Procel 2020], which is the case here. Third, a low flow of 3 sccm of TMB is actually close to the mass flow controller minimal value, which can explain the variability of the activation energy. Finally, note that the accurate measurement of the activation energy in the small range between 30 to 100 meV can also depend on the sample preparation, as shown on Figure A.12 of the appendix.

4.4.2 BF_3-doped layer thickness series

To clarify the absorption of BF_3-doped layers, we processed p-layers with 9.5 and 50 sccm of BF_3 and varied their deposition time. Moreover we varied the chamber coating prior to the ip stack deposition to detect a possible influence from the plate coating on the i-layer properties when using a high dopant flow, as explained in the experimental part. Figure 4.6 presents the results of this study.

The layers have similar thicknesses, low deposition rates of 0.14–0.15 nm/s, and layers start to grow after a delay of 10–50 s which could correspond to the nucleation time [Koh 1999]. For 210 s, which is the same deposition time as the "TMB and BF_3 doping series", we find similar p-layer thicknesses between 25 to 30 nm and confirm a current drop of about 0.4–0.5 mA/cm^2 when going from 9.5 to 50 sccm. Looking at the dependence of J_{sc} upon thickness, we notice that using 50 sccm of BF_3 always leads to higher absorption. This data shows a similar value of current of 40.6–40.7 mA/cm^2 extrapolated for a zero nm-thick layer and almost a twice as large slope for 50 sccm compared to 9.5 sccm with a current loss of 0.06 and 0.03 mA/cm^2/nm, respectively. This factor of two between the slopes is also reproduced using Raman profilometry as shown in Figure 4.6(d). These observations, correlating for multiple samples, confirm that layers prepared with 50 sccm of BF_3 absorb more than those prepared with 9.5 sccm, without any noticeable influence from the chamber coating.

Regarding structural properties, the crystallinity measurements show that using a 50 sccm flow instead of 9.5 sccm slows down slightly the crystallite growth, similarly to [Guo 2011] yet less strongly. The offset is up to 10-12% for 40 nm layers, whereas it tends towards less than 5%

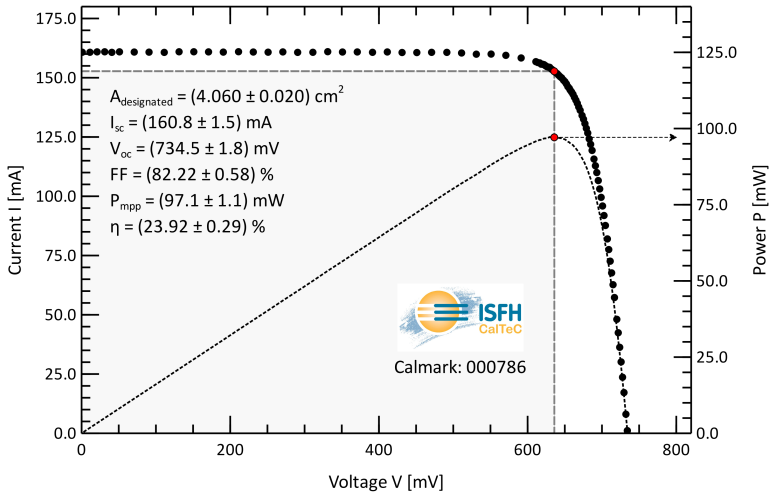

Figure 4.7: IV certification of the optimized device featuring the 4 sccm TMB front nc-Si:H(p) layer.

for a zero thickness. Thus, since the difference is increasing with the growth, we conclude that this effect stems from a bulk modification of the nanocrystalline layer and not its incubation zone. More in-depth characterizations on the boron content, layer porosity and the grain size would be needed to confirm these theories.

4.5 Record cell and outlook

In the previous section, we showed possible to combine high J_{sc} and FF by using p layers prepared with low TMB flows. As an illustration of the potential of this layer, we produced a 2 × 2 cm^2 solar cell with the same structure and processes as for the "TMB and BF_3 doping series". Solar cells featured a 4-sccm TMB p-layer, an indium zirconium oxide layer (allowing higher mobility than ITO for the same optical properties [Morales-Masis 2018, Rucavado 2019]), a single screen-printing step, finished with a 100 nm (on textured wafer) SiO_x layer (see Figure 4.1). A flow of 4 sccm of TMB was used instead of the 3 sccm to avoid using values too close to the minimum of the mass flow controller and allow more reproducible results. A high crystallinity of 67% was also measured for this sample (not shown), showing that the resulting material properties are similar.

The cells were then held in forward-bias conditions for two weeks to improve their passivation properties [Cattin 2020]. Figure 4.7 shows the independently certified results, reaching conversion efficiency of 23.92%, a FF of 82.22%, J_{sc} value of 39.6 mA cm^{-2} and V_{oc} of 734.5 mV. From Figure 4.2, we can suggest that a similar efficiency could be obtained using a BF_3 flow of 9.5 sccm. However, changing the BF_3 flow does not allow to relax the trade-off between transparency and transport, since it increases more the parasitic absorption losses than it decreases the resistive losses, leading to lower efficiency in front junction configuration.

For the BF_3 p-layers, the very low series resistance achieved despite stronger absorption in the UV could be of interest for rear-junction application. Moreover, the integration of nc-Si:H in industrial production is still a challenge due to the low deposition rate. Since BF_3 is less sensitive than TMB to amorphization of the layer, a less dilute regime could be explored to reach faster deposition rates.

For TMB p-layers, it has been shown that higher efficiencies up to 24.1% can be obtained by alloying the layer with oxygen in a multilayer approach [Boccard 2021]. Those results, presented on Figure A.16, show that both configurations benefit from the IZrO/SiOx coupling as well as the forward bias treatment, improving their optical, resistive and passivation properties. Alloying with oxygen increases the series resistance, however this is counter balanced by a high gain in transparency allowing to reach a higher efficiency than with nc-Si:H.

Finally, it is possible to enhance the current of more than 0.6 mA cm^{-2} (see Table 6.4) in the infrared by reducing the absorption in the rear TCO and Ag layer. This can be realized by thinning down the TCO and evaporating through a grid a MgF_2 layer to act as an optical spacer with the Ag rear laye [Boccard 2021]. As the conduction occur only through the opening in the MgF_2 left by the shadow mask, a careful optimization of the TCO thickness and doping should be carried out. Adding to that a further thickness reduction of the front a-Si:H(*i*) and nc-SiO_x:H layers lead to a certified efficiency of 24.44% on a 2 × 2 cm^2 screen-printed front junction device[1].

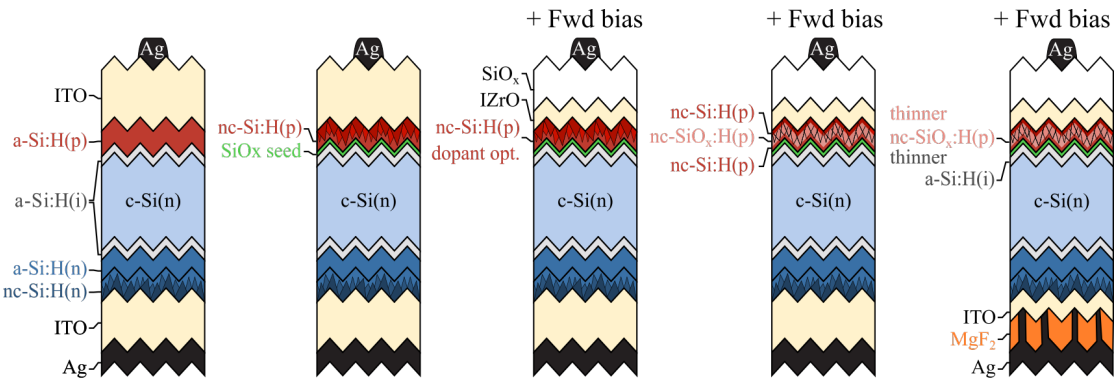

	2018	2019	2020	2020	2021
Eff. [%]	22.7	23.45	23.92	24.09	24.44
J_{sc} [$\frac{mA}{cm^2}$]	38.9	39.4	39.61	39.85	40.75
V_{oc} [mV]	727	734	735	738	731
FF [%]	80.0	81.1	82.2	82.0	82.1

Figure 4.8: Summary of the SHJ structures developed at the PV-Lab throughout this thesis and corresponding certified values of J-V *results.*

[1] For future citation purpose of this result, if possible please refer to "*Loss-Analysis of a 24.4%-Efficient Front-Junction Silicon Heterojunction Solar Cells and Opportunity for Localized Contacts*, Mathieu Boccard, Luca Antognini, Jean Cattin, Julie Dréon, Wenjie Lin, Vincent Paratte, Deniz Türkay, Christophe Ballif, IEEE Journal of Photovoltaics, 2022", under review at the time of this thesis writing.

4.6 Conclusion

We investigated the influence of TMB and BF_3 as dopant sources on the transparency, contact properties of nc-Si:H(p) layers and their integration in solar cells. Both gas precursors allow to reach high efficiencies. Reaching a *FF* above 82% on $2 \times 2\,cm^2$ solar cells is possible by lowering the dark conductivity activation energy of the layers down to 30 meV. A high J_{sc} can be obtained by increasing the crystallinity to 60%. Overall, it is possible to reach both a low E_a and a high crystallinity with a low TMB flow. Based on these findings, the TMB nc-Si:H(p) layer's potential was illustrated by presenting a certified 23.9%-efficient solar cell featuring a 100 nm DARC SiO_x layer. Then, we showed that it is possible to reach slightly higher crystallinity and current by switching from TMB to BF_3 as the dopant source, however at the expense of a higher E_a. A higher BF_3 flow was needed to reach E_a values as low as for TMB, which induces parasitic absorption in the UV and precludes a clear benefit to be seen by using BF_3 or TMB. This parasitic absorption was shown to be not linked to a difference in crystallinity or thickness and it remains to be fully explained. The use of BF_3 remains of specific interest in rear junction configuration since the optical drawbacks are then alleviated, and the electrical benefits would be maintained.

5 Injection dependent Series Resistance Breakdown

5.1 Chapter Structure

In this chapter, we will focus on modelling and characterizing the different resistive losses in the solar cell. The end goal is to perform an accurate breakdown of series resistance losses of the solar cell, taking into account the possible injection dependence of the different components. The structure of this chapter is split as follows:

First, in section 5.2, we will introduce and discuss in depth the particular case of TLM structures involving *p*-type layers deposited on *n*-type wafer (denoted as *pNp* structures). First, we will put into light a specific physical mechanism which can provide charge transport in such devices using large TLM samples and then discuss the differences when using conventional smaller TLM designs. This detour will allow us to justify some of the hypothesis made in the discussion of the TLM results in the next section.

Then, in section 5.3, we will introduce the resistance model used to describe the solar cell, the main parameters entering this one and the way to measure them. Notably, two very important variables are the contact resistivity of the front and rear contact, ρ_c^{front} and ρ_c^{rear}, respectively - or ρ_c^p and ρ_c^n when referring to the contact resistivity of the *p*-type and *n*-type CSPC, respectively. We will investigate different ways to measure those ρ_c independently of the solar cells using TLM or symmetrical vertical structures and perform a breakdown of the series resistance of front junction solar cells developed in chapter 4. Importantly, we will attempt to discuss the effect of the injection level on the contact resistivities. Indeed, in [Haschke 2020] it was well described that injection modulates the sheet resistance of the wafer R_{sh}^{cSi} and therefore impacts the lateral transport of the solar cell when ρ_c^{front} is low enough. However, constant values of ρ_c^{front} were considered and the impact of injection-dependant contact resistivities was not discussed. We will therefore realize TLM and symmetrical structure on different wafer types and perform measurements under variable illumination to extract ρ_c^n and ρ_c^p values. At the end of this first part, we will discuss the accuracy and potential source of errors of the different methods.

5.2 Transport in p/N/p samples under illumination

5.2.1 Motivation

Determining the n- and p-contact resistivity ρ_c^n and ρ_c^p accurately is of importance to model the solar cell resistive losses correctly. In the literature, those parameters are most commonly extracted from either non-illuminated transfer length method (TLM) samples or vertical structures, both featuring isotype junctions [Lachenal 2016, Leilaeioun 2020]. In other words, the measurements are always performed in the dark and with *n*-layer deposited on *n*-type wafer ("*nNn*" samples) to determine ρ_c^n or *p*-layer deposited on *p*-type wafer ("*pPp*") to determine ρ_c^p. However, a SHJ solar cell always has a pn-junction as one of its contacts and operates under illumination. Therefore, it is of interest to study the differences *e.g.* between extraction of ρ_c^p in the dark or under illumination from a *pPp* sample or a *pNp* sample (for *p*-layer deposited on *n*-type wafer). Such differences were already reported in [Senaud 2021b, Senaud 2021a, Basset 2021] in the case of TLM measurements.

Before getting to the R_s breakdown of the solar cell, in this section we will discuss in detail the particular case of *pNp* samples under illumination. Such a *pNp* structure is shown in Figure 5.1(a). As we will see later, the current can flow in this structure when illuminated despite the apparent presence on the current path of two diodes facing each other. In section 5.2.3, using large TLM samples to focus on the transport in the wafer, we will put into light some of the physical mechanisms making transport possible in those devices and we will discuss the particular role of electrons and holes to describe the sheet resistance of the wafer. In section 5.2.4, we will then discuss the differences when using conventional smaller TLM designs for the extraction of the contact resistivity. The arguments developed here will allow us to discuss better the different methodology for ρ_c extraction in section 5.3. Moreover, the illuminated *pNp* structure under study is closely related to bipolar photo-transistors (however, with a very thick base), and therefore results found here could find application in this field as well.

5.2.2 Experimental details

The *pNp* TLM layer architecture and the large TLM and small TLM designs are presented on Figure 5.1. The structures are based on 2 Ω cm, n-type c-Si textured wafers of thickness of $t = (195 \pm 10)$ µm. On one side, an a-Si:H(*i*) layer followed by an a-Si:H(*p*) layer were deposited via PECVD. On top of this, TCO and Ag were sputtered through a shadow mask to form the TLM pads. The stack a-Si:H(i)/a-Si:H(p)/TCO/Ag forms the *p*-type CSPC that we want to characterize. To study the effect of injection, the samples were designed to be illuminated from the non-metallized side of the wafer, where an a-Si:H(i) passivation layer was deposited to allow high level of injection. Additionally, an SiN_x layer was also placed as anti-reflective coating on this side to match closer the illumination conditions of the solar cell, without affecting the current flow. The TLM samples were annealed in air at 210 °C for 30 min to mimic the effect of the screen-printing annealing. They were then cleaved as close as possible to the

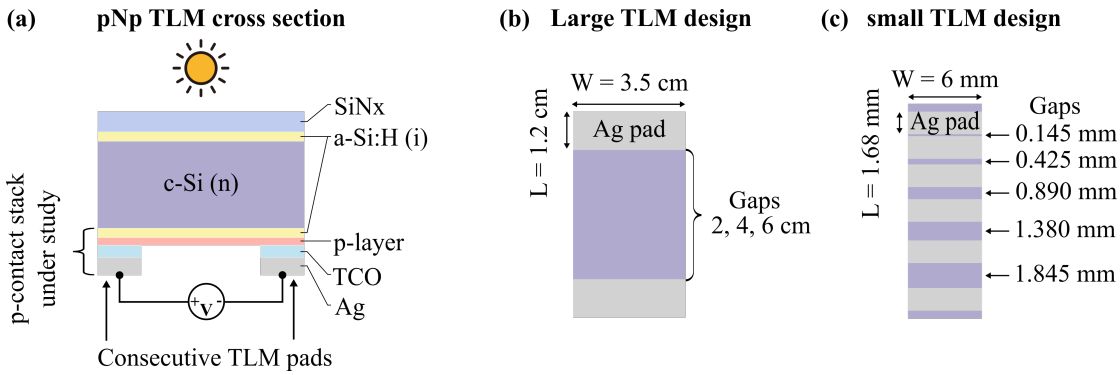

Figure 5.1: (a) Cross section of the experimental pNp *TLM samples, (b) top view showing the large TLM pads design used to study the transport phenomena in* pNp *architecture, and (c) top view of the small TLM sample design used to extract contact resistivity (note the change of units for the scale). Texture is omitted for simplicity.*

pad edges to realize mesa-isolation and avoid current flowing on a larger area than the pad width. The actual distances between each set of pads were measured for each sample with an optical microscope to take into account the eventual TCO/Ag deposition spreading below the mask.

The only difference between the large and small TLM designs is the different shadow mask defining the TCO/Ag pads. The large TLM samples, were processed to investigate further the carrier transport properties inside the c-Si(n) bulk of the p/N TLM architecture (see Figure 5.1(b)). The injection level as a function of illumination in those large samples was characterized using a WCT-120 photoconductance decay (PCD) tester [Sinton 1996] in the middle of the gap. Photoluminescence (PL) images were acquired using an 808 nm laser to illuminate the samples and a CCD camera coupled with a filter that eliminates the signal from the light source [Trupke 2007].

The resistance between each pad was measured at various illuminations between 0.54% to 100% of one sun. For the TLM-analysis, the wafer sheet resistance was computed as the slope of the equation $R_{s,tot}^{TLM}(G) = R_{sh}^{cSi} G/W + 2R_c$, where W is the pad width, G is the pad distance and R_c is the contact resistance. Note that for the large TLM samples, the contact resistance will have only negligible contribution to the total measured resistance, which is dominated by the wafer resistance. Finally, we calculated Δn from the sheet resistance by inverting the relations $R_{sh}^{h} = 1/(q\mu_h(p)pt)$, $R_{sh}^{e} = 1/(q\mu_e(n)nt)$ or $R_{sh}^{eh} = 1/(q\mu_e(n)nt + q\mu_h(p)pt)$, where n and p are the electron and hole concentrations and the mobilities are calculated using Masetti's formula for the carrier concentration dependent mobility [Masetti 1983].

5.2.3 Results and Discussion: Transport in Large TLM Sample

As a first qualitative element of discussion about the role of illumination on the gap and the contacts, Figure 5.2 presents the *I-V* curves of a 4 cm-gap large TLM sample under various

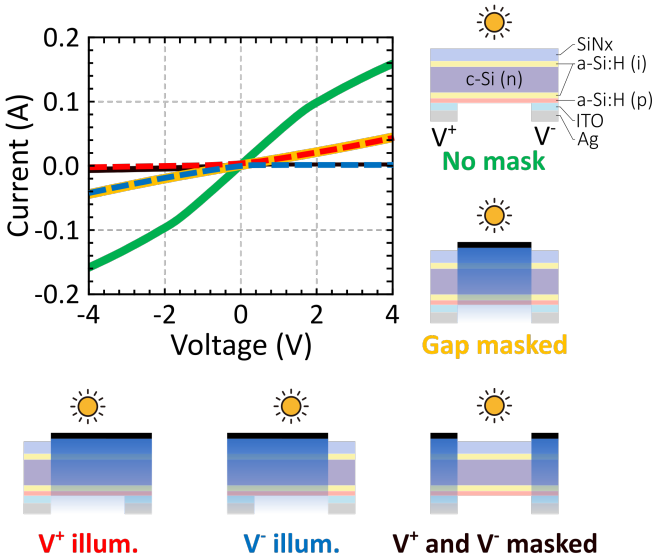

Figure 5.2: I-V *curves of the large TLM samples with a gap of* 4 cm *under uniform illumination (No Mask), masking only the gap (Gap masked), illuminating only the positive (V^+ illum.) or negative (V^- illum.) pole, respectively, and finally with the two contact pads masked (V^+ and V^- masked). Note that for this last case, no current is flowing and the* I-V *curve is hidden behind the others (dark curve).*

conditions of masking under 1 Sun. First, under uniform illumination, we observe that a current can flow in those *pNp* structure with a linear regime around 0 V (green curve), as obtained for small TLM design in [Senaud 2021a, Basset 2021]. Second, when the gap between the two pads is masked (orange curve), current can still flow in the gap, showing that even in the absence of photo-generated charges (sample much longer than the diffusion length) the lateral transport can occur inside the c-Si(n) wafer. We will see later that it is indeed the electron that travels through the wafer and not the holes. Then, masking the area under both pads while keeping the gap illuminated, we observe that no current can flow (black curve). This puts in evidence that the two p-n junctions present below both pads in the dark are facing each other along the current path and thus block the current flow. Finally, when at least one of the contacts is illuminated, a current can flow only either in forward or reverse bias. This can be explained again by the blocking p-n junction present below one of the two pads, blocking the current only in one direction, while the illuminated pad behaves like a resistance. Moreover, those two cases (red and blue curves) combined together are superposed with the masked gap case (orange curve), which stems from a similar bulk resistivity since the total resistance is dominated by the c-Si(n) sheet resistance in those large TLM samples.

Going one step further, Table 5.1 gives the R_{sh} values obtained by measuring under illumination the 2 cm, 4 cm and 6 cm gap TLM samples. For these peculiar large TLM samples, in the case of a uniform illumination, the injection corresponding to this illumination level at open circuit can be obtained from a PCD measurement directly on those samples thanks to the gaps which are larger than the measurement coil. From these measurements, it is observed on

	No Mask		Gap Masked
Illumination (%)	**Δn (cm^{-3})**	**R_{sh} (Ω/sq)**	**R_{sh} (Ω/sq)**
100	1.17×10^{16}	22 (13-29)	110 (100-118)
45.4	8.02×10^{15}	30 (19-40)	110 (99-120)
6.5	2.42×10^{15}	54 (46-60)	114.6 (100-127)
1.7	7.4×10^{14}	102 (82-120)	non-ohmic

Table 5.1: R_{sh} values extracted from the large TLM samples under uniform illumination (No Mask) and with the gap masked (Gap Masked) as presented in Figure 5.2. In the dark, the base doping provides a R_{sh} of 120-125 Ω/sq. For uniform illumination, the injection level Δn at a given illumination is extracted from PCD measurement directly on the finished sample. The numbers in parenthesis give an estimation of the error of on the data.

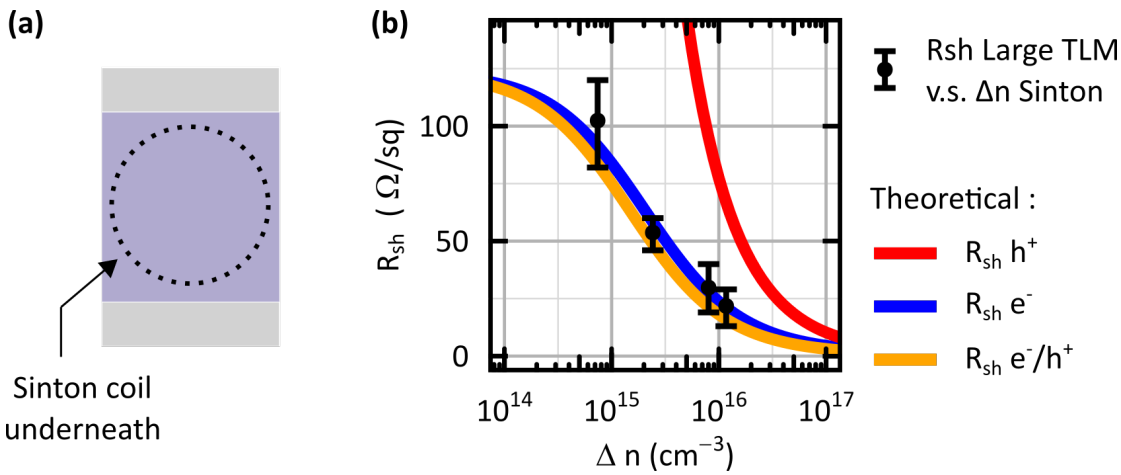

Figure 5.3: R_{sh} as function of injection level (Δn) measured on the large TLM samples and compared to the R_{sh} calculated considering only electron conductivity (R_{sh} e^-), only hole conductivity (R_{sh} h^+), or the sum of both, respectively, R_{sh} e^-/h^+.

Figure 5.3 that the experimental curve of R_{sh} as a function of the injection level (Δn) matches with the theoretical values obtained considering only electrons in the transport rather than considering holes transport inside the c-Si(n). Finally, in Table 5.1 when the gap is masked, the R_{sh} remains constant for all illuminations and corresponds within the error bounds to the R_{sh} of the electrons provided by the base doping of the c-Si(n) wafer.

In summary, despite the presence of two p-type CSPCs allowing only holes to flow through them, we demonstrated that electrons are effectively carrying the current for the lateral transport inside the c-Si(n) wafer. Taking into account the fact that the forward biased contact needs to be illuminated for current to flow, we can formulate the following mechanisms to describe the electrical transport in those samples: First, electron-hole pairs are photo-generated in the c-Si below the first pad, through which holes can be extracted. Holes can also be injected through the second pad into the c-Si wafer. To close the circuit, the photogenerated electrons

travel through the bulk to recombine with the holes below the second pad. Generation and recombination thus occur at spatially separated places.

To observe this mechanism experimentally, a PL setup was adapted in order to illuminate only one contact pad, similarly to how we proceeded for the previous *I-V* measurements presented on Figure 5.2 (red case), while being able to measure the radiative part of the recombination occurring under the second pad. Figure 5.4a presents the modified PL setup together with the physical mechanisms described above on Figure 5.4b. Figure 5.4d presents the corresponding PL images taken with masking (V+ illum) or without masking (No Mask) and at different bias conditions. First, the PL image without masking at 0 V shows that it is possible to distinguish optically the contact pads since they are not optimized for infrared reflection (115 nm TCO / Ag stack). This makes it possible to align correctly our PL laser to illuminate only the positive pad. Then increasing the voltage, a lower PL signal at the left pad is observed, starting from the contact edge, while the signal increases on the right pad. This reveals that recombination mechanisms occur under the second pad, even though it was not illuminated. The absence of recombination in the c-Si(n) bulk when using a mask shows that no minority carrier diffuses there, which leaves the electrons as the only carrier type responsible for the transport in this region. They eventually recombine with holes injected from the external circuit under the second pad, starting probably within a diffusion length of the contact as we will discussed more precisely in the next section.

In summary, we observed low R_{sh} under illumination in TLM samples featuring p-type CSPC deposited on c-Si(n) wafer. Then, we gave a physical explanation to this situation, accounting that the lateral transport is supported by the electrons in these devices. Finally, we provided two experimental proofs to this theory, i.e. that the R_{sh} behavior as a function of injection (Figure 5.3) behaves as the one of electrons, and that electron transport in the bulk in the presence of two p-type CSPCs deposited on n-type c-Si bulk can only be mediated thanks to photogeneration under one pad and recombination under the other (Figure 5.4).

5.2.4 Results and Discussion: Transport below the diffusion length

To extract the contact resistivity with precision, shorter pad distances should be used, typically below 1 mm to minimize the resistive contribution of the wafer. However, below this distance at the lowest illuminations, we also observed a much higher sheet resistance between the pads as can be seen on Figure 5.5a, which indicates that other transport phenomena are at stake with those smaller samples. We can explain this comparing those distances with the diffusion length of holes $L_{D,h}$, which is typically in the range of 1–3 mm for lifetimes of 1–10 ms. When the pad distance starts to become smaller than $L_{D,h}$, holes can diffuse from one contact to the other without recombining and support a larger share of the transport, thus increasing the measured R_{sh}. To further investigate this phenomenon, we performed PC1D simulations in Figure 5.5b, where a uniformly illuminated c-Si(n) is sandwiched between two p-type contacts. We modified $L_{D,h}$ by changing the bulk lifetime τ of the c-Si(n) while increasing

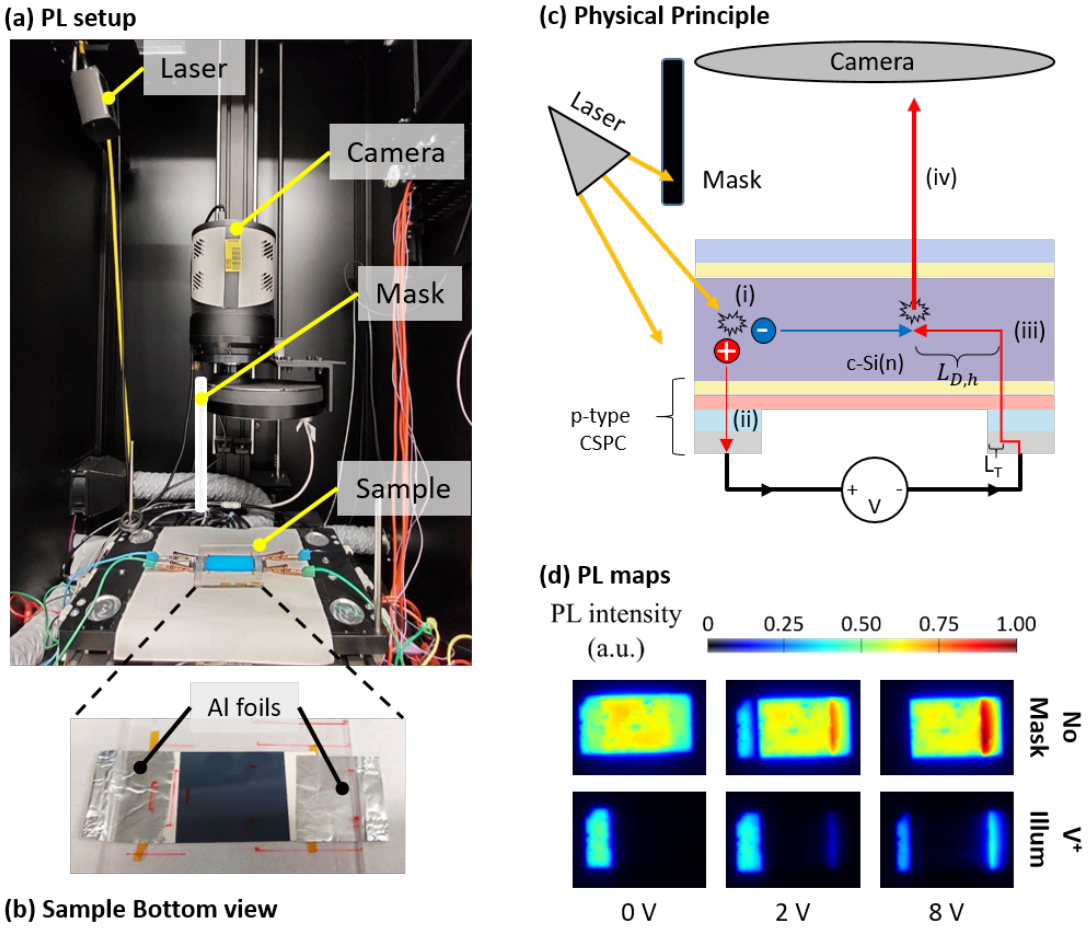

*Figure 5.4: (a) PL setup modified with a mask allowing to illuminate only the left pad of the sample. (b) Bottom view of the sample. The sample is taped to a glass and contacting is made using aluminum foils. (c) Physical principle allowing electrons to flow in between the two p-type CSPCs in p/N TLM samples under illumination, thanks to the (i) e^- / h^+ photo-generation under the positive pad, (ii) holes extraction through the external circuit, and (iv) the e^- / h^+ radiative recombination. In (iii), the holes travel back in the circuit up to their diffusion length, increasing the sheet resistance of the device due to their lower mobility. (d) Corresponding PL images taken at 1 Sun and three different external voltages without mask or with only the left pad illuminated. The pads can be distinguished optically since they are not optimized for infrared reflection (*115 nm *TCO/Ag).*

the illumination level to keep a constant injection level. We see that for large TLM, the total current is mainly driven by the electron current density, while for small gaps it is mostly a current of holes. We see also see that as τ goes from 0.1 ms to 1 ms, increasing thus $L_{D,h}$ from about 0.3 mm to 1 mm, the hole current density increases relatively with respect to the one of electrons up to a distance of $L_{D,h}$ from the edges. For large TLM samples, this does not affect much the transport and electrons are the main carriers transporting current in the device. For smaller TLM however, the impact of τ is more pronounced. Therefore, extracting the injection

directly from the measurement of R_{sh} on short *pNp* TLM samples becomes more challenging as we need to model the transport of both electrons and holes in the wafer. However, we see that if we consider TLM gaps smaller than ≡ 1 mm and lifetime higher than 1 ms, holes are the main carriers for the transport and inverting the relation $R_{sh}^{h^+}(\Delta n)$ should allow to compute the injection level in those devices.

Finally, let us note that on Figure 5.5a, for the highest illuminations there is less difference of slope below and above 1 mm, and the sheet resistance remains quite low. This could stem from the fact that at higher illumination the lifetime decreases, e.g. due to Auger recombination, which would lower the diffusion length of holes and allow a better transport by electrons. This would require dedicated computations to be verified though. E.g. the presence of cleaved edges on the side of the TLM could prevent the injection to reach values high enough to be Auger limited.

5.2.5 Conclusion

We studied in depth the transport in TLM device under illumination for the case of *p*-type contact on a *n*-type wafer. For very large pad distances, electrons are carrying the lateral transport in the c-Si(n). We evidenced this by measuring the sheet resistance as a function of injection using gaps larger than 2 cm, found agreement with the calculated sheet resistance of electrons, and suggested and validated a mechanisms explaining this phenomenon. Therefore, it is possible to extract the injection from the sheet resistance in large TLM samples by inverting the relation $R_{sh}^{e^-}(\Delta n)$. For smaller TLM samples, with electrode distance below 1 mm, the hole current becomes more important as the gap becomes smaller than their diffusion length, and therefore the sheet resistance should theoretically tend to $R_{sh}^{h^+}(\Delta n)$. Finally, the illuminated *pNp* structure under study here is closely related to bipolar photo-transistors (however, with a very thick base), and therefore these results could find application in this field as well.

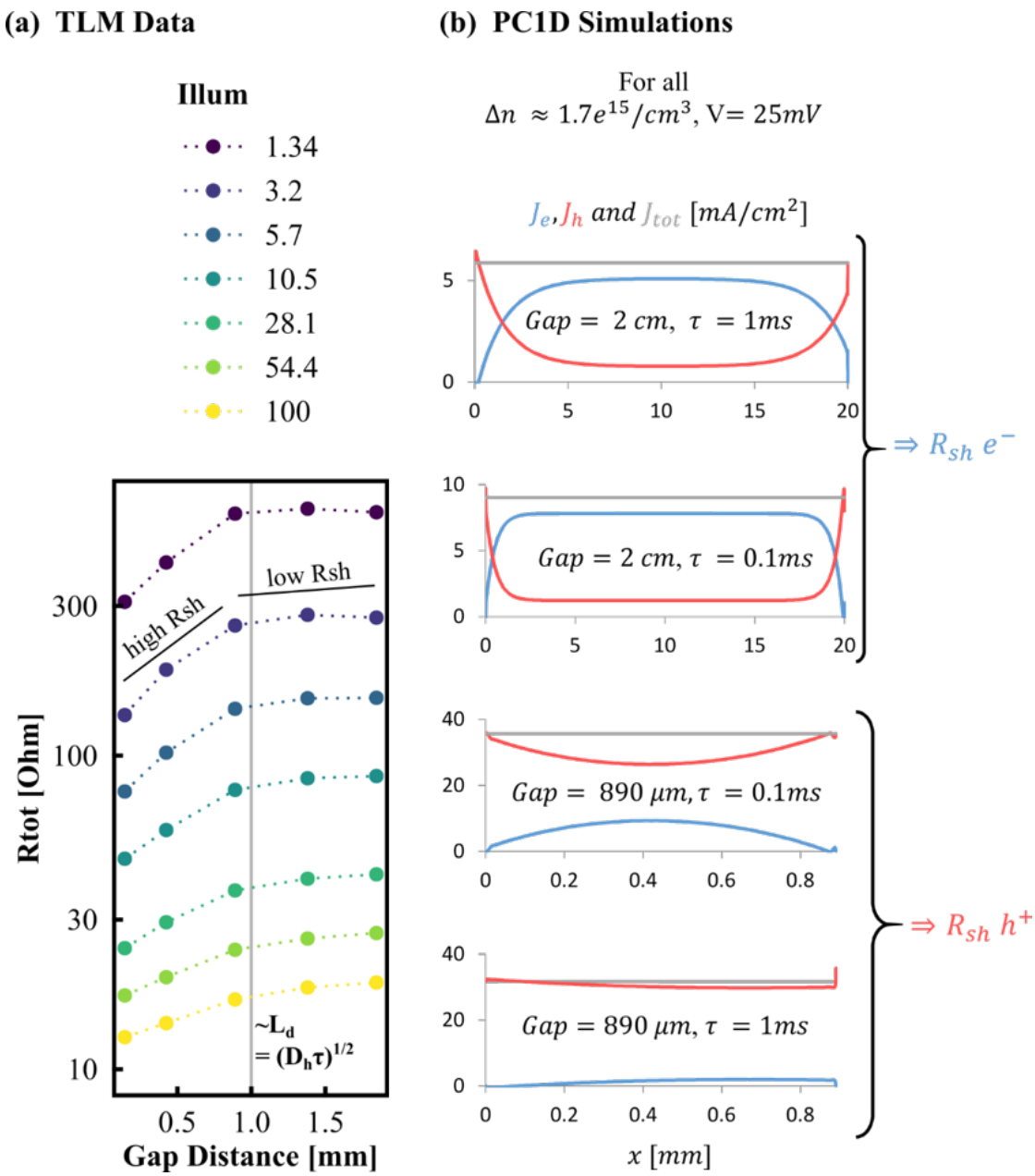

Figure 5.5: (a) Total resistance as a function of gap distance, measured in pNp *small TLM design under illumination. (b) PC1D simulation of the electrons, holes and total current density (J_e, J_h, and J_{tot}, respectively) in device of length* 2 cm *(large TLM) and* 890 µm *(small TLM). In the simulation, the lifetime τ is reduced to decrease the diffusion length, while the illumination is increased to keep the injection level constant to $\Delta n \approx 1.7 \times 10^{15}\,\mathrm{cm}^{-3}$. The applied bias is the same in every simulation (*25 mV*).*

.

5.3 Comparison of TLM and Symmetric Samples for Accurate Series Resistance Breakdown

5.3.1 Abstract

In this section, we use several approaches to perform accurate series resistance (R_s) breakdown of a state of the art $2 \times 2\,cm^2$ screen-printed solar cell reaching 82.5% *FF*. On the one hand, Haschke et al.'s model for the lateral transport through the cell, coupling the TCO and wafer sheet resistances through the contact resistivity (ρ_c), predicts a reduction of R_s with increasing injection (Δn) through the enhanced wafer conductivity [Haschke 2020]. In contrast, we observe that the R_s of the solar cell, obtained from the difference between the *J-V* and J_{sc}-V_{oc} curves, increases with Δn. Similarly, Senaud et al. observed increasing ρ_c with Δn using TLM measurements under illumination [Senaud 2021a, Senaud 2021b]. To investigate the discrepancy between these experimental observations and theoretical expectations, we extract ρ_c values either from dark TLM, illuminated TLM or illuminated symmetrical sample measurements and incorporate them into Haschke et al.'s model to reconstruct the R_s of the solar cell. Detailed series resistance breakdown using ρ_c values from all three tested methods show accurate R_s predictions within $\pm\,0.1\,\Omega\,cm^2$ at MPP, showing that the different approaches have sufficient accuracy to estimate the resistive losses in the solar cell under study. Regarding dependence upon injection, it was only possible to predict an increasing series-resistance trend using contact resistivity from illuminated TLM, therefore matching closer the measured linear increase of the R_s of the solar cell from MPP to open circuit conditions, while the other methods predicted a decreasing trend. We discuss practical differences between the methods and propose possible improvements.

5.3.2 Introduction

For a silicon heterojunction (SHJ) solar cell to reach high efficiency, transport through the absorber, the hole- and electron-selective contacts, transparent conductive oxide (TCO) and metallic grid should occur with minimal losses. SHJ cell can achieve excellent transport properties, as shown by the high reported fill factors (*FF*) up to 86.6% (grid-touch measurement) on a $274.3\,cm^2$ device by *LONGi* [Pv-magazine 2021a] to cite record efficiencies on double side contacted n-type wafer. In chapter 4, we achieved a certified *FF* of 82.2% on a $4.06\,cm^2$ screen-printed solar cell in front-junction configuration using p-type nanocrystalline hydrogenated silicon (nc-Si:H(p)) as window layer and discussed the possibility to achieve an even higher FF of 83% using BF_3 as dopant gas precursor in the p-layer. It is therefore of interest to perform an accurate breakdown of the remaining transport losses and discuss in particular whether and where some gains are still achievable on the total series resistance (R_s).

Recently, *Haschke et al.* proposed a transport model taking into account the modification of the lateral transport by the change of conductivity of the wafer under illumination [Haschke 2020]. Based on this, a complete R_s breakdown of a monofacial front-junction solar cell based on a

n-type wafer with full-area Ag blanket on the backside is given by

$$R_s(\Delta n) = R_s^{lat+C}\left(R_{sh,h^+}^{cSi}(\Delta n), R_{sh}^{TCO}, \rho_c^{front}\right) + R_s^f + R_{s,e^-}^{vert,cSi}(\Delta n) + \rho_c^{rear}, \tag{5.1}$$

where the effective series resistance R_s^{lat+C} is a function of the coupling of the sheet resistance of holes in the wafer and TCO sheet resistance (R_{sh,h^+}^{cSi} and R_{sh}^{TCO} resp.) together with the contact resistivity from the absorber to the front TCO (ρ_c^{front}), Δn is the injected carrier concentration of electrons and holes, R_s^f is the finger resistance, ρ_c^{rear} is the contact resistivity of the rear side, and finally $R_{s,e^-}^{vert,cSi}$ is the vertical resistance of the electrons moving towards the back contact. The latter is computed as

$$R_{s,e^-}^{vert,cSi}(\Delta n) = \frac{t}{q\mu_e(N_D + \Delta n) \times (N_D + \Delta n)} \tag{5.2}$$

where t is the wafer thickness, N_D is the donor density and μ_e is the injection dependant electron mobility, which can be calculated using Masetti's or Klaasen's formula [Masetti 1983, Klaassen 1992]. Note that this equation assumes that all the electrons are generated close to the front surface and move straight in direction of the rear contact, while the holes do not need to travel vertically. It can be indeed verified that more than 2/3 of the photogeneration occurs in the first 10 µm close to the front surface. Nevertheless, in reality both charge carriers have to move vertically and there is a whole variety of possible paths for them to reach their respective contacts. A schematic representation of the parameters of the model is shown in Figure 5.6.

Haschke et al. already showed this analysis to be relevant for the comparison of state-of-the-art a-Si(p) and nc-Si(p) layers incorporated in devices [Haschke 2020]. However, they considered the contact resistivities constant with the injection, whereas *Senaud et al.* observed dependence of ρ_c with Δn for n-layers on an n-type wafer ("*nNn*" samples) [Senaud 2021b] as well as in the case of p-layers on p-type or n-type wafers ("*pPp*" or "*pNp*" samples respectively) [Senaud 2021a]. Moreover, similar observations were reported by another institution [Basset 2021]. Nevertheless, both of them concluded that additional efforts would be required to fully understand the behavior of *pNp* samples under illumination. Therefore, it is of interest to obtain the ρ_c of both n- and p-contacts under illumination and include them into *Haschke et al.*'s transport model to check if this enables a better reproduction of the solar cell series resistance.

In this work, we use several approaches to perform accurate R_s breakdown of a state-of-the-art $2 \times 2\,\text{cm}^2$ screen-printed front-junction solar cell reaching 82.5% *FF*. To clarify the role of the different components under injection, we incorporate into Haschke et al.'s model ρ_c values extracted from dark and illuminated TLM and compare results obtained for p-layers on p- and n-type wafers. Moreover, since TLM-sample fabrication requires patterning of the TCO and silver as well as precise cutting of the sample, we compare the results with those obtained from vertical symmetrical $2 \times 2\,\text{cm}^2$ structures, which share a more similar process with the solar cell preparation.

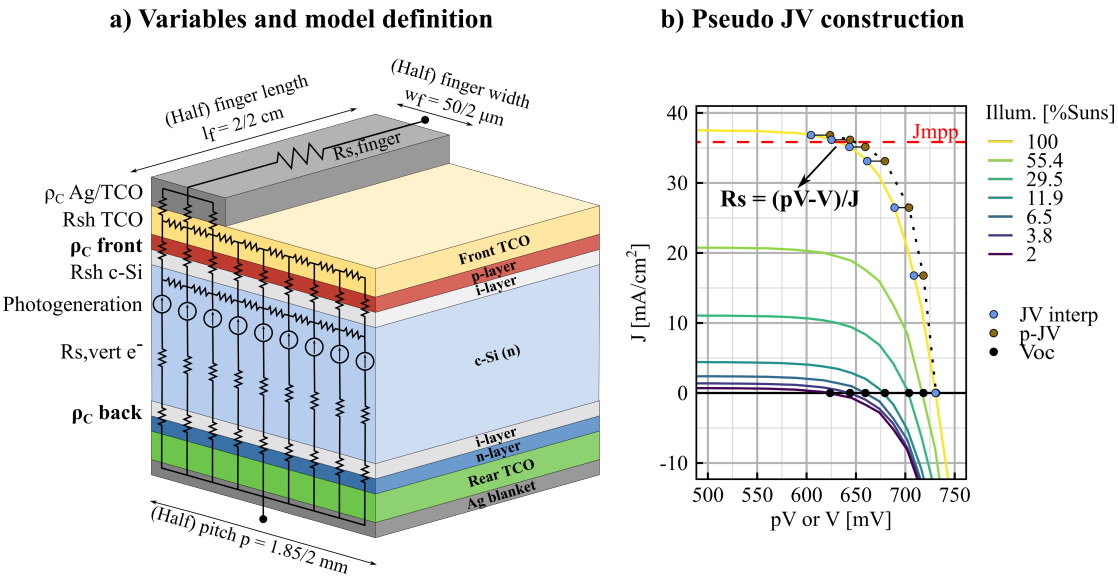

Figure 5.6: a) Schematic representation of a half pitch of the solar cell structure considered in this study, overlaid with the elements of the series-resistance breakdown considered. For the holes, the transport at the front follows the coupled lateral transport model of Haschke et al. For the electrons, lateral transport can be neglected thanks to the full area Ag blanket and only the vertical resistance ($R^{e^-}_{s,vert}$) and rear-contact resistivity (ρ_c^{rear}) are taken into account. b) Pseudo JV curve construction for the series resistance calculation following Bowden's method [Bowden 2001]. The red dashed line indicates the position of J_{mpp} *and the closest data point to this line is taken to compute the series resistance at MPP.*

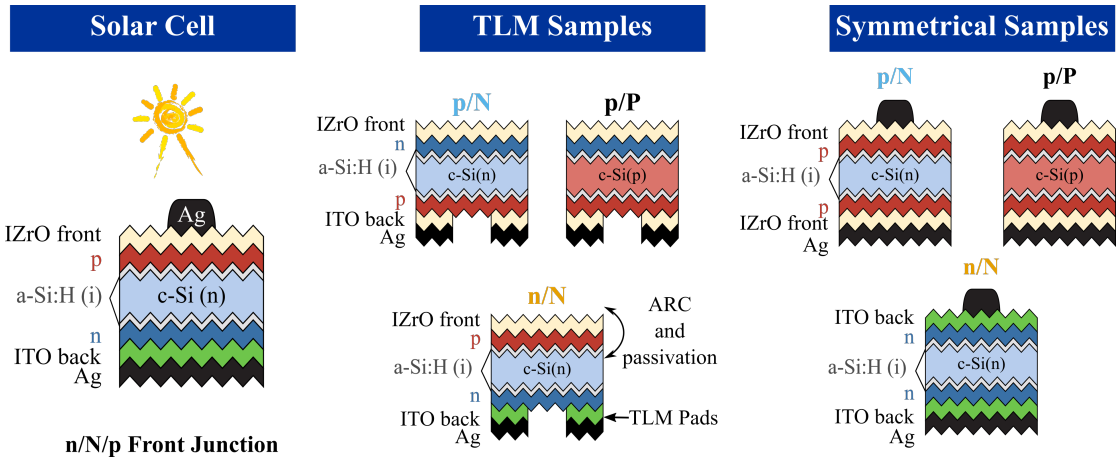

Figure 5.7: Sketches of the samples studied here. All samples are illuminated from the top during measurements.

5.3.3 Experimental details and method

All the structures described in Figure 5.7 are based on 2 Ω cm, n-type or p-type FZ c-Si textured wafers of thickness of $t = (195 \pm 10)\,\mu$m. A $2 \times 2\,\text{cm}^2$ screen-printed solar cell in front-junction configuration was fabricated as described in chapter 4, with in particular a nc-Si:H(p) layer doped with 50 sccm of BF_3 on the front side and an indium zirconium oxide TCO as this configuration showed to yield *FF* up to 83%. The TLM structures feature the same PECVD carrier selective layer stacks as the solar cell (co-deposited) under the pads. On top of those stacks, TCO (co-deposited with the solar cell) and Ag were sputtered through a shadow mask to form the pads. To study the effect of injection, TLM samples were designed to be illuminated from the non-metallized side of the wafer, where an a-Si:H(i) passivation layer was deposited. Additional p- or n-type layer and a IZrO layer were also placed as anti-reflective coating on this side to match closer the illumination conditions of the solar cell, the n- or p-doped layer blocking the holes / electrons respectively to reach the IZrO. The symmetrical samples are $2 \times 2\,\text{cm}^2$ structures using the same TCO patterning and screen-printed front grid as the solar cell. Their front-side was co-processed with the solar cell, while their rear-side layers were deposited in a second run. The TLM samples were annealed in air at 210 °C for 30 min to mimic the effect of the screen-printing annealing. They were then cleaved as close as possible to the pad edges to realize mesa-isolation. The actual distances between each set of pads were measured for each sample with an optical microscope to take into account the eventual TCO/Ag deposition spreading below the mask.

The solar cell R_s was computed using Bowden's method as described in section 2.3.4: the open circuit voltage (V_{oc}) and short-circuit current (J_{sc}) are measured at one sun and at lower illuminations (shaded). The obtained V_{oc} are then shifted by the difference ($J_{SC}^{1sun} - J_{SC}^{shaded}$) to construct the pseudo J-V curve (pJ-V), as shown in Figure 5.6. By construction, the pJ-V curve corresponds to the J-V curve for a same level of internal injection Δn without series-resistance losses and therefore R_s can be computed at each injection level as $R_s = (pV(J) - V(J))/J$.

Moreover, assuming no selectivity losses, the pseudo-voltage is equal to the implied voltage and the injection can be computed using the following equation (see section 2.3.4)

$$\Delta n = \sqrt{\frac{(n_0 - p_0)^2}{4} + n_0 p_0 \exp\frac{iV}{k_B T} - n_0 p_0} - \frac{n_0 + p_0}{2}, \tag{5.3}$$

where $n_0 \approx N_D$, $p_0 \approx n_i^2/n_0$ and n_i and N_D are the intrinsic and donor carrier concentration respectively. Using those relations, it is therefore possible to relate every series resistance to an injection value and construct the curves $R_s(\Delta n)$ or $R_s(pV)$.

The R_{sh}^{TCO} were measured using a four point-probe tool, and was 90 Ω/sq for the front IZrO and 75 Ω/sq for the rear ITO. The series-resistance contribution of the fingers was evaluated to be $(0.12 \pm 0.01)\,\Omega\,\mathrm{cm}^2$ by measuring the line resistance R_{line}^f of the finger over the whole batch of devices, and inserting it in the formula $R_s^f = \frac{1}{3} p (\frac{l_f}{2})^2 R_{line}^f$, where $p = 1.85$ mm is the pitch of the grid and $l_f = 2$ cm is the length of the screen-printed fingers.

For the TLM-sample analysis, gap distances of 145, 425 and 890 µm were considered. This choice is motivated by the fact that below 1 mm, the total resistance remains linear as a function of gap distance for *pNp* samples and the transport in the wafer should be in theory sustained by holes as explained in section 5.2.4. The wafer sheet resistance was computed as the slope A in the linear equation $R_{s,tot}^{TLM}(L) = R_{sh}^{cSi} \frac{L}{W} + 2R_c = A \times L + B$, where W is the pad width, L is the pad distance and $R_c = B/2$ is the contact resistance and B is the y-axis crosses. The transfer length L_T was calculated as $L_T = \frac{B}{2A} = R_c W / R_{sh}^{cSi}$. The contact resistivity was then computed using the formula $\rho_c = R_c L_T W = W \times \frac{B^2}{4A}$, where $L_T \times W$ is the contact area through which the current flows. Finally, we calculated Δn from the sheet resistance by inverting the relations $R_{sh}^{holes} = (q\mu_h(p)pt)^{-1}$ or $R_{sh}^{electrons} = (q\mu_e(n)nt)^{-1}$, where n and p are the electron and hole concentrations and the mobilities are calculated using Masetti's formula for the carrier concentration dependent mobility [Masetti 1983].

For the symmetrical-sample analysis, the total resistances of the devices were measured. Then, since there is no direct way to measure the injection on those samples during the resistance measurement, we calculated Δn for a given illumination using photoconductance decay (PCD) data of the precursor of the samples after PECVD layers deposition. Finally, $\rho_c(\Delta n)$ was fitted to the equation

$$R_s^{Symm}(\Delta n) = R_s^{lat+C}\left(R_{sh,e^-/h^+}^{cSi}(\Delta n), R_{sh}^{TCO}, \rho_c(\Delta n)\right) + R_s^f + R_{s,e^-/h^+}^{vert,cSi}(\Delta n) + \rho_c(\Delta n), \tag{5.4}$$

which is similar to equation 5.1, except that it features the same contact resistivity at the front- and rear-side. The wafer sheet resistance and vertical resistance on the "*pPp*" and "*pNp*" samples are assumed to be the ones of holes, while for the "*nNn*" samples it is assumed to be the one of electrons. Note that for the *pNp* symmetrical samples, this hypothesis is in-line with our observation for thin TLM in section 5.2.4.

5.3.4 Results and discussion

Illuminated TLM

The analysis of the illuminated TLM samples is shown in Figure 5.8(a)-(c). First, looking at the sheet resistances, both "*pPp*" and "*nNn*" sample measurements give at low illumination the expected values from their base resistivity which then decrease upon injection thanks to the enhanced conductivity. Second, for the "*pNp*" sample, we observe that the sheet resistance is orders of magnitude higher in the dark, as would be expected for the transport of holes in an n-type wafer, and then decreases fast below 1000 Ω/sq. However, it is always lower than the sheet resistance computed from PCD measurement and it reaches at 1 sun a surprising low value of 23 Ω/sq, similar to the one of the "*nNn*" sample. This surprising observation was also made in [Senaud 2021a]. This low value of the sheet resistance could indicate that electrons start to sustain the current density in the bulk, as already described in section 5.2.4. As a comparison, the hole sheet-resistance computed from the PCD data on the "*pNp*" PECVD precursor sample reaches a value of 70 Ω/sq at 1 sun.

Second, we observe that for all the samples, the contact resistivity behaviour is quite similar upon illumination or injection. Our n-contact shows a small ρ_c of 20 mΩ cm^2 at low injection that increases close to 30 mΩ cm^2 at high injection. From the "*pPp*" sample, we obtained ρ_c as low as 75 mΩ cm^2 increasing to 115 mΩ cm^2 at high injection. Those magnitudes are consistent with previous literature results [Leilaeioun 2020]. The contact resistivity of our nc-Si:H(p)-based contact could be possibly lowered even more as it was the case for a-Si:H(p) by reducing the i-layer thickness [Leilaeioun 2017], or by using a TCO bi-layer with a lower oxygen content at the interface with the p-layer [Luderer 2021].

Finally, the contact resistivity evaluated from the "*pNp*" samples qualitatively decreases with injection but remains very high, with values ranging between 660 and 1110 mΩ cm^2 around injection conditions corresponding to MPP, which is too high to match with the > 82% *FF* obtained using this contact. To try to understand what could limit this approach, we can make the following arguments considering the sensitivity of the TLM to extract an accurate contact resistivity in the case of the "*pNp*" sample:

1. First, let us consider the problem of measuring a contact resistivity when the lateral resistance in the wafer is high: Considering Δn of 1×10^{15} cm^{-3} (MPP conditions), with the obtained ρ_c of 660 mΩ cm^2 and L_T of 0.035 cm and the pad width W of 6 mm, the contact resistance is $R_c = \rho_c/(WL_T) = 31\Omega$. In comparison, the hole sheet resistance is $R_{sh}^{h^+} \approx 1000\Omega/sq$, which yields a resistance of 24 Ω for transport inside the wafer with the smallest gap of 145 µm and 148 Ω for the gap of 890 µm. Therefore, the contact resistance accounts for more than half the total resistance for the smallest gap, while it is only 17% of the total resistance with the largest gap. Therefore, the latter can lead to large errors on the determination of ρ_c and the analysis would be more precise by considering smaller gaps only.

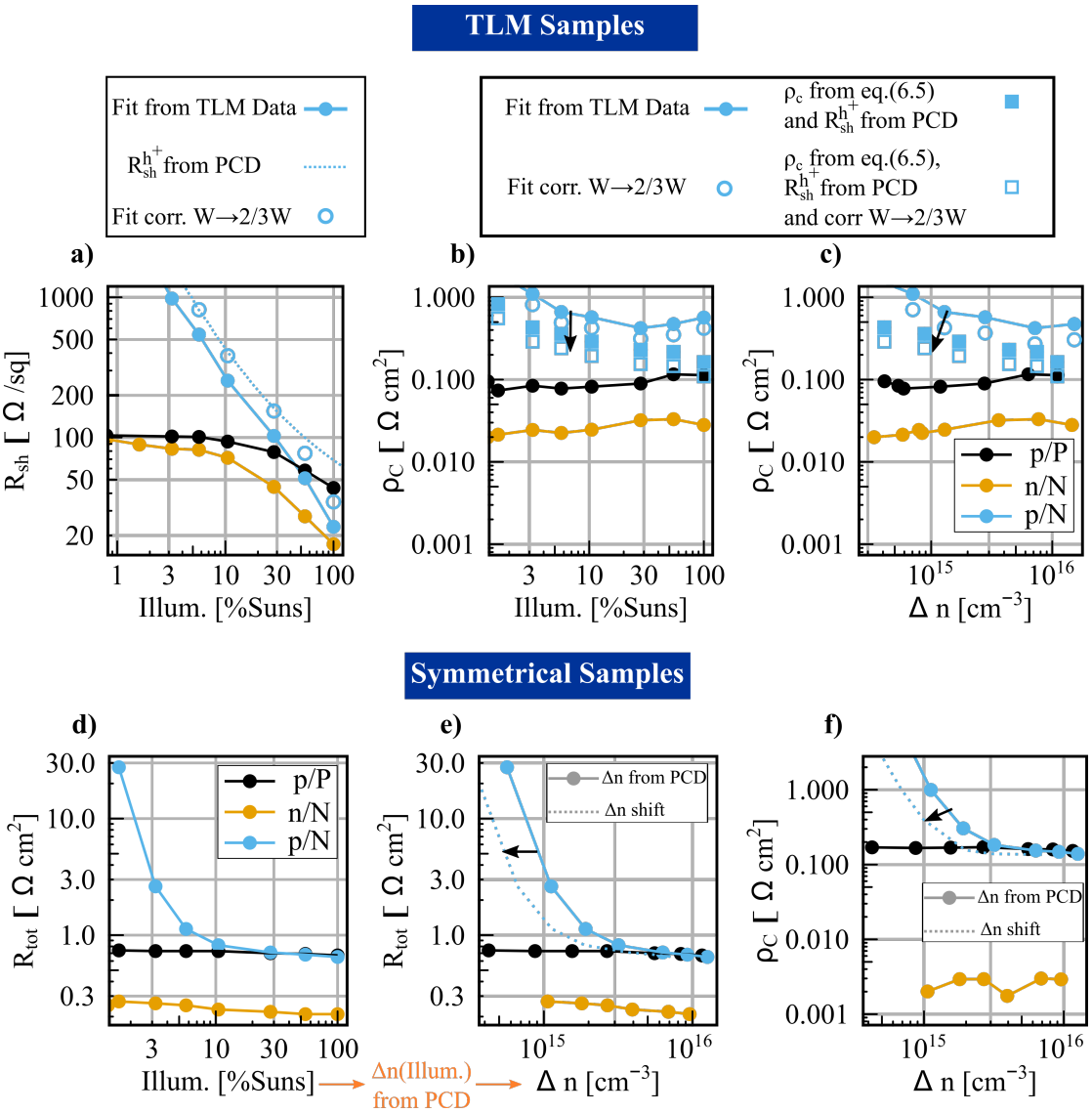

Figure 5.8: Analysis of the TLM and symmetrical samples under illumination for the three types of structures "pPp", "nNn" and "pNp". a) Sheet resistance vs. Illumination, b) contact resistivity vs. illumination and c) contact resistivity vs. the injection, where Δn *is extracted from sheet resistance of TLM samples.*
d) Total resistance vs. illumination, e) Total resistance vs. injection and, f) contact resistivity vs. injection for the symmetrical samples, where Δn *is extracted from PCD data from the sample precursor after PECVD deposition. In a), the dashed line is the computation of* $R_{sh}^{h^+}$ *from PCD data for those illumination. In a) and b), the open symbols correspond to the correction of the data when considering a reduced channel width* $2/3W$ *as depicted on Figure 5.9. In b), the square symbol corresponds to a calculation of* ρ_c *using eq. 5.5 for the first TLM gap of* 145 µm. *In e), the dotted line represents a possible shift of the total resistance as a function of injection for the "*pNp*" sample in the case of an overestimation of* Δn *as a function of illumination for that sample. In f), the dashed line is the corresponding correction of* ρ_c.

2. Second, we can consider the impact of the cleaved unpassivated edges of the TLM samples on the current flow. Due to the presence of defects on the edges (see Figure 5.9), the hole current could be restricted to a channel width $W_{channel} \approx \frac{2}{3}W$. As we can see on Figure 5.8a, after applying this correction to the experimental TLM data (open circles), we find a merges of $R_{sh}^{h^+}$ extracted from the TLM and PCD techniques for illumination below 30%. However, for higher illuminations, the TLM sheet resistance continues to decrease faster, indicating that electrons might also participate to the transport for those higher illuminations. To investigate this, measurements at higher illumination should be performed. Finally, the channel width correction alone also lowers slightly ρ_c (open circles), albeit not enough to reach plausible values. To investigate how the cleaved edges impact the *pNp* TLM data, samples with larger width should be investigated. In this case, it would be worth to consider screen-printed silver pads in order to minimize the voltage drop along the TLM pads [Basset 2021, Senaud 2021a].

3. Finally, let us question now the above-mentioned low sheet-resistance obtained from TLM and compare how it would impact ρ_c if in comparison the sheet resistance in the TLM sample was simply $R_{sh}^{h^+}$ obtained from PCD. Taking the TLM equations, ρ_c can be calculated for a given pad distance

$$\rho_c = \frac{W^2}{4R_{sh}^h}\left(R_{s,tot}^{TLM} - \frac{R_{sh}^h}{W}L\right)^2. \tag{5.5}$$

Considering the pad distance $L = 145\,\mu\text{m}$ and the R_{sh}^h from PCD data, we plotted this correction as filled square on Figure 5.8 (b) and (c). We see that at one sun, the ρ_c thus obtained is $160\,\text{m}\Omega\,\text{cm}^2$ which is a realistic value in comparison to the solar cell series resistance and is much closer to the results of the *pPp* TLM and symmetrical samples (see Figure 5.8 (f)). Indeed, we would expect that with $1 \times 10^{16}\,\text{cm}^{-3}$ carriers injected in the wafer, both n- and p-type wafers have a similar amount of electrons and holes and the result should be independent of the wafer type. Finally we see that if we also apply on top of that the correction for the channel width ($W \rightarrow \frac{2}{3}W$), ρ_c reduces even more and reaches a value about $250\,\text{m}\Omega\,\text{cm}^2$ at $\Delta n = 1 \times 10^{15}\,\text{cm}^{-3}$ and the concordance between the *pNp* and *pPp* samples at $1 \times 10^{16}\,\text{cm}^{-3}$ gets even better, with ρ_c reaching $115\,\text{m}\Omega\,\text{cm}^2$ as well.

While those arguments and corrections might be too simple to explain the complex phenomenon occurring in *pNp* TLM sample on the whole range of injection, it shows the sensitivity of the technique to possible errors in the input data, emphasizing that care should be taken when analyzing these. To go further in the modelling of those devices, the literature on phototransistors should be investigated, since the device we are investigating here is similar to a pNp bipolar transistor where the base (the c-Si(n) wafer) is illuminated and operated in the ohmic region before saturation [Sze 2006].

Illuminated Symmetrical Samples

The analysis of the illuminated symmetrical samples is shown in Figure 5.8 (d) to (f). Similarly to the trends shown by TLM samples, the n-contact transport losses are significantly lower than those of the p-contact as can be already seen by looking at the total resistance of the device. After computing the injection level thanks to PCD data and using Eq. (3) to extract the contact resistivity, we found that for *pPp* samples $\rho_c$varies from 165 mΩ cm^2 at $\Delta n = 10^{15}$ cm^{-3} and reduce towards 150 mΩ cm^2 at $\Delta n = 10^{16}$ cm^{-3}. While the magnitude is comparable to the one found in TLM, the trend with illumination is opposite. This could come from the fact that the total resistance decreases in *pPp* samples because of the lower sheet resistance and vertical resistance at higher illuminations. Therefore, it is possible that the extracted $\rho_c(\Delta n)$ trend is correlated with the decrease of $R_{sh}^{h^+}(\Delta n)$ and $R_{s,h^+}^{vert,c-Si}(\Delta n)$ when the fit is not perfect, hiding a potential increase of 50–150 mΩ cm^2 as observed with the TLM samples.

For the *nNn* samples, once again ρ_c is much lower than for p-contacts, however we found values almost one order of magnitude lower than with TLM analysis. This can be explained by the fact that the total resistance of the *nNn* device is already lower than 0.3 Ω cm^2, which is of the order of magnitude of the sum of TCO and fingers series resistance. An error of 0.02 Ω cm^2 on the contact resistivity is thus not surprising with symmetrical samples and the lower obtained results are not in contradiction with the values extracted from TLM. We note thus that symmetrical samples are limited in precision to measure a contact resistance lower than ≈ 100 mΩ cm^2.

Next, we observe that *pPp* and *pNp* samples behave similarly at high injection, which was observed for TLM samples only after applying multiple corrections to the data as stated above. This matches better the simple explanation that lowly doped n-type or p-type wafers would be similar at a carrier injection of 1×10^{16} cm^{-3} because they contain similar amount of holes and electrons. However, the total resistance increases significantly at lower illumination for the n-wafer, which can stem both from the potential increase of ρ_c as well as from the increase of the vertical resistance to holes at lower injection. However, we should note that in the case of using "p/N" symmetrical samples to evaluate ρ_c, the method can be sensitive to the evaluation of $R_{s,h^+}^{vert,cSi}$ through the correct assessment of Δn. Indeed, as Δn cannot be evaluated by measuring directly the symmetrical samples (like through the pseudo voltage for solar cell or the sheet resistance for TLM), we rely on the PCD measurement on the PECVD precursors of the samples. However, if *e.g.* the sputtering or screen-printing processes yield any degradation in passivation, we will be overestimating Δn for a given illumination. As an illustration, the dotted line in Figure 5.8 (e) and (f) represent the possible shift of the total resistance of the device versus Δn that would occur if the injection was lower by an arbitrary factor of 2 for each illumination. We see that the total resistance at $\Delta n = 10^{15}$ cm^{-3} is lowered by about 1000 mΩ cm^2, which in turn could lower the fitted ρ_c from 1000 mΩ cm^2 to 400 mΩ cm^2. Let us note also that perimeter losses could also act in a similar way [Schäfer 2019] to shift Δn, and that the technique could be improved by using no mask during the measurement and having fine busbars that do not significantly create shading at the front of the device. Alternatively, to

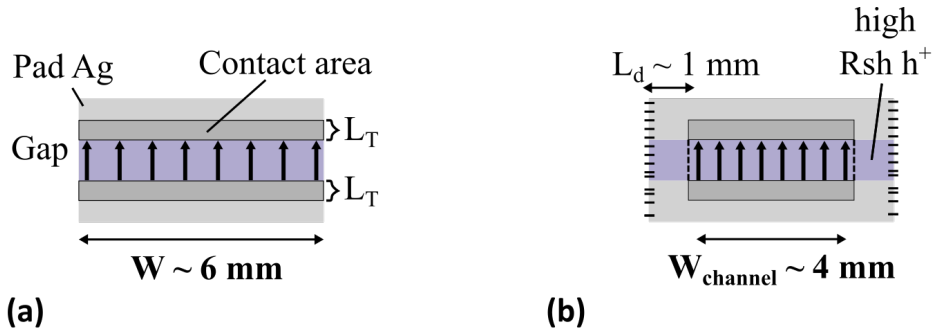

Figure 5.9: Possible edge effects in pNp *TLM Samples. (a) Ideal case without defects at the edges. The hole current can flow in the illuminated c-Si(n) using the hole width of the gap and then enter the contact over a length L_T. (b) Unpassivated edge case. Since the density of holes decreases rapidly within a distance L_d of the edges, $R_{sh}^{h^+}$ becomes very high in this region and the hole current is restricted to a smaller channel width $W_{channel}$.*

improve the method and analyse correctly the contact resistivity as a function of injection, a direct evaluation of the wafer conductivity after metallization should be included, e.g. with calibrated PL measurements.

5.3.5 Solar Cell Series Resistance Breakdown

The series resistance breakdowns of three solar cells are presented in Figure 5.10. R_s at MPP was 0.51 $\Omega\,cm^2$ for cells 1 and 2 and slightly lower for cell 3 with 0.39 $\Omega\,cm^2$. Notably, for all cells the series resistance increases with injection by almost 0.1 $\Omega\,cm^2$ from MPP towards open circuit condition. To discuss this increase, in Figure 5.10(a) we first perform a breakdown analysis assuming constant ρ_c evaluated from TLM measurements in the dark (named here "the classical breakdown" analysis). While a dashed line represents Haschke et al.'s model, we also include here the simpler model that assume that lateral transport occurs only in the TCO ($R_{s,lat}^{TCO} = \frac{1}{12} p^2 R_{sh}^{TCO}$) which allows to easily sum the different contributions of the series resistance. Both models reach a good agreement with the data at MPP, showing that the lateral transport occurs mainly through the TCO for this front junction architecture at this injection. However, none of those two models can predict the increase in R_s with injection if we input constant ρ_c^n and ρ_c^p values. This stems from the fact that these models only incorporate resistive terms decreasing with Δn, through the vertical resistance for the simpler model and additionally through the enhanced lateral transport in the wafer for *Haschke et al.*'s model. This reinforce our interest to investigate injection-dependant contact resistivity.

Regarding the breakdown carried out using the $\rho_c(\Delta)$ extracted from TLM samples (considering the *pPp* and *nNn* samples), we observe a similar agreement at MPP conditions with the classical breakdown. This stems simply from the fact that the contact resistivity at low injection is close to the one in the dark used in the previous analysis. In contrast, this second breakdown approaches better the R_s extracted from the solar cells thanks to the slightly increased values

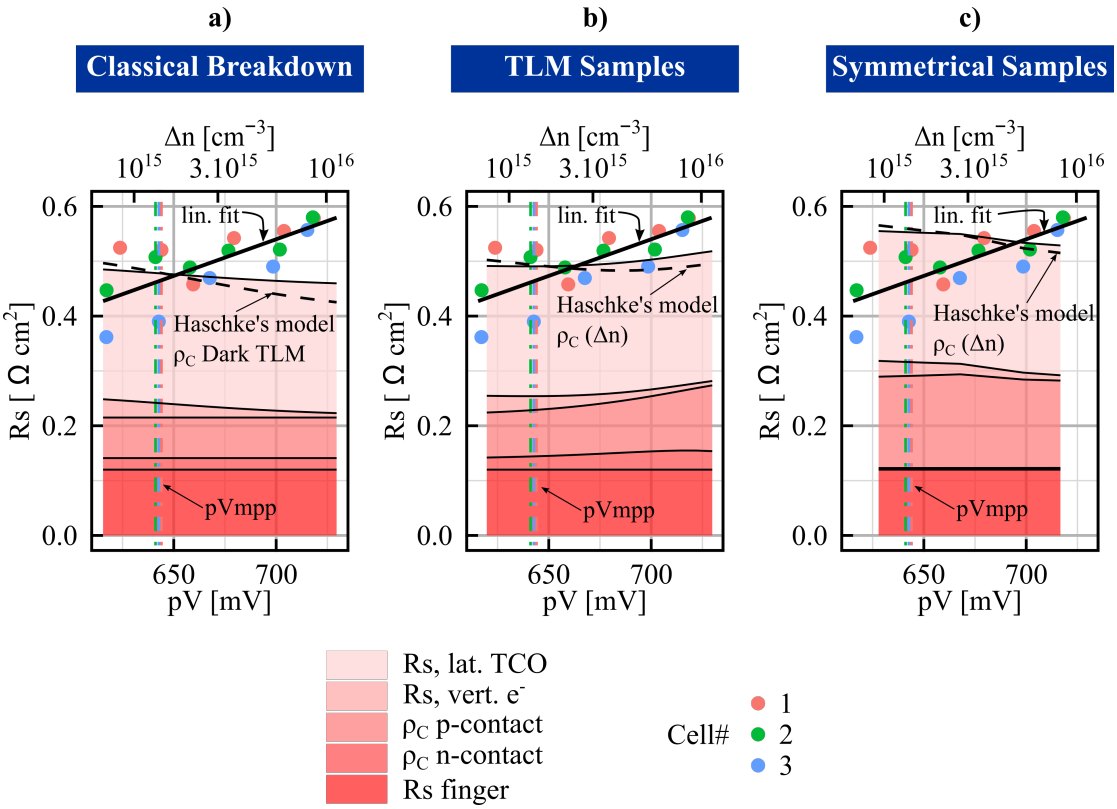

Figure 5.10: Solar cell series resistance breakdown: a) following classical method, using TLM measurement in the dark, b) using the injection dependent contact resistivity extracted from illuminated TLM, and c) from illuminated symmetrical samples respectively. The data points represent three co-processed solar cells, the vertical dashed line shows their, respective MPP around 642 mV, and the straight solid line is the linear fit of their series resistance as a function of pseudo-voltage / injection. The series resistance breakdown is represented in two ways in each graph: Either the lateral transport is assumed to happen only in the TCO and in this case the different elements of the series resistance (indicated by the areas of different colors) can be summed up. Or the lateral transport follows the model of [Haschke 2020] with the coupling of sheet resistance of the wafer, sheet resistance of the TCO and contact resistivity and the total resistance is shown with a dashed line. Note that in c) the ρ_c of the n-contact is lower than $0.01\,\Omega\,\mathrm{cm}^2$ *so that its line is superposed on top of the finger series resistance.*

of ρ_c at higher injection. However, the increase of ρ_c^p and ρ_c^n are not sufficient towards OC conditions where it falls short of $0.05\,\Omega\,\mathrm{cm}^2$, corresponding to about 10% of the total.

Finally, the breakdown carried out using the data from symmetrical samples (considering the *pPp* and *nNn* samples) overestimates slightly the series resistance at MPP due to the higher ρ_c value of the p-contact. It also predicts a reduction in R_s with injection, like the classical breakdown, enhanced by the slight decrease of the p-contact ρ_c, on the contrary to the experimental R_s data.

Note that we did not consider ρ_c^p values extracted from *pNp* TLM or symmetrical samples as they are decreasing with injection and would only lead to stronger misfit of the data. However, the ρ_c^p value measured of a *pNp* device realizing the same junction type as in the solar cell could well behave differently with injection than the one extracted from *pPp* devices and could possibly realize a better fit of the R_s data.

The discussion should also be complemented by investigating possible artefacts occurring during the extraction of the R_s data acquired using *Bowden*'s method as well as possible errors on the extraction of Δn if the assumption of perfect selectivity is broken.

5.3.6 Conclusion

We performed a series-resistance breakdown of an 82.5% *FF* SHJ solar cell. First, it was observed that the R_s obtained using *Bowden*'s method increases linearly with injection, which cannot be predicted by Haschke et al.'s transport model if we consider in this one constant contact resistivity. Series resistance breakdowns using ρ_c values extracted from dark TLM, illuminated TLM or illuminated symmetrical samples measurements showed accurate R_s prediction at MPP within $0.1\,\Omega\,\mathrm{cm}^2$, showing that all three methods have sufficient accuracy to analyze the specific contacts under study at MPP. We observe notably that nc-Si:H(p) layers based on BF_3 dopant gas [Antognini 2021] enable ρ_c^p values in the range of $100\,\mathrm{m}\Omega\,\mathrm{cm}^2$ at MPP and almost one order of magnitude lower for our baseline n-contact based on the stack 15-nm a-Si(n) / 15-nm nc-Si(n).

Regarding the dependence upon injection, the same trends as in [Senaud 2021a] were extracted from TLM samples for ρ_c^n and ρ_c^p. However, a different behaviour was obtained from symmetrical samples in comparison for the *pPp* structures, showing some discrepancies between the methods. This could come from the different artefacts that each method suffers from, making them not prone to determine with precision the injection dependant nature of the contact resistivity. For example, both for TLM and symmetrical samples the values of ρ_c^p extracted from *pNp* architecture reached too high values at injection of $\Delta n = 1 \times 10^{15}\,\mathrm{cm}^{-3}$ to enter the solar cell resistance breakdown.

The values from *pPp* and *nNn* samples could nevertheless be used to perform accurate R_s breakdown of our present solar cell featuring a full area front TCO, allowing to conclude that if the ρ_c^p effectively depends on Δn, this should yield variations below $100\,\mathrm{m}\Omega\,\mathrm{cm}^2$ between MPP

to OC conditions, and similarly for ρ_c^nWhile it does not significantly impact the R_s breakdown of our present solar cell, a change of only 10–20 mΩ cm^2, as reported from the TLM samples, could yield important losses of *FF* in solar cells using localized contact or thin TCOs. This can be seen on Figure 5.11 at R_{sh}^{TCO} above 1000 Ω/sq. Therefore, it remains of importance to clarify the question of the injection dependence of ρ_c.

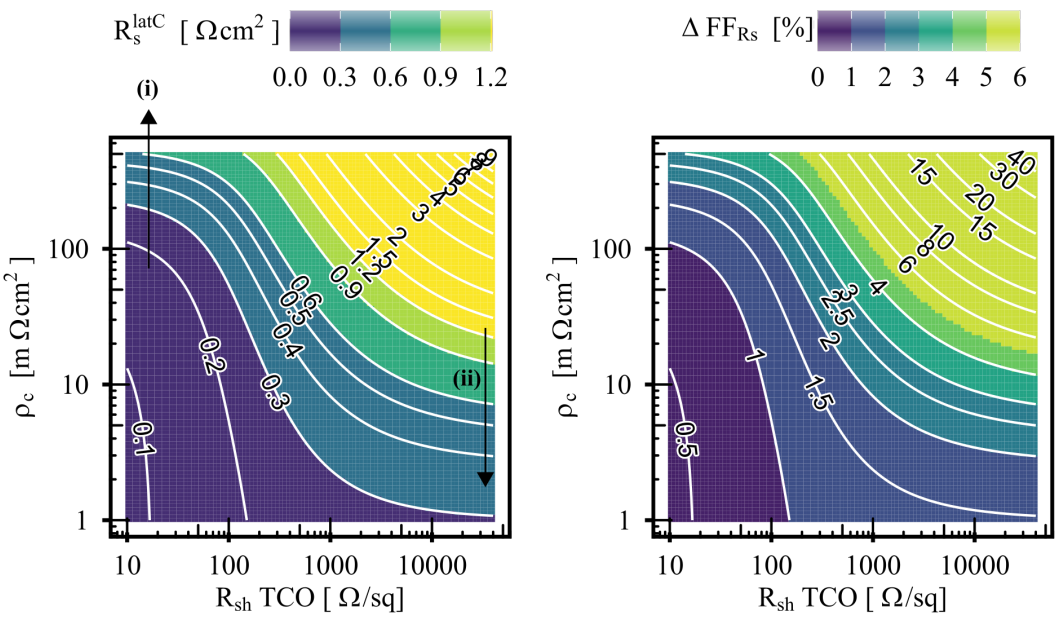

Figure 5.11: R_s^{latC} from Hasche et al.*'s model as function of ρ_c and R_{sh}^{TCO}. We set $R_{sh}^{cSi} = 65\,\Omega$, which corresponds to an implied voltage of* 650 mV *for a* 195 µm *wafer doped with $N_D = 2.2 \times 10^{15}\,\mathrm{cm}^{-3}$. The other parameters of the model were set to $\rho_c^{Ag-ITO} = 1\,\mathrm{m}\Omega\,\mathrm{cm}^2$, $p = 1.85\,\mathrm{mm}$, $w_f = 30\,\mu\mathrm{m}$. Finally, the related* FF *losses were computed as $5 \times R_s^{latC}$, using* Pysch's law, *as presented in appendix A.1. Along (i), the dependance goes as $R_s^{latC} \approx \rho_c^{front} + \frac{1}{12} p^2 R_{sh}^{TCO}$, while along (ii) it can be approximated as $R_s^{latC} \approx \frac{p}{w_f} \rho_c^{front} + \frac{1}{12} p^2 R_{sh}^{cSi}$.*

6 Thin n-type Nanocrystalline Silicon for Rear-Junction application

The results exposed in this chapter were presented during the SiliconPV conference in Konstanz, Germany (March. 2022), and have been proposed for publication in the following SOLMAT special issue for the best 20 abstracts of the same conference as:

- L. Antognini, C. Sthioul, J. Dréon, V. Paratte, D. Turkay, L.-L. Senaud, C. Ballif and M. Boccard, *Integration of thin n-type nc-Si:H layers in the window-multilayer stack of Heterojunction Solar Cells*, Solar Energy Materials and Solar Cells, under review, 2022

6.1 Abstract

N-type nanocrystalline silicon (nc-Si:H(n)) is a good window layer candidate to improve transparency and transport properties in heterojunction solar cells. In this work, we perform thickness series alongside PH_3 doping series to unravel the different characteristics which are desirable along nc-Si:H(n) growth direction. While increasing the PH_3 flow is necessary to improve the conductivity of the layer and the contact properties, we observe that too high flows lead to an amorphization of the first 10–15 nm of the layers. We conclude that this effect results from the following trade-off: either the nc-Si:H(n) layer has a strong doping in the amorphous nucleation zone at the i/n interface at higher PH_3 flow, or the stronger doping is found at the n/TCO interface thanks to the higher crystallinity at intermediate PH_3 flow. This affects the series resistance of the solar cell depending on the ITO doping: the most amorphous layer outperforms the most crystalline one when in contact with a highly doped ITO and oppositely when using lowly doped ITO.

We confirm further those effects and study the integration in the whole stack by introducing a thin a-Si:H(n) layer underneath the nc-Si:H(n) layer as well as studying the impact of higher ITO doping. We also report on the beneficial effect of an additional SiO_x capping not only to form a double anti-reflective coating (DARC), but also to improve contact properties. We observe that all those three features can improve passivation and selectivity as well as reduce strongly the front contact resistivity (ρ_c). Our best results are achieved by using a thin a-

Si:H(n)/nc-Si:H(n) stack together with an IZrO/SiO_x DARC, enabling front ρ_c lower than 15 mΩ cm^2 and an efficiency of 23.7 % on screen-printed 2 × 2 cm^2 solar cells.

Finally, we explore the possibility offered by this low ρ_c to replace partially or completely the front TCO by a more transparent SiN_x. We observe the possibility to gain a further +0.6 mA cm^{-2} of J_{sc} and discuss further optical optimizations proposed in the literature.

6.2 Introduction

Silicon heterojunction (SHJ) solar cells demonstrated the highest conversion efficiency for silicon based devices with up to 26.7 % with an interdigitated back contact (IBC) architecture [Yoshikawa 2017] and recently up to 26.3 % in double side contacted configuration [Pv-magazine 2021a]. For all solar cell technologies, an important requirement to reach high efficiency devices is to optimize together the optical and electrical properties of the solar cell. In the particular case of double side contacted SHJ solar cells, important parasitic absorption is induced by the front contact layers and the front metallic grid leading to lower current with respect to IBC or TOPcon solar cells [Green 2021].

For contacts based on full area hydrogenated amorphous silicon (a-Si:H) for surface passivation (a-Si:H(i)) and selective layers (a-Si:H(n) and a-Si:H(p)), and completed by a transparent conductive oxide (TCO) for lateral charge transport and anti-reflection, it was estimated that the parasitic absorption losses can account for 2–2.5 mA/cm^2 [Holman 2014]. Moreover, for a more recently optimized front contact based on nano-crystalline silicon oxide (nc-SiO_x:H), absorption losses were still shown to represent a large share of the remaining power losses [Boccard 2021]. Therefore, to reproduce results such as in [Pv-magazine 2021a, Adachi 2015, Ru 2020] and push further the efficiency of double-side contacted SHJ, the biggest opportunity is to improve the front side by developing a contact stack as transparent as possible which keeps good passivation and transport properties.

The rear-junction architecture, i.e. with the p-type layer at the back on a n-type c-Si, offers electrical transport advantages since electrons benefit from a high conductivity for the lateral transport in the crystalline silicon wafer: indeed, if the front contact resistivity (ρ_c) is small enough, current can flow laterally both in the TCO and the wafer and reduce the series resistance [Haschke 2020]. For typical screen-printed finger width (~ 30 µm) and c-Si(n) resistivity (~ 2 Ω cm), if a ρ_c value as low as 10 mΩ cm^2 is reached, lateral transport can be sustained by the wafer only [Haschke 2020], opening the possibility to replace part of - or completely - the front TCO by another less absorbing anti-reflective coating stack [Morales-Vilches 2019, Cruz 2019b, Li 2021b, Luderer 2021]. Thus, it is of interest to investigate electron contacts as transparent as possible that can still provide excellent passivation and selectivity as well as small ρ_c.

Hydrogenated nano-crystalline silicon (nc-Si:H) is a promising material to replace a-Si:H doped layers classically used in SHJ solar cells, since it can provide better transparency and

higher doping efficiency [Shah 2010, Seif 2016]. However, nc-Si:H is a complex mixed-phase material inhomogeneous along its growth direction, consisting of crystallites embedded inside an amorphous matrix. Indeed, it consists of an amorphous zone (also called the nucleation zone) in the first nanometers, before having crystallites growing from nucleation sites with a conical or columnar shape and resulting in a higher crystalline volume fraction for the top of the layer [Luysberg 1997, Koh 1999, Mazzarella 2020]. As a result, the layer can be inhomogeneous in doping, i.e. the nucleation zone having a lower doping efficiency than the crystalline top part [Shah 2010], or in density, with often only voids in between the crystals at high crystallinity while the nucleation zone might be denser [Richter 2018]. Moreover, the presence of defects in the material and at its interfaces can reduce the ability of its doping level to form a good contact, inducing e.g. Fermi-level pinning [Shah 2010, Allen 2019]. All of these facts can have direct a impact on the ability of thin nc-Si:H layers to act as efficient carrier selective passivating contacts (CSPC). For example, a poorly doped material could lead to large depletion zone and higher barrier height for the majority carrier (e.g. at the i/n or n/TCO interface) and therefore, lower the carrier selectivity. Therefore, in order to understand nc-Si:H integration in the solar cell, we find it of particular importance to study its properties along its growth, as it is done e.g. in [Umishio 2020] or using structures with different sub-layers as it is done using the so-called *top-down* and *bottom-up* approaches in [Senaud 2021a]. This work aims to apply and push further those methods.

Despite those challenges, high solar cell efficiencies were achieved by alloying the material with oxygen to form nc-SiO_x:H layers [Watahiki 2015, Mazzarella 2017, Mazzarella 2018a, Ru 2020, Qiu 2021]. This demonstrates the advantage of the higher transparency of nc-SiO_x:H compared to nc-Si:H. However, lower conductivities are also reported as oxygen is added to the material, which increases ρ_c of the stack and imposes the use of a TCO at the front side. Therefore, studying non-oxidized nc-Si:H layer is of interest to achieve TCO-free SHJ.

In this work, we develop nc-Si:H(n) layers for front application through a detailed and systematic approach, taking into account the material inhomogeneity along its growth direction and the interaction with the other layers of the stack, ending up demonstrating efficiencies higher than 23.5 %. In the first part of this study (see Figure 6.1(a)), we investigate the material properties (thickness, Raman crystallinity, dark conductivity, transparency) and the device properties (solar cell *J-V* results, EQE, and passivation at different stages of the process) of these layers depending on their thickness and doping level (see *top-down* and *bottom-up* approaches in [Senaud 2021a]) when used as the single n-type layer in the contact stack and discuss in particular the presence and the impact of a lowly doped nucleation zone in the layers.

We will discuss further this point in the second part of this study (see Figure 6.1(b)), by inserting a thin a-Si:H(n) buffer layer (also abbreviated as n-aSi) underneath the nc-Si:H(n). Moreover, we will discuss the interaction of the nc-Si:H layer with the rest of the whole front layer stack, namely the TCO layer as well as a silicon oxide (SiO_x) capping layer used to form a double anti-reflective coating (DARC) but that can also act as a hydrogen source [Herasimenka 2016,

Morales-Vilches 2019, Boccard 2021]. In the first part of this multilayers study, we will show how we use deliberately insufficient doping for the nc-Si:H layer to exacerbate the influence of the other layers and obtain well defined trends, before using high doping conditions to unveil the potential of this contact stack. Then, we will discuss the optical losses in those layers by studying the external quantum efficiency (EQE) and reflectance spectra and characterize with high precision ρ_c of the front n-contact directly from solar cells results by using 20 nm-thick TCO with high sheet resistances.

Finally, in an additional section 6.5, we will investigate the possibility to replace the front TCO by a more transparent SiN_x, either completly or in a TCO / SiN_x bilayer.

6.3 Experimental details and Method

The solar cell structures under study are shown in Figure 6.1 and the co-deposited samples used for material characterization in Figure 6.2. The solar cells were based on 100 mm-wide, 200 µm-thick, 2 Ωcm n-type float-zone (FZ) textured crystalline silicon (c-Si) wafers. The wafers were chemically cleaned and the native oxide was removed using a one minute 5 % hydrofluoric acid bath.

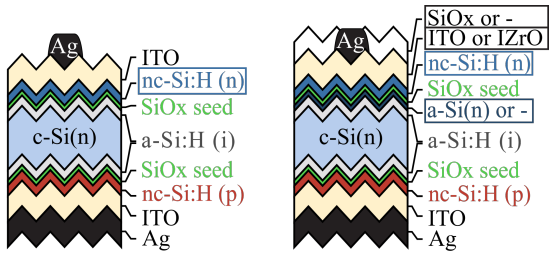

(a) Solar Cell Structure for the nc-Si:H(n) thickness and doping series

(b) Solar Cell Structure for the whole stack integration of nc-Si:H(n)

Figure 6.1: Solar cell structures studied here: (a) Single layer structure, where nc-Si:H(n) grows from a SiO_x seed treatment directly on a-Si:H(i) and ITO is used as front electrode. (b) Multilayer structure, where the presence of an additional thin a-Si:H(n) layer, different TCOs and an additional SiO_x capping layer are studied.

The silicon layers were deposited via PECVD in a parallel-plate plasma box KAI-M system. All intrinsic layers were deposited at a substrate temperature of 200 °C whereas all the other PECVD layers are deposited at 175 °C, in particular to increase the crystallinity of the nc-Si:H layers [Fioretti 2019]. To begin with, a 7–10 nm-thick a-Si:H(i) layer was deposited, followed by a 1–2 nm SiO_x seed layer used to enhance the crystallinity of the subsequent nc-Si:H(p) (as described in more detailed in ref. [Boccard 2018, Antognini 2021]), forming altogether the "ip" contact stack. Note that in the present work, all the layer thicknesses are taken from co-deposited layer stacks on glass if not specified otherwise. For the electron "in" contact stack, we proceeded in two ways as can be seen on Figure 6.1. In the case of the single layer structure, we proceed exactly as for the "ip" contact stack, that is after the deposition of the a-Si:H(i) and SiO_x seed we deposited a nc-Si:H(n) layer using a hydrogen dilution $[H_2]/[SiH_4]$ of 133 and a varying PH_3 dopant gas flow of 0, 4, 9.5, 25, 50 and 100 sccm. In the multilayer architecture, an additional a-Si:H(n) layer was introduced on top of the a-Si:H(i) passivation layer, but before the SiO_x seed layer to prevent affecting the crystallinity of the nc-Si:H(n) layer.

	Annealed 210°C		After SiO_x	
	μ [$cm^2/(Vs)$]	N [cm^{-3}]	μ [$cm^2/(Vs)$]	N [cm^{-3}]
ITO *HD*	29	4.42e20	30	4.57e20
ITO *MD*	25	2.71e20	27	3.29e20
ITO *LD*	11	8.09e19	20	1.24e20
IZrO	44	1.56e20	45	1.62e20

Table 6.1: Mobility (μ) and dopant concentration (N) of the different TCOs present in this study, characterized by Hall effect on the stack Glass/a-Si:H(i)/nc-Si:H(n)/TCO, where the TCO thickness is 115 nm and the nc-Si:H(n) was processed with 50 sccm *of* PH_3 *for* 210 s. *The labels HD, MD and LD correspond to highly, medium and lowly doped ITO, respectively.*

On the "ip" stack, two different TCOs were used, namely a lowly doped ITO layer (denoted *ITO LD*) deposited via DC-sputtering on an In_2O_3(90):SnO_2(10) target at a power of 2.2 W cm^{-2} and a high oxygen partial flow to minimize plasmonic absorption, as well as a highly doped ITO (denoted *ITO HD*) with a lower oxygen partial flow to minimize series resistance for front side applications. On the "in" stack, three different TCOs were used, namely the ITO LD, a medium doped ITO (denoted *ITO MD*) with an intermediate oxygen partial flow, and an indium zirconium oxide (denoted IZrO) allowing a higher mobility than ITO for similar optical properties (See [Boccard 2021, Rucavado 2019]) deposited via RF-sputtering using a target of 2% weight of ZrO_2 in In_2O_3 at a power density of 1.32 W cm^{-2}. The mobility and doping concentration of those different TCOs can be found in Table 6.1. The thickness of all the TCOs was either 115 nm for front application as single anti-reflective coating (ARC), 75 nm for combination with an additional SiO_x layer deposited after metallization to form a double anti-reflective coating (DARC), 20 nm to increase the sheet resistance of the TCO (R_{sh}^{TCO}) and study more accurately ρ_c or 230 nm when used at the rear-side as infrared reflector. Finally, a 150 nm-thick Ag layer was sputtered on the rear side.

Concerning the design and the metallization, the solar cells were fabricated either using 1×1 cm^2 shadow masks for the TCO deposition and realizing a sputtered front silver grid (and finished with an annealing at 210 °C for 30 minutes) or using 2×2 cm^2 area TCO and a screen-printing silver grid (equally cured at 210 °C for 30 minutes). We use the 1×1 cm^2 cells to analyse large trends of open circuit voltage (V_{oc}) and fill factor (*FF*) with typical values lower than 720 mV and 80 %, respectively, while the 2×2 cm^2 cells allow us to discuss higher efficiency trends in more details. Moreover, the small cells were fabricated in front-junction configuration to allow the sputtering of the ITO and Ag blanket on the full area at the back, avoiding alignment issues with the front mask. Finally, the best cells presented here in Figure 6.7 were placed in forward-bias in the dark for two weeks as is done in [Cattin 2021], allowing an increase of V_{oc} and *FF* of +2 mV and +0.7 $\%_{abs.}$, respectively.

The lifetime, implied V_{oc} (iV_{oc}) and implied fill factor (*iFF*) were measured at different stages of the process using a WCT-120 photoconductance decay (PCD) tester in the transient analysis mode. Dedicated samples (quarter-wafer) with the "in" and "ip" stacks were used where the TCO was only sputtered on the n-contact stack in order to follow more closely passivation

damages related to this contact (when non precised otherwise).

I-V curves of each solar cell were collected using a Wacom Electric Co. Super solar simulator with AM 1.5G illumination. The series resistance (R_s) at maximum power point (MPP) was obtained by comparing the *I-V* curve of a device at 1 Sun with the one at 0.03 or 0.05 Sun using the method described in ref. [Bowden 2001]. Pseudo fill factors (*pFF*) were calculated as $pFF = FF(1 + R_s J_{mpp}/V_{mpp})$. The sheet resistance of the TCOs was measured with a four-point probe tool on the "in"/TCO stack deposited on a p-type wafer to block any current flowing through the wafer.

External quantum efficiency (EQE) curves were collected using a 1×1.5 mm^2 monochromatic light spot between the grid fingers of the solar cell. To characterize the optical properties of the n-contact, rear-junction cells were also co-processed (Figure 6.5) using the same TCO doping in contact with the "in" stack as at the back-side of the solar cells presented in Figure 6.3, however with a thickness adapted to form an ARC. For solar cells with strong passivation issues, a light bias was applied to mimic the injection level during the *I-V* test.

The structures of the samples for the characterization of the material properties are shown in Figure 6.2. Raman spectra of nc-Si:H were acquired using a 325 nm UV laser to probe only a depth of 10–15 nm on textured wafers. For thinner layers, a thicker a-Si layer was used to screen the signal coming from the c-Si. To evaluate the transparency of the "in" stack in the visible range, we used a 442-nm wavelength laser that has a penetration depth down to the wafer and follow as a metric the 520 cm^{-1} peak attenuation of the c-Si buried below the "in" stack, as introduced in [Ledinský 2016]. The thicknesses of the layers were measured using spectroscopic ellipsometry from co-deposited "in" stacks on glass substrates. Dark conductivity at room temperature was measured on similar glass samples where 100 nm-thick Al pads were evaporated. More details about the Raman crystallinity X_c, ellipsometry and dark conductivity data processing can be found in [Antognini 2021].

6.4 Results and discussion

6.4.1 nc-Si:H(n) single layer thickness and doping series

nc-Si:H(n) single layer characterization

We present in Figure 6.2 the material characterization of the nc-Si:H(n) layers developed with different deposition times and PH_3 dopant flows. Looking first at the thicknesses in (a), we see that the dopant flow has only a minor influence at the longest deposition time. Deposition rate is thus independent of the PH_3 flow. Nevertheless, for the thinnest layers, the data is more scattered with a trend towards decreasing thickness upon increasing PH_3 flow.

We turn next to the evaluation of the layers transparency in (b). As expected, the c-Si signal decreases when thickening the a-Si:H or nc-Si:H layers. We observe a 2.5 times steeper

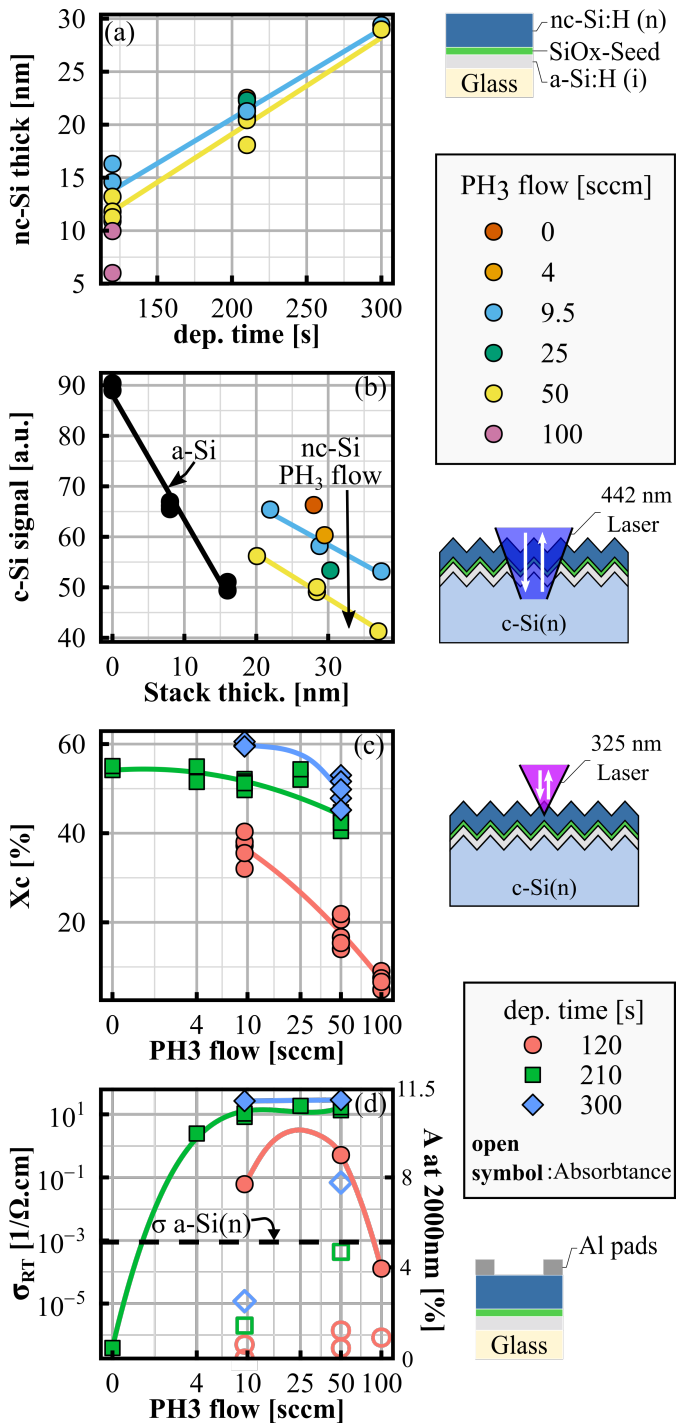

Figure 6.2: Materials parameters of the nc-Si:H(n) layers: (a) Ellipsometry thickness measured on glass as a function of the deposition time for different dopant flow. (b) VIS-Raman 520 cm^{-1} *peak signal of the buried c-Si in the stack nc-Si:H(n)/SiO_x-Seed/a-Si:H(i)/c-Si used as a metric of the transparency of the stack at* 442 nm. *The stack thickness is the flat-equivalent thickness measured on glass plus 8.3 nm for the a-Si:H(i) underneath. (c) UV-Raman crystallinity of the top 10-*15 nm *of the layers. Note that for thinner layers, thicker a-Si layers are used to screen the substrate. (d) Room temperature dark conductivity as a function of the dopant flow for the different deposition times. Solid lines are guide-to-the-eyes.*

decrease for a-Si:H than for nc-Si:H, stemming from the higher transparency of the nc-Si:H layers. This order of magnitude is consistent with the estimation of J_{sc} losses as a function of thickness reported for those materials, with e.g. a loss of 0.16 mA/cm^2/nm for a-Si:H(p) [Holman 2014, Boccard 2019] and in the range 0.029–0.056 mA/cm^2/nm for nc-Si:H(p) [Antognini 2021, Boccard 2019].

We also observe that the c-Si signal drops as the dopant flow is increased, even though the thicknesses remain similar. This suggests that the layers produced with higher dopant flow absorbs more (excluding here a reflectance change as discussed below). Since the slopes of the c-Si signal versus stack thickness are similar for both the 9.5 and 50 sccm flow, we conclude that absorptance evolves identically as the material is grown thicker. Therefore, we attribute the stronger absorption due to higher dopant flow to an initial difference in the nucleation layers. This is consistent with the crystallinity data (discussed below) and was as well confirmed by the observation of the increase of the 480 cm^{-1} amorphous peak (taken with the 442 nm laser) for more highly doped layers (not shown).

Note that the counts in the case of the 0 sccm layer and the thinnest of the 9.5-sccm layers are about 65, which is the same as for the underlying a-Si:H(i) layer alone. This likely stems from a reduction of reflectance when adding a nc-Si:H layer on top, compensating for the increasing absorptance. Since we cannot measure precisely the stack reflectance in the confocal geometry used for measurement, this comes as a limitation of this characterization technique. To assess this possible tendency, we measured the reflectance at 442 nm using a UV-VIS spectrometer equipped with an integrating sphere. Thicker layers did show lower reflectance without any trend among the different dopant flows for a fixed thickness (not shown). However, it is not possible to directly correct the Raman data from those measurements, due to the difference of optical geometry between the setups. Those observations indicate that the slope of absorption with thickness of the nc-Si:H layers is probably slightly underestimated, whereas it strengthens our interpretation of a thicker nucleation zone as the PH_3 flow is increased.

Looking now at UV-Raman data in (c), probing the top 10–15 nm, we can see that all thick layers (with deposition time of 210 or 300 s) have high crystallinity above 40%. The crystallinity nevertheless slightly decreases as we increase the PH_3 flow. For the thinner layers, the dramatic decrease of crystallinity with dopant flow could be put in contrast with the fact that the layers prepared with higher PH_3 flow are also thinner and therefore more amorphous signal could come from the layer underneath. Nevertheless, their reduced crystallinity observed with UV-Raman in (c) coincides with the higher absorptance observed with the 442 nm laser in (b) (see also the full spectra in Figure A.17), which would not be the case if layers were only thinner. Therefore, it confirms the decreasing crystallinity trend at high dopant flow accompanied by a thicker nucleation zone and a delayed crystal growth. Such observations at high PH_3 flow were also reported in the literature [Jiang 2009, You 2021, Qiu 2021]. However, to the contrary of those reports where X_c first increases slightly when adding a small flow of PH_3 and then decreases strongly at larger flows, we do not observe an increase of crystallinity at low PH_3 flow with respect to the undoped layer. This probably stems from the good nucleation properties

provided by our SiO_x seed layer.

Finally, looking at the dark conductivity and infrared absorption of the layers in (d), we observe almost no difference on thicker layers compared to the marked trends present with thinner layers. An optimum of conductivity is reached around 25–50 sccm, that we explain by a trade-off between doping and amorphization of the layers that was similarly reported in the literature [Jiang 2009, You 2021, Qiu 2021]. The optimum of conductivity we reached is about 10 S/cm and is similar to the literature best conductivity for nc-Si:H(n) layers deposited via PECVD [Zhao 2020]. We also see that the thin 100-sccm layer reaches a conductivity as low as our standard a-Si:H(n), consistent with its lower crystallinity. However, the amorphous phase of this layer might be more doped than with the 50 or 9.5 sccm recipes thanks to the higher PH_3 flow.

As the conductivity of thickest 9.5 and 50 sccm-doped layers reaches similar values despite the increased dopant flow, we investigated the absorption in the infrared at 2000 nm (open symbol in Figure 6.2(d)). We saw a stronger absorption for 50 sccm than for 9.5 sccm, stemming from an increased free carrier absorption (FCA) that would indicate higher active dopant concentration. This is contrary to the conductivity data, that show almost constant values when going from 9.5 sccm to 50 sccm, except for the thinnest samples. This shows the complex inhomogeneous nature of nc-Si:H material, which cannot be captured fully by coplanar conductivity measurement while it has to be taken into account to understand the solar cell results shown later [Umishio 2020]. Probably when thicker layers are measured, the current is flowing mostly through the very conductive top nanometers, and no effect of the nucleation layer is visible. However, absorption in the infrared is not easily measurable on very thin layers (such as the ones deposited in 120 s) for which the measured absorption is below 1%, making advanced techniques such as photothermal deflection spectroscopy required.

In summary, for dopant flows higher than 9.5 sccm, we conclude that i) almost no trend on deposition rate with dopant flow is present, ii) the top of the thickest layers have similar crystallinity and conductivity, and iii) a thicker amorphous nucleation layer forms upon increasing PH_3 flow which is correlated with a diminution of the dark conductivity for 10–15 nm thick layers.

nc-Si:H(n) single layer investigation in solar cells

We present on Figure 6.3 the results of the solar cells and passivation samples using nc-Si:H(n) as single doped layer for the n-contact. To discuss the resulting contact properties, we illustrate on Figure 6.4 different relevant energy-band diagrams drawn from PC1D simulations.

V_{oc} improves monotonically with the dopant flow as well as with the deposition time. For a low dopant flow of 9.5 sccm, we can see that increasing the thickness improves the selectivity of the device, while the passivation remains similar. This stems both from the fact that as the layer becomes thicker, first, more highly doped crystals are present, and second, the

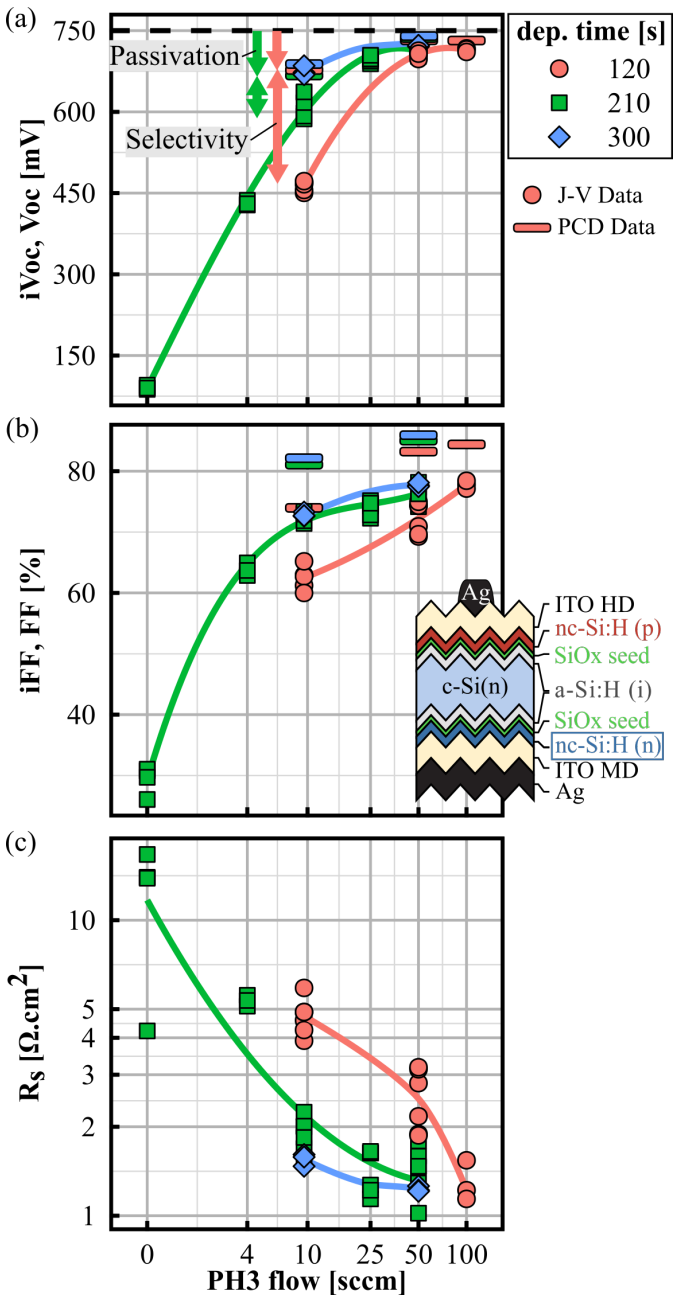

Figure 6.3: Passivation and transport properties of the single layer solar cell structure for different PH_3 dopant flows and deposition times. The solar cells have an area of 1×1 cm^2 *as described in the experimental part. Solid lines interpolation are guide-to-the-eyes.*

layer must become thicker than the depletion zone created by the TCO to act as a good electron contact (see Figure 6.4(a) and 6.4(b)). For higher dopant flow, the influence of the thickness is gradually reduced as the nc-Si:H(n) layers reach sufficient doping to screen more efficiently both barriers at the i/n and n/TCO interface (Figure 6.4(c)). V_{oc} converges quickly towards 710–715 mV (good for our 1×1 cm^2 cell design) for dopant flows larger than 50 sccm,

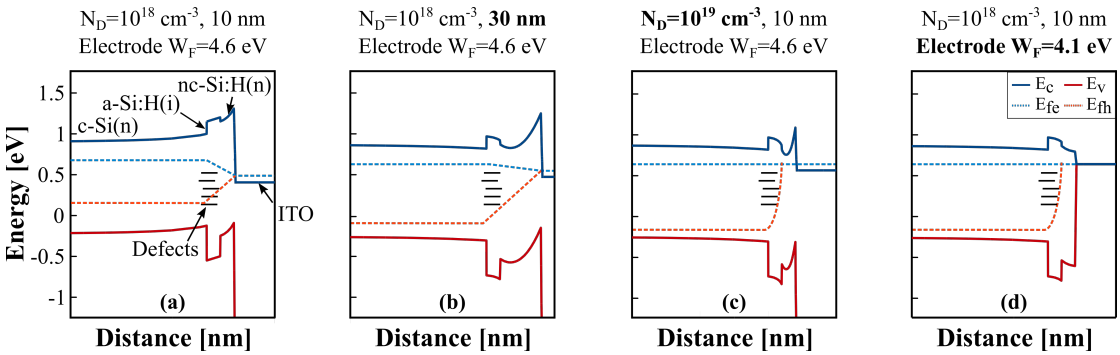

Figure 6.4: Energy-band diagram sketches at V_{oc} *and 1 Sun illustrating different n-type contact situation with (a) lowly-doped and thin layer, (b) lowly-doped and thick layer, (c) highly doped and thin layer, and (d) ideal electrode work-function match.*

even with thin layers. The *FF* however is further improved when reaching 100 sccm, mainly through the series resistance that is decreased further. The fact that V_{oc} converges faster than R_s stems from the fact that the former is improved greatly once the depletion lengths at the i/n and n/TCO interfaces are smaller than the layer thickness, while the latter will still suffer from the presence of those barriers as the current will experience resistive losses when flowing through them. This is a general fact about forming heterojunction contacts, where a high selectivity is obtained once the ratio of electron to hole resistances is small, whereas obtaining a low series resistance needs additionally a low electron resistance in absolute value [Wurfel 2015, Procel 2018, Onno 2019].

Importantly, for very thin layers we note that the best V_{oc} and *FF* are obtained with the layer doped with 100 sccm of PH_3, despite the fact that this layer had a lower crystallinity and lower lateral conductivity than when using 50 sccm. We attribute this to a reduced barrier at the i/n interface thanks to a better doping of the nucleation zone when using 100 sccm. We will reinforce this assertion in the next section, by introducing a thin a-Si:H(n) layer underneath the nc-Si:H(n) layer, that will enhance the screening of the barrier at the i/n interface.

On Figure 6.5(a) we show the EQE of the corresponding rear-junction device using nc-Si:H(n) on the front side. In the UV-blue part of the spectra, we can see that the EQE and the reflectance depend only on the thickness and not on the dopant flow: as the layer thickness is increased, the reflectance is reduced and its minimum shifts to lower wavelengths whereas the EQE is reduced by a stronger absorption in the front layers. Importantly, 120 s deposition-time layers prepared with either 50 sccm or 100 sccm have similar EQE in the UV-Blue. As a matter of fact, when repeating the experiment in another batch, the two EQE curves were again very close, with this time slightly higher values for the 100-sccm-prepared layer. Therefore, using this less crystalline layer does not impede high J_{sc} values. However, this is qualitatively different from our Raman measurements with the 442 nm laser (Figure 6.2(b)). Turning to the visible part of the spectrum, the EQEs increase as the passivation of the solar cell is improved (Figure 6.5(c)), stemming from a better charge carrier collection. In turn, for 120 s deposition time, the less

crystalline 100 sccm layer could have a similar EQE to the 50 sccm layer in the UV-Vis due to the reduced recombination that balances a slightly stronger absorption. Finally, we note a lower reflectance and EQE in the infrared as the layers become thicker or more doped.

To understand better the source of the passivation issues affecting the solar cell performance, we measured the iV_{oc} values after different process steps (Figure 6.5(c)). After the deposition of both the "ip" and "in" stack, we can see that all the values are above 730 mV, regardless of the deposition parameters. In the subsequent steps, the behavior depends strongly on the dopant flow: on the one hand, for the 50-sccm-prepared layer, iV_{oc} is reduced after the sputtering of the ITO and can be recovered after an annealing, as shown in other reports such as [Demaurex 2012, Senaud 2021a]. On the other hand, for the 9.5-sccm-prepared layer the passivation is further reduced after the annealing. After removing the ITO in a HF bath, about 30 mV can be regained. We explain this by the detrimental effect of the ITO on the band-bending which when not properly screened by the n-type layer can lead to minority hole accumulation at the defective interface, as can be seen on Figure 6.4(a). Note that when evaporating aluminum on the contact (no sputtering damage and ideal work function of 4.1 eV), exemplified on Figure 6.4(d), we obtained similarly good photoluminescence signal independently of the dopant flow (not shown). We can notice two other effects impacting the passivation of the lowly doped contact: First, after ITO removal the passivation is not completely recovered and the 9.5-sccm-prepared layer has a lower iV_{oc} of 20 mV as compared with the 50-sccm-prepared layer. As the etching step has only a minor impact, we can attribute this loss to the presence of sputtering defects that are not screened by field effect with the lowly doped layer. Second, we notice that thicker 9.5-sccm-prepared layers have lower iV_{oc} than thinner ones. This can be attributed to H_2 plasma damage during the deposition of the nc-Si:H layers. Fortunately, all those trends are absent with the 50-sccm layer where the passivation quality remains high. This is thanks to the high dopant concentration in the layers, that efficiently screens the TCO workfunction mismatch and provides a sufficient field effect passivation to decrease recombination in defects at the c-Si(n) surface. However, the presence of the n/TCO barrier, that we evidenced on the 9.5-sccm doped sample, can still influence ρ_c with the more doped layers (see Fig. 6.4(c)).

6.4.2 Integration of nc-Si:H(n) in the whole front stack of solar cells

Transport and coupling with a-Si(n), TCO and SiO_x coating

In summary of the previous section, we saw that (i) high V_{oc} values can be obtained with 10-15 nm nc-Si:H(n) layers with high PH_3 flows, (ii) the lowest R_s was obtained with the highest PH_3 flow of 100 sccm which is not the most crystalline layer, and we discussed the impact on the contact quality of (iii) the nucleation zone and (iv) the ITO's doping. In this section, we carry further our understanding of nc-Si:H(n) layers interaction with the rest of the stack. The effect of having a lowly doped nucleation zone is studied by inserting a thin a-Si:H(n) buffer layer underneath the nc-Si:H(n) contact (but before the SiO_x seed to avoid any impact on the

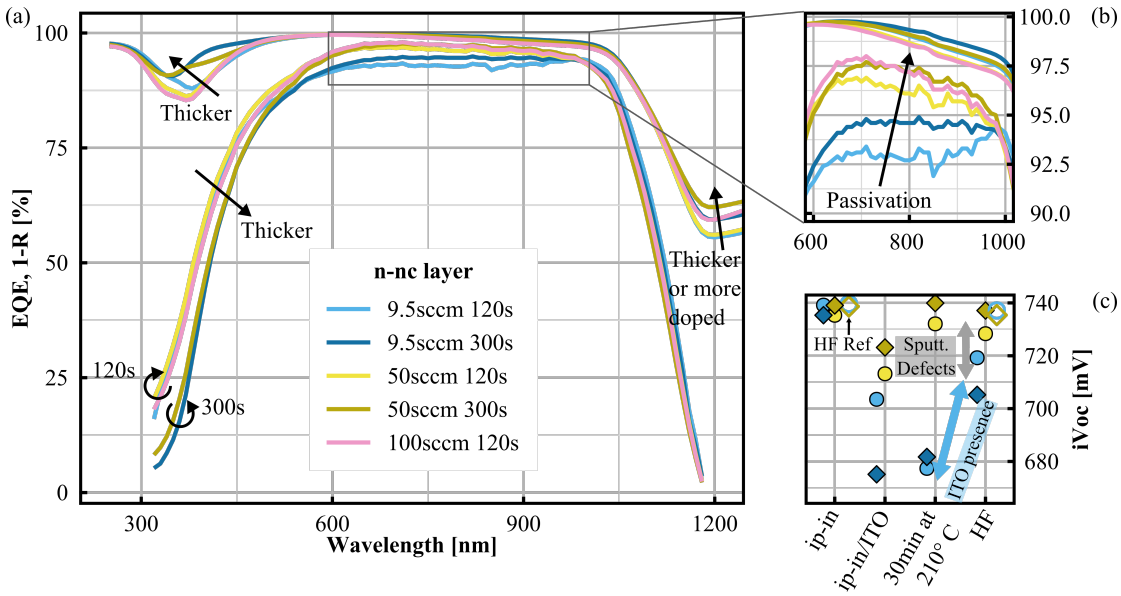

Figure 6.5: (a) EQE and total reflectance of the single layer structure using nc-Si:H(n) in rear-junction configuration for the different PH_3 dopant flows and deposition times and (b) zoom in the 600-1000 nm wavelength range. (c) iV_{oc} *values measured after different process steps.*

crystallinity). The impact of the ITO doping is studied by using two different oxygen flows. Finally, we report on the impact on transport properties (and not only optics) of the silicon oxide layer used to form a DARC. Thus, the structure under study is more complex than in the previous section and is depicted on Figure 6.1b.

On Figure 6.6, we study those three effects by using deliberately insufficient doping for the nc-Si:H(n) layer (9.5 sccm) to exacerbate the influence of the other layers. Looking first at iV_{oc} values, we can see that the passivation is i) unchanged when changing the ITO doping, ii) slightly improved after the SiO_x deposition, and iii) greatly improved when a-Si:H(n) is present. Looking then at the selectivity (iV_{oc} - V_{oc} difference), it improves slightly when using a more doped ITO and greatly after the SiO_x deposition or when a-Si:H(n) is present. Turning to the series resistance, large trends are seen among the samples. As the variation of R_{sh}^{TCO} alone cannot induce such changes, we can attribute those trends to a lowering of the front ρ_c. Qualitatively, ρ_c is improved together with the selectivity. However, once selectivity has reached a sufficiently high value, ρ_c can still be further improved, for the same fundamental properties of heterojunction that were discussed with the PH_3 flow series of Figure 6.3 in the previous section.

Importantly, all the phenomena discussed above can be combined together, meaning that the best passivation and ρ_c are obtained for a highly doped ITO, after SiO_x deposition and when the a-Si:H(n) layer is introduced.

We turn now to solar cells using a higher dopant flow, presented on Figure 6.7. All trends on the transport of Figure 6.6 are reproduced : as a-Si:H(n) is introduced, all the devices reach

V_{oc} values above 725 mV, with additional gains with the SiO_x, while ρ_c is also improved at the same time.

Moreover, we can observe that the nc-Si:H layer prepared with a flow of 50 sccm outperforms the one prepared with 100 sccm. This should be compared to the results of the previous batch (presented on Figure 6.3), which we repeated in Table 6.2 for simplicity. Indeed, in the previous batch better R_s values were obtained using a flow of 100 instead of 50 sccm. However, the layer was in contact with a more doped ITO (ITO MD), indicating that both a high ITO doping and a high crystallinity of the nc-Si:H layer are beneficial to reach low ρ_c values. This could stem from a lower work-function of the ITO when using higher doping, which could shift its Fermi level upwards, and in turn lower the barrier height at the n/TCO interface [Ritzau 2014]. An illustration with an ideal electrode work-function is shown in Figure 6.4(d). Reduced Fermi level pinning at the interface or modification of the energy states at the interface upon changing the oxygen content are other phenomena that could explain the dependence of the transport on the TCO's doping [Ritzau 2014, Procel 2020]. As low R_s values are also obtained when using IZrO as a TCO on top of the stack a-Si:H(n)/nc-Si:H(n), we speculate that the same work function explanation holds for the latter, as it is also highly conductive. However, it should be noted that depending on the contact stack and TCO choice, the TCO doping should sometimes be decreased on the contrary to improve ρ_c, as it is reported e.g. for a-Si:H(p)/AZO contact [Niemelä 2019]. Therefore, the impact of the TCO doping should always be considered with care.

Next, after SiO_x, and when a-Si:H(n) is present, R_s values of 0.65-0.7 Ωcm^2 are obtained. A breakdown of the series resistance considering lateral transport in the wafer [Haschke 2020] allows us to conclude that ρ_c is below 100 $m\Omega cm^2$ after that step, however without further accuracy due to the low R_{sh}^{TCO} employed here that decreases the dependence of R_s upon ρ_c. We will give a more precise evaluation in section 6.4.2.

We discuss now the role of the different elements. First, the a-Si:H(n) buffer improves passivation as it creates a favorable band bending to repulse holes at the c-Si/i/n interface and could as well reduce sputtering damage thanks to the higher density of a-Si:H compared to nc-Si:H. It also improves greatly the selectivity by providing better conductivity to electrons, despite its lower lateral conductivity compared to the 9.5 sccm and 50 sccm nc-Si:H layers, indicating further that those nc-Si:H layers possess a poorly conducting nucleation zone.

The present SiO_x capping layer was known to improve passivation and R_{sh}^{TCO} at the same

Rs [Ω.cm^2]	n-nc 50sccm 120s	n-nc 100sccm 120s
ITO MD	**3.13**	**1.22**
ITO LD	**2.30**	**3.58**

Table 6.2: Median R_s of the solar cells depending on both the ITO and nc-Si:H(n) doping. Note that the first line and the second line cannot be compared in absolute values since the solar cells have different sizes.

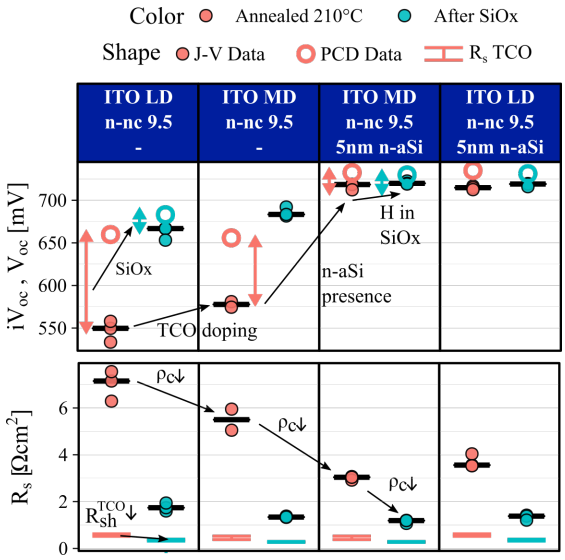

Figure 6.6: Passivation and transport properties of the multilayer solar cell structures showed in Figure 6.1(b) using lowly doped nc-Si:H(n) layers. In the bottom row, the error bars represent the variation of the TCO's contribution to series resistance when assuming no lateral transport coupling with the wafer, i.e. $R_s^{TCO} = \frac{1}{12} p^2 R_{sh}^{TCO}$*, with p the pitch of the grid. The solar cells have an area of* $1 \times 1\,\mathrm{cm}^2$*. PCD data were taken from ip-in/TCO samples after annealing (the rear TCO was omitted to focus on the front side).*

time as forming a DARC when employed in front junction structure [Boccard 2021]. We show here that it can additionally improve strongly ρ_c. As the gas mixture employed for the SiO_x deposition contains hydrogen, it could easily diffuse in the contact stack and passivate different types of defects. It could e.g. passivate the grain boundaries of the crystallites in the nc-Si:H(n), reducing Fermi level pinning at each interface and allowing for a better percolation of electrons through the layer. Indeed, it is known from thin film literature that defects need to be filled to reach higher conductivity in nc-Si:H at moderate doping level [Shah 2010]. In addition, in ref. [Balent 2021], *Balent et al.* discussed that the dangling-bond density in the doped layers should be kept as low as possible to avoid mitigating the beneficial effect of doping and efficiently screen the TCO workfunction mismatch. Likewise, TCO's defects could also be passivated, modifying the transport mechanisms at the n/TCO interface [Procel 2020]. Finally, hydrogen could as well accumulate at the n/TCO interface, increasing the doping there which would lower down ρ_c consistently with our other present observations regarding ITO doping. In any case, the SiO_x capping broadens impressively the window of parameters leading to efficient contacts. A full understanding of the mechanism that allows such improvement could help in the development of new CSPCs beyond the most common doped silicon and transparent conductive oxides.

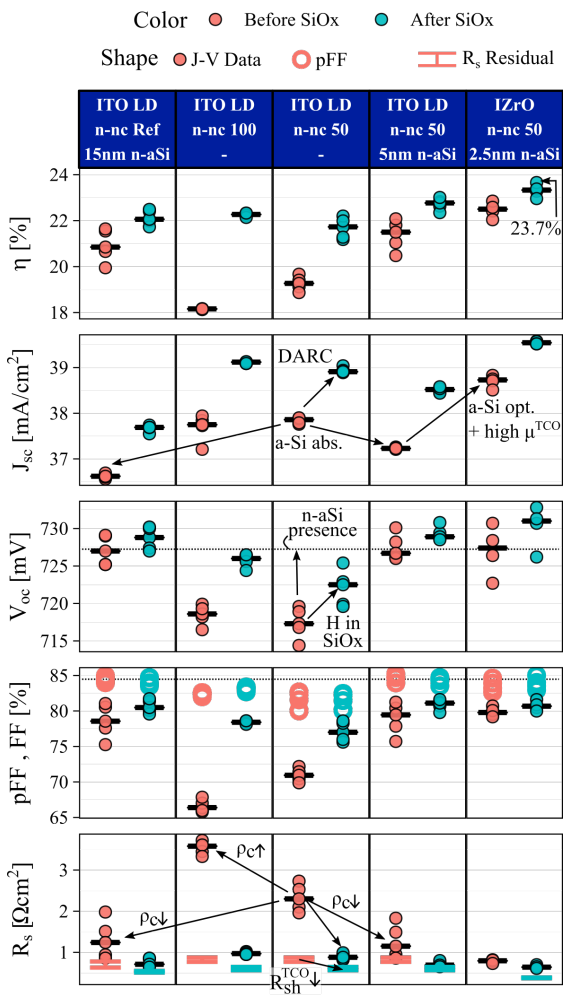

Figure 6.7: Passivation and transport properties of the multilayer solar cell structures showed on Figure 6.1(b) using a highly doped nc-Si:H(n) layers of 12.5 nm. *In the bottom row, the error bars represent the residual series resistance (excluding the front ρ_c) when assuming no lateral transport coupling with the wafer, i.e.* $R_s^{res} = \rho_c^{back} + R_{s,vert}^{h^+} + R_s^{grid} + R_s^{TCO}$. *The solar cells have an area of* $2 \times 2\,\mathrm{cm}^2$.

Optical characterization

We discuss the optical properties of the solar cells thanks to the J_{sc} values and the corresponding EQE presented on Figure 6.8. A current drop proportional to the a-Si:H(n) thickness is observed in the short-wavelength range. All conditions yield similar EQE values in the 600–900 nm range, confirming that passivation quality is sufficient for all devices to not impact J_{sc}. Finally, using IZrO instead of ITO additionally improves the EQE of +0.4 mA cm^{-2} in the IR thanks to a better transparency, enabling an EQE-calculated current density of 40.7 mA cm^{-2}. We estimate that the nc-Si:H layer is still responsible for -0.53 mA cm^{-2} of J_{sc} loss for the 12.5 nm-thick layer employed here (-0.042 mA/cm^2/nm). The a-Si:H(n) layer is still responsible for a loss of -0.33 mA cm^{-2} for a 2.5 nm thick layer (-0.132 mA/cm^2/nm). Note that we have

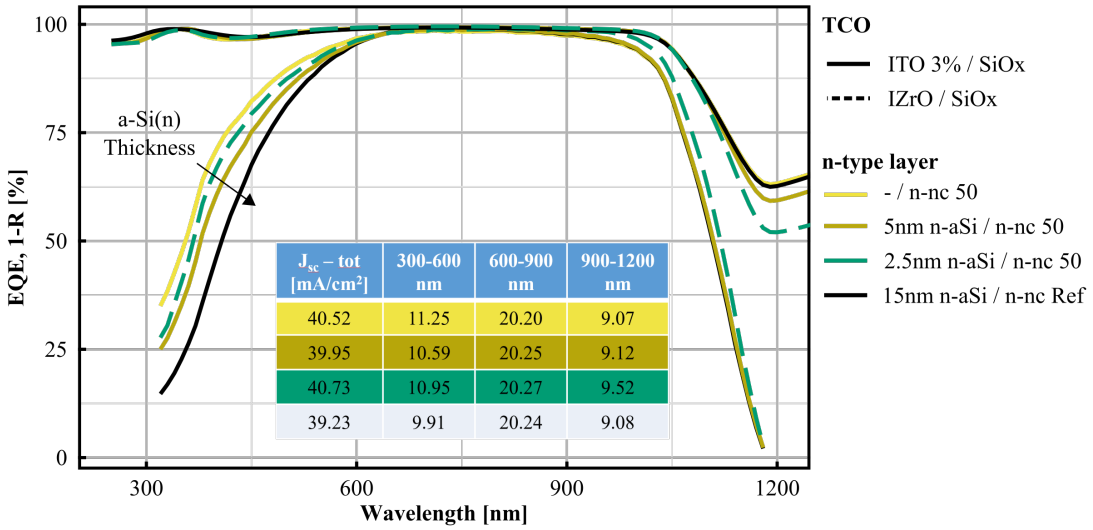

J_{sc} – tot [mA/cm²]	300-600 nm	600-900 nm	900-1200 nm
40.52	11.25	20.20	9.07
39.95	10.59	20.25	9.12
40.73	10.95	20.27	9.52
39.23	9.91	20.24	9.08

Figure 6.8: EQE and total reflectance of the multilayer structure corresponding to the IV results of Figure 6.7. The 50 sccm nc-Si:H(n) layer thickness is 12.5 nm.

not tried thinning down further those layers and there might be still room for improvement. Reducing the TCO's thickness and completing the ARC with a more transparent SiNx deposited after metallization is another promising way to gain a further +0.5–1 mA cm^{-2} [Li 2021b] and should be pursued to realize high current SHJ without requiring any patterning or masking step. However, unintentional increase of FCA in the TCO [Meyer 2021] or contamination by the screen-printing solvents (see sup. info. of ref. [Li 2021a]) complexify its realization and a dedicated study would be required.

Thin TCO and ρ_c evaluation

To evaluate ρ_c, we choose not to rely on TLM measurements, since in our specific case the evaluation of ρ_c after the SiO_x deposition could be problematic due to the large silver pads masking the deposition under the contact. Therefore, we decided to perform a breakdown of the different components of the series resistance of the solar cell and extract ρ_c out of it. For this, we used the model of Haschke *et al.* to take into account the coupling of the lateral transport through the absorber and the TCO when low contact resistivity values are reached [Haschke 2020], which we already introduced in section 5.3.

To increase the dependency of R_s upon ρ_c and improve the accuracy of the method to extract this parameter, we processed similar solar cells as in the last section, except with only 20 nm of IZrO. This increases the sheet resistance of the TCO and therefore increases the dependency of R_s upon ρ_c [Haschke 2020]. The solar cell results and extracted ρ_c values are presented in Table 6.3. More details on the extraction of each parameter are given in the appendix A.4.2. As expected, the single 50-sccm layer yield high ρ_c values which are decreased after the SiO_x deposition or by using a more amorphous layer underneath, such as the 100-sccm layer or the

	n-nc 50sccm 120s -		n-nc 50sccm 60s n-nc 100sccm 60s		n-nc 50sccm 120s 2.5nm aSi(n)		n-nc 50sccm 300s 15nm aSi(n)	
	Before SiO_x	After SiO_x	Before SiO_x	After SiO_x	Before SiO_x	After SiO_x	Before SiO_x	After SiO_x
R_{sh}^{TCO} [Ω/sq]	1900–3000	475–630	950–2000	250–350	1550–2600	300–400	800–1250	250–500
FF [%]	64.27	74.43	74.71	77.07	79.12	80.04	81.07	81.21
pFF [%]	82.47	82.69	82.6	82.86	82.93	83.3	84.19	84.33
Rs [Ω.cm^2]	3.99	1.79	1.79	1.23	**0.8**	**0.73**	0.72	0.61
ρ_c [mΩ.cm^2]	250–700	250–500	70–250	65–250*	**< 15**	**< 15***	< 15	< 15*

Table 6.3: Transport properties of solar cells using a 20 nm-thick IZrO as front TCO. Minimum and maximum of values for ρ_c are extracted from $R_s = R_s^{grid} + R_s^{lat+C}(R_{sh}^{c-Si}, R_{sh}^{TCO}, \rho_c) + R_{s,vert}^{h^+} + \rho_c^{back}$ using the coupled lateral transport model of [Haschke 2020] and taking into account the inaccuracy on the determination of the different input parameters. Note that after SiO_x, the uncertainty of the method increases since the sheet resistance decreases. We therefore capped the values of ρ_c by their maximum values before SiO_x (*), since we demonstrated on Figure 6.6 that this coating tends to decrease ρ_c.

a-Si:H(n) one. When using only 2.5 nm of a-Si:H(n), ρ_c values below 15 mΩcm^2 are obtained, leading to decent *FF* of 79.12 % even with a R_{sh}^{TCO} as high as 1500 Ω/sq. Moreover, increasing the thickness of both the a-Si:H(n) and the nc-Si:H(n) layers does not yield lower ρ_c values, showing that thin a-Si:H(n)/nc-Si:H(n) contact can be used to reach as low contact resistivity without impeding transparency as dramatically. We note a lower *pFF* with the thin contact, which was not the case when using thicker IZrO. More data would be required to determine if the thinner contacts suffer from passivation losses when using a thin TCO.

6.5 Optical gain of replacing front TCO by SiN_x

In the previous sections, we demonstrated it is possible to reach good contact resistivity values ($\rho_c < 15\,\mathrm{m\Omega\,cm^2}$) using a thin stack of 2.5 nm a-Si:H(n) / 12.5 nm nc-Si:H(n). As such a low value decreases the dependency on the TCO to provide lateral transport [Haschke 2020], it opens the opportunity to use more transparent anti-reflective coating schemes. In this section, we explore the optical gain of replacing IZrO by silicon nitride (SiN_x) either completely, as pioneered in [Li 2021b], or using bi-layers of thin IZrO / thick SiN_x.

The first approach, forming the ARC only with SiN_x, is interesting to evaluate the optical gain achievable by replacing totally the TCO. The second bilayer structure is relevant for two reasons: first, the TCO is still required under the fingers to avoid direct metal contact between the silver and the silicon layers and to keep the contact resistivity low. Taking this into account, keeping a thin TCO on the full area avoids the need of a patterning step. Second, even with $\rho_c = 15\,\mathrm{m\Omega\,cm^2}$, a TCO sheet resistance in the range 500–1000 Ω/sq is still required to keep the *FF* losses below 2 % (see Figure 5.11).

Figure 6.9 presents the absorption and reflectance spectra on glass of IZrO and SiN_x layers as well as bilayers of the latter two materials. The SiN_x layer was deposited via PECVD at 250 °C

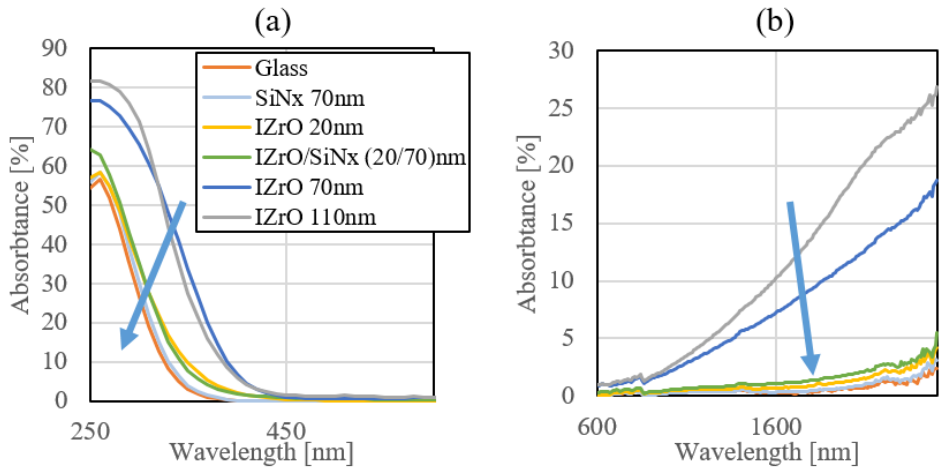

Figure 6.9: Absorptance of layers deposited on glass of: IZrO layers of different thicknesses, a SiN_x layer and a bilayer of the latter two materials. The glass substrate is present as a reference. (a) UV-vis range. (b) Infrared range.

using a gas mixture of SiH_4 and NH_3.

In the UV-Vis wavelength range, we can see that 70 nm and 110 nm of IZrO lead to a similar absorptance, which is significantly stronger than for all the other layers. In contrast, the 70 nm SiN_x layer presents absorptance as low as the glass reference substrate. Promisingly, the 20 nm-thick IZrO layer as well as the 20 nm IZrO / 70 nm SiN_x bilayer absorb only slightly more than the single SiN_x layer. In the infrared, the same trends can be observed, with a strong absorptance of the thick IZrO layers, while the thinnest IZrO, the SiN_x and the bilayer all present an absorptance lower than 1 % at 1200 nm. Nevertheless, it can be noticed that the bilayer possesses more FCA than the single 20 nm-thick IZrO, which itself has a higher absorptance in the IR than the SiN_x layer, as expected as the latter does not have any free carriers. The fact that the bilayer absorbs more could be attributed to a slight increase in dopant concentration of the IZrO due to the hydrogen delivered during the deposition of the SiN_x layer.

Motivated by those results, we processed the three $1 \times 1\,cm^2$ solar cells presented on Figure 6.10(a)-(c). It features first a reference using IZrO to form a single ARC (115 nm on flat substrate). The second cell was realized by localizing the IZrO layer below the sputter front grid using a single shadow mask for both steps and then depositing the SiN_x layer on top via PECVD (110 nm on glass). The cell featuring an IZrO / SiN_x bilayer was processed by first depositing the thin IZrO layer on the full cell area (20 nm), then sputtering the front grid through a shadow mask and finally covering the whole area again with SiN_x (110 nm on glass, as before). All the cells were annealed at 210 °C for 30 min after the front grid deposition, therefore prior to the SiN_x deposition. Note also that as the SiN_x deposition was performed at 250 °C, which could damage the passivation, the lifetime of a dedicated sample featuring the same PECVD

layers was tracked before and after this step and was shown to actually increase by 0.5 ms (at $\Delta n = 1 \times 10^{15}\,\mathrm{cm}^{-3}$), probably stemming from a small hydrogenation provided by the plasma, similar to what we observed with the SiO_x deposition used to forming DARCs. Note also that on the rear side, a 230 nm IZrO layer was used in place of our baseline lowly doped ITO layer, due to an unavailability of the ITO target at the time of this experiment. Therefore, the absorption in the IR might be slightly different than when using our baseline process. Finally, in (d) we recall the structure of the previously used structure featuring a IZrO / SiO_x DARC at the front side, which we will discuss in the comparisons of the EQEs.

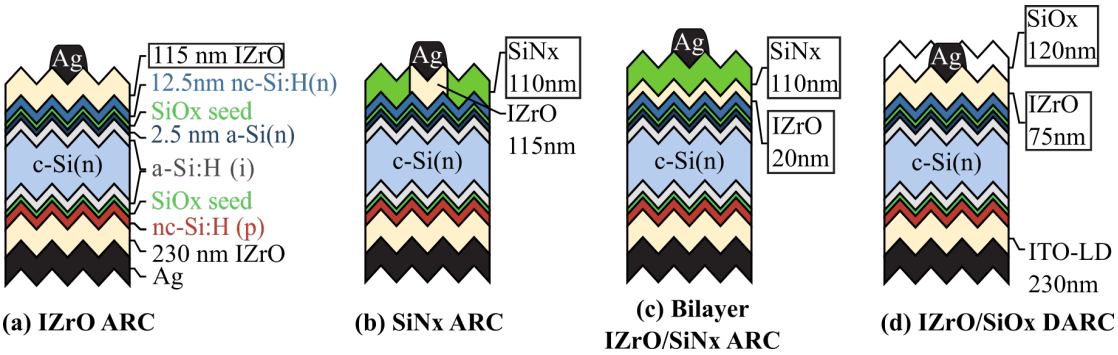

Figure 6.10: Solar cells featuring a single ARC formed with (a) an IZrO single layer, (b) a SiN_x single layer, (c) a thin IZrO / SiN_x bilayers. In (d), the DARC structure used in the previous sections is represented again for comparison. All the thicknesses are given as measured on flat samples. Note that in (b), the thickness of the IZrO might be lower due to the shadow mask, nevertheless the same deposition conditions were used as in (b), thus we keep the same label.

The EQE and reflectance of those three new solar cells are presented on Figure 6.11, together with the DARC structure used in the previous sections as a comparison. It can be seen that the minimum of reflection provided by the SiN_x layer and IZrO / SiN_x bilayer is found at higher wavelengths than for the single IZrO ARC. This indicates that the deposition time of the SiN_x should be optimized to realize thinner layers to form a better ARC. Nevertheless, it can be seen that the loss of reflectivity between 300–600 nm are compensated in the 600–900 nm range, where both the SiN_x and IZrO / SiN_x outperform the single IZrO ARC, being comparable to the IZrO / SiO_x DARC. A gain in the infrared can also be seen for the SiN_x layer, as expected compared to the thicker TCO layers. Unfortunately, we observed that the thin IZrO / SiN_x bilayer is less transparent than the single SiN_x layer in the whole wavelength range. This is surprising compared to our results of absorptance on glass samples (Figure 6.9), where the bilayer was almost as transparent as the SiN_x. This might be due to a reproducibility problem of either our thin IZrO deposition or SiN_x deposition. Also, it is possible that depending on the deposition conditions, the SiN_x reduces chemically the IZrO, which decreases its transparency [Kim 2006]. More investigations should be carried out to conclude on the bilayer performances and thin (> 5 nm) protective oxide layer or NH_3-free plasma for the SiN_x deposition could be envisioned to improve the robustness of the process, as well as using a more resistant TCO towards those reactions [Kim 2006]. Assuming that those issues can be overcome, such as in [Bätzner 2019], in the following we can interpret the single SiN_x results as the maximum

optical gain that could be achieved using this bilayer strategy.

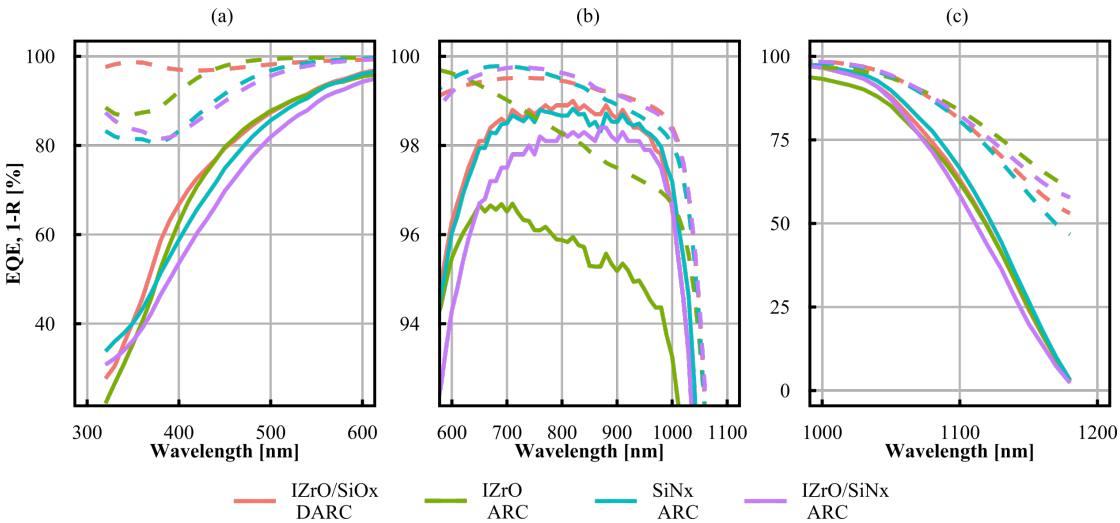

Figure 6.11: EQE and measured reflectance spectra of the structure presented in Figure 6.10.

To provide a quantitative analysis, we computed the different current losses occurring in those four solar cells, including the additional losses of the grid. These are exposed in Figure 6.12. More details on the definition of those losses can be found in [Paviet-Salomon 2015]. We observe quantitatively similar trends already discussed in the previous paragraph : It can be seen that the SiN_x layer and the bilayers reach similar reflectance losses of 1–1.1 mA cm^{-2} compared to the single ARC IZrO, compensating between their stronger reflectance in the UV by a smaller one in the visible range. In the UV, the use of SiN_x allows a gain of +0.2–0.3 mA cm^{-2} on A_{short} compared to the use of a single ARC IZrO or DARC IZrO / SiO_x. In the IR, the SiN_x reduces strongly the absorption losses compared to the single ARC IZrO, lowering this loss of 0.6 mA cm^{-2}. However, unfortunately not all of this current can be collected, due to imperfect light trapping [Paviet-Salomon 2015, Boccard 2018] and therefore about half of it still escapes the solar cell as shown by the increase of the escaped light losses. Nevertheless, these two losses combined result in a gain of +0.3 mA cm^{-2} in the IR when using the SiN_x ARC compared to both the situations using the single IZrO ARC or IZrO / SiO_x DARC. However, the largest share of current loss is still stemming from the absorption of the front layers here. Further decrease of the silicon layer thickness should be carried out. The 8.3 nm-thick a-Si:H(i) layer used here can be accounted for about 0.50 mA cm^{-2} current losses according to [Holman 2014], while we evaluated in the previous section the 2.5 nm a-Si:H(n) and the nc-Si:H(n) layers to be responsible of 0.35 mA cm^{-2} and 0.55 mA cm^{-2}, respectively. This amounts to 1.4 mA cm^{-2}, which compared to the measured 1.7 mA cm^{-2} would indicate that still about 0.3 mA cm^{-2} are absorbed in our 110 nm SiN_x layer.

In Table 6.4, we report the different current gains that could be achieved by adopting additional strategies reported in the literature. We estimate the gain of current that they could generate if applied to our best solar cell so far (first line of the table). Optimistically, reducing the thickness of each front silicon layer by half (assuming this does not impinge on the contact

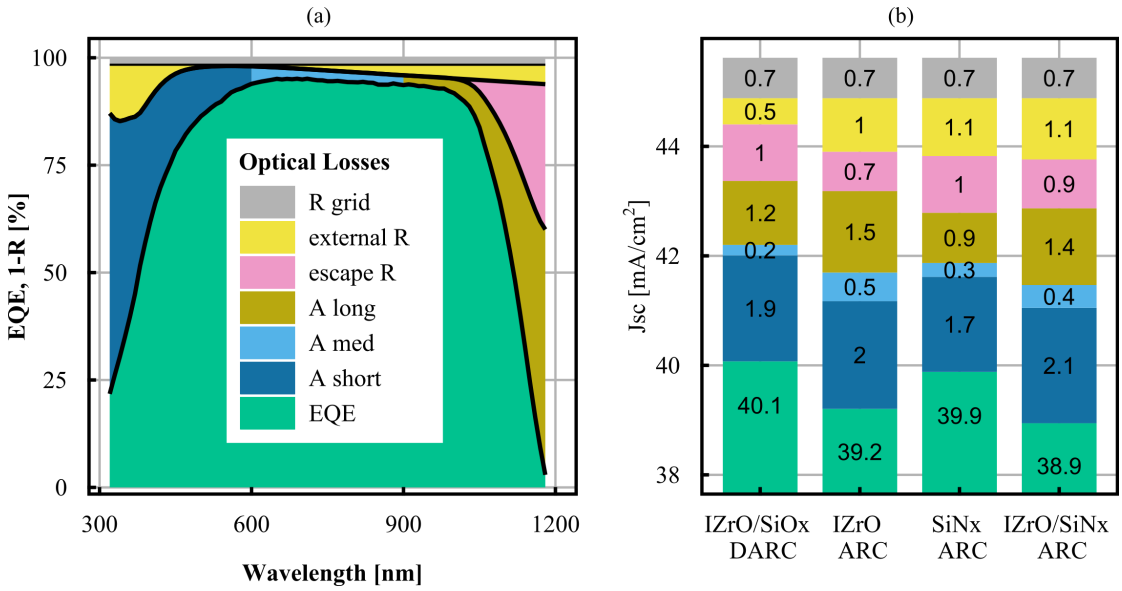

Figure 6.12: (a) Example of a decomposition of the EQE in different sources of losses, namely the grid shadowing (estimated to be equal to the finger width devided by the pitch w_f/p = 30/1850 = 1.6%), the external reflectance (deconvoluted from the measured reflectance that also takes into the escape loss, using a linear fit in the range 700–900 nm*), the escaped photons, and the absorption in the long (*900–1180 nm*), medium (*600–900 nm*) and short (*300–600 nm*) wavelength range. The current losses in (b) correspond to the integral with the AM1.5G spectra of the different areas defined here, for the four samples under study described in Figure 6.10.*

properties) could help to gain an additional 0.5–0.7 mA cm^{-2} current gain [Boccard 2021], which still leaves a 1.0 mA cm^{-2} current loss in those layers.

If a IZrO / SiO_x DARC is used, a gain of +0.5 mA cm^{-2} can be made by improving the external reflection losses. We extrapolated this result to the SiN_x/ SiO_x DARC, which could be interesting to realize in a single PECVD reactor, and would lead a current gain of +1.1 mA cm^{-2}. If the rear reflector properties were improved, *e.g.* by thinning down the rear TCO and using a MgF_2 or SiO_x layer in between the latter and the silver [Boccard 2021, Cruz 2022], a gain of +0.6 mA cm^{-2} could be achieved in the IR.

If two of these strategies are performed together, current higher than 40.3 mA cm^{-2} could be achieved. However, as stated before the gains do not simply add up, as part of the light non-absorbed in a given layer will be either absorbed in another one, or escape the solar cell. Thinning down the layers and managing to realize the front ARC with a SiN_x layer is probably the most industrially relevant option of the three of the second section of the table [Bätzner 2019, Boccard 2018, Cruz 2022] and could be *e.g.* combined in the realization of a front copper plated metallization, which requires indeed a dielectric coating on the whole surface as protection during the plating process, going one step further to realizing an indium and silver free SHJ solar cells [Lachowicz 2021].

Method	Gain Uv-Vis ($mA\,cm^{-2}$)	Gain in IR ($mA\,cm^{-2}$)	Total gain ($mA\,cm^{-2}$)	Total current ($mA\,cm^{-2}$)	Ref.
8nm a-Si(i), 2.5nm a-Si(n), 12.5nm nc-Si(n), IZrO ARC	/	/	/	39.2	This work
Thinning silicon layers by half	0.5-0.7	0	0.5-0.7	39.7-39.9	This work + [Boccard 2021]
DARC IZrO/SiOx	0.5	0	0.5	39.7	Appendix of this work
ARC SiNx	0.3	0.3	0.6	39.8	This work
DARC SiNx/SiOx	0.8	0.3	1.1	40.3	Estimated from previous
Rear reflector	0	0.6	0.6	39.8	[Boccard 2021], [Cruz 2022]
Thinning + ARC SiNx	0.8-1.0	0.3	1.1-1.3	40.3-40.5	From previous
ARC SiNx + Rear refl.	0.3	0.8	1.1	40.3	Estimated from Ray tracing
DARC SiNx/SiOx + Rear refl.	0.8	0.8	1.6	40.8	Estimated from Ray tracing
Thinning + ARC SiNx + Rear refl.	0.8-1.0	0.8	1.6-1.8	40.8-41	From previous
Thinning + DARC SiNx/SiOx + Rear refl.	1.3-1.5	0.8	2.1-2.3	41.3-41.5	From previous
SHJ - FJ - Copper plated - Kaneka	/	/	/	40.8 (ap)	[Adachi 2015]
SHJ-IBC - Kaneka	/	/	/	42.7 (da)	[Yoshikawa 2017]
TOPCon - Fraunhofer ISE	/	/	/	42.9 (da)	[Richter 2017]]
Lambertian limit	/	/	/	44.1	[Boccard 2018]

Table 6.4: Estimated current gains from our present solar cell (first line) using different strategies from the literature, including those presented in this section. The second and third part of the table present the combination of those strategies. As the current gains do not simply add up, some combinations were estimated using ray tracing simulations [PV-Lighthouse 2016]. Finally the last section of the table presents the highest currents certified for relevant technologies and the Lambertian limit. "da" and "ap" mean designated illuminated area and aperture area, respectively.

The third section of Table 6.4 shows that if three of these strategies were realized, current up to 41 $mA\,cm^{-2}$ could be achieved with double side contacted SHJ solar cell. These should be compared with the record front junction solar cell of Kaneka (in terms of J_{sc}), which reaches a current of 40.8 $mA\,cm^{-2}$, close to those predictions. In comparison, IBC[1] and TOPCon solar cells are still reaching much higher current, above 42.5 $mA\,cm^{-2}$, which seems unfortunately inaccessible for double side contacted SHJ solar cells without resorting to contact localisation strategies or finding more transparent materials, such as MoO_x [Dréon 2021].

6.6 Roadmap to increase efficiency

In this last section, we draw a roadmap to improve the efficiency of our device until levels comparable to the one presented recently by LONGi. Indeed, using a RJ bifacial SHJ device, this company reached recently a certified efficiency of (26.30 ± 0.39) % [Pv-magazine 2021a], close to the record of 26.7 % held by SHJ-IBC solar cell [Yoshikawa 2017], increasing the interest of the former architecture.

[1] In comparison, a localized structure or IBC structure which would consists of only the same a-Si:H(*i*) passivation layers capped with SiN_x on the front side will not even loose the 0.55 $mA\,cm^{-2}$ associated to the intrinsic layer absorption in the other structures, as the carriers photogenerated in this layer can be injected into the absorber as long as it is not covered with doped layers as shown in [Paduthol 2018]. Moreover, the IBC structure will not suffer from the additional 0.7 $mA\,cm^{-2}$ loss due to grid shading.

To compute the gains provided by each step of the roadmap, we proceed as follows: first we compute the intrinsic limit for our device using Richter's limit [Richter 2013], given the absorber width W, the donor density N_D and the generated current J_L. To evaluate the latter, we estimate the shading of the grid as w_f/p, where w_f is the finger width and p the pitch of the grid, and apply it on the EQE measured current as $J_L = J_{sc}^{EQE}(1 - w_f/p)$. On top of that, we take into account perimeter losses, which depends on the solar cell length L (assuming a square design). We give the detailed calculations for the latter in section A.5. As explained there, even the best of our solar cells measured in this thesis do not reach the V_{oc} and *pFF* predicted by the theoretical limit, even when taking into account the perimeter losses. Therefore, an extra effective recombination velocity term S_{extra} is added to take this into account in our model. The latter should take moderately low value, between 1–2 cm/s according to our estimation in section A.5. However, one should note that the discrepancy between the best measured V_{oc} and *pFF* and the theoretical limit could also come from selectivity losses, which we did not account for in the present model and should be investigated to improve the accuracy of our predictions[2]. Once the implied *J-V* curve accounting for those recombination mechanisms has been computed, we determine for each injection level the distributed resistance $R_s(\Delta n)$ that takes into account the injection dependence of lateral and vertical transport, as we did in chapter 5 and section A.4.2, using Haschke's model [Haschke 2020]. This includes additional parameters which are R_{line} the finger line resistance, ρ_c^{front} and ρ_c^{rear} the front and rear contact resistivities as well as R_{sh}^{TCO}. Finally, the external voltage is computed for each injection as $V = iV(\Delta n) - R_s(\Delta n) * iJ(\Delta n)$, constructing the *J-V* curve out of which the efficiency, V_{oc} and *FF* are calculated.

As shown in Figure 6.13, we see that already increasing the solar cell size to 274.4 cm^2 (the same as the solar cell of LONGi), results in more than half a percent efficiency gain thanks to a large boost of V_{oc} and *FF*. Note that this assumes a perfect edge passivation as well as an adapted grid design to avoid R_s^{finger} to become too large. In our computation, we kept their lengths at 2 cm, which can be justified as finger lengths as short as 0.43 cm are *e.g.* featured in the smart wire connection technology [Söderström 2020], while the busbars resistive losses can be removed during the *J-V* curve certification [Bassi 2002] (which is the case for LONGi's certification [Pv-magazine 2021a]).

The next step of optimization (#3) is to reduce the thickness of each front silicon layer by two, assuming this do not impact the contact properties, which could yield a boost of 0.5–0.7 mA cm^{-2} [Boccard 2021] as explained in the previous section. After these two steps, efficiencies above 25 % can already be reached, provided a low value of S_{extra}. Then, in step (#4) the use of an IZrO / SiN_x bilayer results in an additional gain in current of 0.6 mA cm^{-2}. However, this is accompanied by a reduced R_{sh}^{TCO} which compensates the efficiency gain (a value of 500 Ω/sq was used). Nevertheless, this can still result in a decrease of costs and reduce indium usage, as shown in [Bätzner 2019]. Then, in step (#5), reducing the wafer thickness to a

[2] However, to our knowledge no simple model has been reported so far that takes into account selectivity effects (as defined by Würfel [Wurfel 2015]) and distributed series resistance effect for the lateral transport such as Haschke's model [Haschke 2020].

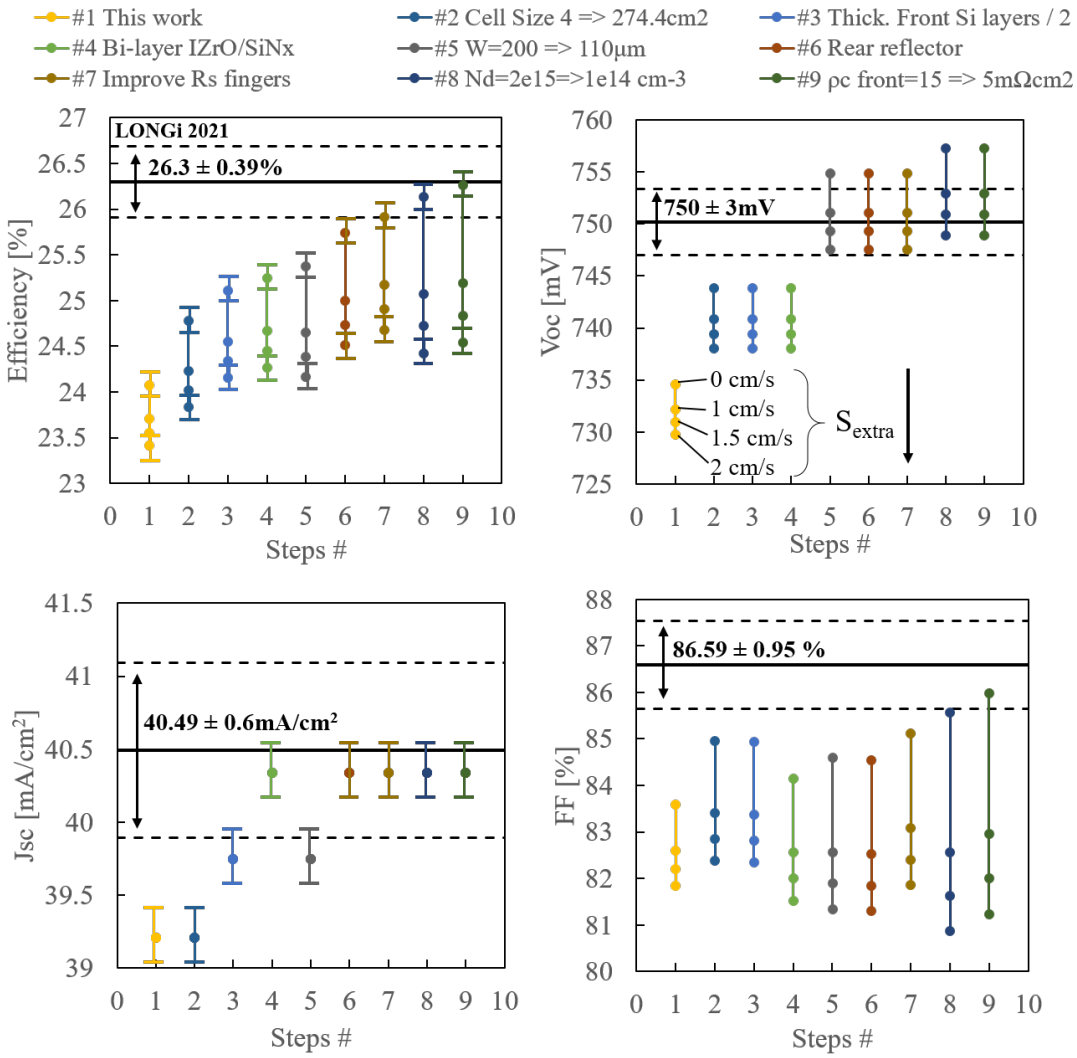

Figure 6.13: Efficiency roadmap for the device presented in this work (#1) corresponding to a $2 \times 2\,\mathrm{cm}^2$ *screen printed solar cell with a 8nm a-Si:H(i) / 2.5nm a-Si:H(n) / 12.5nm nc-Si:H(n) / IZrO ARC stack on the front side, an a-Si:H(i) / nc-Si:H(p) / lowly doped TCO / Ag full area stack on the rear side and a* $200\,\mu\mathrm{m}$ *c-Si(*n*) wafer with* $N_D = 2.2 \times 10^{15}\,\mathrm{cm}^{-3}$*. To model it, we assumed the following parameters* $J_{sc}^{EQE} = 39.85\,\mathrm{mA\,cm}^{-2}$*,* $L = 2\,\mathrm{cm}$*,* $p = 1.85\,\mathrm{mm}$*,* $w_f = 30\,\mu\mathrm{m}$*,* $R_{line} = 1.9\,\Omega/\mathrm{cm}$*,* $R_{sh}^{TCO} = 100\,\Omega/\mathrm{sq}$*,* $\rho_c^{front} = 15\,\mathrm{m\Omega\,cm}^2$ *and* $\rho_c^{rear} = 100\,\mathrm{m\Omega\,cm}^2$*. The solid black line represents the recent record efficiency for the double-side contact RJ SHJ cell of LONGi together with the uncertainties reported on those values [Pv-magazine 2021a]. The different improvement steps of our roadmap are explained in the main text. Note that for every step, we perform the computation with four different additional effective recombination velocities* S_{extra}*, to take into account the remaining drop of* $\mathrm{V_{oc}}$ *and* pFF *of our device compared to the calculated efficiency limit (see appendix A.5). Error bars of* $\pm 0.2\,\mathrm{mA\,cm}^{-2}$ *are added on the estimation of current, due to the differences that can occur between various optical modellings, as well as their respective impact reported on efficiency.*

theoretical optimum of 110 µm [Richter 2013] can improve the V_{oc} by almost 10 mV, however this results in a drop of current of about 0.6 mA cm^{-2} in the infrared. Moreover, if the surfaces are not perfectly passivated, the negative influence of S_{extra} will be stronger with a thinner wafer. Nevertheless, this loss of current can be compensated provided the rear reflector properties are improved (step #6). Note that in the case on LONGi's certification, they used a bifacial solar-cell design measured on top of gold-coated brass chuck [Pv-magazine 2021a], which could also reduce the plasmonic absorption in their characterization and improve the current in the infrared. After those steps, the efficiency reached is still lower than 26 % even with S_{extra} = 0 cm/s, which can be resolved by further improving the finger series resistance (by reducing R_{line} and the finger length to 0.6 Ω/cm and 0.43 mm as for smart wires [Söderström 2020]), decreasing the wafer doping or managing to lower further ρ_c^{front}, which might occur thanks to the thinning of the a-Si:H(*i*) layer in step #2, at least in contacts featuring only amorphous silicon contact [Luderer 2022].

Therefore, according to our computations, realizing those steps could allow the industry to reach an (effective busbarless) efficiency above 26 %, without necessitating any patterning of the layers and contact localization. However, several optimistic assumptions were made along the discussion, and it remained to be seen if as excellent surface passivation and contact properties can be achieved with ultra thin front layers compared to their thicker counterpart in order to reach efficiencies higher than 25 %. In this perspective, additional treatments that boost the passivation such as forward bias [Cattin 2021] or the beneficial hydrogenation provided by SiO_x or SiN_x should help to reach high performances.

6.7 Conclusion and perspectives

We developed nc-Si:H(n) layers for application as window layer in SHJ solar cells through a detailed and systematic approach, taking into account the material inhomogeneity along its growth direction and the interaction with the other layers of the stack. Performing thickness and doping series, we observed that an increase of the PH_3 flow leads to an amorphization of the first 10-15 nm of the layers. This results in an interplay between having a strong doping in the nucleation zone or having a higher crystallinity at the n/TCO interface.

First, in order to improve the low doping of the nucleation zone of nc-Si:H(n) at the i/n interface, a thin a-Si:H(n) buffer layer was used and shown to improve the passivation, selectivity and contact resistivity. Second, increasing the doping of the ITO was also shown to improve the contact resistivity at the n/TCO interface. Finally, we also reported on the beneficial effect of an additional SiO_x capping layer which not only forms a DARC but also improves impressively the passivation, selectivity and contact resistivity, broadening the window of parameters leading to efficient contact. We speculate that the hydrogen provided during the SiO_x deposition could passivate defects in the different layers or increase the ITO doping at the n/TCO interface, which would improve the transport.

Thinning down the a-Si:H(n) layer to 2.5 nm, adding on top the optimally doped 12.5 nm

nc-Si:H(n) layer, and using an IZrO / SiO_x bilayer as DARC allowed to improve the current of the solar cell, resulting in an efficiency up to 23.7 %, V_{oc} of 733 mV, *FF* of 81.6 % and J_{sc} of 39.6 mA cm^{-2}. The a-Si:H(n) and nc-Si:H(n) layers account for -0.33 mA/cm^2 and -0.53 mA/cm^2 current losses respectively. The contact resistivity reached values lower than 15 mΩcm^2, alleviating the need for lateral conductivity of the TCO. This could broaden the range of compatible transparent electrodes for the front side, such as thin TCO/SiNx bilayer to reduce the absorption losses. We explored the possibility offered by this strategy and conclude that it could yield a current gain up to +0.6 mA cm^{-2}. The absorption loss in the front silicon layers remains the highest optical loss, and additionally reducing those layers thickness by half and/or oxidizing part of the nc-Si:H(n) layer could bring the current to above 40.3 mA cm^{-2}, providing this does not impinge on the contact performance. We finished the discussion by presenting an optimization roadmap, showing a possibility for double-side contacted SHJ cells to reach efficiencies above 26 %.

7 Conclusion and perspectives

Today more than ever the world needs clean energy sources and thus a fast deployment and scaling up of the photovoltaic industry. In a context of liberalized economy, the latter is triggered by the decrease of the technology price, induced in particular by the increase of solar cell efficiency. Nowadays, the PERC solar cell, the most mainstream technology, is short from reaching its practical industrial limit of 24 % and a fierce competition opposes its direct next successors, which are most likely the TOPCon and SHJ solar cells, the latter being in the focus of this thesis. While c-Si solar cells have been leading the c-Si single junction record efficiency since 2013, this remained exclusively possible thanks to the IBC architecture which eliminates front grid shading and parasitic absorption in the front contact layers, the most important drawback of SHJ solar cells. However, a 26.7% efficiency was recently demonstrated for double-side contacted solar cells by some important industrial actors [Pv-magazine 2021a], showing that this architecture can reach efficiencies as high as the IBC structure. However, the list of industrial actors realizing such performances remains thin and it is required to democratize the knowledge behind those discoveries in order to create a healthy industrial rivalry.

Throughout this thesis, we explored, described and analysed in depth and carefully the development of doped nano-crystalline silicon layers deposited via PECVD, a promising material to replace classical amorphous silicon layers which provides highly conductive and transparent passivating contacts to SHJ solar cells.

First, in chapter 4, we investigated the influence of TMB and BF_3 as dopant sources on the transparency, contact properties of nc-Si:H(p) layers and their integration in solar cells. We exposed the roles of both gases to modify the crystallinity of the layer and find different optima for both of them leading to high efficiencies. We observed a correlation between the *FF*, reaching up to 83% in $2 \times 2\,\text{cm}^2$ solar cells, and the characterization of the layers in terms of dark conductivity activation energy. The main discrepancies between the dopant precursors were observed in the realization of a high crystallinity above 60% to reach higher J_{sc} and at the same time a low activation energy which correlates with high a *FF*. This was shown possible using very low flow of TMB, whose potential was illustrated by presenting a certified 23.9%-efficient solar cell. In contrast, for BF_3-prepared layers, high dopant flows

were required to reach low activation energy, yielding *FF* up to 83% , *i.e.* slightly higher than for TMB, however at the cost of transparency. Nevertheless, this second type of layers remains of interest for rear side application.

As the nc-Si:H layers are sandwiched between the intrinsic amorphous silicon and the TCO, the interactions among those materials shape the contact stack development into a subtle optimization problem. We reported evidences that a SiO_x seed treatment of the a-Si:H(*i*) layer prior to the deposition of nc-Si:H(*p*) can allow for the growth of crystallites without incubation zone, provided an optimal dopant flow is used. At the other end, we observed that the high nc-Si:H crystallinity influences the subsequent growth of the TCO, reducing its mobility as already reported by other authors [Cruz 2019a]. Hopefully, part of it can be recovered using a PECVD post-metallization SiO_x deposition, which at the same time forms a double anti-reflective coating as well as enhances the passivation. Finally, the current of the solar cell can be bring even further by optimizing the a-Si:H(*i*) and nc-SiO_x:H layer thicknesses on the front side as well as evaporating a MgF_2 layer through a shadow mask at the rear side between the TCO and the Ag layer. Implementing those two strategies yield a certified efficiency of 24.44% for a $2 \times 2\,cm^2$ screen-printed front junction solar cell.

In chapter 5, we performed accurate series-resistance breakdown of our best front-junction solar cells, featuring nc-Si:H(*p*) layers at the front and reaching *FF* above 82.5%. We compared different methods of characterization for the contact resistivity, namely TLM and symmetrical samples, and performed injection dependent analysis using a state of the art model for the lateral transport [Haschke 2020]. We identified precisely a contact resistivity of $100\,m\Omega\,cm^2$ for those layers. We also attempted to resolve a possible injection dependence of the contact resistivity, which could have important impact in the realization of localized contacts. However, we concluded that the methods employed to assess the contact resistivity (*i.e.* here either TLM, symmetrical samples or series resistance breakdown) cannot deliver a precise answer to this question, and that the impact of injection on ρ_c between MPP and OC remains much below $100\,m\Omega\,cm^2$. We suggest that much longer TLM samples, with small gaps between the pads should be used for this purpose in order to remove unwanted edge effects and maximize the sensitivity on contact resistivity. This nevertheless brought us interesting insights into the transport mechanisms of illuminated *pNp* structures, which can be of interest in the understanding of new contact structures and at the same time shares similarities with bipolar transistors.

In chapter 6, we developed *n*-type nc-Si:H layers for application as window layer, pushing further our characterization strategy developed when studying their *p*-type counterpart. First, we observed that the characterization technique often used in the literature to study these layers, such as dark lateral conductivity or UV-Raman crystallinity, can present similar results for thick layers which however lead to very different solar-cell properties. To unravel those characteristics, we performed thickness and doping series to unravel the layer properties along its growth direction. We observed that an increase of the PH_3 flow leads to an amorphization of the first 10-15 nm of the layers.

This results in an interplay between realizing a strong doping in the nucleation zone or a higher crystallinity at the n/TCO interface. In order to improve the low doping of the nucleation zone of nc-Si:H(n) at the i/n interface, a thin a-Si:H(n) buffer layer was used and shown to improve the passivation, selectivity and contact resistivity. More investigations should be carried out to find deposition regimes where the nc-Si:H(n) layer nucleates directly on top of the SiO_x seed layer in order to remove the introduced a-Si:H(n) layer. Increasing the doping of the ITO was also shown to improve the contact resistivity at the n/TCO interface and we believe there is a potential to lower further down ρ_c by exploring other types of TCO as those studied in this thesis, such as AZO due its lower work function. Finally, we also reported on the beneficial effect of the additional SiO_x capping layer which not only forms a DARC but also improves impressively the passivation, selectivity and contact resistivity, broadening the window of parameters leading to efficient contact. We speculate that it is the hydrogen present during the SiO_x deposition that provides those properties and that similar observations might be true when using a SiN_x capping layer.

We then explored an optimization pathway of our n-type layers. Thinning down the a-Si:H(n) layer to 2.5 nm, adding on top the optimally doped 12.5 nm nc-Si:H(n) layer, and using a IZrO / SiO_x bilayer as DARC allowed to improve the current of the solar cell, resulting in an efficiency up to 23.7 %, V_{oc} of 733 mV, FF of 81.6 % and J_{sc} of 39.6 mA cm^{-2}. The a-Si:H(n) and nc-Si:H(n) layers account for -0.33 mA/cm^2 and -0.53 mA/cm^2 current losses respectively. The contact resistivity reached an impressive value for this thin layer lower than 15 mΩcm^2, alleviating the need for lateral conductivity of the TCO. This could broaden the range of compatible transparent electrodes for the front side, such as thin TCO/SiNx bilayers to reduce the absorption losses. We explored the possibility offered by this strategy and concluded that it could yield a current gain up to +0.6 mA cm^{-2}. The absorption loss in the front silicon layers remains the highest optical loss, and additionally reducing those layers thicknesses by half and/or oxidizing part of the nc-Si:H(n) layer could bring the current to above 40.3 mA cm^{-2}, providing this does not impinge on the contact performance. We finished the discussion by presenting an optimization roadmap, showing a possibility for double-side contacted SHJ cells to reach efficiencies above 26 %, a value close to the one of the record IBC devices [Yoshikawa 2017]. To push the efficiency further, the front absorption losses must be tackled. For this a first solution would be to engineer localization of the front TCO and silicon layers. An interesting strategy that might apply to the contact developed in this thesis could be provided by tetramethylammonium hydroxide, which is known to etch selectively silicon layers whereas it is stopped by SiO_x layer [Apet 2006]. Further research in this direction, using the screen-printing grid as a self-aligned mask for the etching, could be of potential interest as our contact stack features a SiO_x-seed layer between the intrinsic and the doped layer.

The other pathway is to develop new non-silicon materials that allow reaching much higher transparency and at the same type acting as efficient CSPC. This still poses understanding challenges as the a priori identification of an efficient contact based on its work function was shown to be challenged in the recent years. This is because properties such as the conduction or valence band positions with respect to vacuum or bandgap have a wide range

of possible values for a given material and are highly dependent on the deposition conditions and substrate. Moreover, interface states can pin the Fermi level and reduce the effect of the work function of the material. All these effects often lead to a problem of selectivity and S-shapes and kinks are commonly observed in the *J-V* curves of such devices.

In chapter 3, we discussed the ability of the simple four ideal diode model of Roe to explain the S-shapes and kinks appearing in heterojunction solar cell *J-V* curves depending on their contact quality. We first discussed from a theoretical point of view how to improve the model by modifying the ideal diodes by other circuit elements. We then considered the impact of additional bulk recombinations on the model, simulated it, and gave simple relationships for the new positions and heights of the S-shapes in this new case for both solar cells and symmetrical samples. Then, we tested our theory experimentally on solar cells where the contacts were deliberately engineered to reach various selectivities. By studying case by case the gradual deviation from Roe's description, we figured out that the single diode kinetics should modified by adding an additional ohmic element in series as well as the possibility of tunnelling at large reverse bias. Our findings should be useful to model and identify bottlenecks occurring when developing new materials for any heterojunction contact technology such as SHJ or perovskite solar cells. It brings also further the fundamental discussion about passivation, selectivity and conductivity of solar cells, as discussed by *Onno et al.* in [Onno 2019], by providing a defined parametrization of the circuit element based on experimental data.

A Appendix

A.1 Pysch's law and impact of R_s on *FF* and η

In this section, we develop approximations to find relationships between values of series resistance, *FF* and efficiency losses.

In order to relate the values of R_s at MPP given in $\Omega\,\mathrm{cm}^2$ to values of *FF* or η given in $\%_{\mathrm{abs.}}$, we use the following arguments from [Pysch 2007] that will gives a simple relationship, which we refer to as *Pysch's law*. This allows to estimate the order of magnitude of the impact of a change of R_s on the other parameters.

First, the series resistance is calculated from the voltage drop at constant current density J_{mpp} between the *J-V* and *pJ-V* curves, free of series resistance:

$$R_s^{mpp} = \frac{pV(J_{mpp}) - V(J_{mpp})}{J_{mpp}}, \tag{A.1}$$

where $V(J_{mpp}) \equiv V_{mpp}$ by definition, but $pV(J_{mpp}) \neq pV_{mpp} \equiv pV(pJ_{mpp})$ since we do not have necessarily $J_{mpp} = pJ_{mpp}$, as can be seen on Figure A.1. Even though we can tell from the graphical example that assuming $pJ_{mpp} \approx J_{mpp}$ is a safe approximation in many cases, we keep the development as general as possible and discuss how close those values are afterwards for the final approximation.

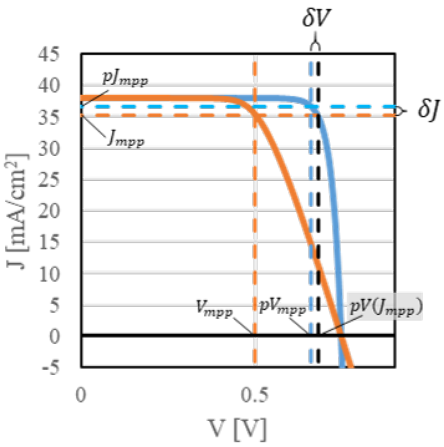

Figure A.1: J-V *curve (orange solid line) and* pJ-V *curve (blue solid line) and definitions of the voltage and current of interest.*

Due to the shift of of the maximal power voltage and current to higher values from the *J-V* curve to the *pJ-V* curve, the presence of series resistance creates the

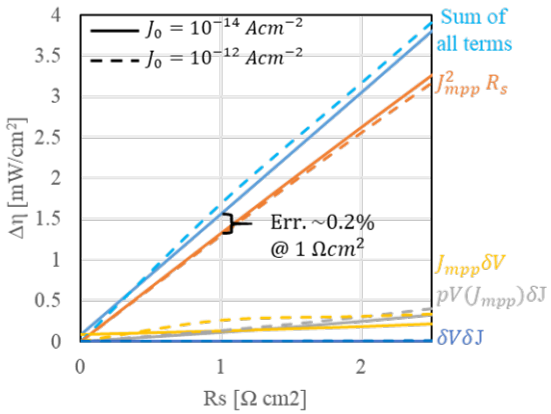

Figure A.2: Calculation of the different terms of equation A.3 using the ideal diode equation with two values of J_0, yielding V_{oc} of 744 and 626 mV respectively, and $J_{ph} = 38\,\mathrm{mA\,cm^2}$.

following difference between *pFF* and *FF*

$$\Delta FF_{R_s} = \frac{1}{V_{oc}J_{sc}}\left(pV_{mpp}pJ_{mpp} - V_{mpp}J_{mpp}\right) \tag{A.2}$$

which can be rewritten in terms of the small voltage and current differences $\delta J = pJ_{mpp} - J_{mpp}$ and $\delta V = pV(J_{mpp}) - pV_{mpp}$ as

$$\Delta FF_{R_s} = \frac{J_{mpp}^2 R_s^{mpp}}{V_{oc}J_{sc}} + \frac{1}{V_{oc}J_{sc}}\left(pV(J_{mpp})\delta J - J_{mpp}\delta V - \delta V \delta J\right) \tag{A.3}$$

To justify why the second term can be neglected, we need to make some hypotheses on the function $V(J)$ and $pV(J)$. We can argue that for good SHJ solar cells, with good surface passivation and no selectivity losses, the *J*-*V* curves can be modelled as a good approximation by diode equations. Since we are looking for the order of magnitude between different quantities and not for absolute values, using those diode equations is a good first approximation. For simplicity, we will restrict ourself to the case of the ideal diode equation $J(V) = J_{ph} - J_0 exp(q(V + JR_s)/k_B T)$, with J_{ph} the photogenerated current density, and J_0 the recombination current of the diode. On Figure A.2, we compute the different terms in equation (A.3) for J_{ph} =38 mA cm^2 and J_0 values in the range of 1×10^{-14}–1×10^{-12} A cm^{-2} which allows for V_{oc} values in the range of 625–745 mV. One can clearly see that the first term of equation A.3 dominates largely the others. For R_s lower than 1 Ω cm^2, the error on the efficiency ($\Delta\eta = V_{oc}J_{sc}\Delta FF_{R_s}$) is lower than 0.2 % and therefore the term in parenthesis in the equation (A.3) can be neglected.

Using the same approximations, the fill factor can be rewritten as

$$\Delta FF \approx \frac{J^{mpp^2}}{V_{oc}J_{sc}}R_s = FF\frac{J^{mpp}}{V^{mpp}}R_s \approx (0.043 \text{ to } 0.054) \times R_s, \tag{A.4}$$

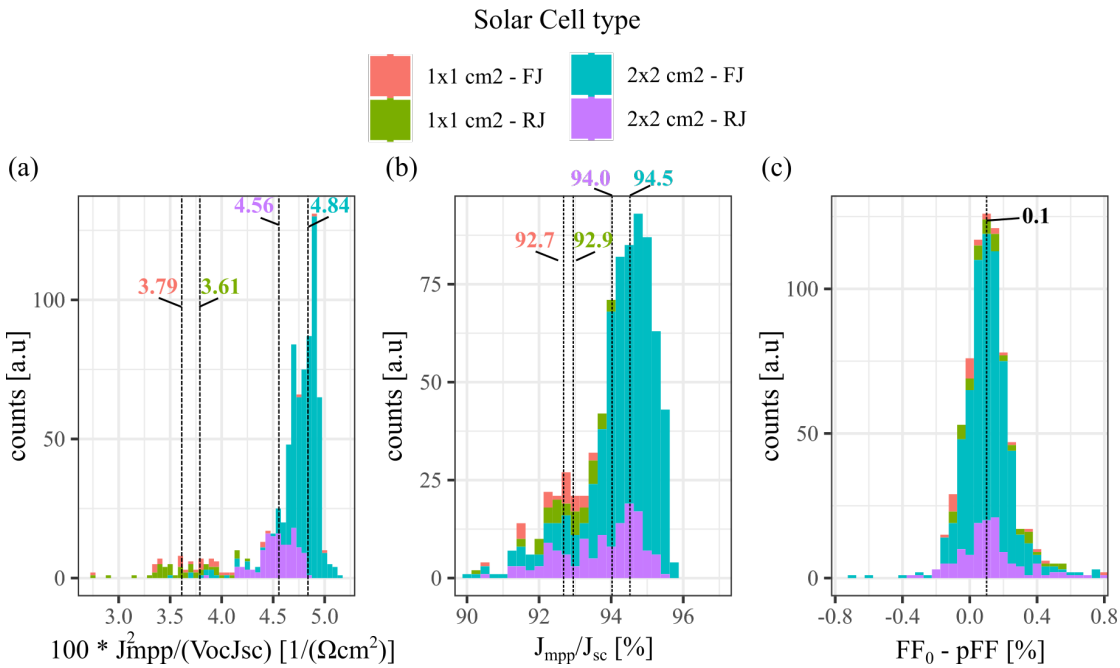

Figure A.3: Histograms of 1450 J-V curves of solar cells measured throughout this thesis, classified for different cell size and architecture. The lines represent the median of each distribution. (a) Prefactor of the R_s term of Pysch's law (eq. A.4) calculated from measured values. (b) ratio of the measured values of J_{mpp} and J_{sc}. (c) Comparison of the present formula for the pseudo-fill factor and Green's formula, based on measured values.

where in the last step, we additionally approximated $\frac{J_{mpp}^2}{V_{oc}J_{sc}}$ using typical values of 720–750 mV for V_{oc} and 38–42 mA/cm^2 for J_{sc} and considered that $J^{mpp} \approx (0.93 \text{ to } 0.97) \times J_{sc}$.

The impact on the efficiency of this fill factor change can be written as

$$\Delta\eta_{R_s} = p\eta - \eta = \frac{V_{oc}J_{sc}}{P_{1sun}}\Delta FF_{R_s} = \frac{\eta}{FF}\Delta FF_{R_s} \tag{A.5}$$

$$\approx (0.25 \text{ to } 0.33) \times \Delta FF_{R_s} \tag{A.6}$$

$$\approx (0.011 \text{ to } 0.018) \times R_s \tag{A.7}$$

considering values of FF and η in typical range of 80–85 $\%_{\text{abs.}}$ and 20–25 $\%_{\text{abs.}}$ respectively for the second line, and using the factor of eq.(A.4) for the second approximation. **Therefore, a R_s of 1 Ω cm^2 yields a loss of approximatively 5 $\%_{\text{abs.}}$ of FF (multiplying by 5) and 1.1–1.8 $\%_{\text{abs.}}$ of η (multiplying by 1.1 to 1.8)**. Note that this factor of 5 between R_s and FF is close to the one found experimentally in [Pysch 2007] using regression lines of FF versus R_s of solar-cell data. Even if not completely accurate, those relationships are good first approximations allowing to easily evaluate the order of magnitude of the impact of series resistance on the output power.

As we can see from Figures A.3(a) and (b), which plot results extracted from 1450 real J-V curve measurements, $\frac{J_{mpp}^2}{V_{oc}J_{sc}}$ is indeed well approximated by a factor of ≈ 5 on a large batch

of solar cells (with a slightly lower value for $1 \times 1\,\text{cm}^2$ solar cells) as well as the relationship $J_{mpp} \approx 0.95 J_{sc}$. It is also relevant to compare the formula for $pFF = FF + \frac{J_{mppp}^2 R_s}{V_{oc} J_{sc}}$ with the one of Green, *i.e.* $FF_0 = (v_{oc} - \ln(v_{oc} + 0.72))/(v_{oc} + 1)$ where $v_{oc} = qV_{oc}/(nk_B T)$. The difference between those two metrics is plotted on Figure A.3(c), which shows that both metric agrees within a standard deviation of $\pm 0.2\%_{abs}$ and a value of FF_0 biased of $+0.1\%_{abs}$ to higher values.

Based on those relationships, we can discuss the impact of the sheet resistance of the TCO R_{sh}^{TCO} and the contact resistivity ρ_c in several limit cases. In every case, we consider a wafer sheet resistance R_{sh}^{cSi} of 60–90 Ω/sq, which is equivalent to the electron sheet resistance of a 2.2 Ω cm wafer under illumination at MPP injection conditions.

High ρ_c^{front}, low R_{sh}^{TCO}

For a front contact, when ρ_c^{front} is high and $R_{sh}^{TCO}$is low so that no significant current is transported in the wafer, the lateral transport and contact resistance contributions to the total resistance can be written as

$$R_s^{lat+C} = \rho_c^{front} + \frac{1}{12} p^2 R_{sh}^{TCO} = \rho_c + 0.00285[\text{cm}^2] \times R_{sh}^{TCO}, \tag{A.8}$$

where p is the pitch of the finger grid and is equal to 0.185 cm throughout this thesis. Therefore, a R_{sh}^{TCO} of 100 Ω/sq leads to 0.285 Ω cm^2 of R_s, and approximatively 1.23–1.54 $\%_{\text{abs.}}$ of FF and 0.30–0.51 $\%_{\text{abs.}}$ of efficiency, and in a similar range for a ρ_c^{front} of 200–300 mΩ cm^2 using *Pysch's law* in the same way.

The same relationship can be used in the case of a rear contact with a full area sputtered silver blanket of approximatively 150 nm (flat equivalent). In this case, we have on a textured wafer $R_{sh}^{Ag} \approx 100$ mΩ/sq, and therefore the lateral transport accounts for 2.8×10^{-4} Ω cm^2 which can be neglected with respect to the other resistive losses in the solar cell.

Localised contact at the front with no TCO

In this case, the current can escape the wafer only through an area proportional to the finger width w_f, which takes values in the 15–50 µm range. Therefore, we have

$$R_s^{lat+C} = \frac{p}{w_f} \rho_c^{front} + \frac{1}{12} p^2 R_{sh}^{cSi} = (37 \text{ to } 123) \times \rho_c^{front} + (0.171 \text{ to } 0.256)[\Omega\text{cm}^2] \tag{A.9}$$

We see that in this case it is important to reach ρ_c values lower than 1 mΩ cm^2 to mitigate the losses as well as to provide an accurate measurement of w_f to evaluate correctly the resistive losses.

Low ρ_c^{front}, low R_{sh}^{TCO}

In the special case where a good $\rho_c^{front} \approx 1$ mΩ cm and a good $R_{sh}^{TCO} \approx 100$ Ω/sq are used, the

contact resistance can be neglected and the lateral resistance is approximatively the parallel resistance of the TCO and the wafer:

$$R_s^{lat+C} \approx \frac{1}{12} p^2 R_{sh}^{TCO//cSi} = \frac{1}{12} p^2 \frac{R_{sh}^{TCO} R_{sh}^{cSi}}{R_{sh}^{TCO} + R_{sh}^{cSi}} = (0.107 \text{ to } 0.135)[\Omega/\text{cm}^2] \tag{A.10}$$

A.2 S-shapes modelling - additional information

A.2.1 Effect of bulk recombination: derivation of S-shape positions

In this section, we give the analytical derivation to find the different S-shape positions for Roe's model extended with a bulk recombination diode, which is described by equations 3.20 to 3.30 and is illustrated on Figure 3.4(a). During the derivation, we will consider the case where $J_{0h}^p < J_{0e}^n$. However, the formula for the opposite case can be found by switching in the equations the role of J_{0h}^p with J_{0e}^n and j_{0h}^n with j_{0e}^p, respectively. After this, we will give as well the formula for the case of symmetric samples.

First, let us consider the three current paths of Figure 3.4(a). We assume a priori that the first step will occur at a voltage V_{step}^{1st} lower than $V_e = \frac{k_B T}{q} \ln J_{0e}^n / j_{0e}^p$ and $V_h = \frac{k_B T}{q} \ln J_{0h}^p / j_{0h}^n$, meaning that the current cannot flow either through the top or bottom line of the circuit. Therefore, it should flow through the blue line, provided that the recombination is strong enough. The condition can be verified a posteriori by checking that $V_{step}^{1st} < V_e, V_h$. If it is not the case, Roe's simpler model can be applied to describe the circuit.

Since no current can flow through diode #1 and #4 (as labelled on Figure 3.3(b)), the voltage applied as a function of J reads as

$$\begin{aligned} V(J) &= V_2(J_2) + V_{rec}(J_{rec}) + V_3(J_3) && \text{(A.11)} \\ &= V_2(J) + V_{rec}(J + J_L) + V_3(J) && \text{(A.12)} \\ &= \frac{k_B T}{q} \ln \left[\left(\frac{J + J_L}{J_{0,rec}} + 1 \right) \left(-\frac{J}{J_{0e}^n} + 1 \right)^{-1} \left(-\frac{J}{J_{0h}^p} + 1 \right)^{-1} \right] && \text{(A.13)} \end{aligned}$$

As we can see from the circuit, the current will end up saturating because of J_{0h}^p and the step mid-height is therefore given by $J_{1st}^{mid} = \frac{1}{2}(J_{0h}^p - J_L)$. Evaluating the last expression at $J = J_{1st}^{mid}$ gives us the threshold voltage V_{step}^{1st} of this S-shape. After reordering the terms, this one reads as

$$V_{step}^{1st} = \frac{k_B T}{q} \ln \left(\frac{\frac{1}{2} J_{0h}^p \left(1 + \frac{J_L}{J_{0h}^p} \right) + J_{0,rec}}{\frac{1}{2} J_{0,rec} \left(1 + \frac{J_L}{J_{0h}^p} \right) \frac{1}{J_{0e}^n} \left(J_{0e}^n + \frac{J_L}{2} - \frac{J_{0h}^p}{2} \right)} \right) \tag{A.14}$$

One can assume further $J_{0h}^p \gg J_{0,rec}$, which simplifies the expression to

$$V_{step}^{1st} \approx \frac{k_B T}{q} \ln \left(\frac{J_{0h}^p J_{0e}^n}{J_{0,rec} \left(J_{0e}^n + \frac{J_L}{2} - \frac{J_{0h}^p}{2} \right)} \right) \tag{A.15}$$

If we can assume further that $J_{0e}^n \gg J_L$ and J_{0h}^p or $J_L \approx J_{0h}^p$, then this equation reduces to

$$V_{step}^{1st} \approx \frac{k_B T}{q} \ln\left(\frac{J_{0h}^p}{J_{0,rec}}\right) \tag{A.16}$$

We can proceed similarly for the second step. This one occurs when current can flow through an additional path, not being restricted by J_{0h}^p anymore. This means that diode #1 needs to open up while no current flows in diode #4. To find V_{step}^{2nd}, we therefore write the voltage for the pink path

$$\begin{aligned} V(J) &= V_2(J_2) + V_1(J_1) && \text{(A.17)} \\ &= V_2(J) + V_1(J - J_{0h}^p) && \text{(A.18)} \\ &= \frac{k_B T}{q} \ln\left(\frac{J - J_{0h}^p + j_{0e}^n}{j_{0e}^n\left(1 - \frac{J}{J_{0e}^n}\right)}\right) && \text{(A.19)} \end{aligned}$$

The current will saturate this time at J_{0e}^n and the step mid-height compared to the previous step is therefore at $J_{mid}^{2nd} = \frac{1}{2}(J_{0e}^n + J_{0h}^p)$. Evaluating the last voltage equation at this point leads to (after reordering the terms)

$$V_{step}^{2nd} = \frac{k_B T}{q} \ln\left(\frac{J_{0e}^n}{j_{0e}^p} \frac{\frac{1}{2}(J_{0e}^n - J_{0h}^p) + j_{0h}^e}{\frac{1}{2}(J_{0e}^n - J_{0h}^p)}\right) \tag{A.20}$$

If one can assume $\frac{1}{2}(J_{0e}^n - J_{0h}^p) \gg j_{0h}^e$, the equation simplifies to

$$V_{step}^{3nd} \approx \frac{k_B T}{q} \ln\left(\frac{J_{0e}^n}{j_{0e}^p}\right) \tag{A.21}$$

Finally, the last step occurs once the current can flow through the green line. We have

$$\begin{aligned} V(J) &= V_4(J_4) + V_1(J_1) - V_{rec}(J_{rec}) && \text{(A.22)} \\ &= V_4(J - J_{0e}^n) + V_1(J - J_{0h}^p) - V_{rec}(J_{0e}^n + J_{0h}^p + J_L - J) && \text{(A.23)} \\ &= \frac{k_B T}{q} \ln\left[\left(\frac{J - J_{0e}^n + j_{0h}^n}{j_{0h}^n}\right)\left(\frac{J - J_{0h}^p + j_{0e}^p}{j_{0e}^p}\right)\left(\frac{J_{0e}^n + J_{0h}^p + J_L + J_{0,rec} - J}{J_{0,rec}}\right)\right] && \text{(A.24)} \end{aligned}$$

Once this path is totally opened, the current will saturate at $J_L + J_{0h}^p + J_{0e}^n$. Evaluating the last expression at the mid-step height (compared to the second step) $J_{mid}^{3rd} = \frac{1}{2}(J_L + J_{0h}^p) + J_{0e}^n$ yields

$$V_{step}^{3rd} = \frac{k_B T}{q} \ln\left(\frac{J_{0,rec}}{j_{0h}^n j_{0e}^p} \frac{1}{2} \frac{(J_L + J_{0h}^p + 2j_{0h}^n)(J_L - J_{0h}^p + 2J_{0e}^n + 2j_{0h}^e)}{(J_L + J_{0h}^p + 2J_{0,rec})}\right) \tag{A.25}$$

This can be simplified if one can assume that $J_{0,rec}$, j_{0h}^n and j_{0e}^p are all negligible when com-

pared to J_L, J^p_{0h} and J^n_{0e}. This yields

$$V^{3rd}_{step} \approx \frac{k_B T}{q} \ln\left(\frac{J_{0,rec}}{j^n_{0h} j^p_{0e}} \frac{1}{2}(J_L - J^p_{0h} + 2J^n_{0e})\right) \tag{A.26}$$

We now consider the case of a symmetric sample with two p-contacts. This means that diodes #1 and #2 are both characterized by j^p_{0e} and diodes #3 and #4 by J^p_{0h}. Applying trivial substitutions give the results for a symmetric samples with two n-contacts.

The first step measurable will occur at a height of J^p_{0h} and a position of 0 V, because current can flow through diodes #3 and #4. Now, we should consider two additional steps: one when the current flows through diodes #1 and #2, saturating at the very low current j^p_{0e}, and one flowing through diodes #1, #4 and the recombination diode, adding J_L to the output current. We cannot know a priori which one occurs first, however, since only negligible current is flowing through the first path we described, we can consider it do not contribute to current at all and we will consider that diode #2 remains close all the time for simplicity. We did however check that it yields the same result at the end of the development if we can assume $J_L \gg j^p_{0e}$.

Therefore, we write the voltage corresponding to the path consisting of diodes #1, #4 and the recombination diode

$$\begin{aligned} V(J) &= V_1(J_1) + V_4(J_4) - V_{rec}(J_{rec}) && \text{(A.27)} \\ &= V_1(J - J^p_{0h}) + V_4(J) - V_{rec}(J^p_{0h} + J_L - J) && \text{(A.28)} \\ &= \frac{k_B T}{q} \ln\left[\left(\frac{J - J^p_{0h} + j^p_{0e}}{j^p_{0e}}\right)\left(\frac{J - J^p_{0h}}{J^p_{0h}}\right)\left(\frac{J_{0,rec}}{J^p_{0h} + J_L + J_{0,rec} - J}\right)\right] && \text{(A.29)} \end{aligned}$$

Evaluating this expression at the mid-step height $J^{symm}_{mid} = J^p_{0h} + \frac{J_L}{2}$

$$V^{symm}_{thresh} = \frac{k_B T}{q} \ln\left[\left(\frac{J_L/2 + j^p_{0e}}{j^p_{0e}}\right)\left(\frac{2J^p_{0h} + J_L/2}{J^p_{0h}}\right)\left(\frac{J_{0,rec}}{J_L/2 + J_{0,rec}}\right)\right] \tag{A.30}$$

This can be simplified if we can assume $J_L \gg j^p_{0e}$and$J_{0,rec}$, yielding

$$V^{symm}_{thresh} \approx \frac{k_B T}{q} \ln\left(\frac{J_{0,rec}}{j^p_{0e}} \frac{2J^p_{0h} + J_L/2}{J^p_{0h}}\right) \tag{A.31}$$

A.2.2 Activation energy plot

In this section, we show the extraction of the Schottky barrier height present in the p(87)-iNi-p(87) sample (Figure A.4). The sample was measured at temperatures between 25 °C to 55 °C. The saturation current density was taken at 1 V, where the curve shows sign of saturation, but before the following linear increase becomes too strong. The data are then fitted with equation

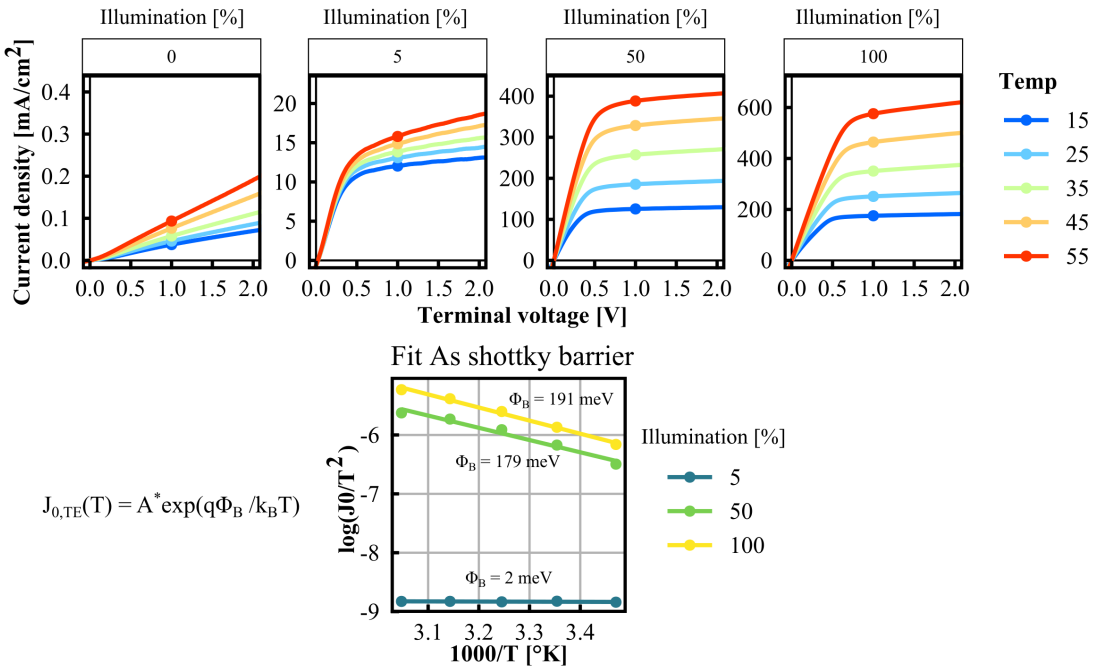

Figure A.4: (top) Extraction of the saturation current $J_{0h}^{p(87)}$ at different illuminations and temperatures. (bottom) extraction of the Schottky barrier height ϕ_B from the activation energy plot.

3.15, *i.e.* $J_0^{TE} = A^* T^2 e^{-\frac{q\phi_B}{k_B T}}$ in an activation energy plot. At high illumination, the data follow well the Schottky behaviour and a barrier height of 179 meV and 191 meV can be extracted for 0.5 sun and 1 sun, respectively. For lower illumination, the data do not follow this Schottky behaviour, and should be analysed with another model, such as those described in section 3.2.2.

A.2.3 S-shape dependence on wafer types

In this section, we report the results of solar cells and symmetrical samples featuring the very same contact layers, however deposited on wafer of different doping types. Both wafers have a resistivity of about 2 Ω cm meaning that $N_D \approx 2.2 \times 10^{15}\,\mathrm{cm}^{-3}$ for the n-type wafer and $N_A \approx 8 \times 10^{15}\,\mathrm{cm}^{-3}$ for the p-type wafer. However, under illumination, a large amount of e^- and h^+ are photogenerated in the bulk, and the wafer loses part of its "doping properties", becoming equivalent in a sense to an "intrinsic" wafer. Indeed, under 1 Sun at MPP we have about $\Delta n = \Delta p = 1 \times 10^{15}\,\mathrm{cm}^{-3}$ excess carrier density, and at OC $\Delta n = \Delta p = 1 \times 10^{16}\,\mathrm{cm}^{-3}$ which starts to be significant compared to N_D and N_A.

We can see on Figure A.5, that the samples deposited on p-type or n-type wafers feature similarities in their J-V curves, showing similar positions of S-shapes and saturations, which coincides with our intuitive explanation of "intrinsic" wafer. One feature remains however

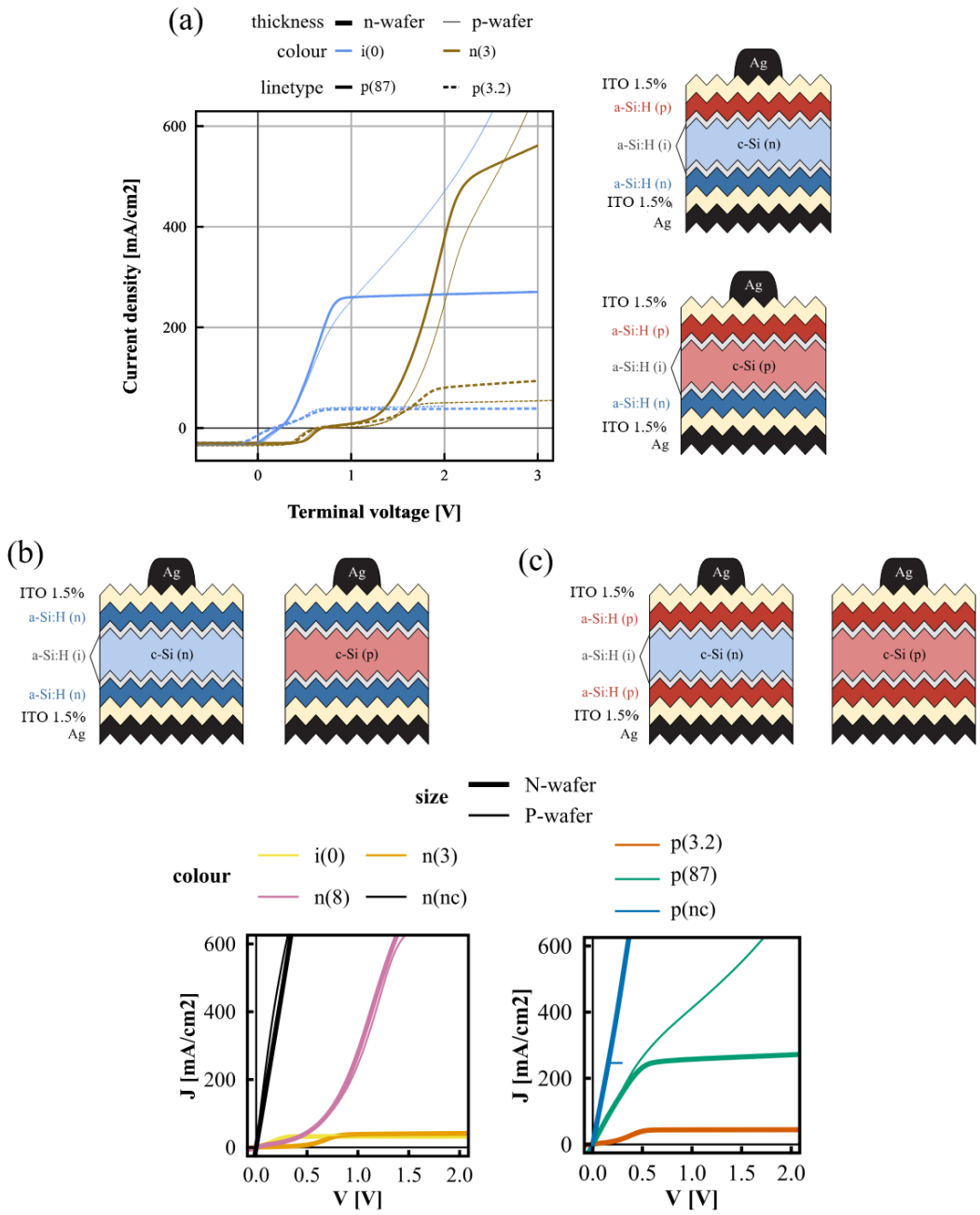

Figure A.5: (a) J-V *curves of solar cells, (b) symmetric n-contacts, and (c) symmetric p-contacts with the same contact layers deposited on* p*-type or* n*-type wafers.*

different on p-type and n-type wafers: it is the exponential increase at large forward bias with the p(87) layers deposited on p-type wafers. However, it should be noted that this p-wafer jas much stronger doping level than the n-wafer, which is not negligible compared to the excess carriers. Additionally, we observe that the symmetric samples and solar cells exhibit

larger linear or exponential increase instead of saturation once the doping of the layers is increased. Putting those last two facts hand-in-hand, we could interpret this phenomenon as the formation of an isotype junction through which tunnelling current can be amplified as the doping is increased on any side of the heterojunction (either in the wafer, or the layer).

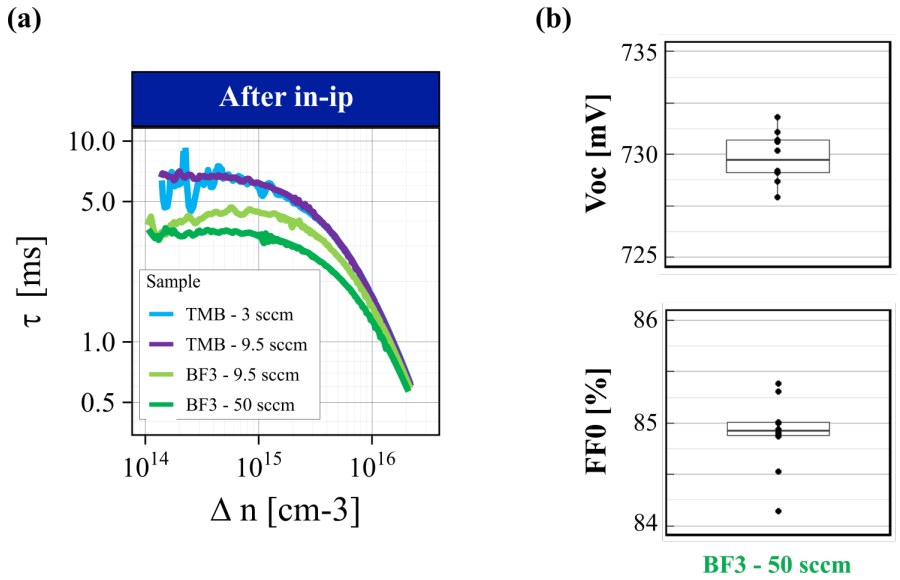

Figure A.6: (a) Injection dependent lifetime of solar cell precursors (after PECVD layer deposition) of the "TMB and BF_3 doping series". (b) J-V *results from another batch of solar cells prepared with high flow of BF_3, showing that high passivation can be obtained as well.*

A.3 Appendix to nc-Si:H(*p*) development

A.3.1 Passivation quality of samples with high BF_3 flows.

On Figure 4.2, we reported a slight loss of V_{oc} for the sample using the highest flow of BF_3. As we can see on Figure A.6(a), this small drop of passivation is already visible on the solar cell precursor for the sample prepared with 50 sccm of BF_3. Nevertheless, as can be seen on Figure A.6(b), a V_{oc} of 730 mV and a FF_0 of 84.9% were also achievable for layers prepared with 50 sccm of BF_3 in another batch of solar cells, similarly to the use of the other p-type layers, suggesting that this is not a systematic feature of the 50-sccm-BF_3 layers and that it is not detrimental to reach high quality passivation .

A.3.2 Effect of the SiOx DARC deposition

In this section, we will discuss in more details the beneficial effects of the deposition of a 100 nm-thick PECVD SiOx layer on the front side of the solar cell to form a double anti-reflective coating (DARC). Three beneficial effects can be listed for the use of this dielectric coating. First, it is indeed possible to reduce even further the reflectance loss of the solar cell by covering the TCO with a layer with refractive index in between the one of the TCO ($n = 2$) and that of air ($n = 1$). In the case of SiO_x which has a refractive index close to 1.45, the optimization of the layers obeys a simple rule, where the thickness of the TCO should be reduced by a factor 2/3 with respect to its single anti-reflective value, while the SiOx should be around 100 nm [Herasimenka 2016, Cruz 2022]. The DARC can greatly enhance the J_{sc} of

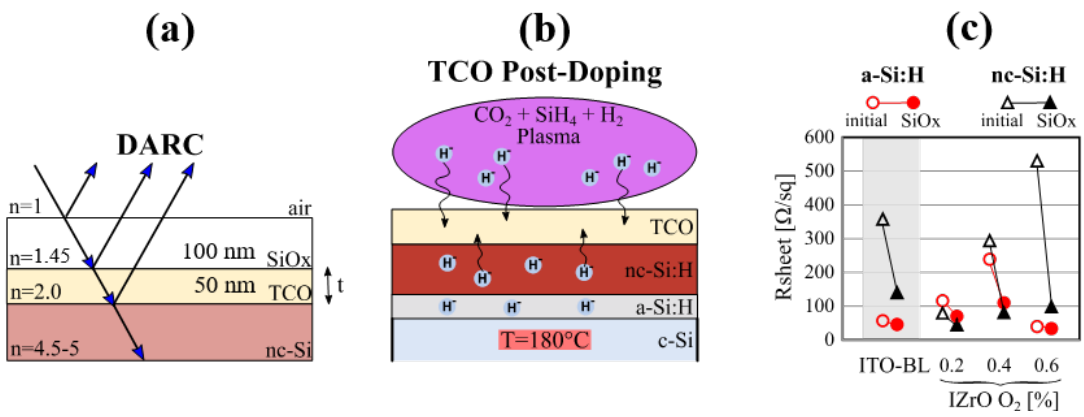

Figure A.7: Silicon oxide layer properties on the solar cell. (a) Double-anti reflective coating. (b) Hydrogenation during deposition. (c) Reducing sheet resistance.

the solar cell, up to +1 mA cm^{-2} as we will show below. Indeed, in this way the refractive index in the stack of materials decreases towards the one of air (n=1), with discontinuous values at each interface (see Figure A.7(a)), which enables lower reflection losses. Unfortunately, this properties doesn't hold once the cell is encapsulated, since the refractive index of the encapsulant is higher than the one of the air and closer to the one of the SiO_x layer (n=1.49-1.52) [Boccard 2018]. Nevertheless, it was shown that the extra SiO_x coating has also beneficial properties on the cell stability under damp-heat [Liu 2020] and is as well a desired step in the manufacturing of copper-plated solar cells [Lachowicz 2021], making this layer still interesting for real module integration. Finally, a third aspect is that the deposition of the SiO_x layer, in our case via PECVD, can modify the underneath solar cell. This can occur due to the diffusion of hydrogen from the plasma to the layers underneath [Herasimenka 2016].

Figure A.7(c) shows how the sheet resistance of TCO evolves before and after this coating, depending on the layer underneath. We can see that before SiO_x deposition, the TCOs have a much higher R_{sh}^{TCO} on nc-Si:H layers than on a-Si:H and much lower oxygen flows should be used to reach similar values on both substrates, which is not ideal as it increases free carrier absorption. This R_{sh}^{TCO} difference comes from the fact that the surface roughness of nc-Si:H can influence the growth of the subsequent TCO [Cruz 2019a]. After SiO_x, we can see that all samples can reach $R_{sh}^{TCO} < 100\,\Omega/\text{sq}$ and reduce the discrepancies among them. This latter point is used in chapter 4 in order to minimize the variation of R_s coming from the TCO among the solar cells to study more precisely the impact of the contact resistivity. Turning to Figure A.8, we can see that the boost of conductivity of those TCOs comes both from an increase in mobility and carrier concentration. Optimizing the oxygen flow to not overcome a limit of $N_{TCO} = 1 \times 10^{20}\,\text{cm}^{-3}$ after SiO_x deposition can thus enable reaching higher conductivity without degrading the J_{sc} [Boccard 2021, Cruz 2022] thanks to the improvement of mobility furnished by the SiO_x deposition.

On Figure A.9, we show the impact of the SiO_x on the cell properties, showing that combined

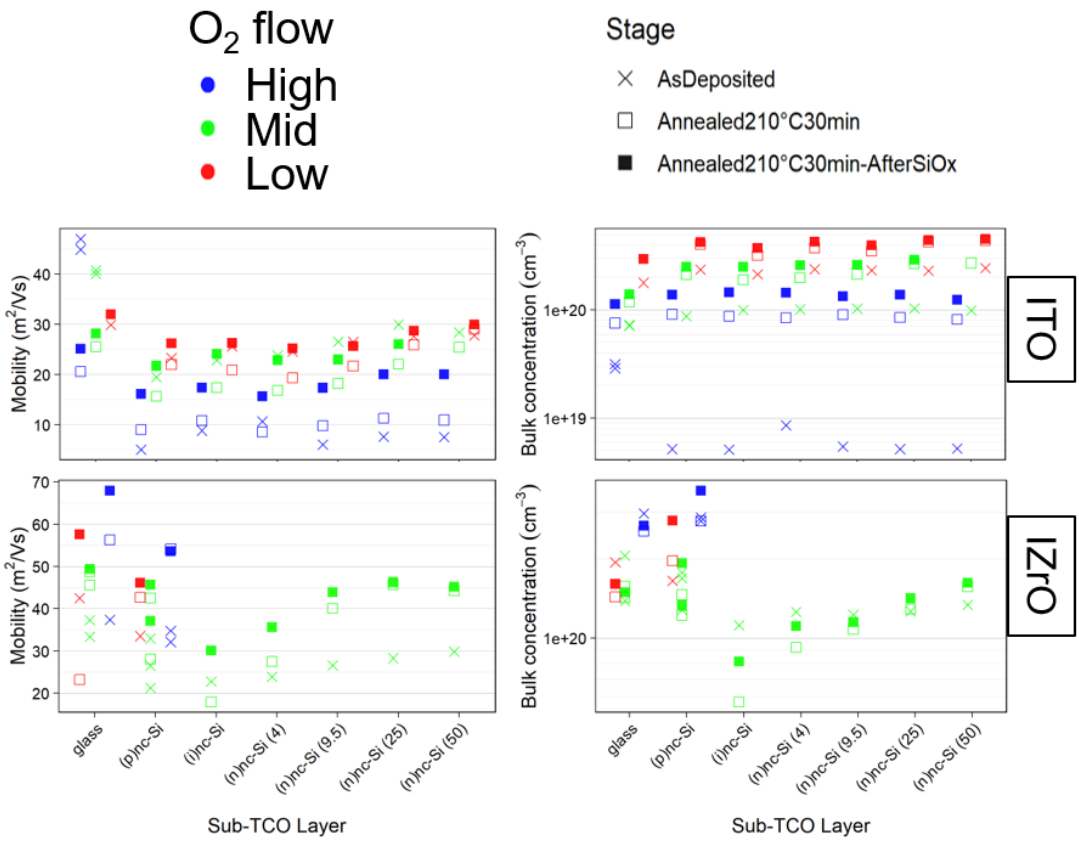

Figure A.8: ITO and IZrO mobility and carrier concentration depending on oxygen flow, substrate and process steps. The n*-type layer will be presented in chapter 6.*

with a nc-Si:H layer and the more transparent IZrO compared to ITO, efficiency close to 24 % can be reached. Two parameters account for that. First the combined effect of the reduced reflectance and the use of the more transparent IZrO increase J_{sc} by almost +1 mA cm^{-2} with respect to a single ARC with ITO (BL). Moreover, the hydrogenation of the TCO as well as the rest of the solar cell by the SiO_x provides a large increase of *FF*, here mainly through a decrease of R_s. The FF_0 being here already quite high remains almost unaffected, but it must be mentioned that with solar cells with lower passivation properties, the SiO_x deposition results generally in a small boost of the passivation as well.

In conclusion, even though a SiO_x coating may not improve further the reflectance of real encapsulated solar cells, it brings non negligible interests regarding passivation, conductivity and stability properties. We will see in chapter 6, that it can even help to achieve better contact selectivity in the case of *n*-type nc-Si:H layer, widening the space of parameters that can be used to create an efficient CSPC.

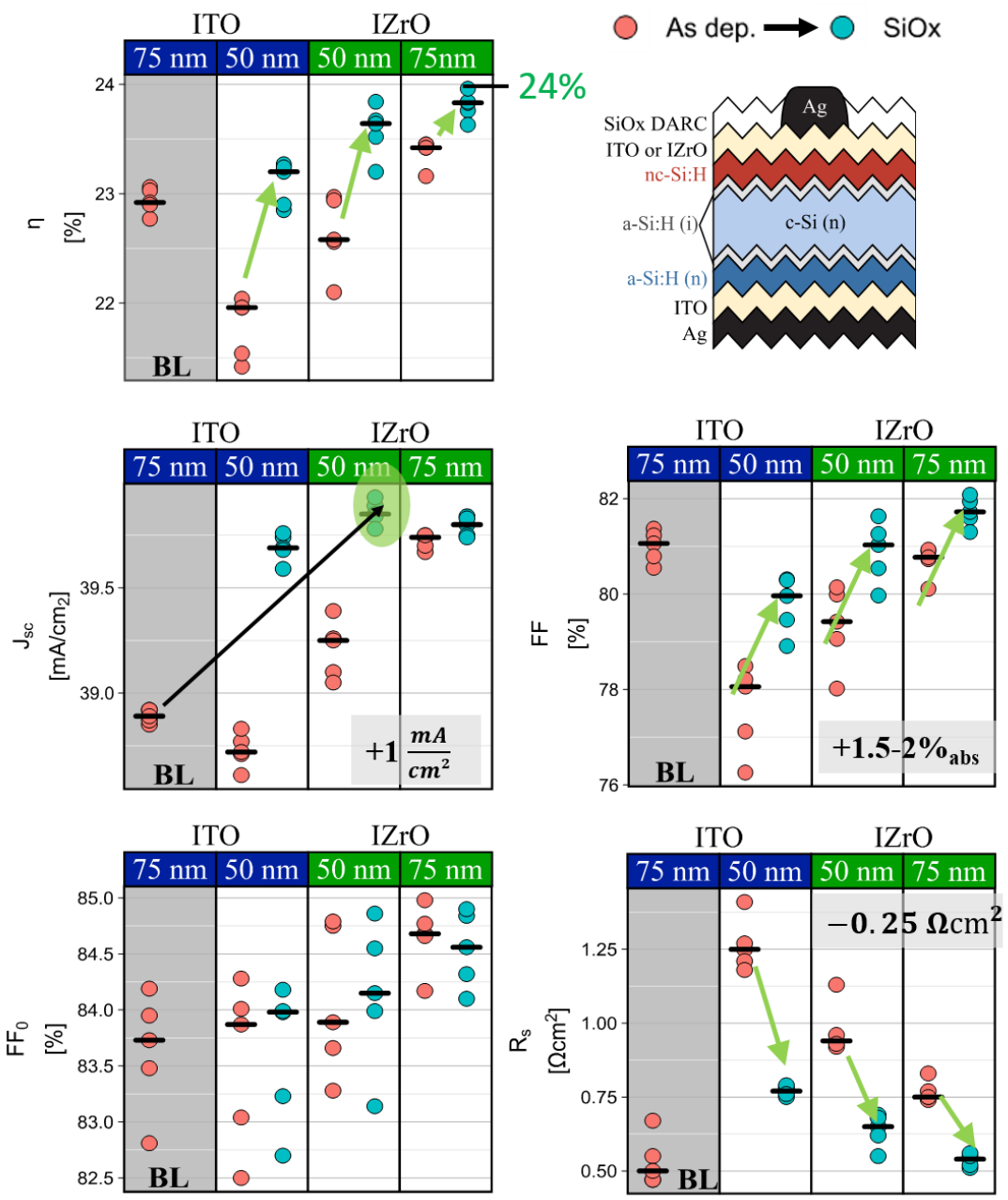

*Figure A.9: Evolution of the solar cell results when forming a DARC with a SiO_x layer via PECVD, for two different TCO, namely ITO and IZrO deposited on nc-Si:H(*p*).*

A.3.3 SIMS chemical composition and AFM surface topography of nc-Si:H(*p*) layers

To link solar-cell transport performance to layer properties, Figure A.10 presents the SIMS profiles of the different chemical elements and the activation energy for layers prepared with the different dopant flows. Figure A.10(a) shows the Si, H, O, F, C, and B profiles of a representative sample, allowing to observe the important transitions between the different layers: One can observe two peaks in almost every profile (except for boron) that are characteristic of the wafer interface and of the SiO_x surface treatment, with in particular similar oxygen profiles for all samples. Also for all samples, the signal of Si and B decreases towards the air interface. This is probably due to the surface roughness of nc-Si:H materials, with peak to valley distances on the order of 15 nm (as observed via AFM on Figure A.11 or fitted from ellipsometry data), leaving less material to be etched during the measurement and thus lower signal.

We can see also that the boron content of all samples goes to zero as we approach the SiO_x interface (except for BF_3, as discussed below), showing that the dopant does not diffuse deeper in the sample. The decrease of signal at the air interface for the 3-sccm TMB and 9.5-sccm BF_3 layers also correlates with their high crystallinity and thus higher surface roughness, while the more constant boron signal of the 9.5-TMB signal can as well be explained by its more amorphous nature.

Carbon profiles show two distinctive peaks at the SiOx interface only for the TMB-prepared samples, showing that the carbon present in the precursor is incorporated mainly at the interface with the seed layer.

The presence of fluor can be seen at the wafer interface for all samples. This is due to the initial HF treatment to remove the native oxide. For BF_3, a large peak of F can be seen, fluor being accumulated at the oxide interface. Then, the hydrogen profile reveals a very distinct peak at the oxide and wafer surface for all samples except for BF_3 where the peak to valley is attenuated in comparison. This flatter profile could indicate that some hydrogen diffuses more in this sample, yet this would need to be confirmed with other measurements or more extensive statistics.

Next, we observed a tailing of the F, H and B profiles for BF_3 samples into the wafer, suggesting a possible diffusion of those species. However, this last affirmation should be put in contrast with the silicon profile of the BF_3 samples, which is less dense near the surface of the wafer, indicating a possibly different porosity of the a-Si(i):H/c-Si interface. If there is indeed diffusion of F, H and B, they are correlated with the particular surface condition of this sample and we cannot conclude that this is only an effect triggered in BF_3-prepared samples.

A.3.4 Activation energy influence on samples treatments

In this section, we present the effect of sample treatments upon the measured activation energy E_a. Different treatments were applied to the a-Si(i):H / nc-Si(p):H samples co-deposited on

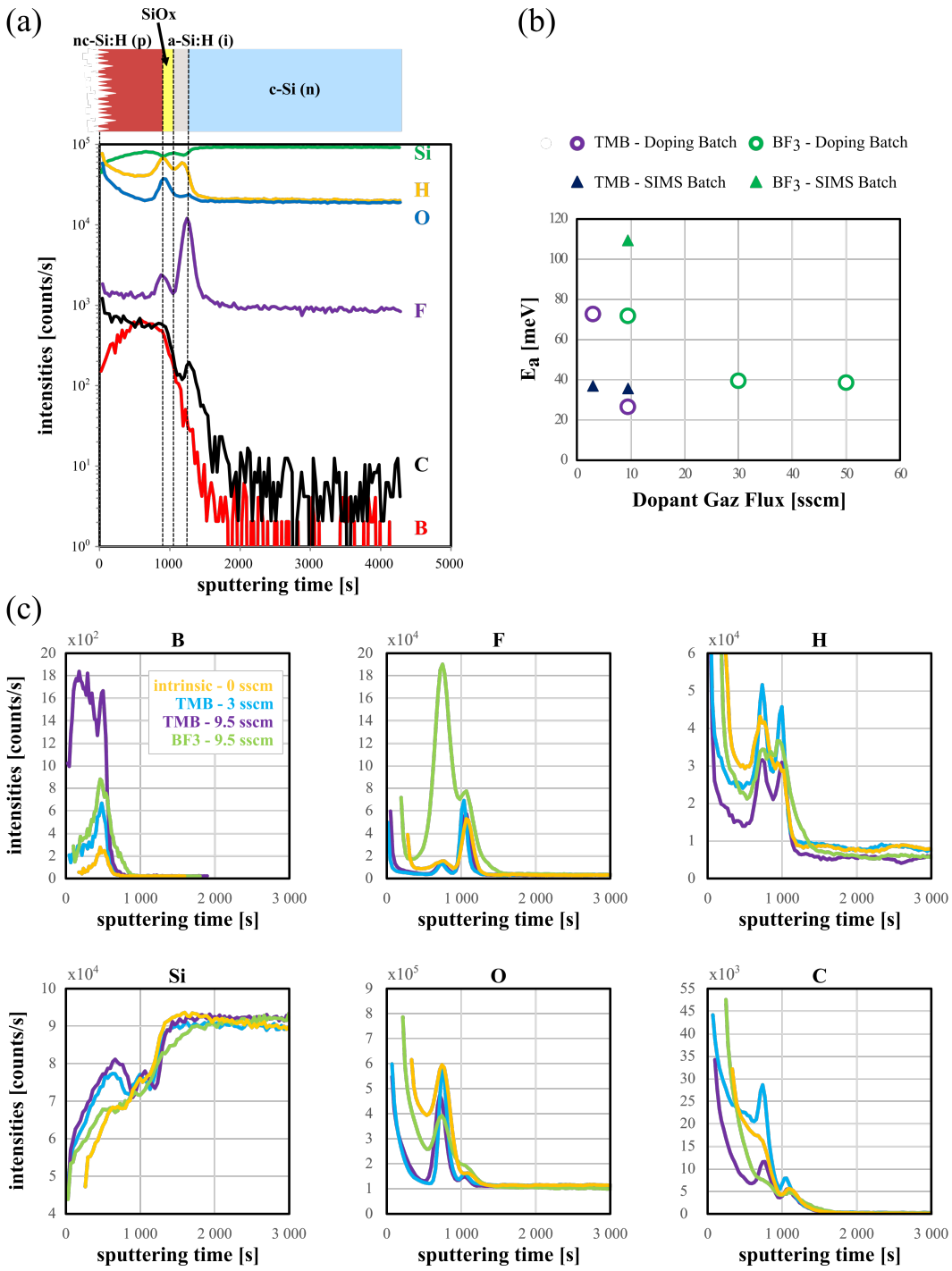

Figure A.10: SIMS profile of ip stacks deposited on DSP wafer. (a) Example of a nc-Si:H(p) / SiOx / a-Si:H (i) / c-Si(n) contact analysis, featuring the layer prepared with 9.5 sccm TMB. Note the impact of the surface roughness that decreases the signals intensities for early sputtering time. (b) Activation energy of the nc-Si:H(p) layer for different dopant flows and dopant sources and two different batches of samples. (c) Profiles of B, F, H, Si, O, and C compared for different doping flows and dopant sources. Note that in (a) and (c), the difference in the spectra of the B, F and O species arise due to the different mode of measurement, the second one being more accurate to measure those atoms concentrations (see section 4.3.3).

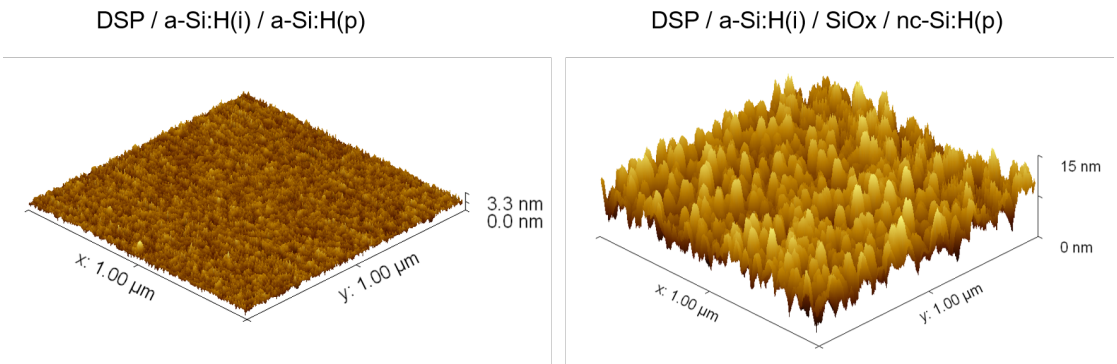

Figure A.11: Atomic force microscope surface topography of amorphous and nano-crystalline silicon deposited on double side polished wafer. Note the strong surface roughness of the nc-Si:H(p) (15 nm from peak to valley).

glass: samples were dipped in HF or pre-annealed in N_2/air prior to the Al pad evaporation, or post-annealed in N_2, as well as exposed to combinations of those treatments. Note that the value reported in the main text corresponds to a 2 hour annealing in N_2, consistent with our standard characterization method. On Figure A.12, we see that all doping preparation can lead to E_a values of 30 meV upon long enough post-annealing in N_2 atmosphere. This effect cannot be attributed to dopant activation since samples annealed before the Al pad deposition did not exhibit such reduction of E_a. However, for the samples prepared with 9.5 sccm of BF_3 that were dipped in HF right before the Al pad evaporation, the E_a value remains high in all the cases, showing that attention should be paid to surface oxidation.

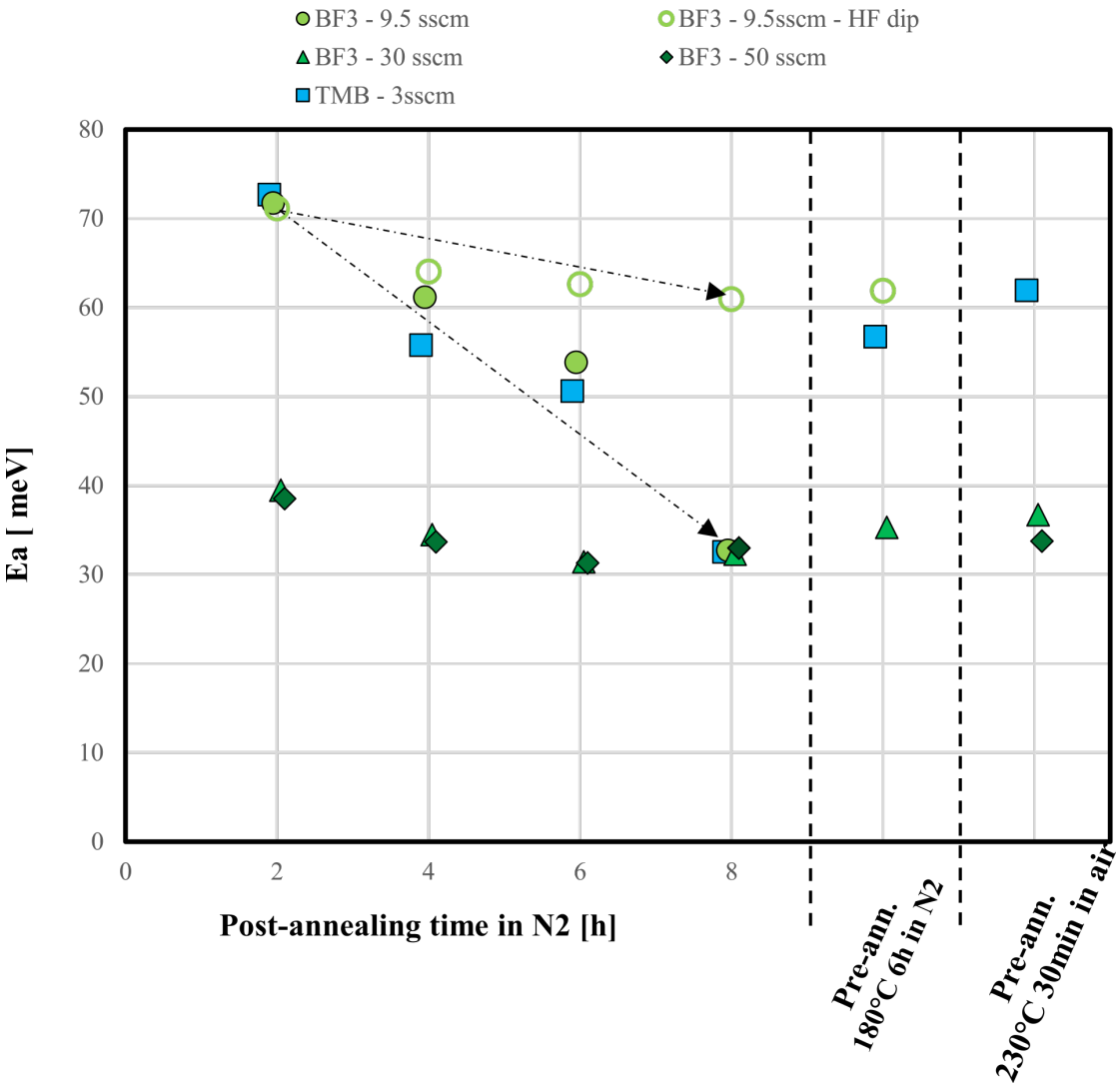

Figure A.12: Activation energy of the doping series after different treatments. Pre-annealing and "HF dip" refer to treatment prior to the Al pad evaporation on the contrary to post-annealing. Measurements shown in the main text correspond to the first 2 hours of post-annealing in N_2

A.3.5 Variability of ellipsometry data fit

Figure A.13 presents the variability on the thicknesses extracted from ellipsometry as a function of different fitting models and initial conditions for the algorithm. It can be seen that the variability on total thickness of the layers (d_{tot}) remains below ± 1 nm, making it a robust metric. The roughness was more sensitive to the initial conditions of the fit, starting with a low-refractive index material leading to zero surface roughness.

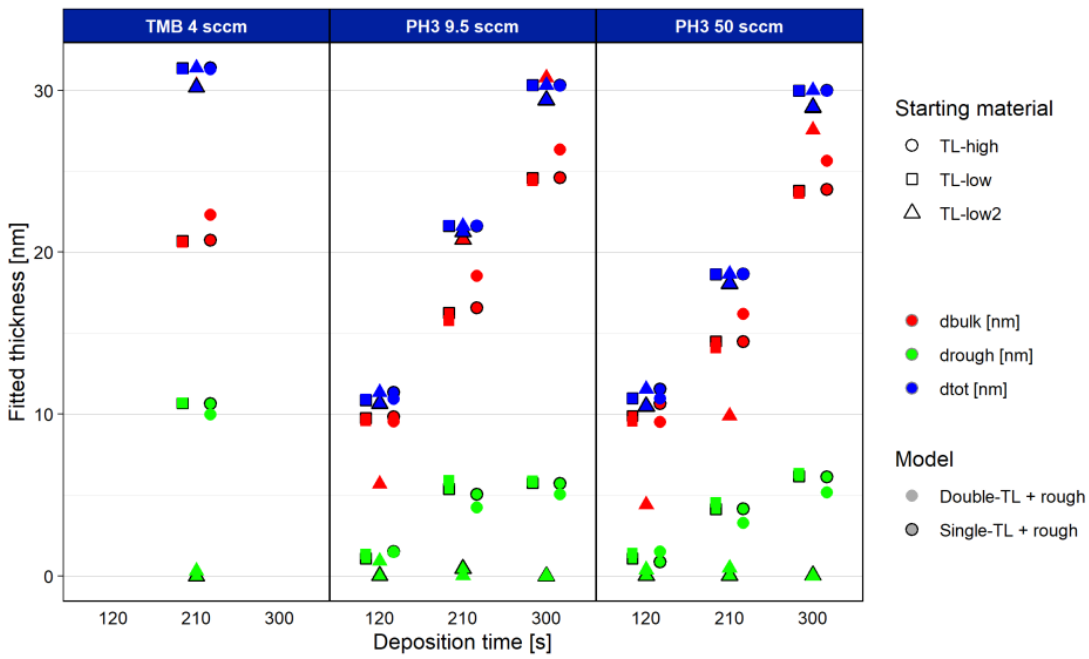

Figure A.13: Bulk thickness, roughness thickness and total thickness of various nc-Si:H layers deposited with different deposition times, as a function of the fitting model and initial conditions, the latter corresponding to the starting material "TL-high", "TL-low" and "TL-low". The main difference between those starting points is the overall amplitude of the refractive index, with $n > 6$ at 600 nm for "TL-high", $n \approx 2$ for "TL-low" and $n \approx 1$ for "TL-low2".

A.3.6 BF_3 thickness series - transport properties

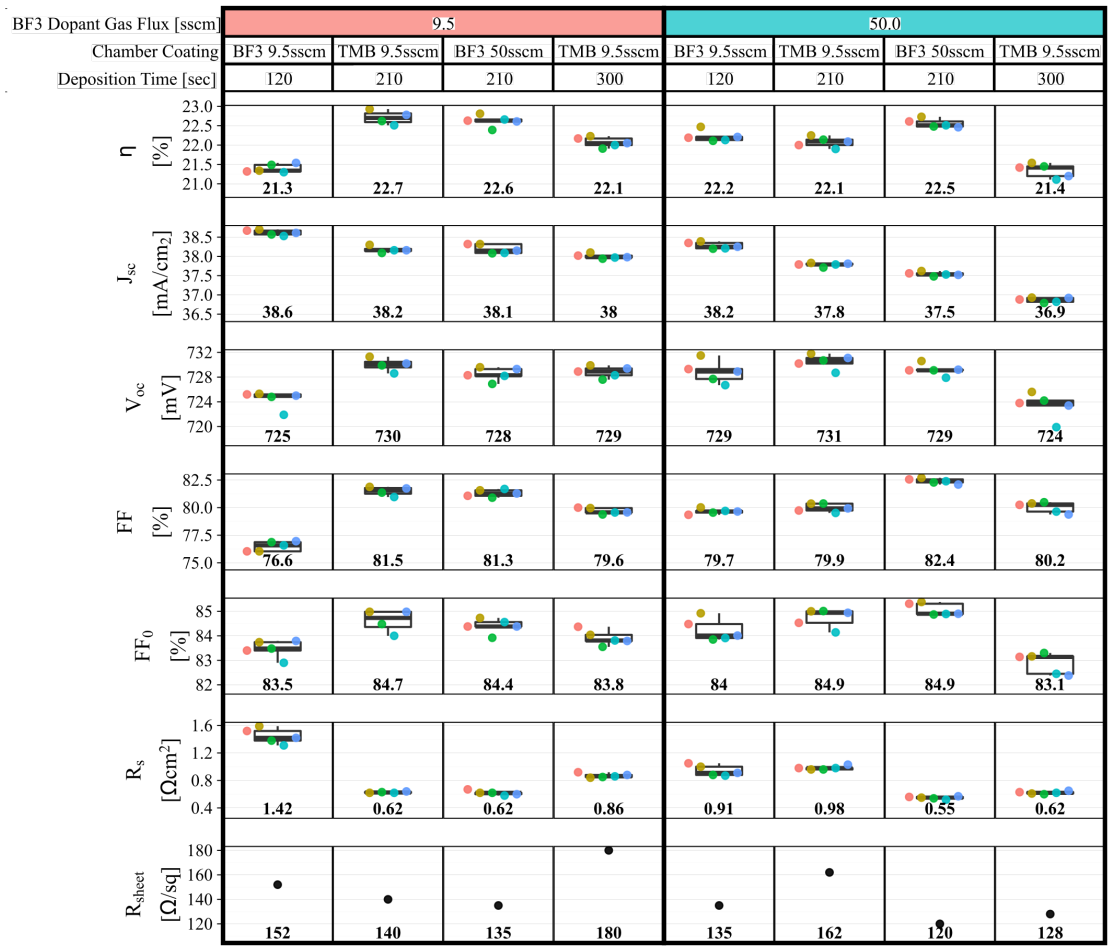

Figure A.14: Full J-V *results of the BF_3 thickness series, as well as front TCO sheet resistance. Two BF_3 flows are used during deposition, 9.5 and 50 sccm, and the thicknesses are varied through the deposition time (120 s, 210 s, 300 s). The chamber precoating before the nc-Si:H(p) layer deposition is also reported.*

In this section we report the full *J-V* results of the BF_3 thickness series, from which the optical properties were discussed in section 4.4.2. The results are presented on Figure A.14. We observe that for the layer prepared with 9.5 sccm of BF_3, the V_{oc} FF_0 and R_s all start to deteriorate when using too thin layers. For the layer prepared with 50 sccm of BF_3, the V_{oc} remains close to 730 mV for 120 s deposition time. The R_s and FF_0 are lower than with the best layer (50 sccm, 210 s and pre-coating of 50 sccm of BF_3), however we can see that another deposition with the same parameters as the best layer except the chamber pre-coating (50 sccm, 210 s and pre-coating of 9.5 sccm of TMB) yields similar increase of R_s than for the thinner layer. It is therefore not clear if we can thin down layer with 50 sccm of BF_3 without impacting their transport properties. More data would be needed to reduce the sample to sample variations. We can note however that even the thinnest 50 sccm BF_3 layer suffers from

important parasitic absorption, leading to a current of 38.2 mA cm^{-2} which is lower than that obtained *e.g.* with thicker TMB layers, as well as with worse transport properties. Therefore, we conclude there is no interest in doing thinner BF_3-based layer for front application and that its use is more interesting for rear contact. Testing a mixture of both TMB and BF_3 flow would also be an interesting option to find a better trade-off of crystallinity vs doping concentration.

A.3.7 Additional certified *J-V* results

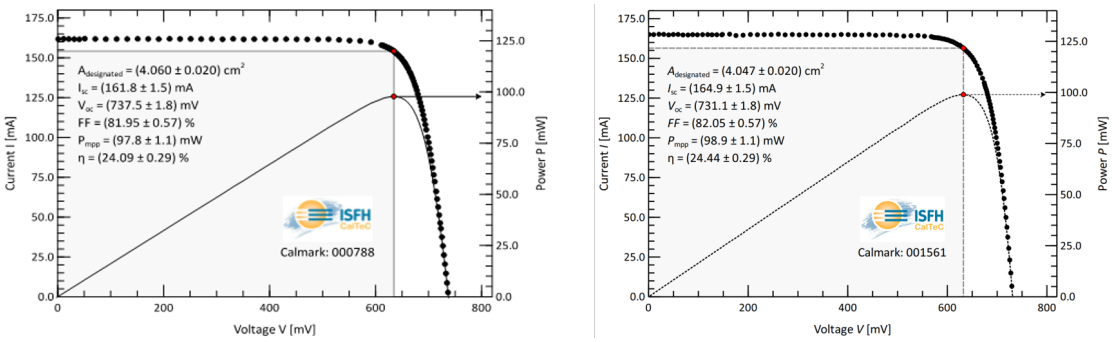

Figure A.15: Additional certified J-V *results for the cell structure presented on Figure 4.8.*

A.3.8 Additional *J-V* results - nc-Si:H vs. nc-SiO_x:H DARC and forward bias.

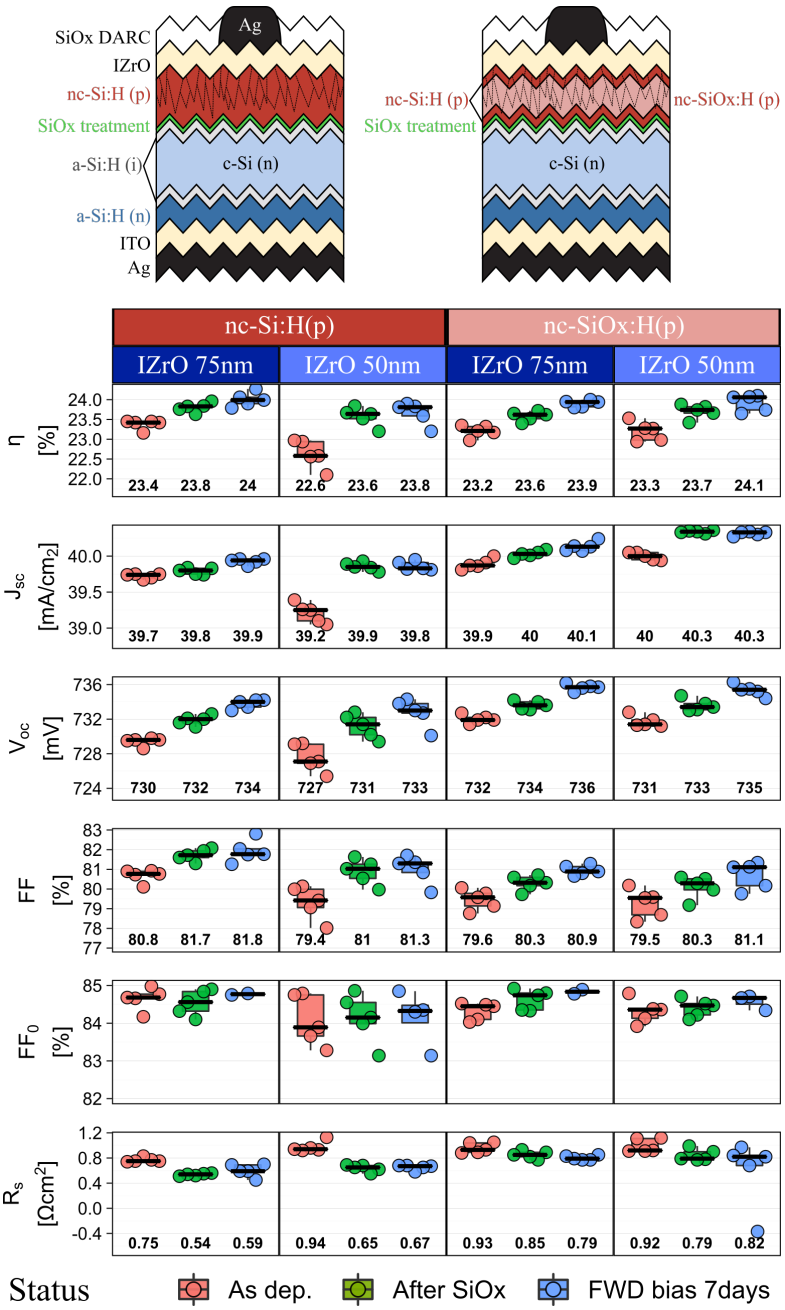

*Figure A.16: Solar cell results depending on the combination of nc-Si:H(*p*) and nc-SiO_x:H(*p*) with IZrO, double anti-reflective coating and forward bias, allowing to reach efficiencies higher than* 24%

A.4 Appendix to nc-Si:H(*n*) development

A.4.1 Raman spectra as a function of dopant flow

We present Raman spectra measured with a 442 nm-wavelength laser of nc-Si:H(*n*) layers prepared with different dopant flows and a fixed deposition time of 210 s. Those spectra correspond to the data shown in Figure 6.2 of the main text. All the layers have a similar thickness, measured via ellipsometry on glass to be 20 nm. We observe that as the dopant flow is increased, the weight of the amorphous silicon peak at 480 cm^{-1} increases while that of the crystalline peak at 520 cm^{-1} decreases. As the layer thicknesses are similar for all the samples, this indicates an amorphization of the bottom part of the layer.

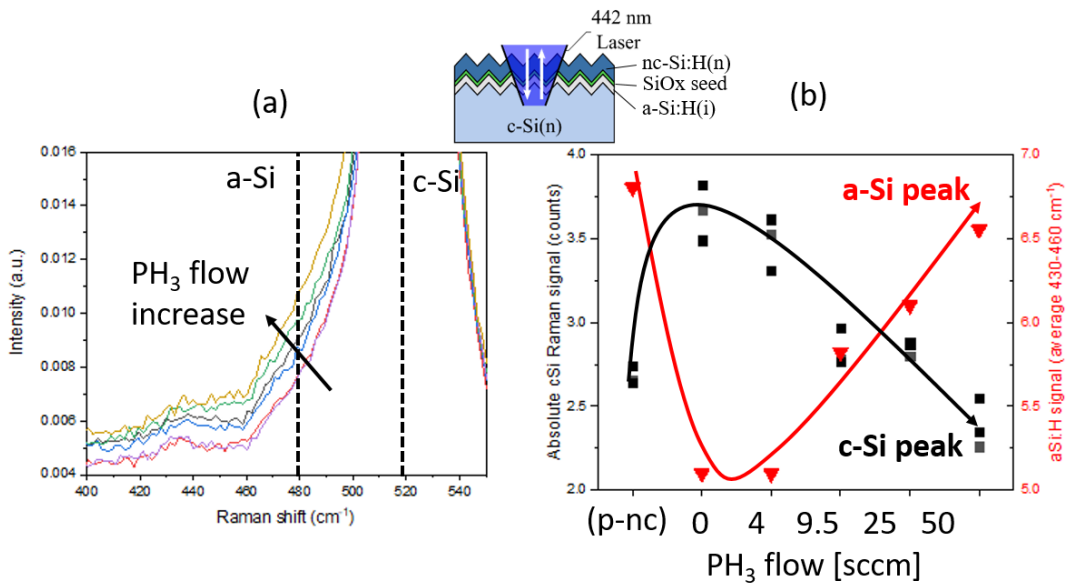

Figure A.17: (a) VIS-Raman spectra of nc-Si:H layers for different dopant flows. (b) Crystalline and amorphous peak signal as a function of the dopant flow.

A.4.2 Contact resistance extraction from thin TCO solar cells

In this section, we expose in detail the method we used to extract the contact resistivity of the *n*-type CSPCs presented in section 6.4.2 of the main text. As explained in the main text, we choose not to rely on TLM measurements, since in our specific case the evaluation of the contact resistivity after the SiO_x deposition could be problematic due to the larger silver pads masking the deposition under the contact. Therefore, we rely on performing accurate series resistance breakdown of solar cells and extract the contact resistivity of interest out of it.

The main strategy was to use a thin TCO layer on the front of the solar cell in order to increase the precision of the method. Indeed, in this case the high sheet resistance of the front TCO

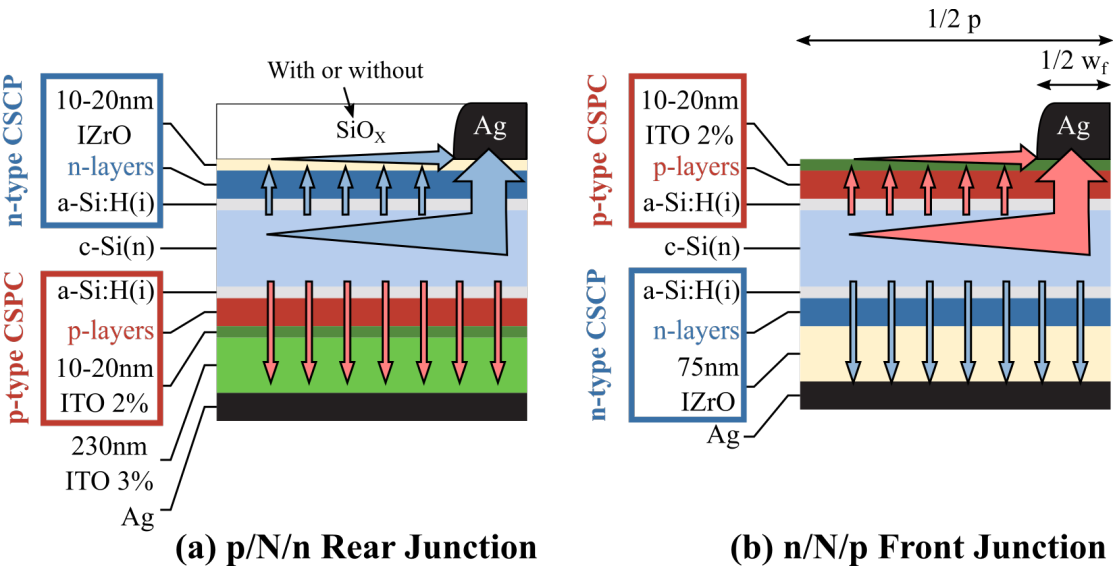

Figure A.18: Sister solar cells in rear (a) and front junction (b) configurations, both with a thin front TCO. Only half a pitch ($p = 1.85$ mm) and finger width ($w_f = 30$ µm) is represented. Note that the p-type and n-type CSPCs consist of the same stack of layers in both devices. The red and blue arrows indicate the hole- and electron-current, respectively. Due to the high front TCO resistivity, the hole/electron current accumulates in the wafer in the front/rear junction cell and leads to high resistive losses when flowing through the small finger section. Texture is omitted for simplicity.

increases the dependence of the solar cell series resistance upon the front contact resistivity and allows a better evaluation of the latter. We support our conclusions by evaluating the sensitivity of the different parameters upon the determination of ρ_c^p and ρ_c^n. This axis of research allows also to study directly the functioning of solar cell in situations closer to interesting optimization pathways using *e.g.* front localized contact or thin TCO / dielectric bilayer.

Results and discussion

To proceed with the evaluation of ρ_c^n, we process similar RJ solar cells as in the main text, *i.e.* featuring the same layers except the front IZrO that is thinned down to 10–20 nm (Figure A.18(a)). Moreover, we process FJ solar cells to evaluate ρ_c^p, featuring the reference *p*-type CSPC used in the other device at the front covered with the same 10–20 nm-thin ITO (Figure A.18(b)).

Then, we process as follows to perform the series resistance breakdown. First, we measure the *J*-*V* curves of those solar cells at 1 sun and various lower illuminations in order to find which one leads to a pV_{mpp} value similar to the one reached by the corresponding cells with thicker TCO (*i.e.* in the 630–650 mV range). Next, we then compute R_s from those measurements using the J_{sc}-V_{oc} method described in 2.3.4.

Then, we decompose the series resistance using Haschke's model [Haschke 2020], for which we recall here the expression for a monofacial front junction

$$R_s(\Delta n) = R_s^{lat+C}\left(R_{sh,h^+}^{cSi}(\Delta n), R_{sh}^{TCO}, \rho_c^p\right) + \overbrace{R_s^f + R_{s,e^-}^{vert,cSi}(\Delta n) + \rho_c^n}^{=R_s^{res}}, \tag{A.32}$$

and a rear junction

$$R_s(\Delta n) = R_s^{lat+C}\left(R_{sh,e^-}^{cSi}(\Delta n), R_{sh}^{TCO}, \rho_c^n\right) + \overbrace{R_s^f + R_{s,h^+}^{vert,cSi}(\Delta n) + \rho_c^p}^{=R_s^{res}}, \tag{A.33}$$

where the effective series resistance R_s^{lat+C} is a function of the coupling of the sheet resistance of the minority carriers in the wafer and in the TCO sheet resistance ($R_{sh,h^+/e^-}^{cSi}$ and R_{sh}^{TCO}, respectively) together with the contact resistivity from the absorber to the front TCO ($\rho_c^{p/n}$), Δn is the injected carrier concentration of electrons and holes, R_s^f is the finger resistance, $\rho_c^{n/p}$ is the contact resistivity of the rear side, and finally $R_{s,e^-/h^+}^{vert,cSi}$ is the vertical resistance of the minority carriers moving towards the back contact. At the end of the day, once the residual resistance R_s^{res} has been subtracted and R_{sh}^{TCO} and $R_{sh,h^+/e^-}^{cSi}$ have been evaluated, taking into account the precision on each term, a range for the contact resistivity can be estimated from the contour plots of R_s^{lat+C}, such as those presented in Figure A.19.

In the following paragraphs, we discuss the evaluation of the different terms entering into these equations, as well as the error bound on each of them:

- The evaluation of the $R_{sh,h^+/e^-}^{cSi}$ is performed using the formula [Haschke 2020]

$$R_{sh,h^+/e^-}^{cSi}(\Delta n) = \begin{cases} \left(q\mu_e(N_D+\Delta n)(N_D+\Delta n)\,t\right)^{-1}, & \text{for FJ} \\ \left(q\mu_h(\Delta n)(\Delta n)\,t\right)^{-1}, & \text{for RJ} \end{cases} \tag{A.34}$$

  where t is the wafer thickness, N_D is the donor density, and μ_e and μ_h are the injection dependant electron and hole mobilities respectively, which can be calculated using Masetti's or Klaasen's formula [Masetti 1983, Klaassen 1992]. Moreover, assuming perfect selectivity losses ($pV_{mpp} = iV_{mpp}$), the injection can be computed using

$$\Delta n = \sqrt{\frac{(n_0-p_0)^2}{4} + n_0 p_0 \exp\frac{pV_{mpp}}{k_B T} - n_0 p_0} - \frac{n_0+p_0}{2}, \tag{A.35}$$

  where $n_0 \approx N_D$, $p_0 \approx n_i^2/n_0$ and n_i is the intrinsic carrier concentration.

- For the evaluation of R_{sh}^{TCO} of the thin ITO and IZrO layers, co-deposited TLM were prepared on quarter wafers, featuring the same PECVD layers underneath the TCO. To block the current flowing inside the wafer in those structure, the n-type CSPC was deposited on a p-type wafer and reciprocally for the p-type CSPC. The TLM silver pads were then

sputtered through a shadow mask, the samples annealed at 210 °C for 30 minutes and cut to form mesa-isolation. The sheet resistance was found to vary significantly among the different samples, which we assume comes from the substrate influence as it correlates with the overall crystallinity of the stack [Cruz 2019a, Boccard 2021], justifying the approach. Three TLM samples were realized for each condition, leading to a range of errors for R_{sh}^{TCO} for each contact stack.

- R_s^f was evaluated to be in the 145–162 mΩ cm^2 range as measured from the 6 line resistance structures of this batch (see sec. 2.2.8).

- The vertical transport term is computed as

$$R_{s,e^-/h^+}^{vert,cSi}(\Delta n) = \begin{cases} t\left(q\mu_e(N_D+\Delta n)(N_D+\Delta n)\right)^{-1}, & \text{for FJ} \\ t\left(q\mu_h(\Delta n)(\Delta n)\right)^{-1}, & \text{for RJ} \end{cases} \tag{A.36}$$

  where once again μ_e and μ_h can be calculated using Masetti's or Klaasen's formula [Masetti 1983, Klaassen 1992]. For example, considering an injection of $\Delta n = 1.7 \times 10^{15}\,\text{cm}^{-3}$ equivalent to $iV_{mpp} = 650\,\text{mV}$ and $N_D = 2.2 \times 10^{15}\,\text{cm}^{-3}$ for our 2 Ω cm wafer, using Masetti's formula results in $R_{s,e^-}^{vert,cSi} = 20\,\text{m}\Omega\,\text{cm}^2$ for a FJ solar cell and slightly higher for a RJ solar cell, $R_{s,h^+}^{vert,cSi} = 150\,\text{m}\Omega\,\text{cm}^2$, since the vertical transport is done by holes which have a lower mobility (about 1/3) and carrier concentration (about 1/2). However, the present formula is an approximation for two reasons: first it assumes that only one carrier type participates to the vertical transport while the other assumes the role of the lateral transport. In practice, as 66% of the carriers are generated in the 10 µm close to the front surface, both will diffuse downwards in the wafer to homogenise the concentration profile to a certain extent (balanced by the carrier extraction). Second, as both carriers diffuse in the same direction on some parts of the path, the ambipolar diffusion coefficient should be used instead, which typically lowers the difference between electron and hole series resistance, reaching an intermediate value [Kane 1988]. To account for this source of bias in our R_s breakdown, we consider for every case that the vertical resistance is in the range given by both $R_{s,e^-}^{vert,cSi}$ and $R_{s,h^+}^{vert,cSi}$ using Masetti's mobilities in eq. A.36.

- Finally, to evaluate ρ_c^p of the *p*-type CSPC contact featured at the rear of the RJ device, we applied the full procedure to the FJ device where this contact is at the front, and assuming a priori a safe large range of values for the rear reference ρ_c^n of 0–100 mΩ cm^2.

After removing the R_s^f, R_s^{vert} and ρ_c^{rear} terms from the measured R_s, as well as after having evaluated R_{sh}^{cSi} from pV_{mpp}, ρ_c^{front} can be found by looking at the contour plot of R_s^{lat+C} versus R_{sh}^{TCO} and ρ_c^{front} as presented in Figure A.19 for four different examples. In (a)-(b), we show how using a thin TCO instead of the regular thickness employed to form an ARC or DARC can improve the accuracy on the evaluation of ρ_c^{front} from this series resistance breakdown. In (c), we show the analysis carried out on the FJ solar cell to extract ρ_c^p from the p contact. In (d), we

show that our thin n-type contact stack reaches values below 15 mΩ cm^2. The evaluation of all the terms of the model are presented in Table A.1 for completeness.

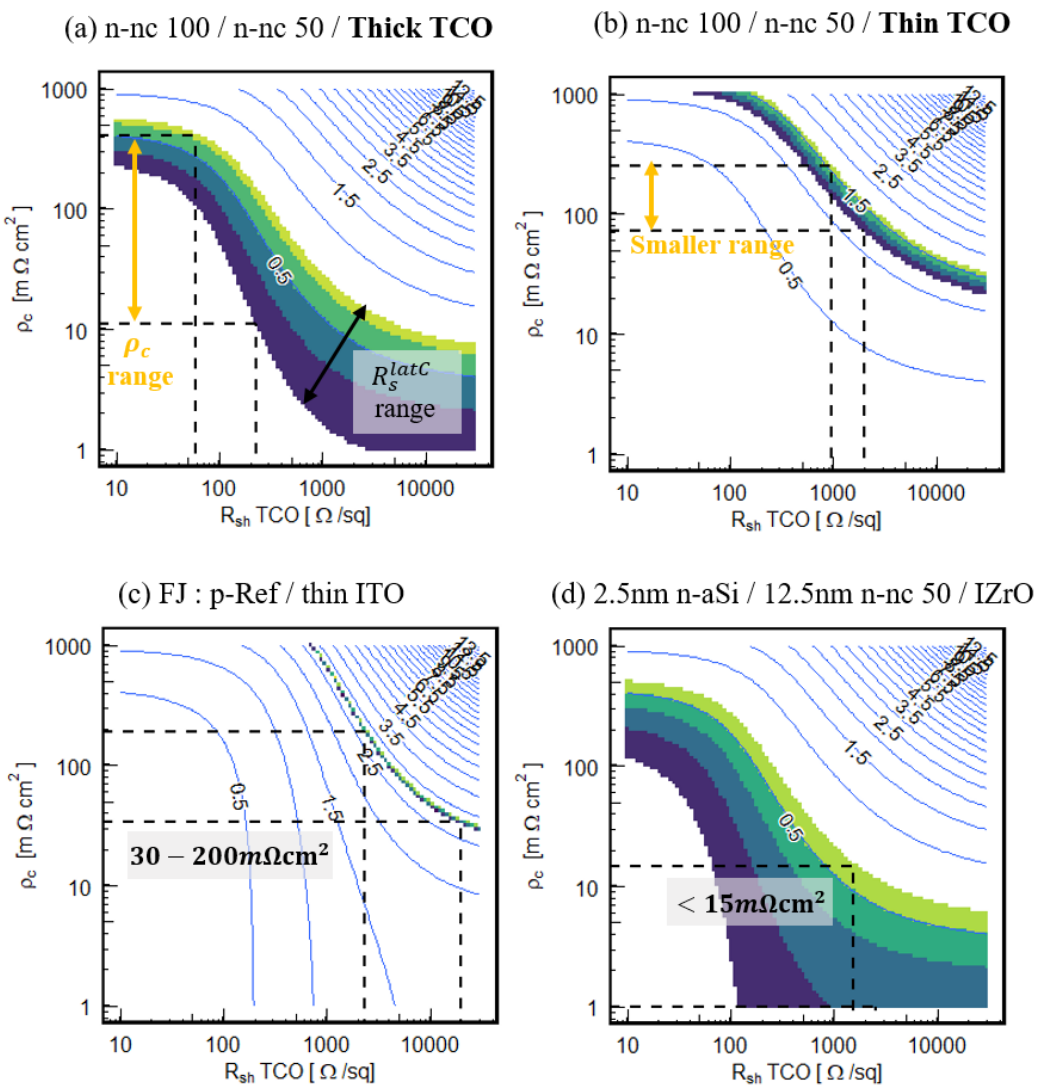

Figure A.19: Contour plot of R_s^{lat+C} versus R_{sh}^{TCO} and ρ_c^{front} for four different contact stacks. The coloured areas correspond to the range within which lies R_s^{lat+C} once R_s^f, R_s^{vert} and ρ_c^{rear} have been removed from the measured R_s*, taking into account an error bound on each parameter. The two vertical dashed lines correspond to the minimum and maximum values of R_{sh}^{TCO}, and the horizontal dashed lines to the minimum and maximal values that can take ρ_c^{front} taking into account the variations of all the other parameters.*

Front TCO	10-20 nm ITO MD	10-20nm IZrO					
Front PECVD layers	**P-ref**	**18nm n-nc 50 12.5nm n-nc 100**		**12.5nm n-nc 50 2.5nm aSi(n)**		**30nm n-nc 50 15nm aSi(n)**	
Rear layers	15nm aSi (n) 30nm n-uc IZrO	P-ref ITO MD					
Stage	Before SiOx	Before SiOx	After SiOx	Before SiOx	After SiOx	Before SiOx	After SiOx
R_s [$\Omega\,\mathrm{cm}^2$]	3.01	1.79	1.23	0.8	0.73	0.72	0.61
R_{sh}^{TCO} [Ω/sq]	2360-20000	950-2000	250-350	1550-2570	300-400	820-1225	266-470
R_s^f [$\Omega\,\mathrm{cm}^2$]	0.146-0.162	0.146-0.162	0.146-0.162	0.146-0.162	0.146-0.162	0.146-0.162	0.146-0.162
$\rho_c\ rear$ [$\Omega\,\mathrm{cm}^2$]	0 or 0.1	0.03-0.2	0.03-0.2	0.03-0.2	0.03-0.2	0.03-0.2	0.03-0.2
pV_{mpp} [mV]	642	636	627	636	654	643	649
R_{sh}^{c-Si} [Ω/sq]	504	74	80	74	61	69	65
R_s^{vert} [$\Omega\,\mathrm{cm}^2$]	0.03	0.02-0.23	0.02-0.29	0.02-0.23	0.02-0.14	0.02-0.19	0.02-0.16
$R_s^{lat+C}max$ [$\Omega\,\mathrm{cm}^2$]	2.83	1.59	1.03	0.60	0.53	0.52	0.41
$R_s^{lat+C}min$ [$\Omega\,\mathrm{cm}^2$]	2.72	1.20	0.58	0.21	0.23	0.17	0.09
$\rho_c front$ [$\Omega\,\mathrm{cm}^2$]	30-200	70-250	65-350	<15	<15*	<15	<25

Table A.1: Summary of the series resistance breakdown and ρ_c evaluation using thin TCO for three different n*-type contacts and the reference* p*-type contact, corresponding to those presented in Figure A.19.*

A.5 Perimeter Losses

Perimeter losses occur due to the escape by diffusion and then recombination of photogenerated carriers inside the non-illuminated area of the absorber adjacent to the active area of the solar cell. Those losses are notably important as they represent one of the largest share of power losses in high efficiency small area silicon solar cells [Fong 2016, Richter 2017, Giglia 2022]. This concept can be extended to full area solar cells, where the edges of the wafer can present a higher surface recombination velocity than the front and rear surfaces, and therefore particular care should be taken to avoid additional losses in these places [Altermatt 1996, Giglia 2022]. Several strategies exist to minimize perimeter losses, such as decreasing the ratio of the perimeter to area of the solar cell, developing a suitable chemical or field-effect passivation scheme for the edges [Altermatt 1996], reducing the TCO-free region close to the edges or increasing the c-Si resistivity [Giglia 2022].

A.5.1 Mathematical model

In this section, we develop a simple estimation of the perimeter losses occurring in our $1 \times 1\,\text{cm}^2$ and $2 \times 2\,\text{cm}^2$ solar cells, where carriers are lost to the dark side. For more advanced mathematical models and experimental verifications of the effect of perimeter losses using *e.g.* photoluminescence imaging, we refer the reader to the literature [Altermatt 1996, Fong 2016, Luque 1993, Haase 2018, Giglia 2022].

We treat the perimeter losses as a first approximation as a 2D problem, where passivation issues not only occur at the front and rear surfaces, but also in the non-illuminated parts of the wafer. Figure A.20 presents the difference between a situation without perimeter losses, where the injection level Δn can reach its maximal values taking into account the effective bulk lifetime τ_{eff}, and a situation with perimeter losses which induce an additional recombination process and leads to a lower injection level in the active area of the solar cell Δn_0^*.

In the absence of perimeter losses, the balance of photogeneration and recombination reads

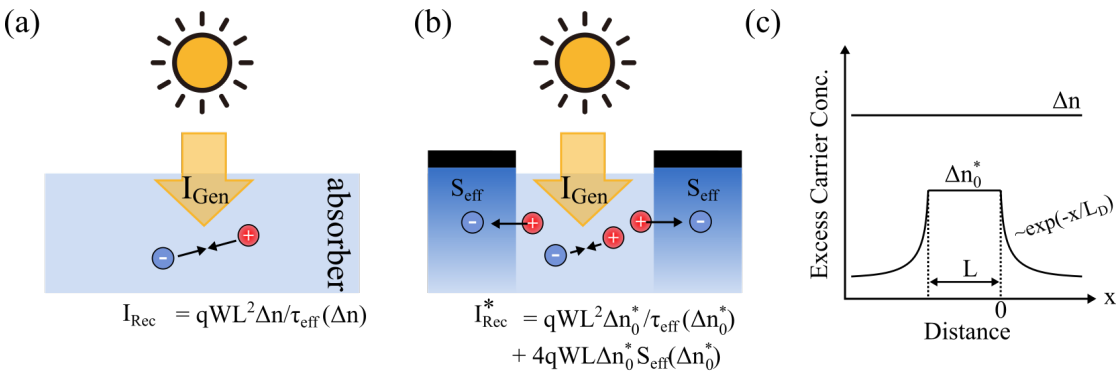

Figure A.20: (a)-(b) Absorber without and with perimeter losses. (c) Sketch of the excess carrier concentration profile in both cases.

as

$$qWG = qWR \equiv qW\frac{\Delta n}{\tau_{eff}(\Delta n)} \tag{A.37}$$

where W is the wafer thickness, G and R are the generation and recombination rates (in [$\mathrm{cm}^{-3}\,\mathrm{s}^{-1}$]), Δn is the carrier concentration and $\tau_{eff}(\Delta n)$ is the effective lifetime in the absence of any perimeter losses. In particular, the function $\tau_{eff}(\Delta n)$ can be either extracted from PCD measurements on real samples or calculated theoretically *e.g.* using Richter's limit [Richter 2013].

When the outside area of the cells is shaded, the perimeter losses can be accounted by an effective surface recombination velocity S_{eff} occurring at each edge of the solar cell. The generation/recombination balance equation then reads over the whole volume as

$$I_{Gen} = qWL^2G = qWL^2\frac{\Delta n_0^*}{\tau_{eff}(\Delta n_0^*)} + 4qWL\Delta n_0^* S_{eff}(\Delta n_0^*) = I_{rec} \tag{A.38}$$

where L is the length along one edge of the illuminated area (we assume a square solar cell) and Δn_0^* is the excess carrier density in the illuminated region when perimeter losses are present.

Several assumptions are underlying this definition. First, we assume that the carrier density is homogeneous in the illuminated part, whereas PL images can show that actually the density decreases towards the edges. This hypothesis can also be broken close to the busbars or fingers, which reduce the carrier concentration in their vicinity as charges are extracted. However, the theory might still be used considering an average of the minority carriers in the illuminated area [Luque 1993]. Moreover, a more uniform concentration profile can be realized *e.g.* if the cell is covered uniformly of a very conductive TCO which will allow to match closer to the hypothesis. Finally, carriers can also escape through the corners of the solar cells which we do not take into account here, which could result in additional losses.

Next, by continuity we should have a balance of the charge carriers crossing the perimeter region and those recombining in the non-illuminated area. This can be written as

$$qWL\Delta n_0^* S_{eff} = qWL\int_0^\infty \frac{\Delta n^*(x)}{\tau_{eff}(\Delta n^*(x))}dx \tag{A.39}$$

where $\Delta n^*(x)$ is the excess carrier concentration in the shaded area. To compute this integral, we need to know the function $\Delta n^*(x)$. In the non-illuminated area, the excess carrier concentration follows the diffusion equation (since no field is present), which is a classic treatment of this problem [Sze 2006]. This reads as

$$\frac{\partial \Delta n^*}{\partial t} = 0 = -\frac{\Delta n^*}{\tau_{eff}(\Delta n^*(x))} + D_p\frac{\partial^2 \Delta n^*}{\partial x^2} \tag{A.40}$$

with boundary conditions $\Delta n^*(x=\infty) = 0$ and $\Delta n^*(x=0) = \Delta n_0^*$. Neglecting the small dependence of D_p on carrier concentration and assuming τ_{eff} only depends on Δn_0^*, the

solution to this equation is

$$\Delta n^*(x) = \Delta n_0^* \exp\left(-\frac{x}{\sqrt{D_p \tau_{eff}(\Delta n_0^*)}}\right) \tag{A.41}$$

where $L_D \equiv \sqrt{D_p \tau_{eff}(\Delta n_0^*)}$ is the minority carrier diffusion length. Using equation A.41 allows to compute the integral of equation A.39 and the solve the equation to find

$$S_{eff} = \sqrt{\frac{D_p}{\tau_{eff}(\Delta n_0^*)}} \tag{A.42}$$

This term is then used to compute $I_{rec}(\Delta n_0^*)$ by using equation A.38. To compute the *iJ-V* curve, we use the fact that for each Δn_0^*, there exists an implied voltage given by

$$iV = \frac{k_B T}{q} \ln\left(\frac{(\Delta n + N_D)\Delta n}{n_i^2}\right) \tag{A.43}$$

and a corresponding implied current that can be extracted from the solar cell

$$iJ = J_{sc}^{1Sun} - \frac{I_{rec}(\Delta n_0^*)}{L^2} \tag{A.44}$$

provided a reference current J_{sc}^{1Sun}. Given the *iJ-V* curve, it is trivial to numerically compute the iV_{oc} and *iFF* for a given solar cell size L when perimeter losses are present.

A.5.2 Perimeter losses and wafer thickness impact on solar cell

Figure A.21 presents the impact of the perimeter losses on iV_{oc} and *iFF* using different input parameters and compare them to the best V_{oc} and *pFF* measured during this thesis on $1 \times 1\,\text{cm}^2$ and $2 \times 2\,\text{cm}^2$ solar cells. The perimeter losses were computed using Richter's model to evaluate the Auger and radiative part of the function $\tau_{eff}(\Delta n)$. On top of that an extra recombination velocity parameter S_{extra} was added to equation A.38, to model an additional bulk SRH or surface recombination term. As a summary, the five inputs of the model presented here are the wafer thickness W, the length of the solar cell side L, the short-circuit current J_{sc}^{1Sun}, the extra recombination velocity S_{extra}, and N_D, the donor density.

We observe that by increasing the solar cell size beyond $10 \times 10\,\text{cm}^2$, large gains of V_{oc} and *pFF* could be achieved, reaching about 748 mV and 87.6 % respectively for a 200 µm wafer, whereas even larger values could be reached by switching to thinner wafers. However, the latter gains would be compromised by a decrease of the J_{sc} in the infrared, and an optimal thickness should be around 110 µm as computed in [Schäfer 2018]. Also note that to simplify the discussion, we fixed $N_D = 2.2 \times 10^{15}\,\text{cm}^{-3}$ corresponding to our *n*-type FZ wafers, however we could compute additional improvements of V_{oc} (about 2 mV) and *iFF* (about 0.3 $\%_{\text{abs.}}$)

when using $N_D = 1 \times 10^{14}\,\mathrm{cm}^{-3}$ and $S_{extra} = 0\,\mathrm{cm/s}$.

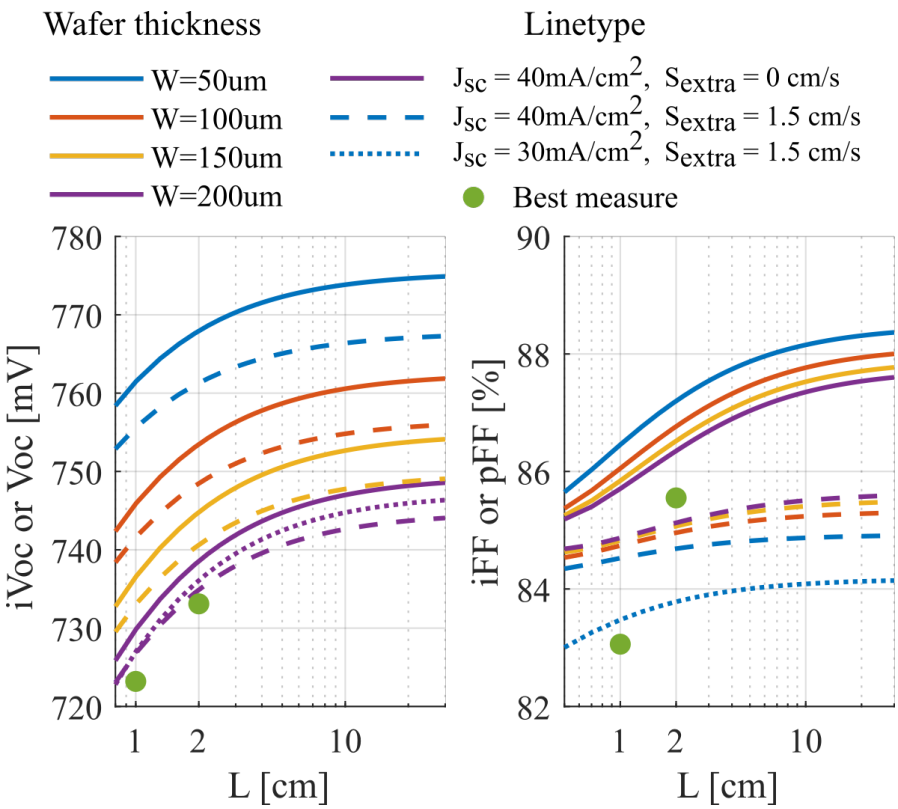

Figure A.21: Impact of the perimeter losses on $\mathrm{iV_{oc}}$ *and* iFF *for different solar cell sizes (L). For each curve calculation, we assumed* $N_D = 2.2 \times 10^{15}\,\mathrm{cm}^{-3}$. *The data points represent the best* $\mathrm{V_{oc}}$ *and* pFF *measured on* $1 \times 1\,\mathrm{cm}^2$ *and* $2 \times 2\,\mathrm{cm}^2$ *solar cells throughout this thesis, which were processed on* 200 µm *FZ wafer with donor density equal to* N_D.

Looking closer at the data, we can see that for the V_{oc} of our best solar cells follows an increase with cell size parallel to the calculated curve. It is however about 5 mV lower than the curve computed with a wafer thickness of $W = 200\,\mu\mathrm{m}$ and $S_{extra} = 0$. This suggests that some passivation or selectivity losses are still present in our devices. Indeed, adding a small $S_{extra} = 1.5\,\mathrm{cm/s}$ is already sufficient to decrease the discrepancy with the experimental data. This could easily come from unperfect surface passivation or a small amount of SRH recombination still present in the bulk. Another possibility for this discrepancy could come from the underestimation of the perimeter losses of our model, since it neglected the losses by the corners of the solar cell.

Regarding the measured *pFF*, the $2 \times 2\,\mathrm{cm}^2$ solar cells would require a value of S_{extra} lower than 1.5 cm/s to be accurately fitted, but still non-zero. This larger misfit than for V_{oc} might stem from the fact that we assume S_{extra} to be injection independent, whereas SRH and surface recombination are usually stronger at low injection than high injection. Finally, for the $1 \times 1\,\mathrm{cm}^2$ solar cells, it is important to consider the large reduction of current of those devices to accurately fit the *pFF* data. Nevertheless, note that variations of J_{sc} in the 39–43 $\mathrm{mA\,cm}^{-2}$

range did not yield significantly different curves than those presented here and therefore similar trends for V_{oc} and FF should be valid for the best $2 \times 2\,\mathrm{cm}^2$ solar cells presented in this thesis, no matter the variation of optical properties as long as it stays in this range.

Bibliography

[Adachi 2015] Daisuke Adachi, José Luis Hernández and Kenji Yamamoto. *Impact of carrier recombination on fill factor for large area heterojunction crystalline silicon solar cell with 25.1% efficiency.* Applied Physics Letters, vol. 107, no. 23, pages 1–4, 2015.

[Allen 2019] Thomas G. Allen, James Bullock, Xinbo Yang, Ali Javey and Stefaan De Wolf. *Passivating contacts for crystalline silicon solar cells.* Nature Energy, vol. 4, no. 11, pages 914–928, 2019.

[Altermatt 1996] Pietro Altermatt. *Numerical Quantification and Minimization of Perimeter Losses in High-efficiency Silicon Solar Cells.* Progress in Photovoltaics: Research and Applications, vol. 4, no. May, pages 355–367, 1996.

[Antognini 2021] Luca Antognini, Vincent Paratte, Jan Haschke, Jean Cattin, Julie Dréon, Mario Lehmann, Laurie-Lou Senaud, Quentin Jeangros, Christophe Ballif and Mathieu Boccard. *Influence of the Dopant Gas Precursor in P-Type Nanocrystalline Silicon Layers on the Performance of Front Junction Heterojunction Solar Cells.* IEEE Journal of Photovoltaics, vol. 11, no. 4, pages 944–956, 2021.

[Apet 2006] P P Apet, O N Ichiporuk, A F Ave, A K Aminski, B B Azer Achi and M L Emiti. *TMAH texturisation and etching of interdigitated back-contact solar cells.* Materials Science-Poland, vol. 24, no. 4, 2006.

[Augusto 2020] A. Augusto, J. Karas, P. Balaji, S. G. Bowden and Richard R. King. *Exploring the practical efficiency limit of silicon solar cells using thin solar-grade substrates.* Journal of Materials Chemistry A, vol. 8, pages 16599–16608, 2020.

[Balent 2021] Jošt Balent, Franc Smole, Marko Topič and Janez Krč. *Numerical Analysis of Selective ITO/a-Si:H Contacts in Heterojunction Silicon Solar Cells: Effect of Defect States in Doped a-Si:H Layers on Performance Parameters.* IEEE Journal of Photovoltaics, vol. 11, no. 3, pages 634–647, 2021.

[Basset 2021] Léo Basset, Wilfried Favre, Olivier Bonino, Julien Sudre, M Gilles and Jean-Pierre Vilcot. *In depth analysis of transfer length method application on passivated contacts under illumination.* Solar Energy Materials and Solar Cells, vol. 230, no. July, 2021.

[Bassi 2002] Nicolas Bassi, Charles Clerc, Yanik Pelet, Jonas Hiller, Vahid Fakhfouri, Corinne Droz, Mathieu Despeisse, Jacques Levrat, Antonin Faes, Derk Bätzner and Pierre Papet. *GRIDTOUCH: Innovative Solution For Accurate IV measurement of Busbarless Cells In Production And Laboratory Environments.* In 29th European Photovoltaic Solar Energy Conference and Exhibition, pages 1–6, 2002.

[Battaglia 2016] Corsin Battaglia, Andres Cuevas and Stefaan De Wolf. *High-efficiency crystalline silicon solar cells: status and perspectives.* Energy Environ. Sci., vol. 9, no. 5, pages 1552–1576, 2016.

[Bätzner 2019] D L Bätzner, P. Papet, B. Legradic, D. Lachenal, R. Kramer, T Kössler, L. Andreetta, S. Pitteloud, N. Holm, J. P. Cardoso and B. Strahm. *Alleviating performance and cost constraints in silicon heterojunction cells with HJT 2.0.* In 2019 IEEE 46th Photovoltaic Specialists Conference (PVSC), pages 1471–1474. Institute of Electrical and Electronics Engineers Inc., jun 2019.

[Berger 1972] H. H. Berger. *Contact Resistance and Contact Resistivity.* Journal of the Electrochemical Society, vol. 119, no. 4, page 507, 1972.

[Bermejo 1979] Dionisio Bermejo and Manuel Cardona. *Raman scattering in pure and hydrogenated amorphous germanium and silicon.* Journal of Non-Crystalline Solids, vol. 32, pages 405–419, 1979.

[Bivour 2013] Martin Bivour, Sebastian Schröer and Martin Hermle. *Numerical analysis of electrical TCO / a-Si:H(p) contact properties for silicon heterojunction solar cells.* Energy Procedia, vol. 38, pages 658–669, 2013.

[Bivour 2014] M. Bivour, M. Reusch, S. Schroer, F. Feldmann, J. Temmler, H. Steinkemper and M. Hermle. *Doped layer optimization for silicon heterojunctions by injection-level-dependent open-circuit voltage measurements.* IEEE Journal of Photovoltaics, vol. 4, no. 2, pages 566–574, 2014.

[Bivour 2017] Martin Bivour, Christoph Messmer, Lisa Neusel, Florian Zähringer, Jonas Schön, Stefan W. Glunz and Martin Hermle. *Principles of carrier-selective contacts based on induced junctions.* PV European PV Solar Energy Conference and Exhibition, pages 25–29, 2017.

[Boccard 2018] Mathieu Boccard, Raphaël Monnard, Angela N. Fioretti, Luca Antognini and Christophe Ballif. *Silicon Oxide Treatment to Promote Crystallinity of p-type Microcrystalline Layers for Silicon Heterojunction Solar Cells.* In Proceedings of SiliconPV2018, AIP, page 040003. AIP Publishing LLC, 2018.

[Boccard 2019] Mathieu Boccard, Luca Antognini, Jean Cattin, Julie Dréon, Olivier Dupré, Angela Fioretti, Raphaël Monnard, Monica Morales-masis, Vincent Paratte, Esteban Rucavado, Sihua Zhong, Bertrand Paviet-salomon, Matthieu Despeisse and Christophe Ballif. *Paths for maximal light incoupling and excellent electrical performances in*

silicon heterojunction solar cells. In 2019 IEEE 46th Photovoltaic Specialists Conference (PVSC), pages 2541–2545, 2019.

[Boccard 2021] Mathieu Boccard, Luca Antognini, Vincent Paratte, Jan Haschke, Minh Truong, Jean Cattin, Julie Dréon, Wenjie Lin, Laurie-lou Senaud, Bertrand Paviet-salomon, Sylvain Nicolay, Matthieu Despeisse and Christophe Ballif. *Hole-selective front contact stack enabling 24.1%-efficient silicon heterojunction solar cells.* IEEE Journal of Photovoltaics, vol. 11, no. 1, pages 9–15, 2021.

[Bowden 2001] S Bowden and A Rohatgi. *Rapid and accurate determination of series resistance and fill factor losses in industrial silicon solar cells.* In 17th European Photovoltaic Solar Energy Conference, 2001.

[BP 2021] BP. *Statistical Review of World Energy.* 2021.

[Brendel 2016] Rolf Brendel and Robby Peibst. *Contact Selectivity and Efficiency in Crystalline Silicon Photovoltaics.* IEEE Journal of Photovoltaics, vol. 6, no. 6, pages 1413–1420, 2016.

[Bullock 2016] James Bullock, Mark Hettick, Jonas Geissbühler, Alison J. Ong, Thomas Allen, Carolin M. Sutter-Fella, Teresa Chen, Hiroki Ota, Ethan W. Schaler, Stefaan De Wolf, Christophe Ballif, Andrés Cuevas and Ali Javey. *Efficient silicon solar cells with dopant-free asymmetric heterocontacts.* Nature Energy, vol. 1, no. 3, page 15031, 2016.

[Carpenter III 2017] Joe V Carpenter III, Mark Bailly, Allison Boley, Jianwei Shi, Michael Minjares, David J Smith, Stuart Bowden and Zachary C Holman. *Substrate-independent analysis of microcrystalline silicon thin films using UV Raman spectroscopy.* Physica status solidi (b), vol. 254, no. 9, page 1700204, 2017.

[Cattin 2020] Jean Cattin. *Characterization of silicon heterojunction solar cells beyond standard test conditions.* PhD thesis, EPFL, 2020.

[Cattin 2021] Jean Cattin, Laurie-lou Senaud, Jan Haschke, Bertrand Paviet-salomon, Matthieu Despeisse, Christophe Ballif and Mathieu Boccard. *Influence of Light Soaking on Silicon Heterojunction Solar Cells With Various Architectures.* IEEE Journal of Photovoltaics, vol. 11, no. 3, pages 575–583, 2021.

[CEA 2021] CEA. *25%!!! New world-class certified record for heterojunction solar cell efficiency,* 2021.

[Chen 2019] Daniel Chen, Moonyong Kim, Jianwei Shi, Bruno Vicari Stefani, Zhengshan Yu, Shaoyang Liu, Roland Einhaus, Stuart Wenham, Zachary Holman and Brett Hallam. *Defect engineering of p-type silicon heterojunction solar cells fabricated using commercial-grade low-lifetime silicon wafers.* Progress in Photovoltaics: Research and Applications, no. December 2018, pages 1–15, 2019.

[Cho 2018] Jun-sik Cho, Eunseok Jang, Dongmin Lim, Seungkyu Ahn, Jinsu Yoo, Ara Cho, Joo Hyung, Kihwan Kim and Bo-hun Choi. *Wide-bandgap nanocrystalline silicon-carbon alloys for photovoltaic applications.* Solar Energy Materials and Solar Cells, vol. 182, no. January, pages 220–227, 2018.

[ClimateWatch 2021] ClimateWatch. *Climate Watch Historical Country Greenhouse Gas Emissions Data (1990-2018)*, 2021.

[CRM-alliance 2020] CRM-alliance. *Critical Raw materials*, 2020.

[Cruz 2019a] Alexandros Cruz, Florian Ruske, Alberto Eljarrat, Pawel P Michalowski, Anna B Morales-Vilches, Sebastian Neubert, Er-Chien Wang, Christoph T Koch, Bernd Szyszka, Rutger Schlatmann*et al. Influence of silicon layers on the growth of ITO and AZO in silicon heterojunction solar cells.* IEEE Journal of Photovoltaics, vol. 10, no. 2, pages 703–709, 2019.

[Cruz 2019b] Alexandros Cruz, Er Chien Wang, Anna B. Morales-Vilches, Daniel Meza, Sebastian Neubert, Bernd Szyszka, Rutger Schlatmann and Bernd Stannowski. *Effect of front TCO on the performance of rear-junction silicon heterojunction solar cells: Insights from simulations and experiments.* Solar Energy Materials and Solar Cells, vol. 195, no. October 2018, pages 339–345, 2019.

[Cruz 2022] Alexandros Cruz, Darja Erfurt, Philipp Wagner, Anna B Morales-Vilches, Florian Ruske, Rutger Schlatmann and Bernd Stannowski. *Optoelectrical analysis of TCO+ Silicon oxide double layers at the front and rear side of silicon heterojunction solar cells.* Solar Energy Materials and Solar Cells, vol. 236, page 111493, 2022.

[Cuevas 1989] Andres Cuevas and Miguel A Balbuena. *Review of analytical models for the study of highly doped regions of silicon devices.* IEEE Transactions on Electron Devices, vol. 30, no. 36, page 3, 1989.

[Cuevas 1996] Andrés Cuevas, Paul A. Basore, Gaëlle Giroult-Matlakowski and Christiane Dubois. *Surface recombination velocity of highly doped n-type silicon.* Journal of Applied Physics, vol. 80, no. 6, 1996.

[Cuevas 2014] Andres Cuevas. *The recombination parameter J0.* Energy Procedia, vol. 55, pages 53–62, 2014.

[Cuevas 2018] Andres Cuevas, Yimao Wan, Di Yan, Christian Samundsett, Thomas Allen, Xinyu Zhang, Jie Cui and James Bullock. *Carrier population control and surface passivation in solar cells.* Solar Energy Materials and Solar Cells, vol. 184, no. February, pages 38–47, 2018.

[De Wolf 2009] Stefaan De Wolf and Michio Kondo. *Nature of doped a-Si:H/c-Si interface recombination.* Journal of Applied Physics, vol. 105, no. 10, 2009.

[Demaurex 2012] B. Demaurex, S. De Wolf, A. Descoeudres, Z. C. Holman and C. Ballif. *Damage at hydrogenated amorphous / crystalline silicon interfaces by indium tin oxide overlayer sputtering.* Applied Physics Letters, vol. 171604, no. July 2012, pages 1–5, 2012.

[Dréon 2020] Julie Dréon, Quentin Jeangros, Jean Cattin, Jan Haschke, Luca Antognini, Christophe Ballif and Mathieu Boccard. *23.5%-Efficient Silicon Heterojunction Silicon Solar Cell Using Molybdenum Oxide As Hole-Selective Contact.* Nano Energy, vol. 70, no. December 2019, page 104495, 2020.

[Dréon 2021] Julie Dréon, Jean Cattin, Gabriel Christmann, Davi Fébba, Vincent Paratte, Luca Antognini, Wenjie Lin, Sylvain Nicolay, Christophe Ballif and Mathieu Boccard. *Performance Limitations and Analysis of Silicon Heterojunction Solar Cells Using Ultra-Thin MoO x Hole-Selective Contacts.* IEEE Journal of Photovoltaics, vol. 11, no. 5, pages 1158–1166, 2021.

[Fébba 2021] Davi Fébba, Graduate Student Member, Vincent Paratte, Luca Antognini, Julie Dréon, Julien Hurni, Jonathan Thomet, Rero Rubinger, Edson Bortoni, Christophe Ballif and Mathieu Boccard. *Effects of Work Function and Electron Affinity on the Performance of Carrier-Selective Contacts in Silicon Solar Cells Using ZnSnxGe1- x N2 as a Case Study.* IEEE Journal of Photovoltaics, vol. 11, no. 6, pages 1350–1357, 2021.

[Fioretti 2018] Angela N. Fioretti, Mathieu Boccard, Adele C. Tamboli, Andriy Zakutayev and Christophe Ballif. *Nitride layer screening as carrier-selective contacts for silicon heterojunction solar cells.* AIP Conference Proceedings, vol. 1999, no. 1, page 040007, 2018.

[Fioretti 2019] Angela N. Fioretti, Mathieu Boccard, Raphael Monnard and Christophe Ballif. *Low-Temperature p-Type Microcrystalline Silicon as Carrier Selective Contact for Silicon Heterojunction Solar Cells.* IEEE Journal of Photovoltaics, vol. 9, no. 5, pages 1158–1165, 2019.

[Fong 2016] Kean Chern Fong, Milan Padilla, Andreas Fell, Evan Franklin, Keith R Mcintosh, Teng Choon Kho, Andrew W Blakers, Yona Nebel-jacobsen and Sachin R Surve. *Perimeter Recombination Characterization by Luminescence Imaging.* IEEE Journal of Photovoltaics, vol. 6, no. 1, pages 244–251, 2016.

[Giglia 2022] V Giglia, R Varache, J Veirman and E Fourmond. *Influence of cell edges on the performance of silicon heterojunction solar cells.* Solar Energy Materials and Solar Cells, vol. 238, no. October 2021, page 111605, 2022.

[Glunz 2017] S W Glunz, M Bivour, C Messmer, F Feldmann, R Müller, C Reichel, A Richter, F Schindler, J Benick, M Hermle and Energy Systems. *Passivating and Carrier-selective Contacts – Basic Requirements and Implementation.* In 2017 IEEE 44th Photovoltaic Specialist Conference (PVSC), pages 2064–2069, 2017.

[Glunz 2021] Stefan W Glunz, Christoph Luderer, Bernd Steinhauser, Benjamin Grübel, Jana-isabelle Polzin, Tim Niewelt, Asmaa M O M Okasha, Mathias Bories, Henning Nagel, Katrin Krieg, Armin Richter, Martin Bivour, Martin Hermle and Frank Feldmann. *Silicon-based passivating contacts : The TOPCon route.* Progress in Photovoltaics: Research and Applications, no. November, pages 1–19, 2021.

[Green 1981] Martin A. Green. *Solar cell fill factors: General graph and empirical expressions.* Solid State Electronics, vol. 24, no. 8, pages 788–789, 1981.

[Green 2014] Martin A Green, Keith Emery, Yoshihiro Hishikawa, Wilhelm Warta and Ewan Dunlop. *Solar cell efficiency tables (version 44).* Prog. Photovolt: Res. Appl, vol. 22, 2014.

[Green 2021] Martin A Green, Masahiro Yoshita, Ewan D Dunlop Jochen Hohl-Ebinger, Nikos Kopidakis and Xiaojing Hao. *Solar cell efficiency tables (Version 58).* Progress in Photovoltaics: Research and Applications, vol. 7, no. June, pages 657–667, 2021.

[Guo 2011] Liqiang Guo, Jianning Ding, Jichang Yang, Zhiyong Ling, Guanggui Cheng, Ningyi Yuan and Shubo Wang. *Nanostructure, electrical and optical properties of p-type hydrogenated nanocrystalline silicon films.* Vacuum, vol. 85, no. 6, pages 649–653, 2011.

[Haase 2018] Felix Haase, Christina Hollemann, Sören Schäfer, Agnes Merkle, Michael Rienäcker, Jan Krügener, Rolf Brendel and Robby Peibst. *Solar Energy Materials and Solar Cells Laser contact openings for local poly-Si-metal contacts enabling 26 . 1 solar cells.* Solar Energy Materials and Solar Cells, vol. 186, no. June, pages 184–193, 2018.

[Hadjadj 2010] A. Hadjadj, N. Pham, P. Roca I Cabarrocas, O. Jbara and G. Djellouli. *Ellipsometry investigation of the amorphous-to-microcrystalline transition in a-Si:H under hydrogen-plasma treatment.* Journal of Applied Physics, vol. 107, no. 8, 2010.

[Hallam 2014] Brett Hallam, Yael Augarten, Budi Tjahjono, Thorsten Trupke and Stuart Wenham. *Photoluminescence imaging for determining the spatially resolved implied open circuit voltage of silicon solar cells.* Journal of Applied Physics, vol. 115, no. March, page 044901, 2014.

[Haschke 2018] Jan Haschke. *Silicon heterojunction solar cells: Recent technological development and practical aspects - from lab to industry.* Journal of Management Education, vol. 15, no. 3, pages 279–294, 2018.

[Haschke 2020] Jan Haschke, Gabriel Christmann, Christoph Messmer, Martin Bivour, Mathieu Boccard and Christophe Ballif. *Lateral transport in silicon solar cells.* Journal of Applied Physics, vol. 127, no. 11, 2020.

[Herasimenka 2016] Stanislau Y. Herasimenka, William J. Dauksher, Mathieu Boccard and Stuart Bowden. *ITO/SiOx:H stacks for silicon heterojunction solar cells.* Solar Energy Materials and Solar Cells, vol. 158, pages 98–101, 2016.

[Hermle 2020] Martin Hermle, Frank Feldmann, Martin Bivour, Frank Feldmann, Martin Bivour, Jan Christoph Goldschmidt and Stefan W Glunz. *Passivating contacts and tandem concepts : Approaches for the highest silicon-based solar cell efficiencies Passivating contacts and tandem concepts : Approaches for the highest silicon-based solar cell efficiencies.* Applied Physics Review, vol. 021305, no. November 2019, page 021305, 2020.

[Holman 2014] Zachary C. Holman, Antoine Descoeudres, Loris Barraud, Fernando Zicarelli Fernandez, Johannes P. Seif, Stefaan De Wolf and Christophe Ballif. *Current Losses at the Front of Silicon Heterojunction Solar Cells.* IEEE Journal of Photovoltaics, 2014.

[IEA 2021] IEA. *Net Zero by 2050 - A Roadmap for the Global Energy Sector.* Rapport technique, Paris, 2021.

[III 2009] Joel W Ager III, Lothar A Reichertz, Yi Cui, Yaroslav E Romanyuk, Daniel Kreier, Stephen R Leone, Kin Man Yu, William J Schaff, Wladyslaw Walukiewicz, Lawrence Berkeley and Cyclotron Rd. *Electrical properties of InGaN-Si heterojunctions.* physica status solidi (C), vol. 416, no. 6, pages 413–416, 2009.

[Ingenito 2018] Andrea Ingenito, Gizem Nogay, Quentin Jeangros, Esteban Rucavado, Christophe Allebé, Santhana Eswara, Nathalie Valle, Tom Wirtz, Jörg Horzel, Takashi Koida, Monica Morales-Masis, Matthieu Despeisse, Franz-josef Haug, Philipp Löper and Christophe Ballif. *A passivating contact for silicon solar cells formed during a single firing thermal annealing.* Nature Energy, vol. 3, no. September, 2018.

[IPCC 2014] IPCC, Patrick Eickemeier, Steffen Schlömer, Ellie Farahani, Susanne Kadner, Steffen Brunner, Ina Baum and Benjamin Kriemann. Climate Change 2014 Mitigation of Climate Change Working Group III Contribution to the Fifth Assessment Report of the Intergovernmental Panel on Climate Change. Cambridge University Press, Cambridge, United Kingdom and New York, NY, USA, 2014.

[IPCC 2018] IPCC, Hoegh-Guldberg O., D. Jacob, M. Taylor, M. Bindi, S. Brown, I. Camilloni, A. Diedhiou, R. Djalante, K.L. Ebi, F. Engelbrecht, J. Guiot, Y. Hijioka, S. Mehrotra, A. Payne, S.I. Seneviratne, A. Thomas, R. Warren and G. Zhou. *Impacts of 1.5^{o}C Global Warming on Natural and Human Systems.* Global Warming of 1.5°C. An IPCC Special Report on the impacts of global warming of 1.5°C above pre-industrial levels and related global greenhouse gas emission pathways, in the context of strengthening the global response to the threat of climate change,, 2018.

[IRENA 2019] IRENA. Future of Solar Photovoltaic: Deployment, investment, technology, grid integration and socio-economic aspects (A Global Energy Transformation: paper). Abu Dhabi, 2019.

[Jarolimek 2015] K Jarolimek, E Hazrati, R A De Groot and G A De Wijs. *Band offsets at the crystalline/amorphous silicon interface from first-principles.* In APS March Meeting Abstracts, pages A8—-013, 2015.

[Jiang 2009] C.-S. Jiang, Y. Yan, H.R. Moutinho and M. M. Al-Jassim. *Phosphorus and Boron Doping Effects on Nanocrystalline Formation in Hydrogenated Amorphous and Nanocrystalline Mixed-Phase Silicon Thin Films.* In MRS Online Proceedings Library (OPL), volume 1153, 2009.

[Kane 1988] David E Kane and R.M. Swanson. *Electron-hole collisions in concentrator solar cells.* In Conference Record of the Twentieth IEEE Photovoltaic Specialists Conference, pages 512–517, 1988.

[Kerr 2002] Mark J. Kerr, Andres Cuevas and Ronald A. Sinton. *Generalized analysis of quasi-steady-state and transient decay open circuit voltage measurements.* Journal of Applied Physics, vol. 91, no. 1, pages 399–404, 2002.

[Kerr 2003] Mark J Kerr, Andres Cuevas and Patrick Campbell. *Limiting Efficiency of Crystalline Silicon Solar Cells Due to Coulomb-Enhanced Auger Recombination.* Progress in Photovoltaics: Research and Applications, vol. 104, no. June 2002, pages 97–104, 2003.

[Khanna 2013] Ankit Khanna, Thomas Mueller, Rolf A Stangl, Bram Hoex, Prabir K Basu and Armin G Aberle. *A Fill Factor Loss Analysis Method for Silicon Wafer Solar Cells.* IEEE Journal of Photovoltaics, vol. 3, no. 4, pages 1170–1177, 2013.

[Kim 2006] Byoung-June Kim, Youn-Mo Choi, Kunal Girotra, Sung-Hoon Yang, Shi-Yul Kim, Soon-Kwon Lim and Jun-Hyung Souk. *A study of oxygen reduction of Tin-or Zinc-doped indium oxide (ITO or IZO) film induced by deposition of silicon nitride film in PECVD process.* In MRS Online Proceedings Library (OPL), volume 936, 2006.

[Klaassen 1992] D. B. M. Klaassen. *A unified mobility model for device simulation-I. Model equations and concentration dependence.* Solid State Electronics, vol. 35, no. 7, pages 953–959, 1992.

[Koh 1999] Joohyun Koh, H. Fujiwara, R. J. Koval, C. R. Wronski and R. W. Collins. *Real time spectroscopic ellipsometry studies of the nucleation and growth of p-type microcrystalline silicon films on amorphous silicon using B2H6, B(CH3)3 and BF3 dopant source gases.* Journal of Applied Physics, vol. 85, no. 8 I, pages 4141–4153, 1999.

[Kruse 2020] Christian Kruse, Felix Haase, Martin Rudolph, Thorsten Dullweber, Maximilian St, Verena Mertens, Robby Peibst, Rolf Brendel, Birgit Beier and J Philip. *Solar Energy Materials and Solar Cells Evolutionary PERC + solar cell efficiency projection towards 24 shadow-mask-deposited poly-Si fingers below the Ag front contact as next improvement step.* Solar Energy Materials and Solar Cells, vol. 212, no. May, pages 1–8, 2020.

[Kurtz 2020] Sarah R Kurtz, Ashling Mehdi Leilaeioun, Richard R King, Ian Marius Peters, Michael J Heben, Wyatt K Metzger and Nancy M Haegel. *Revisiting the Terawatt Challenge.* Material Matters, vol. 45, no. March, pages 159–164, 2020.

[Lachenal 2016] Damien Lachenal, Derk Baetzner, Walter Frammelsberger, Boris Legradic, Jerôme Meixenberger, Pierre Papet, Benjamin Strahm and Guillaume Wahli. *Heterojunction and Passivated Contacts: A Simple Method to Extract Both n/tco and p/tco Contacts Resistivity.* Energy Procedia, vol. 92, pages 932–938, 2016.

[Lachowicz 2021] Agata Lachowicz, Gaëlle Andreatta, Nicolas Blondiaux, Julien Gay, Antonin Faes, Nicolas Badel, Jun Zhao, Christophe Allébe, Antoine Descoeudres, Bertrand Paviet-Salomon, Sylvain Nicolay and Christophe Ballif. *Patterning Techniques for Copper Electoplated Metallization of Silicon Heterojunction Cells.* In 2021 IEEE 48th Photovoltaic Specialists Conference (PVSC), pages 1530–1533, 2021.

[Ledinský 2016] Martin Ledinský, Bertrand Paviet-Salomon, Aliaksei Vetushka, Jonas Geissbühler, Andrea Tomasi, Matthieu Despeisse, Stefaan De Wolf, Christophe Ballif and Antonín Fejfar. *Profilometry of thin films on rough substrates by Raman spectroscopy.* Scientific Reports, vol. 6, no. 1, pages 4–10, 2016.

[Lehmann 2019] Mario Lehmann, Nathalie Valle, Jörg Horzel, Alisa Pshenova, Philippe Wyss, Max Döbeli, Matthieu Despeisse, Santhana Eswara, Tom Wirtz, Quentin Jeangros, Aïcha Hessler-wyser, Franz-josef Haug, Andrea Ingenito and Christophe Ballif. *Solar Energy Materials and Solar Cells Analysis of hydrogen distribution and migration in fired passivating contacts.* Solar Energy Materials and Solar Cells, vol. 200, no. March, page 110018, 2019.

[Leilaeioun 2017] Mehdi Leilaeioun, William Weigand, Pradyumna Muralidharan, Mathieu Boccard, Dragica Vasileska, Stephen Goodnick and Zachary Holman. *TLM measurements varying the intrinsic a-Si:H layer thickness in silicon heterojunction solar cells.* In 2017 IEEE 44th Photovoltaic Specialist Conference (PVSC), pages 1790–1793. IEEE, 2017.

[Leilaeioun 2020] Mehdi Ashling Leilaeioun, William Weigand, Mathieu Boccard, Zhengshan J. Yu, Kathryn Fisher and Zachary C. Holman. *Contact resistivity of the p-Type amorphous silicon hole contact in silicon heterojunction solar cells.* IEEE Journal of Photovoltaics, vol. 10, no. 1, pages 54–62, 2020.

[Li 2021a] Shenghao Li, Manuel Pomaska, Andreas Lambertz and Weiyuan Duan. *Supplemental information front contacts for high-efficiency silicon heterojunction solar cells.* Joule, vol. 5, no. 6, page sup. info., 2021.

[Li 2021b] Shenghao Li, Manuel Pomaska, Andreas Lambertz, Shenghao Li, Manuel Pomaska, Andreas Lambertz, Weiyuan Duan, Karsten Bittkau, Depeng Qiu, Zhirong Yao, Martina Luysberg, Paul Steuter and Malte Ko. *Transparent-conductive-oxide-free front contacts for high-efficiency silicon heterojunction solar cells.* Joule, vol. 5, no. 6, pages 1535–1547, 2021.

[Lin 2020] Wenjie Lin, Mathieu Boccard, Sihua Zhong, Vincent Paratte, Quentin Jeangros, Luca Antognini, Jean Cattin, Jonathan Thomet, Zongtao Liu, Zhiming Chen, Zongcun

Liang, Pingqi Gao, Julie Dre, Hui Shen and Christophe Ballif. *Degradation Mechanism and Stability Improvement of Dopant-Free ZnO/LiF.* ACS Applied Nano Materials, vol. 3, no. 11, pages 11391—-11398, 2020.

[Liu 2020] Wenzhu Liu, Liping Zhang, Xinbo Yang, Jianhua Shi, Lingling Yan, Lujia Xu, Zhuopeng Wu, Renfang Chen, Jun Peng, Jingxuan Kang, Kai Wang, Fanying Meng, Stefaan De Wolf and Zhengxin Liu. *Damp-Heat-Stable, High-Efficiency, Industrial-Size Silicon Heterojunction Solar Cells.* Joule, vol. 4, no. 4, pages 913–927, 2020.

[LONGi 2019] LONGi. *LONGi Solar établit un nouveau record mondial avec ses cellules solaires mono-PERC bifaciales à 24,06 pour cent*, 2019.

[Luderer 2021] Christoph Luderer, Leonard Tutsch, Christoph Messmer, Martin Hermle and Martin Bivour. *Influence of TCO and a-Si:H Doping on SHJ Contact Resistivity.* IEEE Journal of Photovoltaics, vol. 11, no. 2, pages 329–336, 2021.

[Luderer 2022] Christoph Luderer, Dilara Kurt, Anamaria Moldovan, Martin Hermle and Martin Bivour. *Solar Energy Materials and Solar Cells Intrinsic layer modification in silicon heterojunctions : Balancing transport and surface passivation.* Solar Energy Materials and Solar Cells, vol. 238, no. January, page 111412, 2022.

[Luque 1993] A Luque and I Tobias. *Perimeter recombination in planar solar cells.* Journal of applied physics, vol. 73, no. 8, pages 4042–4047, 1993.

[Luysberg 1997] M Luysberg, P Hapke, R Carius and F Finger. *Structure and growth of hydrogenated microcrystalline silicon : Investigation by transmission electron microscopy and Raman spectroscopy of films grown at different plasma excitation frequencies.* Philosophical magazine A, vol. 75, no. 1, pages 31–47, 1997.

[Manzoor 2021] Salman Manzoor and Mariana Bertoni. *Degradation of Surface Recombination Velocity at a-Si/c-Si interface under light and temperature.* In 2021 IEEE 48th Photovoltaic Specialists Conference (PVSC), pages 1286—-1288. IEEE, 2021.

[Masetti 1983] Guido Masetti, Maurizio Severi and Sandro Solmi. *Modeling of Carrier Mobility Against Carrier Concentration in Arsenic-, Phosphorus-, and Boron-Doped Silicon.* IEEE Transactions on electron devices, vol. 30, no. 7, pages 764–769, 1983.

[Matsui 2004] Takuya Matsui, Michio Kondo and Akihisa Matsuda. *Doping properties of boron-doped microcrystalline silicon from B2H6 and BF3 : Material properties and solar cell performance.* Journal of Non-Crystalline Solids, vol. 338-340, no. 1 SPEC. ISS., pages 646–650, 2004.

[Matsui 2020] Takuya Matsui, Martin Bivour, Martin Hermle and Hitoshi Sai. *Atomic-Layer-Deposited TiOx Nanolayers Function as Efficient Hole-Selective Passivating Contacts in Silicon Solar Cells.* ACS Applied Materials & Interfaces, vol. 12, no. 44, pages 49777—-49785, 2020.

[Mazzarella 2015] L. Mazzarella, S. Kirner, B. Stannowski, L. Korte, B. Rech and R. Schlatmann. *P-type microcrystalline silicon oxide emitter for silicon heterojunction solar cells allowing current densities above 40 mA/cm2.* Applied Physics Letters, vol. 106, no. 2, 2015.

[Mazzarella 2017] Luana Mazzarella, Simon Kirner, Onno Gabriel, Sebastian S. Schmidt, Lars Korte, Bernd Stannowski, Bernd Rech and Rutger Schlatmann. *Nanocrystalline silicon emitter optimization for Si-HJ solar cells: Substrate selectivity and CO2 plasma treatment effect.* Physica Status Solidi (A) Applications and Materials Science, vol. 214, no. 2, 2017.

[Mazzarella 2018a] Luana Mazzarella, A. B. Morales-Vilches, L. Korte, R. Schlatmann and B. Stannowski. *Ultra-thin nanocrystalline n-type silicon oxide front contact layers for rear-emitter silicon heterojunction solar cells.* Solar Energy Materials and Solar Cells, vol. 179, no. January, pages 386–391, 2018.

[Mazzarella 2018b] Luana Mazzarella, Ana Belen Morales-Vilches, Max Hendrichs, Simon Kirner, Lars Korte, Rutger Schlatmann and Bernd Stannowski. *Nanocrystalline n-type silicon oxide front contacts for silicon heterojunction solar cells: Photocurrent enhancement on planar and textured substrates.* IEEE Journal of Photovoltaics, vol. 8, no. 1, pages 70–78, 2018.

[Mazzarella 2020] Luana Mazzarella, Anna B. Morales-Vilches, Lars Korte, Rutger Schlatmann and Bernd Stannowski. *Versatility of Nanocrystalline Silicon Films : from Thin-Film to Perovskite/c-Si Tandem Solar Cell Applications.* Coatings, vol. 10, no. 8, page 759, 2020.

[Mcintosh 2017] Keith R Mcintosh. *On effective surface recombination parameters.* Journal of Applied Physics, vol. 014503, no. April 2014, 2017.

[Meier 1984] Daniel L. Meier and Dieter K. Schroder. *Contact Resistance: Its Measurement and Relative Importance to Power Loss in a Solar Cell.* IEEE Transactions on Electron Devices, vol. 31, no. 5, pages 647–653, 1984.

[Messmer 2018] Christoph Messmer, Martin Bivour, Jonas Schön, Stefan W Glunz and Martin Hermle. *Numerical Simulation of Silicon Heterojunction Solar Cells Featuring Metal Oxides as Carrier-Selective Contacts.* Ieee Journal of Photovoltaics, vol. 1, pages 1–9, 2018.

[Meyer 2021] Frank Meyer, Arnaud Savoy, Juan J Diaz, Marc Persoz, Xavier Niquille, Christophe Alleb, Sylvain Nicolay, Franz-josef Haug and Andrea Ingenito. *Solar Energy Materials and Solar Cells Optimization of front SiNx/ITO stacks for high-efficiency two-side contacted c-Si solar cells with co-annealed front and rear passivating contacts.* Solar Energy Materials and Solar Cells, vol. 219, no. 219, page 110815, 2021.

[Morales-Masis 2018] Monica Morales-Masis, Esteban Rucavado, Raphael Monnard, Loris Barraud, Jakub Holovsky, Matthieu Despeisse, Mathieu Boccard and Christophe Ballif. *Highly Conductive and Broadband Transparent Zr-Doped In2O3 as Front Electrode for Solar Cells.* IEEE Journal of Photovoltaics, vol. 8, no. 5, pages 1202–1207, 2018.

[Morales-Vilches 2019] Anna B. Morales-Vilches, Alexandros Cruz, Sebastian Pingel, Sebastian Neubert, Luana Mazzarella, Daniel Meza, Lars Korte, Rutger Schlatmann and Bernd Stannowski. *ITO-Free Silicon Heterojunction Solar Cells With ZnO:Al/SiO2 Front Electrodes Reaching a Conversion Efficiency of 23%.* IEEE Journal of Photovoltaics, vol. 9, no. 1, pages 34–39, 2019.

[Moro 2018] Alberto Moro and Laura Lonza. *Electricity carbon intensity in European Member States : Impacts on GHG emissions of electric vehicles.* Transportation Research Part D, vol. 64, no. November 2016, pages 5–14, 2018.

[Nagel 1999] Henning Nagel, Christopher Berge and Armin G. Aberle. *Generalized analysis of quasi-steady-state and quasi-transient measurements of carrier lifetimes in semiconductors.* Journal of Applied Physics, vol. 86, no. 11, pages 6218–6221, 1999.

[Niemelä 2019] Janne-petteri Niemelä, Bart Macco, Loris Barraud, Antoine Descoeudres, Nicolas Badel, Matthieu Despeisse, Gabriel Christmann, Sylvain Nicolay, Christophe Ballif, Wilhelmus M M Kessels and Mariadriana Creatore. *Rear-emitter silicon heterojunction solar cells with atomic layer deposited ZnO:Al serving as an alternative transparent conducting oxide to In2O3:Sn.* Solar Energy Materials and Solar Cells, vol. 200, no. May, page 109953, 2019.

[Olibet 2007] Sara Olibet, Evelyne Vallat-Sauvain and Christophe Ballif. *Model for a-Si:H/c-Si interface recombination based on the amphoteric nature of silicon dangling bonds.* Physical Review B - Condensed Matter and Materials Physics, vol. 76, no. 3, pages 1–14, 2007.

[Onno 2019] Arthur Onno, Christopher Chen, Priyaranga Koswatta, Mathieu Boccard and Zachary C. Holman. *Passivation, conductivity, and selectivity in solar cell contacts: Concepts and simulations based on a unified partial-resistances framework.* Journal of Applied Physics, vol. 126, no. 18, page 183103, 2019.

[Opdorp 1969] Christianus Johannes Marinus Van Opdorp. *Si-Ge isotype heterojunctions.* PhD thesis, 1969.

[OurWorldInData 2020a] OurWorldInData, Hannah Ritchie and Max Roser. *CO2 and Greenhouse Gas Emissions.* Our World in Data, 2020.

[OurWorldInData 2020b] OurWorldInData, Hannah Ritchie and Max Roser. *Why did renewables become so cheap so fast?* Our World in Data, 2020.

[Paduthol 2018] Appu Paduthol, Mattias K Juhl, Gizem Nogay, Philipp Löper, Andrea Ingenito and Thorsten Trupke. *Impact of different capping layers on carrier injection efficiency between amorphous and crystalline silicon measured using photoluminescence.* Solar Energy Materials and Solar Cells, vol. 187, no. March, pages 55–60, 2018.

[Paviet-Salomon 2015] Bertrand Paviet-Salomon, Andrea Tomasi, Antoine Descoeudres, Loris Barraud, Sylvain Nicolay, Matthieu Despeisse, Stefaan De Wolf and Christophe Ballif.

Back-Contacted Silicon Heterojunction Solar Cells : Optical-Loss Analysis and Mitigation. IEEE Journal of Photovoltaics, vol. 5, no. 5, pages 1293–1303, 2015.

[Peibst 2014] R Peibst, EP Rugeramigabo and KR Hofmann. *Electrical characterization and modelling of n – n Ge-Si heterojunctions with relatively low interface state densities.* Journal of Applied Physics, vol. 124502, no. November 2012, page 124502, 2014.

[Procel 2018] Paul Procel, Guangtao Yang, Olindo Isabella and Miro Zeman. *Theoretical evaluation of contact stack for high efficiency IBC-SHJ solar cells.* Solar Energy Materials and Solar Cells, vol. 186, no. June, pages 66–77, 2018.

[Procel 2020] Paul Procel, Haiyuan Xu, Aurora Saez, Carlos Ruiz-Tobon, Luana Mazzarella, Yifeng Zhao, Can Han, Guangtao Yang, Miro Zeman and Olindo Isabella. *The role of heterointerfaces and subgap energy states on transport mechanisms in silicon heterojunction solar cells.* Progress in Photovoltaics: Research and Applications, vol. 28, no. 9, pages 935–945, 2020.

[PV-Lighthouse 2016] PV-Lighthouse. *Wafer Ray tracter*, 2016.

[Pv-magazine 2021a] Pv-magazine. *Longi improves efficiency of its heterojunction cell from 25.82 to 26.30% in just one week.* pv-magazine, 2021.

[PV-magazine 2021b] PV-magazine and Ralph Diermann. *Meyer Burger wants to build another 400 MW factory.* 2021.

[PV-TECH 2019] PV-TECH and Finlay Colville. *PV CellTech 2020 to explain why n-PERT emerging as differentiated play for Chinese leaders*, 2019.

[Pysch 2007] D. Pysch, A. Mette and S. W. Glunz. *A review and comparison of different methods to determine the series resistance of solar cells.* Solar Energy Materials and Solar Cells, vol. 91, no. 18, pages 1698–1706, 2007.

[Qiu 2021] Depeng Qiu, Weiyuan Duan, Andreas Lambertz, Zhuopeng Wu, Karsten Bittkau, Kaifu Qiu, Zhirong Yao, Uwe Rau and Kaining Ding. *Function Analysis of the Phosphine Gas Flow for n-Type Nanocrystalline Silicon Oxide Layer in Silicon Heterojunction Solar Cells.* ACS Applied Energy Materials, vol. 4, no. 8, pages 7544–7551, 2021.

[Richter 2013] Armin Richter, Martin Hermle and Stefan W. Glunz. *Reassessment of the Limiting Efficiency for Crystalline Silicon Solar Cells.* IEEE Journal of Photovoltaics, vol. 3, no. 4, pages 1184–1191, oct 2013.

[Richter 2017] Armin Richter, Jan Benick, Frank Feldmann, Andreas Fell, Martin Hermle and Stefan W Glunz. *n-Type Si solar cells with passivating electron contact : Identifying sources for efficiency limitations by wafer thickness and resistivity variation.* Solar Energy Materials and Solar Cells, vol. 173, no. May, pages 96–105, 2017.

[Richter 2018] Alexei Richter, Vladimir Smirnov, Andreas Lambertz, Keita Nomoto, Katharina Welter and Kaining Ding. *Versatility of doped nanocrystalline silicon oxide for applications in silicon thin-film and heterojunction solar cells.* Solar Energy Materials and Solar Cells, vol. 174, no. April 2017, pages 196–201, 2018.

[Richter 2021] Armin Richter, Ralph Müller, Jan Benick, Frank Feldmann, Bernd Steinhauser, Christian Reichel, Andreas Fell, Martin Bivour, Martin Hermle and Stefan W Glunz. *Design rules for high-efficiency both-sides- contacted silicon solar cells with balanced charge carrier transport and recombination losses.* Nature Energy, 2021.

[Ritzau 2014] Kurt-Ulrich Ritzau, Martin Bivour, Sebastian Schröer, Heiko Steinkemper, Patrick Reinecke, Florian Wagner and Martin Hermle. *TCO work function related transport losses at the a-Si:H/TCO-contact in SHJ solar cells.* Solar Energy Materials and Solar Cells, vol. 131, pages 9–13, 2014.

[Roe 2019] Ellis T. Roe, Kira E. Egelhofer and Mark C. Lonergan. *Exchange current density model for the contact-determined current-voltage behavior of solar cells.* Journal of Applied Physics, vol. 125, no. 22, 2019.

[Ru 2020] Xiaoning Ru, Minghao Qu, Jianqiang Wang, Tianyu Ruan, Miao Yang, Fuguo Peng, Wei Long, Kun Zheng, Hui Yan and Xixiang Xu. *25.11% Efficiency Silicon Heterojunction Solar Cell With Low Deposition Rate Intrinsic Amorphous Silicon Buffer Layers.* Solar Energy Materials and Solar Cells, vol. 215, no. June, page 110643, 2020.

[Rucavado 2019] Esteban Rucavado, Federica Landucci, Max Döbeli, Quentin Jeangros, Mathieu Boccard, Aïcha Hessler-Wyser, Christophe Ballif and Monica Morales-Masis. *Zr-doped indium oxide electrodes: Annealing and thickness effects on microstructure and carrier transport.* Physical Review Materials, vol. 3, no. 8, pages 1–9, 2019.

[Schäfer 2018] Sören Schäfer and Rolf Brendel. *Accurate Calculation of the Absorptance Enhances Efficiency Limit of Crystalline Silicon Solar Cells With Lambertian Light Trapping.* IEEE Journal of Photovoltaics, vol. 8, no. 4, pages 1156–1158, 2018.

[Schäfer 2019] S Schäfer, F Haase, C Hollemann, J Hensen, J Krügener, R Brendel, R Peibst, Solarenergieforschung Hameln and Am Ohrberg. *Solar Cells 26%-efficient and 2 cm narrow interdigitated back contact silicon solar cells with passivated slits on two edges.* Solar Energy Materials and Solar Cells, vol. 200, no. July, page 110021, 2019.

[Seif 2016] Johannes P. Seif, Antoine Descoeudres, Gizem Nogay, Simon Hanni, Silvia Martin De Nicolas, Niels Holm, Jonas Geissbuhler, Aicha Hessler-Wyser, Martial Duchamp, Rafal E. Dunin-Borkowski, Martin Ledinsky, Stefaan De Wolf and Christophe Ballif. *Strategies for Doped Nanocrystalline Silicon Integration in Silicon Heterojunction Solar Cells.* IEEE Journal of Photovoltaics, vol. 6, no. 5, pages 1132–1140, 2016.

[Senaud 2021a] Laurie-Lou Senaud. *Electrical Losses Mitigation in Silicon Heterojunction Solar Cells.* PhD thesis, EPFL, 2021.

[Senaud 2021b] Laurie-Lou Senaud, Paul Procel, Gabriel Christmann, Antoine Descoeudres, Jonas Geissbühler, Christophe Allebé, Nicolas Badel, Philippe Wyss, Mathieu Boccard, Olindo Isabella, Miro Zeman, Sylvain Nicolay, Matthieu Despeisse, Christophe Ballif and B. Paviet-Salomon. *Advanced method for electrical characterization of carrier-selective passivating contacts using transfer-length- method measurements under variable illumination.* Journal of Applied Physics, vol. 129, no. 19, page 195707, 2021.

[Shah 2010] Arvind Shah. Thin-film silicon solar cells. EPFL press Lausanne, 2010.

[Shockley 1961] William Shockley and Hans J. Queisser. *Detailed balance limit of efficiency of p-n junction solar cells.* Journal of Applied Physics, vol. 32, no. 3, pages 510–519, 1961.

[Sinton 1996] R.A. Sinton, A. Cuevas and M. Stuckings. *Quasi-steady-state photoconductance, a new method for solar cell material and device characterization.* Conference Record of the Twenty Fifth IEEE Photovoltaic Specialists Conference - 1996, pages 457–460, 1996.

[Sinton 2000] Ronald A. Sinton and A. Cuevas. *A Quasi-Steady-State Open-Circuit Voltage Method for Solar Cell Characterization.* In 16th European Photovoltaic Solar Energy Conference, numéro May, pages 1–4, 2000.

[Smit 2003] C. Smit, R. A.C.M.M. Van Swaaij, H. Donker, A. M.H.N. Petit, W. M.M. Kessels and M. C.M. Van de Sanden. *Determining the material structure of microcrystalline silicon from Raman spectra*, 2003.

[Söderström 2020] Thomas Söderström, P. Papet, Y. Yao and J. Ufheil. *Smartwire Connection Technology.* Rapport technique, 2020.

[Stradins 2009] Paul Stradins, Charles W. Teplin and Howard M. Branz. *Phase evolution in nanocrystalline silicon films: Hydrogen dilution and the cone kinetics model.* Philosophical Magazine, vol. 89, no. 28-30, pages 2461–2468, 2009.

[Sze 2006] S. M. Sze and K. Ng Kwok. Physics of semiconductor devices. Wiley-Interscience, 2006.

[Tiedje 1984] Tom O M Tiedje, Eli L I Yablonovitch, George D. G.D. Cody and Bonnie G. B.G. Bonnie G Brooks. *Limiting Efficiency of Silicon.* IEEE transactions on electron devices, vol. 31, no. 5, pages 711–716, 1984.

[Tomasi 2017] Andrea Tomasi, Bertrand Paviet-Salomon, Quentin Jeangros, Jan Haschke, Gabriel Christmann, Loris Barraud, Antoine Descoeudres, Johannes PeterSeif, Sylvain Nicolay, Matthieu Despeisse, Stefaan De Wolf and Christophe Ballif. *Simple processing of back-contacted silicon heterojunction solar cells using selective-area crystalline growth.* Nature Energy, vol. 2, no. 5, pages 1–8, 2017.

[Trupke 2007] T Trupke, R A Bardos, M C Schubert and W Warta. *Photoluminescence imaging of silicon wafers.* Applied Physics Letters, vol. 044107, no. October 2005, pages 1–4, 2007.

[Umishio 2020] Hiroshi Umishio, Hitoshi Sai, Takashi Koida and Takuya Matsui. *Nanocrystalline-silicon hole contact layers enabling efficiency improvement of silicon heterojunction solar cells: Impact of nanostructure evolution on solar cell performance.* Progress in Photovoltaics: Research and Applications, no. July, pages 1–13, 2020.

[UNECE 2021] UNECE. *Life Cycle Assessment of Electricity Generation Options.* Rapport technique, United Nations Economic Commission for Europe, 2021.

[Valdes 1952] L B Valdes. *Resistivity Measurements on Germanium for Transistors.* In Proceedings of the IRE, volume 29, pages 420–427, 1952.

[VDMA 2021] VDMA. *International Technology Roadmap for Photovoltaic*, 2021.

[Verlinden 2020] P. J. Verlinden. *Future challenges for photovoltaic manufacturing at the terawatt level.* Journal of Renewable and Sustainable Energy, vol. 053505, no. October, 2020.

[Victoria 2021] Marta Victoria, Nancy Haegel, Ian Marius Peters, Ron Sinton, Arnulf Ja, Carlos Can, Christian Breyer, Matthew Stocks, Andrew Blakers and Izumi Kaizuka. *Perspective Solar photovoltaics is ready to power a sustainable future.* Joule, pages 1041–1056, 2021.

[Watahiki 2015] Tatsuro Watahiki, Takeo Furuhata, Tsutomu Matsuura, Tomohiro Shinagawa, Yusuke Shirayanagi, Takayuki Morioka, Tetsuro Hayashida, Yohei Yuda, Shintaro Kano, Yuichi Sakai, Hidetada Tokioka, Yoshihiko Kusakabe and Hiroyuki Fuchigami. *Rear-emitter Si heterojunction solar cells with over 23% efficiency.* Applied Physics Express, vol. 8, no. 2, page 021402, 2015.

[Wilson 2020] Gregory M Wilson, Mowafak Al-jassim, Wyatt K Metzger, Stefan W Glunz, Pierre Verlinden, Gang Xiong, Lorelle M Mansfield, Billy J Stanbery, Kai Zhu, Yanfa Yan, Joseph J Berry, Aaron J Ptak, Frank Dimroth, Brendan M Kayes, Adele C Tamboli, Robby Peibst, Kylie Catchpole, Matthew O Reese, Christopher S Klinga, Paul Denholm, Mahesh Morjaria, Michael G Deceglie and Dana B Sulas-kern. *The 2020 photovoltaic technologies roadmap.* Journal of Physics D: Applied Physics, vol. 53, no. 49, page 493001, 2020.

[Wolf 1963] Martin Wolf and Hans Rauschenbach. *Resistance effects on solar cell measurements.* Advanced Energy Conversion, vol. 3, pages 455–479, 1963.

[Wurfel 2015] Uli Wurfel, Andres Cuevas and Peter Wurfel. *Charge carrier separation in solar cells.* IEEE Journal of Photovoltaics, vol. 5, no. 1, pages 461–469, 2015.

[Yan 2021] Di Yan, Andres Cuevas, Ibarra Michel, Chun Zhang, Yimao Wan and Xinyu Zhang. *Polysilicon passivated junctions : The next technology for silicon solar cells ?* Joule, vol. 5, no. 4, pages 1–18, 2021.

[Yoshikawa 2017] Kunta Yoshikawa, Hayato Kawasaki, Wataru Yoshida, Toru Irie, Katsunori Konishi, Kunihiro Nakano, Toshihiko Uto, Daisuke Adachi, Masanori Kanematsu, Hisashi Uzu and Kenji Yamamoto. *Silicon heterojunction solar cell with interdigitated back contacts for a photoconversion efficiency over 26%.* Nature Energy, vol. 2, no. 5, 2017.

[You 2021] Jiachuan You, Lei Zhao, Hongwei Diao and Wenjing Wang. *Synergistic effect of CO2 and PH3 on the properties of n-type nanocrystalline silicon oxide prepared by plasma-enhanced chemical vapor deposition.* Journal of Materials Science: Materials in Electronics, vol. 32, no. 3, pages 2814–2821, 2021.

[Yuguchi 2012] Tetsuya Yuguchi, Yosuke Kanie, Nobuyuki Matsuki and Hiroyuki Fujiwara. *Complete parameterization of the dielectric function of microcrystalline silicon fabricated by plasma-enhanced chemical vapor deposition.* Journal of Applied Physics, vol. 111, no. 8, 2012.

[Zhao 1998] Jianhua Zhao, Aihua Wang, Martin A Green and Francesca Ferrazza. *19.8% efficient "honeycomb" textured multicrystalline and 24.4% monocrystalline silicon solar cells.* Applied physics letters, vol. 1991, no. July, pages 1–4, 1998.

[Zhao 2018] J Zhao, M König, Y Yao, Y C Wang, R Zhou, T Xie, H Deng, Meyer Burger, Germamy Gmbh and An Der Baumschule. *> 24% silicon heterojunction solar cells on meyer burger's on mass production tools and how wafer material impacts cell parameters.* In 2018 IEEE 7th World Conference on Photovoltaic Energy Conversion (WCPEC), pages 1514–1519, 2018.

[Zhao 2020] Yifeng Zhao, Luana Mazzarella, Paul Procel, Can Han, Guangtao Yang, Arthur Weeber, Miro Zeman and Olindo Isabella. *Doped hydrogenated nanocrystalline silicon oxide layers for high-efficiency c-Si heterojunction solar cells.* Progress in Photovoltaics: Research and Applications, vol. 28, no. 5, pages 425–435, 2020.

[Zhong 2019] Sihua Zhong, Monica Morales-Masis, Mathias Mews, Lars Korte, Quentin Jeangros, Weiliang Wu, Mathieu Boccard and Christophe Ballif. *Exploring co-sputtering of ZnO:Al and SiO2 for efficient electron-selective contacts on silicon solar cells.* Solar Energy Materials and Solar Cells, vol. 194, no. February, pages 67–73, 2019.

[Zhong 2020] Sihua Zhong, Julie Dreon, Quentin Jeangros, Erkan Aydin, Stefaan De Wolf, Fan Fu, Mathieu Boccard and Christophe Ballif. *Mitigating Plasmonic Absorption Losses at Rear Electrodes in High-Efficiency Silicon Solar Cells Using Dopant-Free Contact Stacks.* Advanced Functional Materials, vol. 30, no. 5, pages 1–9, 2020.

Remerciements

Je garderai toute ma vie un magnifique souvenir des mes années passées au PV-Lab. Cette période aura été pour moi un moment de maturation professionnel, rempli de rencontres et collaborations inoubliables avec des personnes chaleureuses, brillantes et amicales.

Tout d'abord, je remercie évidemment Christophe de m'avoir accueilli au sein du PV-Lab. Je te remercie particulièrement pour ton énorme implication, tant scientifique que politique, dans un établissement concret du PV à large échelle, plus que jamais nécessaire aujourd'hui - mais aussi de créer un esprit de cohésion au sein de cette communauté. Je remercie Mathieu, mon superviseur et chef de groupe durant toutes ces longues années, qui m'a guidé dans ce domaine complexe et suivi chaque semaine durant plus de quatre ans. Je te remercie particulièrement d'avoir gardé tes engagements jusqu'à la fin de ma thèse, même lorsque tu avais démarré sous d'autres horizons professionnels.

Je remercie également du fond du cœur Laurie-Lou ... pardon Dr. Senaud!... pour m'avoir présenté et introduit dans le monde du PV-Lab, ainsi que d'avoir été une aussi bonne amie et mentor toutes ces années. De nombreux résultats présents dans cette thèse n'auraient pas été réalisés sans tes précédents développements sur les mesures TLM ou la caractérisation des couches nano-cristallines. J'espère que tu liras ces lignes avec plaisir et que l'on continuera de résoudre des énigmes ensemble. Un grand merci également à Deniz, pour son dynamisme et pour avoir toujours accepté de commenter mon travail et de discuter de questions théoriques complexes. Je le remercie particulièrement de m'avoir autorisé à utiliser son modèle pour le calcul des pertes au périmètre.

Je remercie (et souhaite bonne chance!) à Julie, avec qui l'on a traversé ensemble les épreuves de la thèse avec ses hauts et ses bas. Je te remercie pour ton amitié et soutient et pour ton énergie investie dans l'organisation de toutes ces activités pour faire vivre Microcity! Un grand merci à Jean, pas seulement pour avoir été un super bon mentor, mais pour m'avoir encouragé à aller transpirer un peu, même dans les périodes chargées! Merci de m'avoir montrer que doctorat et vie saine ne sont pas des oxymores! Je remercie également Wenjie pour ses enseignements philosophiques, qui ont été cruciaux pour moi pour finir cette thèse, ainsi qu'à Alejandro pour avoir apporté cette dose fraiche d'humour dont on avait besoin. Un merci spécial à Mario également, pour avoir partagé toute cette aventure EPFL ensemble, et pour avoir emmener c'te équipe à des illustres sommets. Et encore un grand merci pour tout

les moments partagés ensemble et bon courage à mes plus jeunes (ou énergétiques) collègues pour la suite : Sofia, Ezgi, Quentin, Audrey, Jonathan, Olatz, Luca, Julien, Fabiana, Kerem et Samira. Je remercie également mes étudiants, Lison et Corentin, pour leur engagement, autonomie, détermination et patience. J'ai eu un énorme plaisir à travailler avec vous et je me réjouis de savoir que vous continuerez l'aventure solaire!

Je tiens aussi à remercier tous les autres membres du PV-Lab, qui réalisent chaque jour mille et une tâche rendant possible notre travail: Aïcha, Karine, Cédric, Nicolas F., Aymeric, Sylvain, Xavier, Joël, Hassan, Nicolas W., Franz : un grand merci! Je suis aussi également reconnaissant envers tous les anciens membre de mon groupe, Vincent, Jan, Angela, Sihua et Raphaël pour tout le travail que vous avez réalisé, mais aussi pour tous les bons moments passés ensemble. Je remercie également Gabriel, Bertrand, Matthieu, Nicolas B., ainsi que tous les autres membres du CSEM pour leur collaboration amicale.

Je remercie tous mes amis d'avoir été présents durant ces années et d'avoir crée autant de moments de joie. En particulier, un grand merci à vous, ainsi qu'à mon frère, d'avoir accepté des relire certains passages de ma thèse. Je te remercie d'ailleurs toi, lecteur, d'avoir atteint cette ligne - ça fait plaisir d'avoir un fan! À ma famille, qui m'a toujours apporté amour et soutient, et sans qui rien n'aurait été possible (merci Papa, merci Maman!), je tiens à exprimer ma plus profonde et sincère reconnaissance. Je me réjouis des nouvelles choses que nous promet l'avenir et de pouvoir être présent pour vous à mon tour. Finalement, à celle qui m'a toujours donné de l'amour et du support durant cette période de rédaction, et m'a accepté avec une patience infinie, du fond de mon cœur, merci.

Lausanne, May 6, 2022

Luca Antognini

Luca Antognini

E-mail : luca.antognini@gmail.com

Phone : +41 77 457 26 81

Adress : Faubourg du Lac 52, 2000 Neuchâtel.

Summary

Following my engagement towards renewable energies, I engaged myself towards the obtaining of a Ph.D degree within the Photovoltaics and Thin Film Laboratory (PV-Lab) of EPFL. My research interests included improvements for high efficiency crystalline silicon solar cells as well as development of new materials for photovoltaics. Along my research, a particular focus was given to technics allowing cost-efficient integration in industry to allow for a fast scaling-up of the results. I pursue actually a post-doctoral research in the field of silicon detectors, allowing myself to perfect my competences in microfabrication, project management as well as written and oral presentation skills.

Professional experiences and formation

01.2018 – 04-2022
Research Scientist • Photovoltaics-and Thin Film Laboratory, EPFL, Neuchâtel
- Development of silicon detectors for particles detection towards medical application.

01.2018 – 04-2022
PhD student • Photovoltaics-and Thin Film Laboratory, EPFL, Neuchâtel
- Study and improvements of contacts for high efficiency crystalline silicon heterojunctions solar cells.

06.2017–09.2017
Project collaborator during Civil Service • Photovoltaics-Laboratory, EPFL, Neuchâtel
- Study of semiconductor thin films and characterization of solar cells.

08.2016–06.2017
Project collaborator during Civil Service • Terragir, Meyrin
- Creation and animation of pedagogical sessions on the topic of renewable energies for primary school.

04.2016–08.2016
Scientific collaborator • Laboratory of Food and Soft Materials, ETHZ, Zürich
- Valorization of Master thesis and publication in *The Journal of Chemical Physics.*

2013–04.2016
Master degree in Physics and minor in computational neuroscience • EPFL, Lausanne
- Specialization in theoretical and computational physics, final grade 5.68/6

Skills

- Project Management : R&D methodologies, interdisciplinary coordination, scientific writing and oral communication
- Material science : PECVD, sputtering, evaporation, thin films electric and microscopic characterization
- Programming and desktop tool : R, Matlab, C/C++, Excel, Mathematica, Bash, Word, Latex, vectorial drawing

Language

French :mother tongue **English**: C1/C2 **German**: B1/B2, Master project in Zürich **Italian**: A2, weekly lecture

Personal interests and other Experiences

1998 – 2017
Piano et apprentissage de la musique classique
- Certificat AVCEM et certificat supérieur. Membre du comité de l'organisation d'un festival classique.